DISSERTATION

Self-assembly of photo-crosslinkable block copolymers and their application in 3D printing

Britta Sophie Weidinger

2023

DISSERTATION

zur

Erlangung der Doktorwürde (Dr. rer. nat.)

der

Gesamtfakultät für Mathematik, Ingenieur- und Naturwissenschaften

der

Ruprechts-Karls-Universität Heidelberg

vorgelegt von

Britta Sophie Weidinger

aus München

Tag der mündlichen Prüfung

24.11.2023

Self-assembly of photo-crosslinkable block copolymers and their application in 3D printing

Gutachter

Prof. Dr. Eva Blasco

Prof. Dr. Petra Tegeder

It is familiarity more than anything else that defines difficulty.

ACKNOWLEDGEMENTS

First and foremost, I want to thank you, Eva, for trusting me with this topic for the master thesis, for letting me continue during the doctoral studies, and for having the faith that we would make it work. Thank you for your guidance and your support, especially when it comes to academic writing or creating graphical material presenting my work to the outside world.

Prof. Petra Tegeder I want to thank for agreeing to be the second corrector of this work and for the fruitful collaboration regarding the SNOM analysis of block copolymers.

Prof. Rasmus Schröder, Dr. Irene Wacker and Ronald Curticean, I am beyond grateful for your collective expertise, for teaching and training me, for your continuous support and troubleshooting and for giving me such uncomplicated and unlimited access to labs and instruments. Without you, these projects would not have been possible this way, and I have enjoyed applying the methods a lot.

Prof. Hermann Nirschl, Guohui Yang and Dr. Julian Ungerer I thank for the SAXS measurements that deeply supported my data.

Dr. Christian Huck, Dr. Tanja Schmitt and Nadine von Coelln I thank for the SNOM measurements, especially Nadine for her quick efforts beyond the expected.

Dr. Martin Maier I thank for teaching me most of what I know about organic synthesis. Seldom was there a day in the lab I did not profit from something you taught me.

I also want to thank the varying members of the Blasco group for the nice, collaborative environment and all the fun times we had, as well as the lunch and coffee breaks.

Martina, thank you for taking such great care of the administrative work in the past months, always going above and beyond.

Moritz, thank you for your synthetic efforts during the Forschi time, it was a pleasure to work with you. Good luck during your master thesis!

My master students Ian, Mehran and Viktoria I want to thank for their work towards their respective projects and sticking to them even when things looked dire.

Xiaobing Shi I want to thank for the nice work on the RAFT-project together.

Christoph, thank you for over three years of good office company, building the Heidelberg lab together and for building up my confidence in the project & always having an open ear.

Li-Yun and Joel, thank you for Nano-Café lunches in the very beginning, and thank you Li-Yun for hosting and cooking good food for us.

Samantha, I thank you for all the good times in and outside the lab, troubleshooting not only reactions but also personal matters. It has been very valuable to have you in my life throughout this journey.
Clara, you kept this group running for a long time. Thank you for being an organizational mastermind, your kindness and all the good memories.
Duc, you were a rather late and yet very important addition to 101. Thanks for being my coffee break conspirer, a fellow plant enthusiast, and keeping me updated with duck memes.
Pia, thank you for the running, crafting, and letting me borrow your iPad as well as your Anki cards.
Philipp, thank you for our countless swim-swims, and thank you Finn, Oihane, Lilli and Luna for swims; and the nice summer evenings.
Thank you to Vanessa, Niklas, and the rest of the Thomas group for letting me tag along to your bouldering sessions!

Thank you to Samantha Catt, Pia Klee, Nathalie Kurrle, Duc Tran and Sonja Weißenberger for proof-reading this thesis and providing feedback.

Thank you to all the artists whose music has accompanied me through everything from lab work to the microtome to writing this thesis, with a specific mention of Florence Welsh (and a warning to everyone reading this: Don't play "no rest for the wicked" on a daily basis, you won't be able to listen to it again).

Thank you to all members of the „Bienen-WG" I had the pleasure of living with, for making Heidelberg a home, especially in the pandemic beginning.
Nathalie, Rachel, Sonja, and Tiffany I want to thank for the past 10 years, you were there (literally) from day one. Onto the next 10!
I am indebted to my family who made studying this way possible and supported ideas from Sweden over Hamburg to Baden-Württemberg.
Ben, you got the hard part. Thank you for everything.

ABSTRACT

Natural materials are composed of a limited number of molecular building blocks, e.g. amino acids, carbohydrates), and their exceptional properties are governed by their intricate hierarchical structure on multiple length scales. While 3D printing has emerged as the standard method for the precise fabrication of minute devices, this level of precision is unattainable with current state-of-the-art materials for 3D printing.

A common method of obtaining such nanoscale structure in systematic systems exploits the potential for polymers to self-assemble under certain conditions. One important class of polymers which has the ability to form self-assembled structures at a scale of 5- 50 nm are amphiphilic block copolymers. They are tunable over a broad variety of morphologies, ranging from micelles and vesicles to continuous network structures, which can form in both undiluted melt or solution. While these properties have been extensively investigated in 2D films, they have not yet been exploited to generate 3D structures entailing high resolution features, complex geometries and a controlled nanostructure.

To that end, in the current PhD thesis, new self-assembled printable materials based on block copolymers (BCPs) that enable precise control of the nanostructure in 3D are investigated. In particular, well-defined BCPs consisting of a poly(styrene) block and a poly(methacrylate)-based copolymer decorated with printable units are selected as suitable self-assembling materials. A broad library of BCPs with different compositions and molecular weight is synthesized using controlled radical polymerization. A subsequent extensive investigation of the phase behavior before and after the functionalization is performed using SAXS, SEM, and SNOM. Lamellar, cylindrical and gyroid morphologies are observed dependent on the composition as well as the molecular weight, allowing the phase diagram of the system to be generated. The dependency of the domain spacing d on the molecular weight of the polymer is found to be described by a power law, which is in accordance with that published for other systems both experimentally as well as in theory.

The synthesized library of BCPs is then utilized to create printable formulations for the fabrication of complex 3D microstructures using two-photon laser printing. By fine-tuning the BCP composition and solvent in the formulations, the fabrication of precise 3D nano-ordered structures is demonstrated for the first time. Hereby, the key achievement is a controlled nano-order within the entirety of the 3D structures. To show this, imaging of the cross-sections of the 3D printed samples is performed, enabling visualization also from the inside. A detailed view of both lamellar as well as cylindrical morphology, dependent on the polymer design, is presented. The morphologies are fitting well with those found in the respective bulk polymer analysis, as well as SAXS measurements of the printing ink formulation.

KURZFASSUNG

Natürliche Materialien setzen sich aus einer begrenzten Anzahl molekularer Bausteine zusammen (wie etwa Aminosäuren oder Kohlehydrate), und ihre herausragenden Eigenschaften sind durch ihre komplexe hierarchische Struktur bestimmt. Während 3D-Druck sich als eine Standardmethode für die präzise Herstellung exakter Geräte etabliert hat, ist dieses Niveau an Präzision ist mit den aktuellen „State of the art"-Materialien für 3D-Druck nicht erreichbar.

Eine übliche Methode, solche Strukturen auf der Nanoskala in systematischen Systemen zu erhalten nutzt die Fähigkeit einiger Polymere sich unter bestimmten Bedingugnen selbst anzuordnen. Eine wichtige Polymerklasse, die die Fähigkeit besitzt, selbstangeordnete Strukturen auf einer Skala von 5-50 nm zu bilden, sind amphiphile Blockcopolymere (BCPs). Sie sind über einen breiten Bereich an Morphologien einstellbar, von Mizellen und Vesikeln bis zu durchgängigen Netzwerkstrukturen reichend, welche sich sowohl in unverdünnter Schmelze als auch in Lösung bilden können. Während diese Eigenschaften in 2D Filmen untersucht wurden, wurden sie noch nicht genutzt um 3D Strukturen mit hochaufgelösten Merkmalen, komplexer Geometrie und einer kontrollierten Nanostruktur zu erschaffen.

Zu diesem Zwecke wurden in der vorliegenden Doktorarbeit neue, selbstangeordnete druckbare Materialien basierend auf BCPs untersucht die eine präzise Kontrolle der Nanostruktur in 3D ermöglichen. Im speziellen wurden wohldefinierte BCPs die aus einem Polystyrol-Block sowie einem Polymethylmethacrylate-basiertem Block, welcher mit druckbaren Einheiten dekoriert ist, bestehen, als geeignete selbst-anordnende Materialien ausgewählt. Eine umfassende Bibliothek von BCPs mit unterschiedlichen Zusammensetzungen sowie Molekulargewichten wird mittels kontrollierter radikalischer Polymerisation synthetisiert, und darauffolgend wird eine umfassende Untersuchung des Phasenverhaltens vor und nach der Funktionalisierung mittels SAXS, SEM und SNOM durchgeführt. Lamellare, zylindrische und gyroidale Morphologien werden in Abhängigkeit von der Zusammensetzung und des Molekulargewichts beobachtet, was erlaubt, das Phasendiagramm des Systems zu erstellen. Die Abhängigkeit des Domänenabstandes d vom Molekulargewicht des Polymers kann mittels eines Potenzgesetzes beschrieben werden, in Einklang mit dem, was für andere Systeme sowohl experimenteller als auch theoretischer Natur veröffentlicht wurde.

Die synthetisierte Bibliothek an BCPs wird dann genutzt, um druckbare Formulierungen für die Herstellung komplexer 3D Mikrostrukturen mittels Zweiphotonenlaserdrucken zu erstellen. Durch Feinabstimmen der BCP- Zusammensetzung sowie des Lösemittels in der Mischung kann die Herstellung präziser, 3D nano-geordneter Strukturen zum ersten Mal gezeigt werden. Hierbei ist der Schlüsselerfolg die kontrollierte Nanoordnung in der Gesamtheit der 3D Strukturen. Um dies zu zeigen, werden die Querschnitte der 3D gedruckten Proben abgebildet, was eine Visualisierung auch aus dem

Inneren ermöglicht. Ein detaillierter Einblick sowohl von lamellarer als auch zylindrischer Morphologie, in Abhängigkeit vom Polymerdesign, wird präsentiert. Die Morphologien sind im Einklang mit denen, die in der Analyse des Grundmaterials sowie den SAXS-Messungen der druckbaren Tinten beobachtet wurden.

ABBREVIATIONS

2D	2 dimensional
3D	3 dimensional
AIBN	Azoisobutyronitril
ATRP	Atom Transfer Radical Polymerization
BHT	Butylhydroxytoluene
BCP	Block copolymer
CAC	Critical Assembly Concentration
CAD	Computer Aided Design
CLP	Controlled Living Polymerization
CNC	Computerized Numerical Control
CPDB	Cyanopropyldithiobenzoate
CTA	Chain Transfer Agent
Đ	Dispersity
DCM	Dichloromethane
DETC	7-Diethylamino 3-thenoylcoumarin
DMAc	Dimethylacetamid
DMAP	Dimethylaminopyridine
DMF	Dimethylformamide
DNA	Deoxyribonucleic acid
DP	Degree of Polymerization
EαBr*i*B	Ethyl α bromo isobutyrate
Et_2O	Diethyl ether
fs	femtosecond
GPC	Gel permeation Chromatography
HEMA	Hydroxy ethyl methacrylate
IC	Internal conversion
iPrOH	2-Propanol
IR	Infrared
ISC	Intersystem crossing
ISR	Intermediate Segregation Range
MeCN	Acetonitrile
MeOH	Methanol
MMA	Methyl methacrylate
M_n	Number-average molecular weight
M_w	Mass-average molecular weight
NEt_3	Triethylamine
NMP	Nitroxide Mediated Polymerization
NMR	Nuclear Magnetic Resonance
OPA	One Photon Absorption
P()	Poly()
P4VP	Poly(4-vinyl-pyridine)
PAN	Polyacrylonitrile

PEO	Polyethyleneoxide
PhMe	Toluene
PLA	Poly Lactic Acid
PMMA	Polymethylmethacrylate
PRE	Persistent Radical Effect
PS	Polystyrene
PVC	Polyvinylchloride
RAFT	Reversible-Addition-Fragmentation Chain-Transfer Polymerization
RDRP	Reversible Deactivation Radical Polymerization
RT	Room temperature
SAXS	Small Angle X-Ray Scattering
SCFT	Self Consistent Field Theory
SEM	Scanning Electron Microscope
SNOM	Scanning Near-Field Optical Microscopy
SSR	Strong Segregation Range
STED	Stimulated Emission Depletion
T	Temperature
TBAF	Tetrabutylammonium Fluoride
TEM	Transmission Electron Microscope
T_g	Glass transition temperature
THF	Tetrahydrofuran
TMS	Tetramethylsilyl
TPA	Two Photon Absorption
TPLP	Two Photon Laser Printing
vol%	volume %
w%	weight %

Contents

List of Publications and Conference Contributions:

The results described in this thesis were partially published in scientific journals and presented at conferences. Publications, conference contributions and additional related works are listed in the following:

Journal articles

Investigations of the phase behavior of a functional PS-*b*-P(MMA-HEMA) block copolymer
B. Weidinger, G. Yang, N. von Coelln, H. Nirschl, I. Wacker, P. Tegeder, R. R. Schröder, E. Blasco, *manuscript in preparation*.

3D Printing Hierarchically Nano-ordered Structures
B. Weidinger, G. Yang, N. von Coelln, H. Nirschl, I. Wacker, P. Tegeder, R. R. Schröder, E. Blasco, *Adv. Sci.* **2023**, *10*, 2302756.

Deconstructing 3D Structured Materials by Modern Ultramicrotomy for Multimodal Imaging and Volume Analysis Across Length Scales
I. Wacker*, R. Curticean, D. Ryklin, **B. Weidinger**, F. Mayer, L. Huang, J. Hofmann, M. Islam, N. von Coelln, T. Schmitt, C. Huck, P. Tegeder, F. Feist, J. A. Kammerer, C. Barner-Kowollik, M. Wegener, E. Blasco, U. Gengenbach, R. R. Schröder, *Adv. Funct. Mater.* **2023**, 202302025.

Understanding the Optical Properties of Doped and Undoped 9-Armchair Graphene Nanoribbons in Dispersion
S. Lindenthal, D. Fazzi, N. F. Zorn, A. A. El Yumin, S. Settele, **B. Weidinger**, E. Blasco, J. Zaumseil, *ACS Nano* **2023**, acsnano.3c05246.

Confererences

- Makro 2023, Freiburg, 16.-17.02.2023, *Poster presentation*.
- The 3DMM2O Conference, Schöntal, March 2023, *Poster presentation, Awarded with the Best Poster Award*.

1 Introduction

Polymers have been an invaluable material in close to every aspect of our daily lives – from medical products to packaging to building blocks for the transportation industry. Recently, advances have been made both in the synthesis of polymers with specifically targeted properties – from conductivity to super-absorbing properties to the design of nanocarriers for drug delivery, as well as in the development of additive manufacturing processes (also known as 3D printing). These make it possible to fabricate highly customized geometries at low quantities using a wide range of materials, giving a variety of material properties as well as over a vast span of length scales. On the big scale, 3D printing concrete can be used to print houses, while polymer composites have been used for the 3D printing of functional boats. In the consumer sector, 3D printers can be found in many households, university laboratories, and community spaces such as libraries. The widespread availability of custom designs could even influence the toy industry. Moving to smaller features, extrusion 3D printing can not only be used to manufacture custom medical devices such as splints, 3D printing of gel-like inks can be used to model tissue or even organs to generate a more life-like environment for cells to facilitate research of possible treatments for cancer and further diseases. In the dental industry, 3D printing can also be widely used, and decreasing the feature size even further, optical materials such as microlense arrays can be fabricated. A multitude of 3D printing techniques has been developed. Extrusion-based processes are used in the household filament printer and direct ink writing, while a lot of the techniques with precise resolution rely on light induced photopolymerization. On the macroscale, direct light processing and stereo-lithography are common, while for the microscale multiphoton laser printing is a versatile method. Most commonly, acrylate or epoxy-based photoresists are used, but alternative backbones are also being explored.

Both the extrusion-based and light-based approaches have limits regarding the achievable scale - For large objects, processing time as well as the necessary build space limit the universality, while for the small scale, the resolution is limited by the size of the tool – either the size and precision of the extrusion nozzle or the diffraction limit when using light. As in the dialogue of Drexler and Smalley, where the limitation of the miniaturization of devices in nanotechnology is described as the “fat finger - sticky finger” problem, to generate structures and functionalities beneath a certain size, an alternative approach is needed. Moving away from a top-down approach relying on external manipulation towards a bottom-up approach utilizing inherent properties of the employed materials, such as those present in nature, where the functionality relies on the precise hierarchical order, such as in DNA or enzymes. The field of DNA origami and DNA nanotechnology has been researched intensively to create functional devices on the nanoscale, but utilizing synthetic materials, such as polymers, can open up further possibilities.

One polymer class that is very interesting for achieving defined small-scale features are block copolymers. They have feature sizes in the nanometer range with controllable, tunable, intrinsic self-assembly. While they have found some application in macroscopic 3D printing, it has not yet been realized on the microscale. Within this thesis the application of self-assembled block copolymers for 3D printing on the microscale is described, with detailed investigation and characterization of the phase behavior of the employed block copolymer system.

The current thesis is separated in six chapters. Each chapter will be shortly described in the following. Chapter 2 describes the chemistry, physics and methods underlying this work, providing the general and theoretical background of the synthetic methods used as well as giving an overview over the employed printing techniques and the analytic methods. Chapter 3 gives a closer insight into the motivation and aims of this thesis as well as describing the strategies employed to reach these goals. Chapter 4 describes and discusses the results, detailing the successful synthesis of the functional block copolymers while also reporting less successful pathways. A synthesis strategy for functional, cross-linkable block copolymers based on PS-*b*-PMMA is provided. Then, the analysis of the self-assembly of the block copolymer with different analytical methods as well as the necessary sample preparation is described, focusing on the observed morphologies before and after the functionalization. Lastly, the 3D printing of hierarchically ordered microstructures based on the block copolymers is introduced and the in-depth analysis of both the printing inks as well as the microprinted structures is described. Chapter 5 summarizes the thesis and presents the next steps for expanding the scopes of the methods. Chapter 6 contains a precise description of the experimental procedures, synthesis routes and characterization that were necessary for successfully obtaining the results presented in the previous chapters, while complementary analytical data as well as detailed synthetic procedures are presented in the appendix in chapter 7.

2 General and Theoretical Background

2.1 Polymers

It was Hermann Staudinger who coined the term macromolecule when describing the behavior of materials such as rubber and proving that their long chains are made of short repeating molecular units linked by covalent bonds.[1] A polymer is then defined as a substance composed of macromolecules, classified by its high molecular mass and the repeat of small units.[2]

2.1.1 Structural Classification

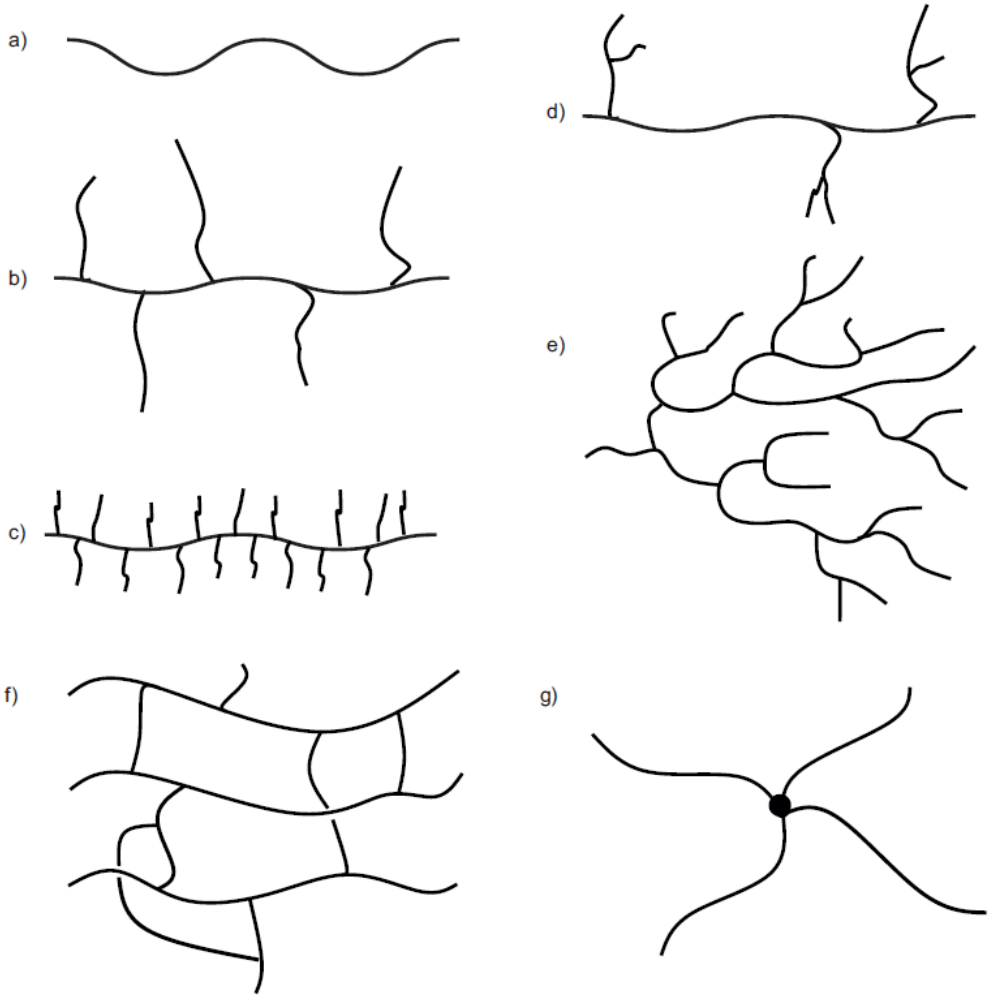

Figure 1: Representation of common polymer structures. a) linear polymer, b) graft polymer, c) bottlebrush polymer, d) branched polymer, e) hyperbranched polymer, f) polymer network, g) star-shaped polymer.

Polymers can be structurally quite different when considered globally, as presented in Figure 1. The simplest, typical case is a linear polymer. It is possible to graft sidechains onto the main chain, either longer, spaced out, or short and close together as is the case for bottlebrush polymers. The complexity

and potential asymmetry can be increased with branched branches and hyperbranched polymers. For star-shaped polymers, branches expand from a central moiety. In polymer networks, the chains are inter-connected *via* another chain.

Especially, but not only, the cross-linking density heavily influences the mechanical and thermal properties of a polymer. Thermoplastic polymers are only physically crosslinked and therefore shapeable upon warming. Polymers with a low covalent crosslinking degree and a high mobility of the molecule segments are elastomers, which are viscoelastic materials that are insoluble but swell in suitable solvents. Duroplasts are highly crosslinked, insoluble, hard, and hardly swelling.[3]

To expand the functionality of polymers to introduce conductivity, biodegradability or liquid crystalline properties, functional monomers can be incorporated or added *via* post-functionalization.

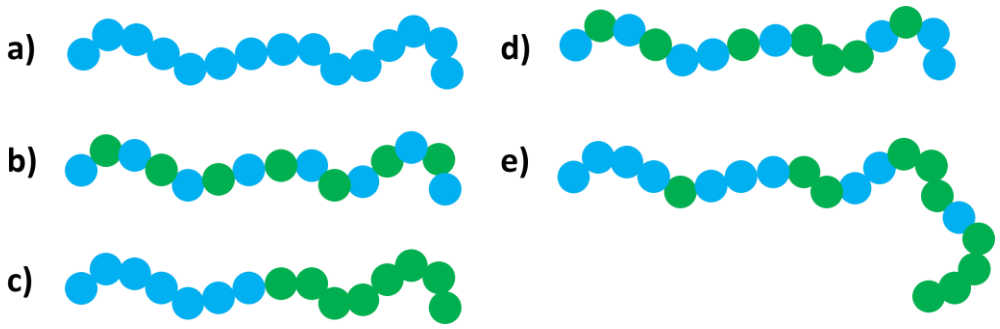

Figure 2: Different sequence types within a linear polymer. a) Homopolymer, b) alternating polymer, c) block copolymer, d) statistical copolymer, e) gradient polymer.

Not only the global structure of a polymer can be varied, but also the composition of the chains. In a homopolymer, each monomer unit is the same, whereas in a statistical copolymer, different monomers are incorporated at random. In alternating polymers, the order of the monomer units is controlled, whereas in gradient polymers the concentration of one component varies continuously from one end to the other. A block copolymer is classified by two or more individual blocks connected at the end, where each block can be made up of one or more monomers.[3,4]

2.1.2 Molecular Weight and Dispersity

Three main characteristics of a linear polymer are its constitution, molecular weight, and dispersity. The molecular weight *M* is defined by:

$$M = DP * M_{ru} \tag{1}$$

with *DP* being the degree of polymerization, the number of repeated units per macromolecule, and M_{ru} the molecular weight of the repeating unit.

Unless for special cases like the synthesis of sequence-defined polymers, polymerizations are statistical processes. Thus, the molecular weight is distributed, and the polymers are polydisperse.
One way to determine the dispersity Đ, which describes the width of the molecular weight distribution, is using two weight averages of the polymer, the number average M_n and the weight average M_w. M_n is defined as:

$$M_n = \frac{\sum_{i=1}^{\infty} n_i M_i}{\sum_{i=1}^{\infty} n_i} \tag{2}$$

Where n_i is the number of molecules possessing the molecular weight M_n. M_n can be described by considering the weight of each chain and averaging over the number of chains. Experimentally measurable properties can also depend on M_w, which is described by considering the weight of the respective chain w_i for every monomer. Mathematically, it is defined as:[5]

$$M_w = \frac{\sum_{i=1}^{\infty} w_i M_i}{\sum_{i=1}^{\infty} w_i} = \frac{\sum_{i=1}^{\infty} w_i M_i^2}{\sum_{i=1}^{\infty} w_i M_i} \tag{3}$$

The polydispersity Đ is then defined as:

$$Đ = \frac{M_w}{M_n} \tag{4}$$

Molecular Weight Determination

There is a variety of methods to determine the molecular weight of a polymer. These can be divided into absolute methods (such as end-group analysis, osmometry, mass spectrometry and static light scattering) on the one hand, which are not suitable for all types of polymers or relatively complex or expensive. Relative methods on the other hand include the solution viscosity as well as fractionation. One of the most common methods is size exclusion/ gel permeation chromatography (SEC/GPC). Hereby, the dissolved polymer is separated by elution over column packed with swollen resin containing pores of different sizes. During elution, smaller molecules travel down the column slower as they can get caught in more of the pores. The size of the polymer is determined by the hydrodynamic radius in the respective utilized solvent. This makes molecular weight determination by GPC a relative method that requires calibration with a sample of well-known size and distribution. Ideally, the standard is chemically close to the polymer type to ensure more accurate results.[5]

2.1.3 Polymer Synthesis

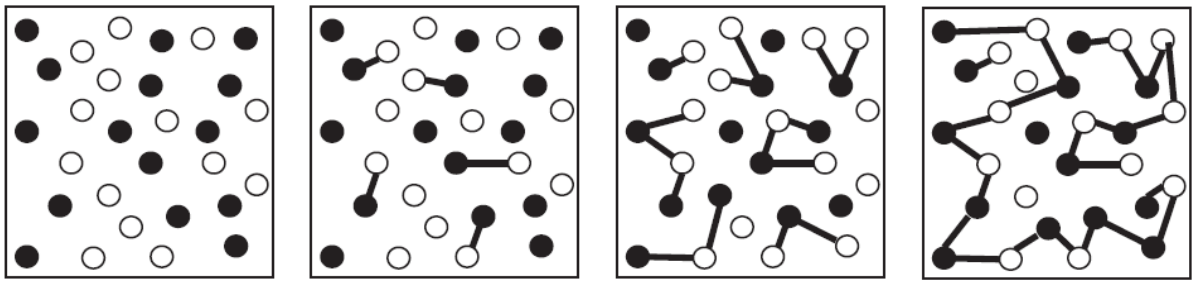

Figure 3: Schematic representation of step growth polymerization. Many small chains form oligomers, combining to high DP polymers only at very high monomer conversions.

In general, two modes of polymerization can be differentiated. The first, as depicted in Figure 3, is step growth polymerization, which can be divided into polycondensations and polyadditions. Hereby, each molecule needs to possess two or more functional groups, and can be the starter of an oligomer chain. Many small chains form individually, growing in a stepwise manner, and only combine to high DP polymers at high monomer conversions – at 90% conversion the DP is still only 10.

In contrast, in chain growth polymerization, depicted in Figure 4, the number of polymer chains is defined by the number of active chains to which the next monomer is added. These active species are generated by the addition of an initiator and grow consecutively.[3]

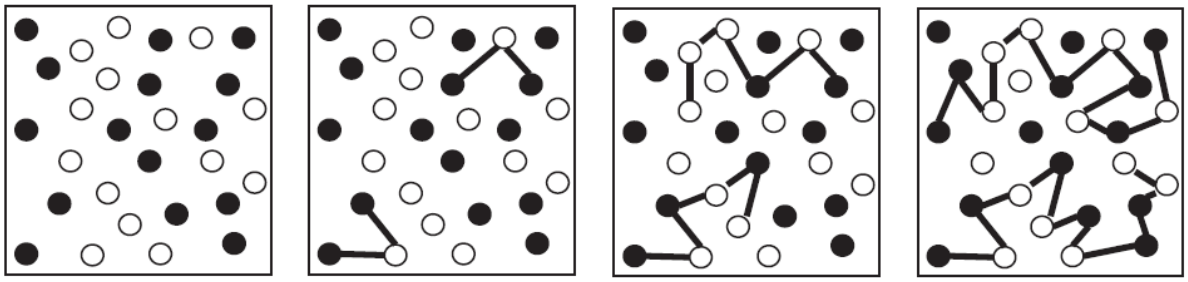

Figure 4: Schematic representation of chain growth polymerization. Active species equally react with monomers, forming a defined number of chains in the beginning that consecutively grow.

While the basic principles of all chain growth polymerizations are the same, several techniques with different mechanisms have been developed.

Free radical polymerization

Free radical polymerization represents the simplest case – each initiator molecule (often activated thermally or by light resulting in the formation of a radical species) can start a chain that is then elongated by repeated addition of monomers. Due to the high concentration of radicals, several side reactions such as termination or recombination can occur during the polymerization and the polymerization speed is not the same globally, leading to a high dispersity of the polymer.

Living polymerization

Anionic polymerization is a true living polymerization – without external influences such as a protic solvent or oxygen, the polymerization only stops when the "food", meaning unpolymerized monomer, is depleted. It is limited by its need for precise, controlled reaction conditions and the limited range of suitable monomers.[6]

"Living" polymerization - Reversible Deactivation Radical Polymerization

To solve the issue of poor control over the molecular weight distribution in combination with uncontrolled termination and side reactions for free radical polymerizations, a new approach called reversible deactivation radical polymerization (RDRP), previously also named controlled living polymerization (CLP), was developed.[7]

RDRPs should fulfil several criteria, similar to those for truly living polymerizations. The initiation happens quickly, and no termination reactions are taking place so that the number of propagating molecules stays constant. Thus, the reaction shows a first-order kinetic behavior, meaning that the logarithm of the monomer concentration is a linear function of time:

$$R_p = \frac{-d[M]}{dt} = k_p[P^*][M] \tag{5}$$

$$ln\frac{[M]_0}{[M]} = k_p[P^*]t = k_p^{app}t \tag{6}$$

where R_p is the propagation rate and k_p is the propagation rate constant. Plotting this function as presented in Figure 5, the linear graph represents a constant P^*, whereas the upward curve resembles a slow initiation, and the downward curve indicates termination or side reaction. For controlled/living polymerizations a direct control of the degree of polymerization is given by the monomer conversion, as presented in Figure 5.

$$DP_n = \frac{[M]_n}{[M]_0} = \frac{\delta[M]}{[I]_0} = \frac{[M]_0}{[I]_0} * (conversion) \tag{7}$$

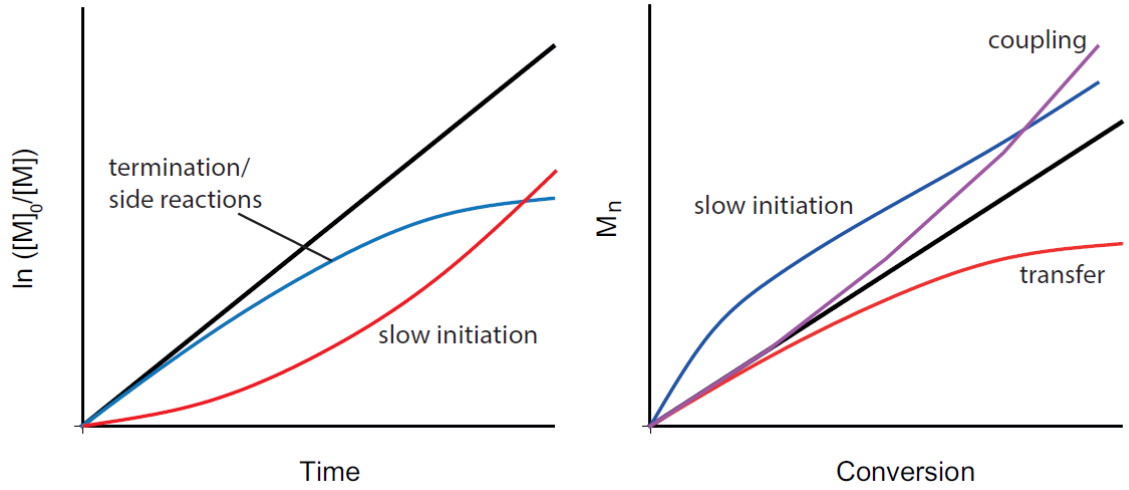

Figure 5: a) Graph of ln([M]$_0$/[M]) vs. time b) Graph of molecular weight M_n vs. conversion.

Another desirable factor, even if not inherently a condition for living polymerizations is a narrow molecular weight distribution. This requires comparable rates of initiation and propagation, and that the exchange between species of different reactivities is comparable to the rate of propagation. The chain transfer and termination must be negligible and the rate of depropagation significantly lower than that of the propagation. The system must be homogeneous and mixed fast.[8]

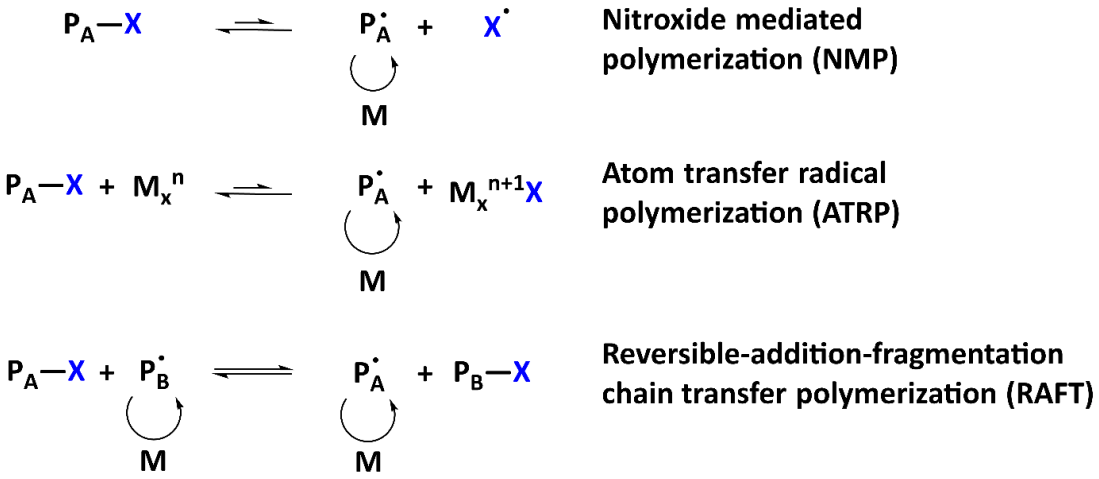

Figure 6: Scheme describing the origin of the polymerization control for each of the CRP methods.[7]

The general principles of the RDRP techniques are presented in Figure 6. To avoid early termination, a fast equilibrium between dormant and active chain ends must be achieved – either by using deactivation/activation (relying on the persistent radical effect (PRE)[9]) as is the case for Nitroxide Mediated Polymerization (NMP)[10] and Atom Transfer Radical Polymerization (ATRP)[11]; or by a degenerative exchange as is the case for Reversible Addition-Fragmentation Chain Transfer Polymerization (RAFT)[12].

The main RAFT mechanism is presented in Figure 7, as proposed by Moad et al.[12] The initiator is activated in the initiation step and then reacts with one or several monomers to form the radical species P_n. This radical species can react with a monomer in the reversible chain transfer/propagation, but it is also in equilibrium with the dormant radical species via addition to the thiocarbonylthiocompound. The R group can then be cleaved to take part in the re-initiation step, reacting with monomers to the radical species P_m. The chain propagation is another step, in equilibrium, with radical species P_m and P_n reacting with further monomers after their cleavage, with the thiostabilized species in between. When the species P_m and P_n react with each other to a dead polymer, termination occurs. A key aspect of this mechanism is the higher reactivity towards radical addition that the C=S bond shows in comparison to the C=C bond. Thus, the functional Z and R groups need to be selected carefully. The Z group regulates the stability of the intermediate radical and the reactivity of the C=S group towards radical addition. R must provide good homolytic leaving and initiation properties.[13,14]

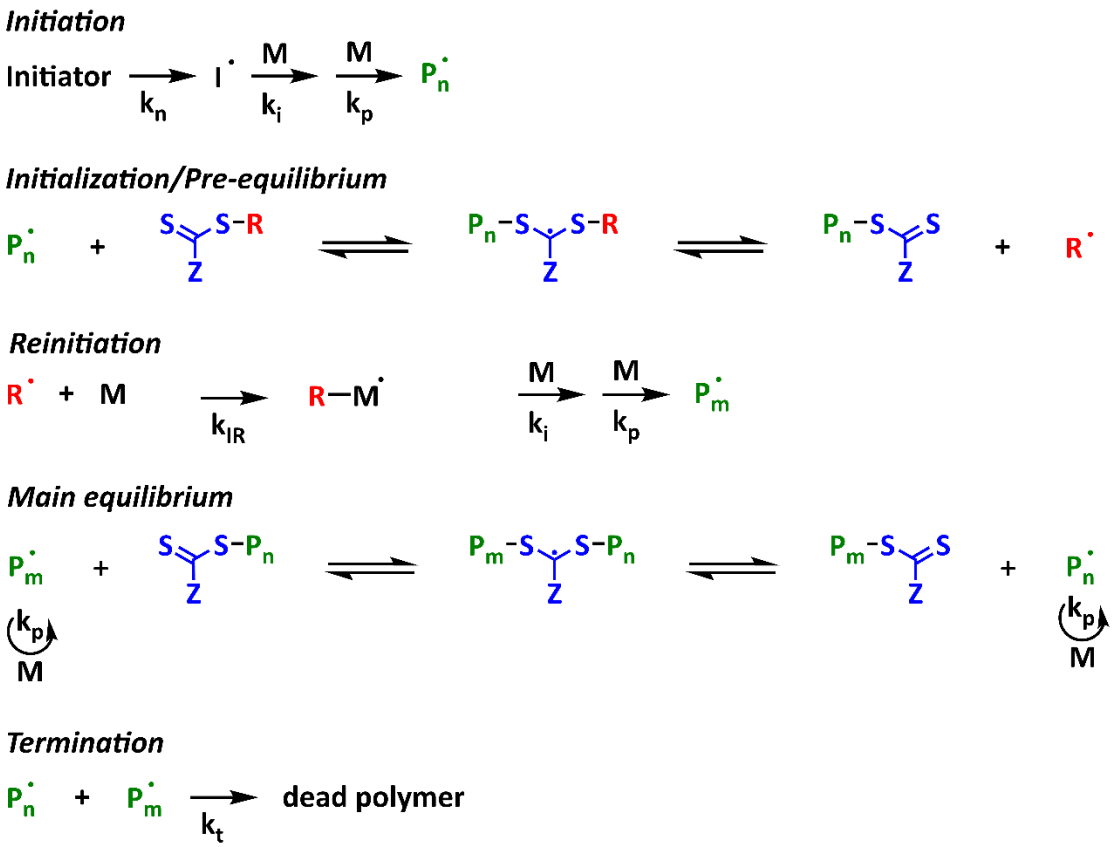

Figure 7: Scheme for the general mechanism of RAFT polymerization, as presented by Moad et al.[12]

What differentiates RAFT from other RDRP systems is the requirement for an external radical source, as the number of radicals does not change during the activation-deactivation process. In such a degenerative transfer system the use of a radical source (such as a free radical initiator) is advantageous. Tuning of the system is possible (for both the polymerization rate as well as the number

fraction of living chains). The number of chains with bimolecular termination corresponds to the number of radicals in the system, typically from the decomposition of the radical initiator.

Thus, unlike for systems based on reversible deactivation, bimolecular termination does not equal the loss of a living chain end (here meaning the ω-end containing the thiocarbonylthio end-group). The number of chains with the thiocarbonylthio end-group is constant.

Additionally, the number of dead chains can be predicted ahead and controlled. In the case of using a thermal initiator such as a diazo or a peroxide compound, the number of dead chains is known. The products of the polymerization can be both chains with and without a thiocarbonylthio end-group at the ω-end. There are also two types of chains in regard to the nature of the initiation (meaning the α-end), it can be either the initiator fragment or the R-group of the RAFT agent. The relative numbers between these four families of chains can be predicted from the number of radicals from the initiator as well as the number of RAFT agent moieties. Thus, there is a clear picture of the species available at the end.

Assuming that termination is only happening by disproportionation, the number of dead chains can be derived from the number of chains generated from the initiator and contains both chains with initiator fragments as well as the R-group at the α-end. The different types of generated chains are presented in Figure 8, starting from two initiator radicals and 5 chain transfer agent molecules, to yield seven polymer chains.

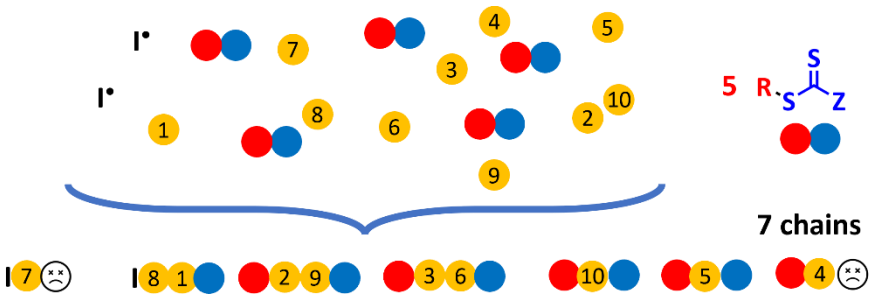

Figure 8: Schematic representation of the RAFT-process, adapted from Perrier.[15] Two radicals (I) are present in a system containing ten monomers (yellow) and five RAFT agents (red R-group and blue Z-C(=S)S-group). After polymerization, seven chains are present, comprising two dead chains and five living chains. This gives a livingness of the system L(%) of 5/(5+2) x 100 = 71%. Dead chains may have the R-group as α-end, while living chains may have the initiator fragment I as α-end.

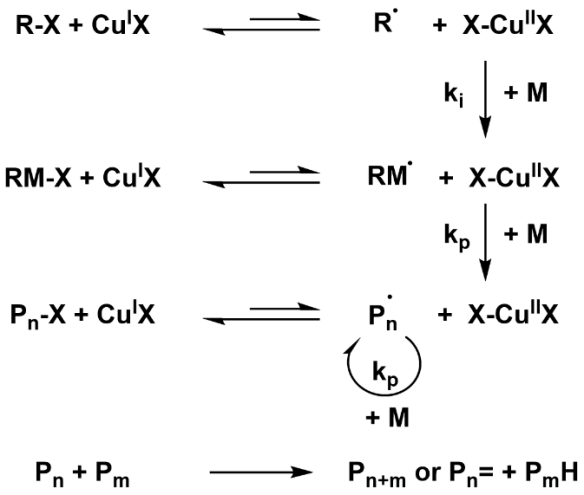

Figure 9: Schematic mechanism of copper catalyzed ATRP.

The mechanism of copper catalyzed ATRP, discovered independently by Matyjaszewski[16] and Sawamoto[17], is presented in Figure 9. With the right ligand/initiator combination it is suitable for a wide range of monomers. An alkyl halogenide reacts with a Cu^{I} halogenide, which is oxidized to a Cu^{II} complex, reversibly generating the active radicals. This radical species reacts with a monomer molecule before reacting with the Cu^{II} to a deactivated species RM-X. The chain growth occurs by reaction of activated species P_n which is reversibly deactivated to P_nX. The termination is caused by recombination or disproportionation of two activated species.

2.1.4 Block copolymers and their Self-Assembly

Over recent years, nanostructures have generated more and more interest. The scale of 10 to 200 nm relates to specific properties related to increased surface areas, altered electronic states and the formed lattice structures. Effects such as magnetic, optical, biological and mechanical properties can be utilized specifically.[18,19] One approach for the fabrication of nanostructures is the self-arranging of block copolymers.[20] The architecture of the amphiphilic polymers can be controlled, influencing the nanostructures formed in undiluted melt or in solution. The structures can easily be tuned over a broad variety of morphologies ranging from micelles and vesicles to continuous network structures. Therefore, designing interfaces with different chemical functional groups and geometrical properties is possible. To exploit these possibilities, various approaches for the synthesis of block copolymers have been established.

Strategies for the synthesis of block copolymers

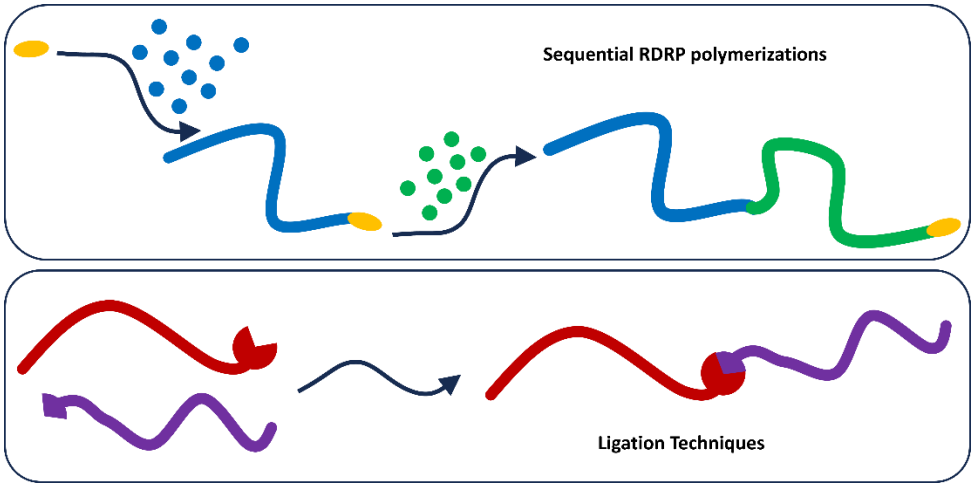

Figure 10: Synthetic strategies for the preparation of linear block copolymers include sequential polymerization or the ligation of two individually prepared blocks.

The two main approaches for the synthesis of linear block copolymers, as presented in Figure 10, include the sequential polymerization of the different monomers, which is feasible for both anionic polymerization and RDRP. Especially in anionic polymerization, a second monomer can be added directly to extend the chain without additional steps if the monomer conversion is complete.[21,22] As for RDRP, lower conversions are often desirable, and sometimes different polymerization techniques are combined. In this case, a work-up in between polymerization steps is required, and the polymer is used as a macroinitiator when reinitiating the polymerization.[23,24]

The other main strategy is the joining of pre-synthesized blocks *via* so-called modular ligation. Many of the various developed approaches fulfill the click-reaction conditions stated by Sharpless in 2001.[25] The reaction types include the nitrile-imine-mediated tretrazole-ene cyclodaddition (NITEC), RAFT hetero Diels-Alder reaction, the oxime reaction and the thioaldehyde or the photoenol reaction. Additionally, the copper^{I} catalyzed click-reaction between an azide-terminated polymer chain and an alkyne-terminated polymer chain can be used, as depicted in Figure 11.[26]

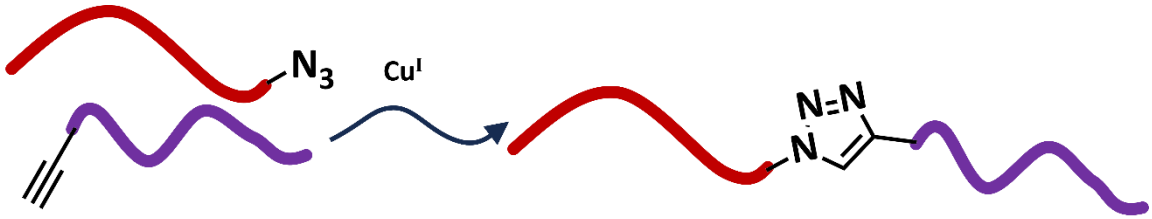

Figure 11: Cu^{I} catalyzed click reaction between an azide and an alkyne terminated polymer.

Self-assembly in bulk

Describing the self-assembly in the bulk, the phase separation induced by immiscible fragments is directly related to the size of the polymer chains, giving morphologies with a periodicity mostly in the 10 – 100 nm range. Both the order/disorder transition temperature and the specific pattern motifs are functions of the polymer properties as well as the molecular weight, segmental interactions and especially the volumetric composition. Flory and Huggins developed a general scheme to describe the mixing properties. For two components, the change in Gibbs free energy must be considered. If there are n_A moles of polymer A in volume ν_A and n_B moles of polymer B in volume ν_B, by mixing the boundary is removed and thus:

$$\nu = \nu_A + \nu_B \tag{8}$$

Gibb's free energy of mixing is described as

$$\Delta G_{(mix)} = \mathrm{G_{(AB)}} - (G_A + G_B) \tag{9}$$

To consider the change in volume, if necessary, Gibbs energy instead of Helmholtz energy is used. By the Flory-Huggins treatment, the mixing energy is described as:

$$\Delta G_{(mix)} = -\mathrm{TS_t} + \Delta \mathrm{G_{(loc)}} \tag{10}$$

Due to the motion of the center of mass of all polymer molecules the mixing process increases the entropy and influences the change of local interactions and motions of monomers (ΔG_{loc}). ΔS_t is always in favor of mixing while ΔG_{loc} is dependent of the molecule. Similar monomers will have bigger Van der Waals forces, while mixing increases the possible number of configurations.

While this term describes the main aspects of the mixing process, an explicit expression is needed for calculations. The increase in translational entropy is described by:

$$\frac{\Delta S_t}{\tilde{R}} = \widetilde{n_A} ln \frac{\nu}{\nu_A} + \widetilde{n_B} ln \frac{\nu}{\nu_B} \tag{11}$$

With $\phi_{A,B} = \frac{\nu_{A,B}}{\nu}$,

$$\frac{\Delta S_t}{\tilde{R}} = -\widetilde{n_A} \ln \phi_A - \widetilde{n_B} \ln \phi_B \tag{12}$$

The change in local interactions is:

$$\Delta G_{loc} = \tilde{R} T \frac{\nu}{\widetilde{v_c}} \chi \phi_A \phi_B \tag{13}$$

Where $\widetilde{v_c}$ is the volume of a reference unit common to both polymers, and χ is the Flory-Huggins parameter, dimensionless and describing the change in local free energy. For a symmetric di-block copolymer the phase separation occurs for:

$$\chi(\mathrm{N_A} + \mathrm{N_B}) > 10.5 \tag{14}$$

This condition results in the phase diagram presented in Figure 12 as simulated by SCFT.[27] The corresponding nanostructures are shown in Figure 13.

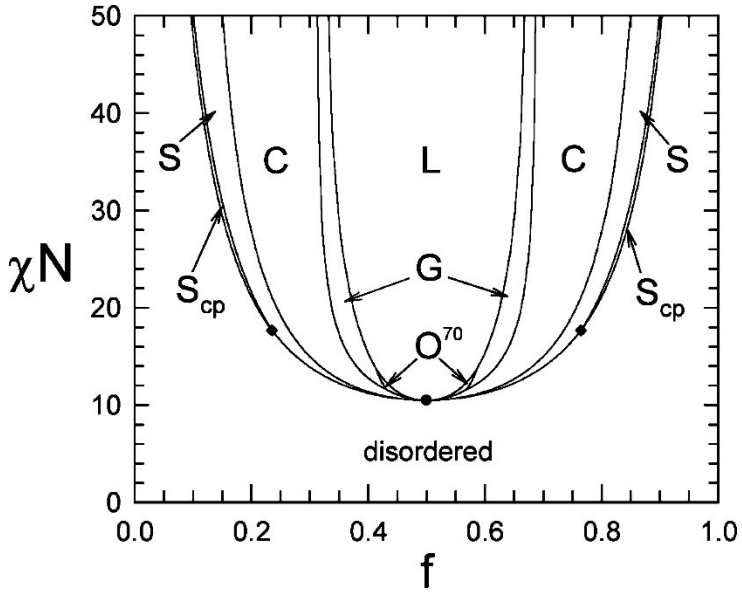

Figure 12: Phase diagram for melts of AB diblock copolymers, showing the stability regions of the ordered lamellar (L), cylindrical (C), bcc spherical (S), hcp spherical (Scp), gyroid (G), and Fddd (O^{70}) morphologies. The dot denotes a mean-field critical point. Reprinted from Matsen et al. with permission.[27]

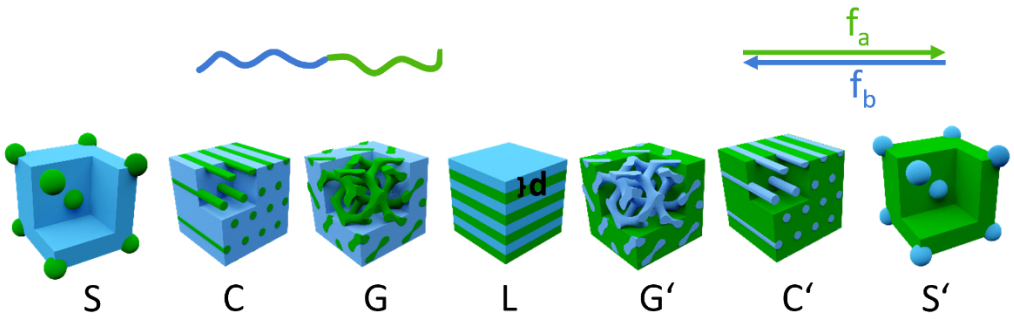

Figure 13: Schematic representation of the nanostructures formed by a block copolymer with different proportions of the two blocks. S = spheric, C = cylinders, G = gyroids, L = lamellae.

Experimental phase diagrams

While the theoretical phase diagrams calculated using SCFT gives an overview over the possibly formed morphologies, it has been found that the experimental phase diagrams often display different behavior regarding the phase borders, the symmetry as well as other possibly formed morphologies. Several factors of the block copolymers can influence the phase diagrams. One important factor is the influence of the dispersity. Several cases all have different influences on the phase diagram:

If in an A,B-diblock copolymer one block has a narrow Đ ≤ 1.05 while the other has a bigger dispersity Đ = 1.18−2.00, the composition-dependent microphase windows shift, in agreement with the increased interfacial curvature towards the polydisperse segment. With increasing polydispersity there is an

increase in spacing. In summary, there is a polymer composition-dependent (de)stabilization of the polydisperse microphase in comparison to their narrow-dispersity analogues.[28–30] When not only one, but both of the blocks are polydisperse, the formation of classical spherical, cylindrical, and lamellar morphologies is still allowed, with again larger increases in the domain spacing and increased values of the T_{ODT}.[31–33]

Moving from an AB-block-copolymer system to a BAB triblock (with polydisperse B blocks, and relatively narrow Đ A blocks), the microphase separation behavior aligns with the above results. When the polydisperse B segment is in the middle of an ABA copolymer chain, the ends are pinned at two block junctions. This center B block polydispersity causes large shifts in the composition windows associated with the well-known morphologies compared to the corresponding monodisperse triblock copolymers. This reveals the ability of molecular heterogeneity to entropically stabilize these supramolecular assemblies by filling the space more efficiently and relieving copolymer chain stretching in the self-assembled structures.[34]

Other experimental phase diagrams were for example recorded for a PS-PVP diblock copolymer by Schulz et al., finding HEX, LAM, HPL and gyroid morphologies.[35] Hadjuk et al. investigated the behavior of poly(ethylene oxide)−poly(ethylethylene) block copolymers both in the melt and in solutions with different concentrations.[36]

Liberman et al. investigated the impact of side-chain length on the self-assembly of linear-bottlebrush diblock copolymers, finding that architectural asymmetry seems to induce phase coexistence and shift the phase boundaries towards higher compositions.[37] Furthermore they found that the domain spacing of architecturally asymmetric linear-brush diblock copolymers varies more weakly with the degree of polymerization than previously documented for linear–linear diblock copolymers.[38]

Self-assembly in solution

In solution, the block copolymers can behave comparable to natural phospholipids, detergents, and soap in water. This can be expanded to many selective solvent conditions, making an assembly into a defined architecture accessible. The geometry and the degree of order depend on the concentrations as well as the volume ratio between the insoluble and soluble block(s) – the insoluble soluble ratio (ISR). At the specific critical aggregation concentration (CAC) the block copolymers start to self-assemble. As the molecular mass and the ISR increase, the CAC starts to decrease.[39]

Moving from a dilute solution to a concentrated solution, the presented morphologies switch from the micelles and vesicles typical for dilute solution to the morphologies also presented in the bulk, strongly dependent on the solvent. For example, Kathrein investigated the influence of electric fields on the alignment and the order to order as well as the order to disorder transitions for block copolymers in

32-43% solution in a good, non-selective solvent in her thesis.[40] Salomon Marques et al. studied the influence of the solvent mixture as well as the solvent concentration on the general assembly, the long-range order and the domain spacing of a PS-*b*-P4VP polymer.[41] Radjabian et al. also found a solvent (mixture) and concentration dependency for the behavior of a PS-*b*-P4VP polymer.[42] Patel et al. investigated the concentration dependent behavior of PS-*b*-PLA Bottlebrush diblock copolymers in a neutral solvent, observing the transition from dilute/semi-dilute chains to microphase separated, ordered lamellae at a concentration of 30%, as shown in Figure 14.[43]

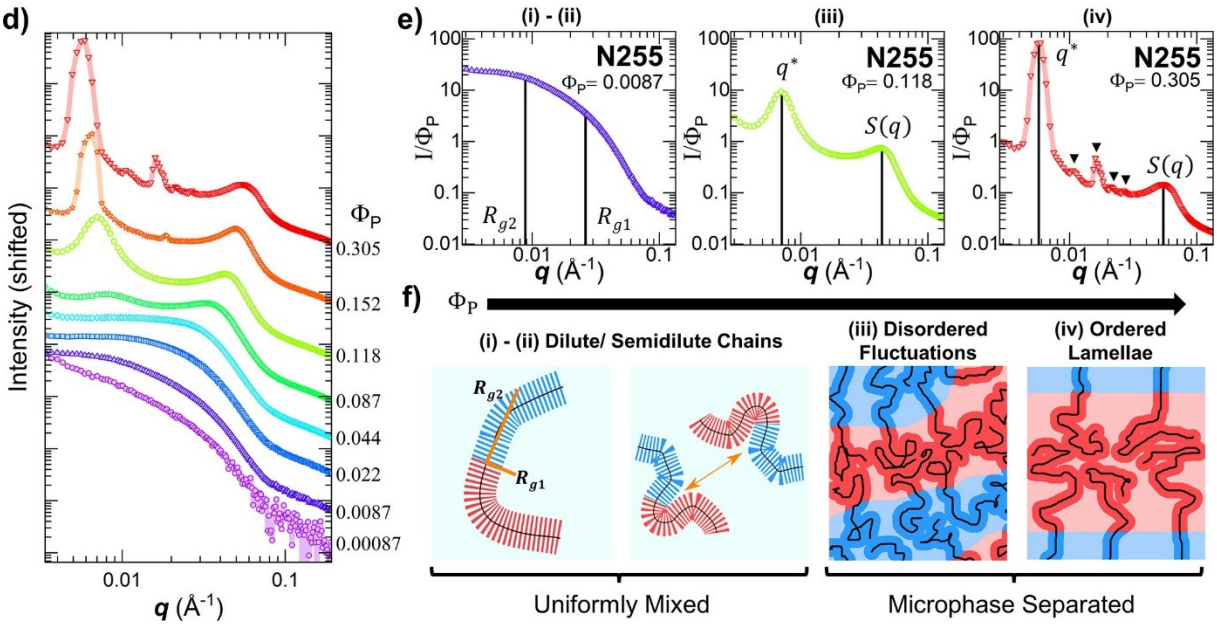

Figure 14: Small-angle X-ray scattering (SAXS) data for N255 BBCP in toluene at various concentrations. Curves are vertically shifted for clarity. (e) Characteristic concentration-normalized scattering curves for the three phases observed, taken as a subset of the curves for N255 in (d). S(q) indicates the structure factor peak emerging from interactions between adjacent BBCP molecules regardless of chemical identity, while q* arises from the PS/PLA compositional fluctuations in the disordered phase and from ordered lamellae. (f) Cartoons of the microstructure within each regime corresponding to labels (i)–(iv) in panel (e). Reprinted from Patel et al. under the CC BY-NC-ND 4.0 DEED license.[43]

Strategies for the self-assembly of block copolymers

For the self-assembly of block copolymers in the solid, several strategies can be applied for self-assembly either in the bulk material or in thin films. Especially regarding the application of block copolymers in the thin film, a wide range of strategies has been applied to influence the self-assembly behavior. Depending on the surface energies, a block copolymer might not exhibit structuring perpendicular to the substrate, but instead in parallel, if the substrate is preferential to one of the blocks. A common pathway to circumvent this issue is the anchoring of a random copolymer of the

monomers comprising the blocks to the substrate to create a non-selective surface.[44] It is also helpful to keep the domain spacing in mind for the film thickness, as multiples of L are advantageous.[45]

It is often beneficial to provide a pathway for the molecules to move from the kinetically trapped state they enter in the rapid evaporation during e.g. spin-coating, which can be done either by thermal or solvent vapor annealing. Thermal annealing is a straight forward possible method[46,47], but depending on the T_g of the polymers as well as the decomposition temperatures it may be too harsh. Solvent vapor annealing involves the risk of de-wetting but is otherwise very versatile in regard to the ability to use a wide range of solvents, and even to tune the final morphology depending on the solvent composition.[48,49] To specifically influence the direction of the structuring, several possibilities exist. The direction can be influenced by using lithographically etched trenches along which the block copolymers can orient themselves.[50] Additionally, the use of either magnetic[51] or electric fields[52] as well as employing mechanical forces such as shear stress[53] is possible.

(Post)-functionalization and its influence on the morphology of block copolymers

Not only can the self-assembly behavior and the represented morphology be influenced by the degree of polymerization and the composition of the polymer, it is also possible to influence the self-assembly properties using a post-functionalization process. Dong et al. showed that by increasing the length of a CF_2 containing side chain in a PS-PGMA BCP the morphology transitions from lamellar to hexagonally packed as the side chain becomes longer.[54]

Feng et al. used the controlled functionalization of a poly(styrene-block-butadiene) (PS-*b*-PB) using thiol-ene "click" functionalization to impart covarying properties such as χ and surface energy γ (e.g. the widely used PS- *b*-PMMA has a $\Delta\gamma$ of 0 at industry relevant T). For directed self-assembly it has gained traction to sequentially synthesize BCP with a high χ, but this often means a $\Delta\gamma$ not 0, which is unfavorable because it requires annealing processes for perpendicular BCP domains. Ideally, the feature size (by variation of χ) or the morphology (by variation of f) is tunable while $\Delta\gamma = 0$. This was here achieved by the conversion of a single parent BCP into a series of different polymers by use of thiol-ene chemistry, incorporating four polar thiols with different polarities/sizes while also varying the functionalization degrees φ, as shown in Figure 15.

χ was estimated from L_0 which was determined from SAXS. The functionalization degree φ was between 40 and 65%, and the composition of the PS-*b*-PB was M_n = 16.5 kg mol^{-1}, PS/PB molar ratio = 0.356:0.644, PS/PB volume ratio = 0.479:0.521, Đ = 1.10. Characterization was done using NMR, TGA, DSC, SAXS and contact angle measurements.

The results showed that the morphology changed from lamellar to cylindrical for the bulky thiols, which can be reasoned with the change in f. When using less bulky, more polar thiols, the lamellae were maintained.

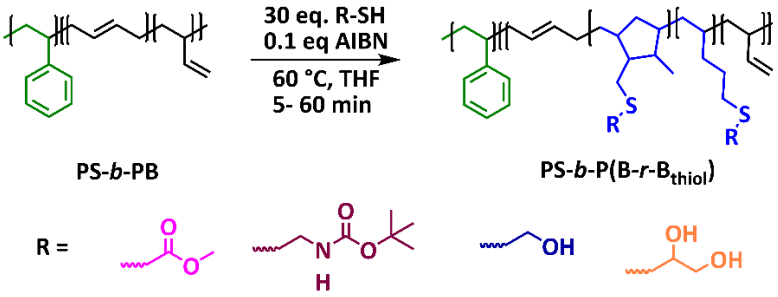

Figure 15: The block copolymer and its functionalized equivalents investigated by Feng et al. The graphic was adapted from Feng et al.[55]

The domain size is given by L = 2π/q, and it changed with φ. Additionally, upon increasing φ, the lamellae changed from symmetric to asymmetric. Thus, the volume of the thiol moiety must be taken into consideration when evaluating χ. For the bulky thiol MBOC, the spacing L_0 increased whereas χ decreased, opposed to intuition, because the statistical number of segments N probably changed.

Estimation of χ could then be done using $L_0 = caN^{(2/3)}\chi^{(1/6)}$. This applies to the strong segregation range (SSR), whereas the investigated polymers are in the intermediate segregation range (ISR), but the results should still be appropriate. While it is the value for lamellae, adequate results were received for other morphologies.

The formula can be used to derive an estimate of χ, but for more precise calculations, temperature dependent SAXS would be necessary where the issue of crosslinking would need to be addressed. Using this way of calculating values for χ, they are self-consistent, under the assumption that a is constant and determined using the known χ for the unfunctionalized polymer system.

McCallum et al. where able to synthesize a BCP with switchable χ-parameters to obtain tunability of the phase separated morphology. Hereby, they used a polystyrene-poly-6-O-methacryloyl-D-galactopyranose diblock copolymer where the galactose was protected with more hydrophobic acetonides during the synthesis. Solubility of the high χ-polymers is often an issue for spin-coating, so the deprotection was performed after spin-coating. Upon deprotection, they observed either a disorder-to-order transition or an order-to-order transition, indicating the large difference in χ.[56]

Conversely, Bosson et al. used the post-functionalization approach to introduce a nonpolar group in of the blocks, increasing the volume fraction of that block as well as matching the solubility parameters of both blocks to inhibit the nanopatterning of the BCP.[57]

2.2 3D Printing

Additive manufacturing, often used synonymously with the term 3D printing, was introduced in the 1980, serving highly specialized needs of model making and rapid prototyping. It has evolved as a massive trend in the past decades, gaining traction not only in the consumer area, where it had a growing impact on the toy industry, providing significant savings opposed to commercially available products, but also in industrial fabrication, with application fields such as biomedicine, optics or aerospace.[58–60] It is a versatile technology for the combination of computer aided design (CAD) and rapid manufacturing. This allows for the fabrication of customized parts without needs for molds or machining. making it an agile and fast technology with the ability to meet the demands of individuals or specific applications. Additionally, it allows to produce structures with a high shape complexity.

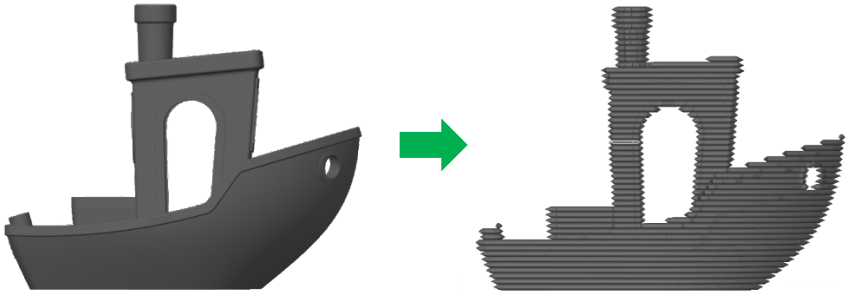

Figure 16: A virtual object created using CAD is digitally sliced into layered data.

A virtual object created by CAD is digitally sliced so it can then be manufactured in a layer-by-layer manner, as presented in Figure 16. Overall, AM is slower than injection molding and subtractive techniques such as CNC, but it allows for the CAD fabrication with multifunctional materials, with complex shapes and functionalities, and is even suitable for biofabrication. This makes it very flexible, time saving and depending on the case even financially advantageous in comparison injection molding.[58]

According to ASTM International Committee F42 on Additive Manufacturing Technology[61] in 2009, 3D printing techniques are generally classified in seven distinct categories including:

- Material Extrusion
- Material jetting
- Binder jetting
- Vat photopolymerization
- Powder bed fusion
- Directed energy deposition
- Sheet lamination

Each of these techniques has different parameters regarding the suitable materials, the processing conditions as well as the achievable resolution in the printed objects. One classification parameter is the so-called “voxel”. While the label “pixel” is the abbreviation for a picture element in two dimensions, the corresponding volume element in three dimensions is the voxel. The voxel can be defined and positioned by either mechanical means (e.g. a narrow nozzle), electric means (e.g. a strong electric field) or by photochemical means (such as a laser focus) depending on the chosen AM technology. Here, currently the laser has the advantage in regards of the minimum voxel size and the overall accessible number of voxels. Due to the utilization of nonlinearities and super resolution, the resolution can be below the wavelength of visible light. Currently, approaches to increase the writing speed, the resolution and the incorporable chemical functionality are being followed.[62]
In this work, vat photopolymerization with a focus on two-photon laser printing (TPLP) will be described in detail.

2.3 Vat photopolymerization

In vat polymerization techniques a liquid polymeric or monomeric resin is selectively cured by a light-activated polymerization process. The first approaches were made in the 1980s by Kodama and Herbert[63,64], and the first patents were independently filed in 1984 by Chuck Hull and André et al.[65,66] Most commercial photoresists are either acrylate- or epoxy- based. Depending on the desired size of the printed structure as well as the necessary solution, either one photon processes such as stereolithography (SLA) or direct light printing (DLP), or printing techniques based on multiphoton processes such as two photon laser printing can be employed.[58]

2.3.1 Two-photon laser printing

Two photon absorption (TPA) was first postulated by Maria Göppert-Mayer in 1931[67], before this nonlinear absorption process was experimentally shown in 1961 by Kaiser and Garret.[68] With the availability of solid state femtosecond pulsed lasers, it became accessible in laboratories. In a common one-photon-process, where a photon with the energy $h\nu_1$ excites an electron from the ground level S_0 directly to the excited state S_1 from where transition to the triplet state and thus the radical pathways can start. During a two-photon-excitation process, however, a photon with the energy $h\nu_2 = h\nu_1/2$ excites the electron to a virtual level. The electron in this level is then excited by another photon of the energy $h\nu_2$ to the excited level S_1.

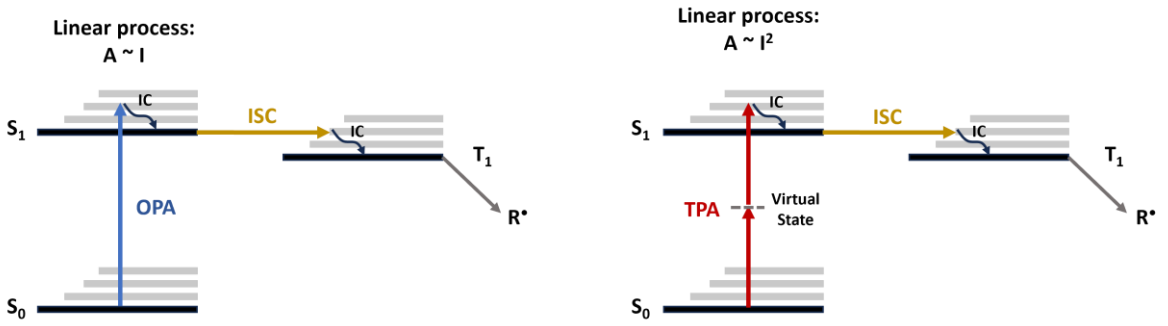

Figure 17: Simplified Jablonski diagram comparing the absorption A and radical generation process in case of linear one-photon absorption (OPA) and non-linear two-photon absorption (TPA).

Because the virtual state is extremely short-lived (on the fs timescale), the photon density and thus the light intensity needs to be high. To obtain these high local intensities, most often pulsed lasers with a short pulse duration of around 100 fs are used.

After internal conversion (IC) to the ground state of the excited level S_1, intersystem crossing (ISC) to the excited triplet state T_1 takes place. From this state, the molecule can undergo several pathways such as transition to a radical state, from which it can then initiate a radical photopolymerization, as shown in Figure 17.

Because two photons are necessary, the absorption probability is proportional to the intensity I squared, meaning that the absorption criterion can only be fulfilled very close to the focus. A graphic representation of this is shown in Figure 18, where the fluorescence of a dye is shown in dependency of the underlying process, a one-photon process (a) or a two-photon process (b).

Figure 18: Two-photon fluorescence vs normal fluorescence, using the same fluorescence marker for both experiments. Image created by Steve Ruzin and Holly Aaron, The CNR Biological Imaging Facility.

Because of the small excitation volume, the voxel size is significantly smaller than for a one-photon printing process, especially in z-direction, giving full control over printing in all three dimensions. Depending on the used printing ink, resolutions well below 150 nm can be reached, enabling the precise fabrication of structures at the microscale.[62,69–74]

The range of possible applications is wide, with the ability to incorporate properties such as conductivity[75], biocompatibility[76] or adaptivity[77]. TPLP faces the limitation of the diffraction limit, which can be circumvented by using e.g. an approach similar to STED microscopy.[78] Additional challenges are the writing speeds to make the process more scalable and thus more commercially applicable, where one solution could be the parallelization of the printing process e.g. by using multiple foci.

2.4 Characterization Techniques

2.4.1 Small Angle X-ray Scattering

X-rays are electromagnetic radiation occupying the spectrum from 10^{-2} to 10^{2} Å in wavelength, making them applied for the study of material in the range of 0.5 to 2.5 Å. Studies on polymers often use the Kα radiation from a copper target tube with a wavelength of 1.5418 Å. Alternatively, a synchrotron radiation source with a broad spectrum can be used in combination with a monochromator.

X-rays move with the speed of light, meaning that the relation between frequency and wavelength can be described with

$$\lambda = \frac{c}{\nu} \tag{15}$$

The wavelength of around 1 Å has the same order of magnitude as interatomic distances, which gives x-rays an important role when it comes to probing the structure of molecules, meaning the arrangement of the atoms.

Wave-particle duality applies to x-rays, giving the relationship of

$$E = h\nu \tag{16}$$

$$p = \frac{h}{\lambda} \tag{17}$$

The energy of a Cu K_α radiation source is thus E = 8.04 keV.

Small angle x-ray scattering (SAXS) is used to investigate structures on the order of 10 Å or larger. To gather information on these relatively large structures, the intensity of scattered x-rays (or, for small angle neutron scattering, neutrons) at a small angle, $2\theta < 2°$ is considered.

According to Bragg's law:[79]

$$n\lambda = 2d\,sin\theta \tag{18}$$

The reciprocity of d as the domain size and q as the scattering vector means that for larger feature sizes, q is smaller. This relationship between q and 2θ is expressed by:

$$q = 4\pi sin\theta/\lambda \quad (19)$$

And thus:

$$d = 2\pi/q \quad (20)$$

The spatial proximity of the scattered x-rays to the incident beam is a concern so that the incident beam must be carefully collimated. The schematic set-up for a SAXS measurement is presented in Figure 19.

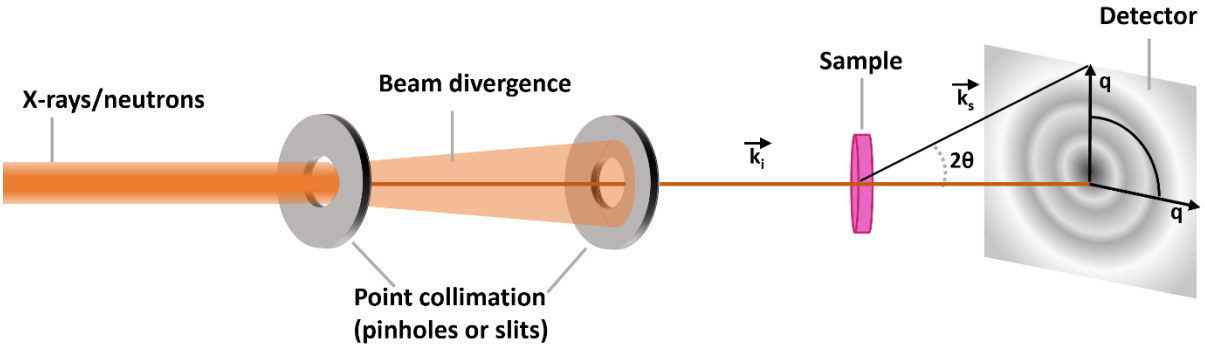

Figure 19: Schematic representation of the setup for a transmission SAXS measurement involving delivering a collimated beam through a sample.[80]

Scattering of Block Copolymer Microstructures

When analyzing polymers with SAXS, the peaks are broadened both because of imperfections in the lattice as well as a limited size of the domains with lattice coherence. Thus, often only the first Bragg reflections are well recognizable, with the higher order peaks possessing a lower intensity or being indistinguishable from the background.

Table 1: Ratios of Bragg reflections for the classic morphologies of AB diblock copolymers.

Morphology		**1**	**2**	**3**	**4**	**5**	**6**
Spheres	(hkl)	110	200	211	220	310	222
	q_{hk}/q_{100}	1	√2	√3	√4	√5	√6
Cylinders	(hkl)	110	110	200	210	300	320
	q_{hk}/q_{100}	1	√3	√4	√7	√9	√12
Gyroid	(hkl)	211	220	321	400	420	332
	q_{hk}/q_{100}	√3	√4	√7	√8	√10	√11
Lamellae	(hkl)	100	200	300	400	500	600
	q_{hk}/q_{100}	1	2	3	4	5	6

If in a polymer showing a lamellar nanostructure the q and 3q are exhibited, while 2q is not exhibited strongly, this indicates that both blocks have the size.[81]

2.4.2 Microscopy Techniques

Several microscopy characterization methods can be employed to characterize the BCP morphologies in the bulk and in thin films. The general principles of these microscopy techniques are shown in Figure 20. Transmission electron microscopy (TEM) is using the principle of (1). Detected are electrons transmitted through a very thin specimen that were either Rutherford or inelastically scattered depending on the sample.[82,83]

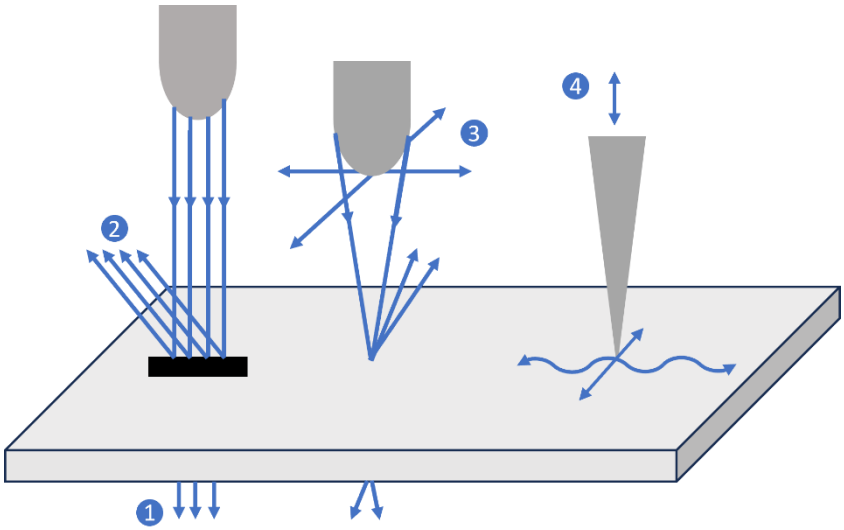

Figure 20: The different modes of operation for different microscopy techniques. A beam of electrons or light is transmitted through a sample in transmission electron/light microscopy (1) or reflected back (2). If the beam is focused and scanned over the sample either the transmitted signal, or the reflected/back scattered signal can be detected (3). If a tip is in direct contact with the surface, the direct forces or other physical properties can be investigated (4).[83]

Scanning Electron Microscopy (SEM)

In scanning electron microscopy, a focused electron beam is scanned over the sample surface. The measured signals are the interactions between the beam and the sample surface. It is possible to detect the secondary electrons as well as the back scattered electrons. Remarkable for SEM is the large depth of field.[83]

As for optical microscopy, the resolution of samples is limited by the wavelength of the used probe, in this case the De Broglie wavelength of the electrons, which results in the improved resolution by orders of magnitude, especially when comparing to visible light microscopy. Downsides of conventional electron microscopy are the damages inflicted to the samples by the electron beam, as well as the need for a high vacuum, preventing physiological measurement conditions. Depending on the sample, the structures of interest may be chemically similar so that the electron contrast is poor, and charging problems may also occur. A way of improving the last two factors is the use of a heavy metal staining

agent, such as osmium or ruthenium tetroxide, phosphotungstic acid, lead acetate or even uranyl acetate. Alternatively, the sample surface can be sputter coated with a conductive material, such as carbon, gold, or platinum; or blends such as platinum/palladium. The latter covers the material contrast which may not align with the measurement aims. The former is problematic both for environmental and handling reasons as well as proposing limitations regarding the applicability for different material combinations.

2.4.3 Infrared (scattering) Scanning Nearfield Optical Microscopy (IR-(s)SNOM)

One method to overcome the limitations of the electron microscope is the use of probing techniques such as atomic force microscopy (AFM). A variation of AFM is the combination of the probe tip with a focused IR laser, giving access to locally resolved IR signals with a resolution of down to 10 nm.

This makes use of the absorption of IR light due to excitation from the ground vibrational level to a higher energy state and can provide information on the molecular structure (individual functional groups), molecular interactions as well as supramolecular assemblies. Bulk IR only gives averaged information over the whole sample while IR microscopy can provide mapping with a resolution down to the Abbe limit. To overcome the diffraction limit, a small aperture was used to employ a near-field source. Further developments use a sharp metallic tip illuminated with a focused laser beam as the near field source, giving the scattering SNOM. The spatial resolution is limited by the tip curvature size.[84]

Using this non-destructive method under ambient conditions e.g. the detection of individual polymer molecules was possible[85], and it has also been applied to the detection of block copolymer self-assembly.[86]

3 Motivation and Aims

The exceptional performance of natural materials, comprised of a limited number of molecular building blocks (e.g. amino acids, carbohydrates), is the result of hierarchical order on multiple length scales.[87,88] While the perfection of the structure-function relationship was the results of evolution over billions of years, self-assembled synthetic materials have been the focus of investigation for many researchers within the last decades.[89–91]

Recently, considerable efforts have been made to introduce the order of natural materials into 3D printing, particularly for light-based 3D-printing.[92] One pathway of incorporating hierarchical, inherently porous domains into 3D printed objects is exploiting the use of photoinitiated polymerization-induced microphase separation using DLP as the 3D printing method.[93,94] Upon printing, phase-separation between the polymer and a porogen such as organic solvents is happening. The pore sizes of the formed porous 3D structure can be tuned with the printing formulation. A similar principle has also been used for the realization of macroscopic objects exhibiting different nanoscale morphological features by Boyer and co-workers.[95,96] Hereby, BCPs formed in situ during the 3D printing process utilizing RAFT polymerization, leading to a polymerization-induced microphase separation. The resulting materials exhibited a variety of nanoscale domains. While this method enables remarkable nanoscale control in 3D printed structures, the self-assembly takes places during the printing process. This means that the polymer network is formed in a kinetically trapped state, leading to fixed morphologies that are not in the thermodynamic equilibrium. Thus, the formed order was not yet achieved on the long range, limiting the potential applications.

Furthermore, Patel et al. were able to influence the domain spacing and thus the structural color of a bottlebrush block copolymer printed with inkjet printing by tuning the printing temperature and speed, making it possible to incorporate multiple colors into one structure.[97]

Transitioning from macroscale printed objects to those fabricated on the microscale, Raut et al. used a regular assembly of polystyrene nanospheres infiltrated with a TPLP ink as the printing material – after development and dissolving of the nanospheres, microstructures with an inverse opal structure, leading to structural color, were created.[98]

On the other hand, Kawarazaki et al. where able to photo-crosslink a benzophenone-functionalized, self-assembled block copolymer, enhancing the thermal stability while preserving the morphology.[99] This is in agreement with the findings by Sims et al., who used 2+2-cycloaddition of coumarin-functionalized block copolymers to investigate the self-assembly of the nondestructively photo-crosslinked block copolymers.[100]

While self-assembled BCPs exhibiting highly ordered nanostructures have been investigated extensively in thin films[101,102], so far they were not applied to generate 3D structures combining high

resolution, complex geometry and a controlled nanostructure. Thus, the goal of my doctoral thesis was to fill this gap and introduce a high, hierarchical order into 3D printed microstructures.

In particular, I selected functional BCPs as perfect candidates because they not only show self-assembling behavior, but the size of the self-assembled structures can also be tuned depending on the chosen polymers and the molecular weight. Two-photon laser printing was chosen as the 3D printing technique as it offers fast, high-resolution printing and opposed to other vat photopolymerization techniques high viscosity as expected from a rather large polymer is not a downside, but can even aid the printing of complex, well-resolved geometries.

To achieve my ambitious aim, the following steps, illustrated in Figure 21 will be taken. 1) Functional BCPs, based on PS-*b*-PMMA, are synthesized and characterized. 2) Self-assembly in the bulk will be studied extensively using SEM, SAXS and SNOM. 3) The functional BCPs synthesized and analyzed should be formulated into self-assembled inks using a photo-initiator and a suitable solvent. Defined 3D printed microstructures will then be created using TPLP. Importantly, the self-assembly both in the printing inks as well as the printed structures should be investigated.

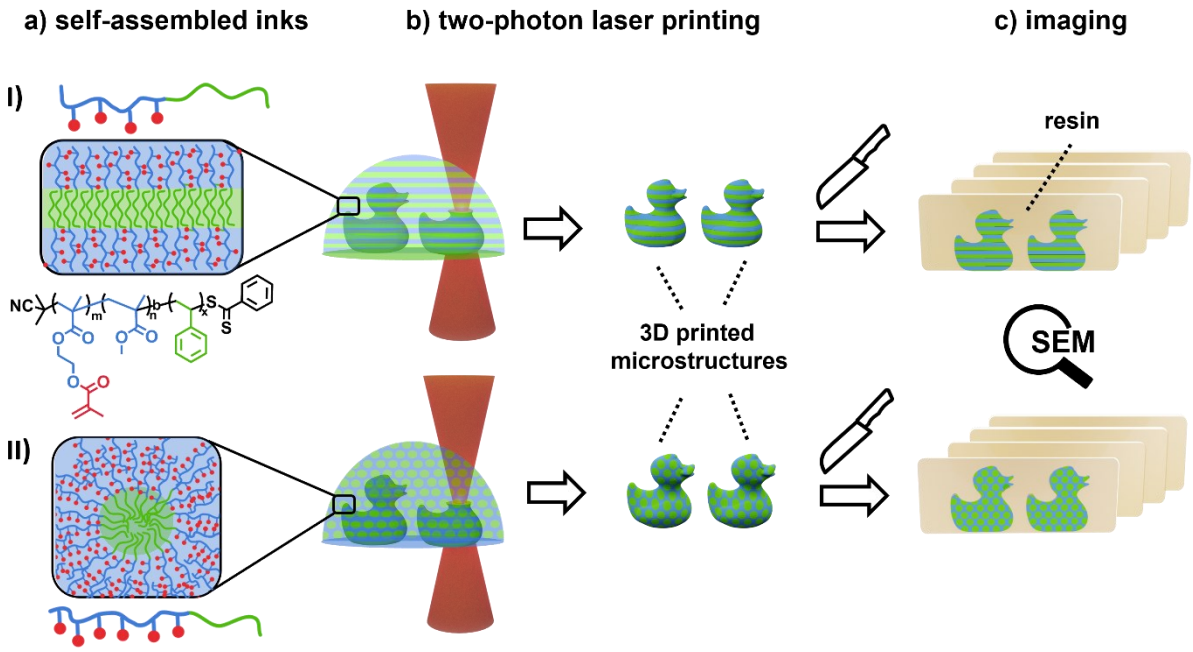

Figure 21: Schematic illustration of the printing approach. a) Pre-assembled functional BCP based inks exhibiting lamellar (I) or cylindrical morphology (II) are utilized for b) the fabrication of defined 3D structures exhibiting nano-order using TPLP. c) For characterization, the 3D printed microstructures are embedded into epoxide resin, sectioned using an ultramicrotome, and the internal nanostructure is imaged via SEM. Note: the nanodomains of lamella and cylindrical structures are “oversized” for illustrative purposes.

4 Results and Discussion

4.1 Block copolymer synthesis and functionalization

BCPs consisting of a polystyrene block and a polymethylmethacrylate based block were chosen, since PS-*b*-PMMA is a well-studied system in terms of self-assembly.[103–105] Secondly, by introducing a functional methacrylate co-monomer in the PMMA block, hydroxyethyl methacrylate (HEMA) in this case, a post-modification route is possible, which is key for the anchoring of photo-cross-linkable groups for printing, as shown in the target molecules in Figure 22.

Hereby, several different techniques were investigated to reveal the method best suited for the synthesis of a library of block copolymers with precisely controllable properties that can be characterized for their self-assembly.

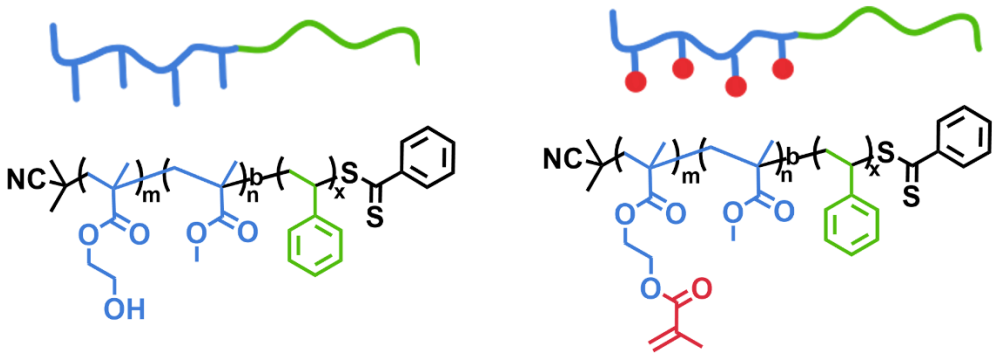

$S_{1\text{-}f}$-MH_f-M_n $S_{1\text{-}f}$-MH_f^*-M_n

Figure 22: Structural formulas and nomenclature of the targeted BCPs. M_n is the molecular weight in kDa and **f** is the molar fraction of the methacrylate block, where-as * indicated introduction of the methacrylate group.

Several approaches were tested to find the optimal synthesis conditions for the functional BCP. The several polymerization pathways as well as the optimization of the post-functionalization are presented in the following. The BCPs are named according to their composition and molecular weight, $S_{1\text{-}f}$-MH_f-M_n, where f is the fraction of the methacrylate based block and M_n is denoted in kDa. The functionalization is denoted by *. In the case of partial functionalization, it is denoted with the percentage, and samples functionalized with acrylate instead of methacrylate groups are denoted as ^{A}*.

4.1.1 Click chemistry

First approaches towards the block copolymers were made using copper catalyzed click chemistry. Hereby, one functional ATRP initiator containing a protected alkyne-group was used, while on the counterpart, the endstanding bromine of ethyl-α-bromoisobutyrate was used, as shown in Figure 23.

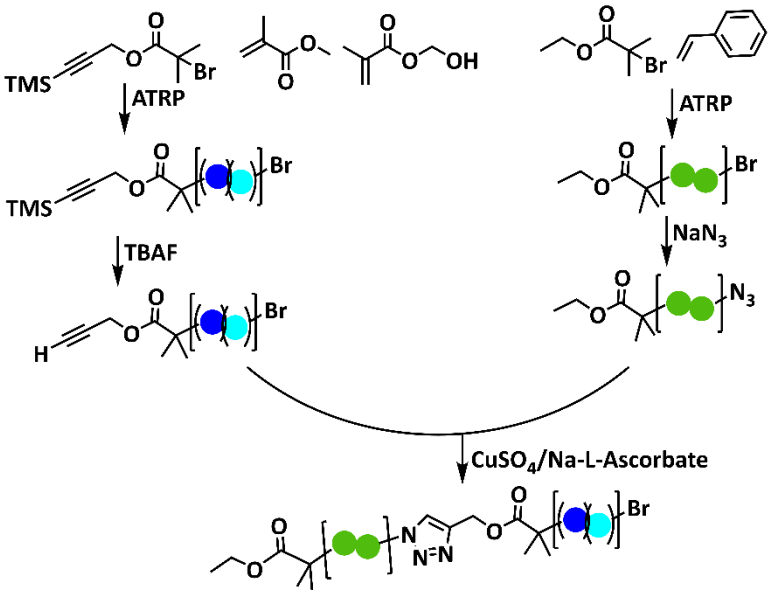

Figure 23: Reaction schemes for the synthesis of a BCP using click chemistry. The two blocks are prepared using functional ATRP initiators which are transformed towards having an alkyne and azide moiety, respectively. Coupling with $CuSO_4$/Na-L-ascorbate yields the BCP which could then be functionalized.

After deprotection of the alkyne using TBAF and conversion of the endstanding bromine into the azide using sodium azide, the coupling reaction was performed using a $CuSO_4$/Na-L-ascorbate system. While, under some conditions, coupling took place, the coupling was not complete as indicated by the shape of the GPC traces (shown in Figure 24), the calculated molecular weight and the presence of polystyrene in the supernatant after precipitation.

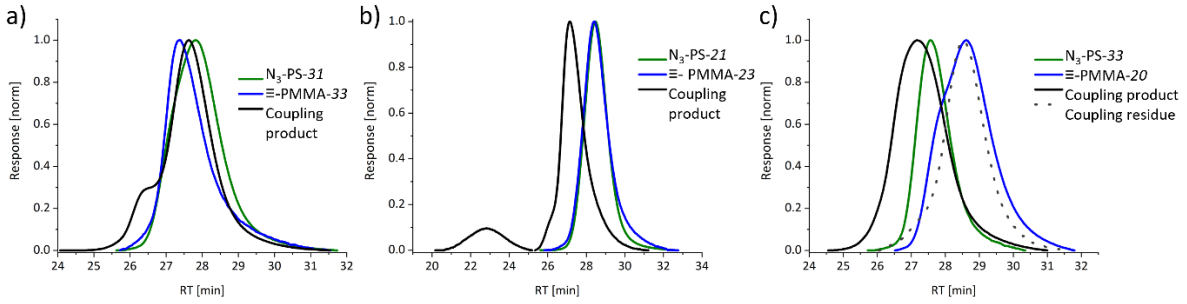

Figure 24: GPC traces of three different coupling reactions, showing a) incomplete coupling, b) a promising reaction with some aggregation of coupled polymer and c) incomplete coupling with unreacted polystyrene in the residue after precipitation.

Using a 1:1 ratio of the reactants is required to receive a clean product under ideal circumstances, which is a downside compared to small molecule chemistry. A control reaction of the small molecule initiators showed full conversion after the reaction time, indicating that the problem could root in the accessibility of the endstanding groups on the polymers with a molecular weight of several ten thousand Da. Using azide capped insoluble Merrifield resin to capture the unreacted alkyne after using it in slight excess could be a possibility but would require complete conversion of the alkyne-capped counterpart, which was not granted in this case, as additionally, some batch-to-batch variation was noted. Due to the problems arising with this originally promising route, alternative synthetic strategies were sought out.

4.1.2 ATRP

As the next approach, the synthesis of the BCP using ATRP for the synthesis of a macroinitiator followed by a chain extension was explored, both using a one-pot as well as a sequential approach.

When following a one-pot approach as shown in Figure 25, chain extension was possible, but both using MMA or styrene as the first monomer had some drawbacks. Using MMA as first block, the conversion was 94%, but after adding styrene the GPC traces showed that the chain extension was incomplete, yielding a bimodal GPC trace (Figure 26). Conversely, when using styrene as the first block, the chain extension seemingly took place nearly completely, but the dispersity increased strongly and as the conversion for the first block was only 77%, the unreacted styrene also took part in the chain extension reaction, giving poor control over the composition of the final polymer.

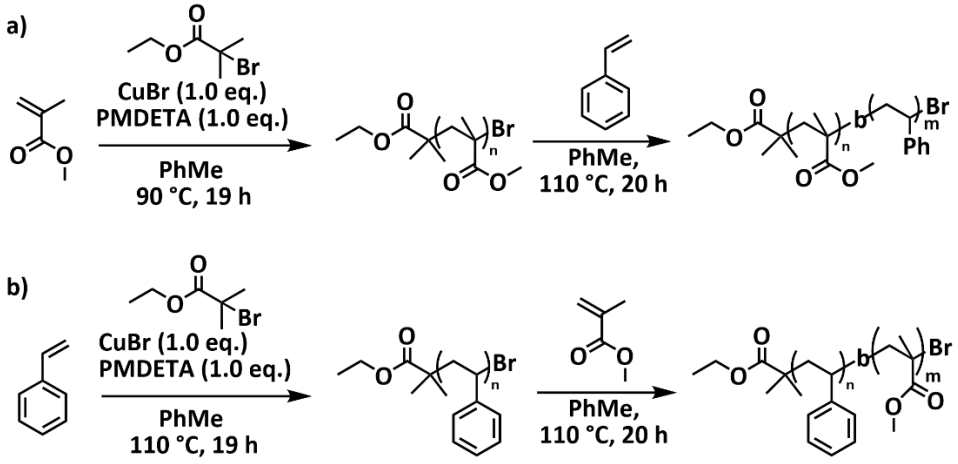

Figure 25: Synthesis scheme of a one-pot ATRP approach. a) Using MMA as the first monomer, b) using styrene in the first block.

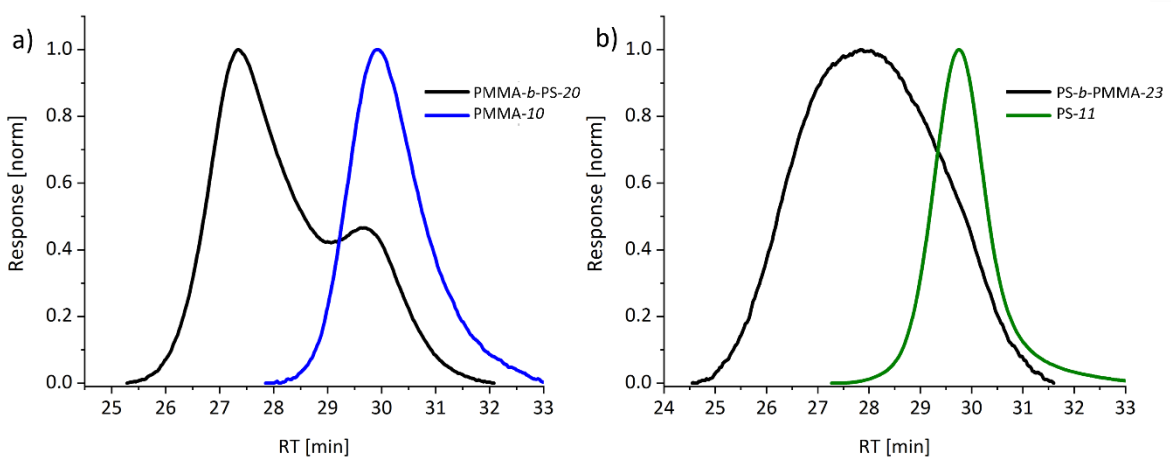

Figure 26: GPC traces of the ATRP one-pot synthesis, a) with MMA in the first reaction, b) with styrene in the first reaction.

The chain extension of ATRP synthesized polystyrene (as shown in Figure 27) also showed several difficulties: For those successfully chain extending to the desired degree, the dispersity strongly broadened and continued so with ongoing reaction, and the degree of chain extension varied for the two otherwise identical reactions presented (Figure 28 a,b). Additionally, investigating the linearity of the system showed deviations from the optimum, indicating that the polymerization is not as controlled as would be the optimal case, as shown by the plots in Figure 28 c,d.

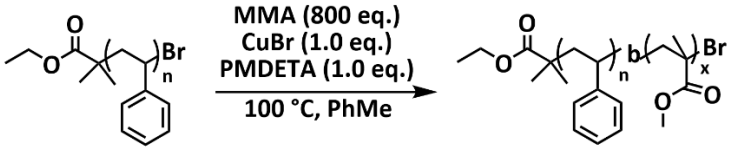

Figure 27: Synthesis of a BCP by chain extending a macro initiator with MMA using ATRP.

Concluding, while it was possible to synthesize the BCPs using ATRP, problems such as poor reaction control and irreproducibility arose and another synthesis approach was sought out.

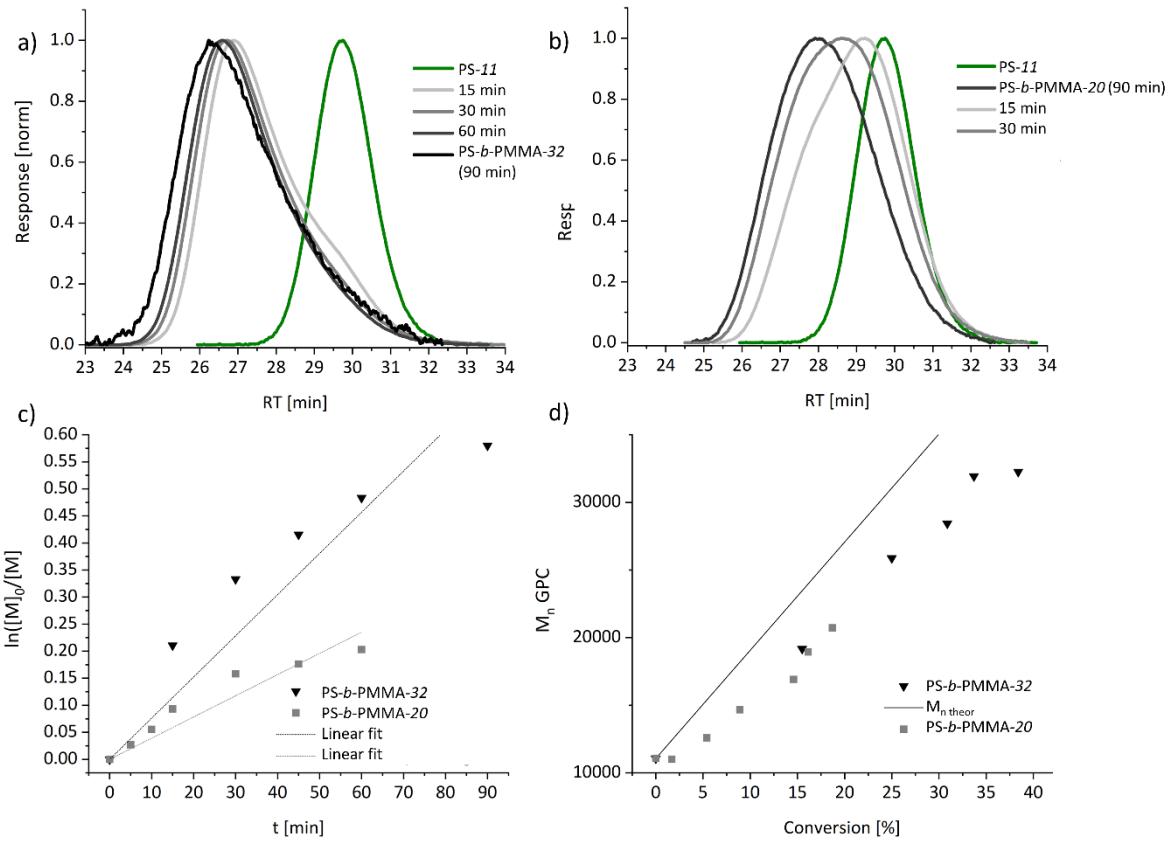

Figure 28: a) b) GPC traces at varying time points during the reaction, for two reactions under identical conditions. c) Graph of $\ln([M]_0/[M]_t)$ vs. time for both reactions with the corresponding linear fits; d) conversion as determined via ^{1}H NMR against $M_{n\,GPC}$; with the theoretical molecular weight as comparison.

4.1.3 RAFT polymerization

As an alternative controlled radical synthesis pathway, sequential RAFT polymerization was investigated. While RAFT polymerization at temperatures of 60-70 °C did also not yield the desired polymers, a switch to the conditions proposed by Varadharajan and Dellaitre [106] - a reaction temperature of 90 °C, and short reaction times (30 min to 3 h) - was successful.

Macro-CTA Synthesis

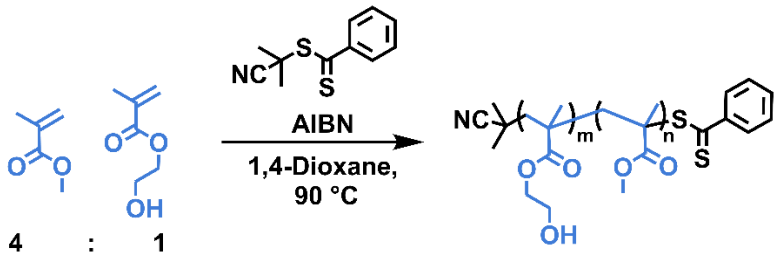

Figure 29: Scheme of the macroCTA synthesis.

The copolymerization of methylmethacrylate (MMA) and hydroxyethylmethacrylate (HEMA) with cyanopropyldithiobenzoate (CPDB) as the chain transfer agent (CTA) to fabricate the MacroCTAs as shown in Figure 29 was unproblematic, as both monomers are well miscible with each other as well as 1,4-dioxane as the solvent, and the molar fraction of HEMA in the final polymer equals the feed ratio of the monomers, making control over the HEMA content easily feasible.

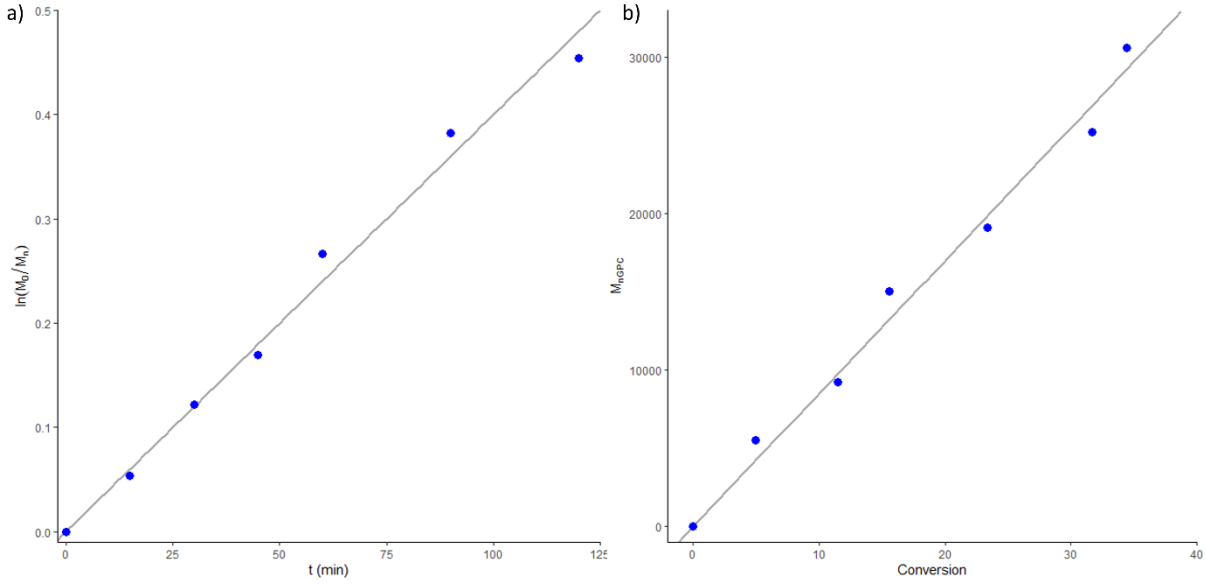

Figure 30: Kinetic data of a HEMA/MMA copolymerization with RAFT initiator CPDB. a) Graph of ln($[M]_0$ $[M]_t$) vs. time. Linear fit: y = 0.004 x and R^2_{corr} = 0.995. b) Conversion as determined via ^{1}H NMR against $M_{n\,GPC}$; linear fit of with y = 849.5 x and R^2_{corr} = 0.994.

The kinetic analysis of the reaction was done by plotting $\ln(M_0/M_t)$ against the reaction time t, which showed a linear behavior the same way the plot of conversion against M_n (GPC) showed, confirming that the polymerization follows the controlled behavior that is expected from the RAFT polymerization, as shown in Figure 30. The conversion as well as $[M]_t$ were calculated from ^{1}H NMR signals (presented in Figure 32) of the HEMA group, by calculating the ratio between the monomer and polymer signal. The GPC chromatogram showing the traces at the different measurement times is shown in Figure 31.

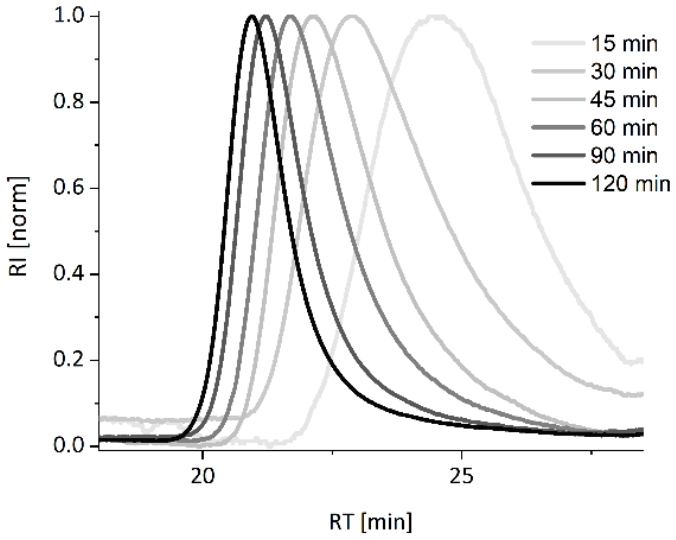

Figure 31: GPC chromatogram showing the traces at the different measurement times for the synthesis of macroCTA-*31*.

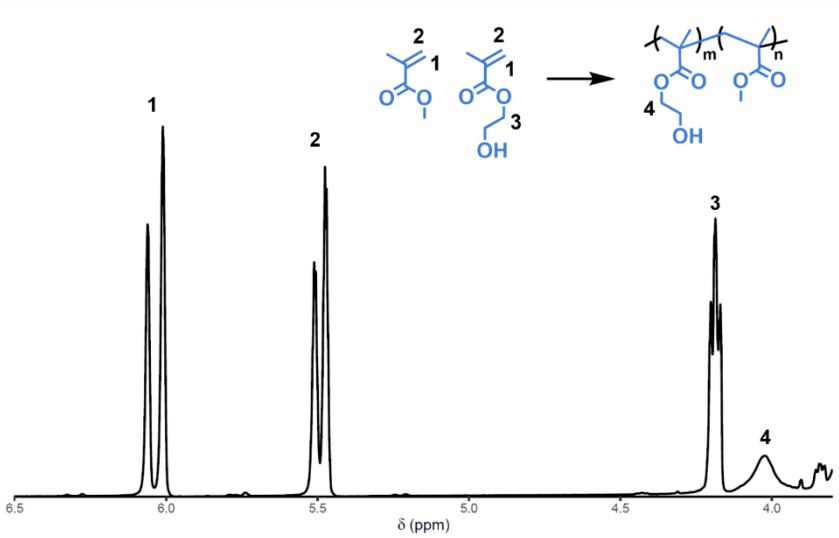

Figure 32: Excerpt of the ^{1}H NMR spectrum of the polymerization for macroCTA-*31* after 60 min. **1** and **2** are the vinyl signals, **3** is a HEMA CH_2 group in the monomer and **4** the corresponding polymer signal.

The GPC curves showed a monomodal curve over the range of polymerizations conducted, with the MMA:HEMA ratio ranging from 80:20 to 60:40, and the monomer:initiator ratio ranging from 280:1 to 1023:1.

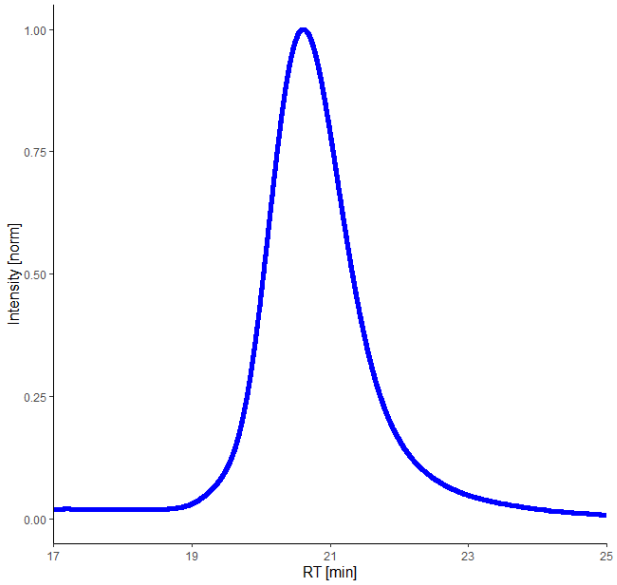

Figure 33: GPC trace of macroCTA-*38*.

An example is shown in Figure 33 as well as an exemplary NMR spectrum (Figure 34), while full analytical data as well as an overview over the reaction conditions of all macroCTAs can be found in the appendix (Table A1, Figure A8– Figure A 31).

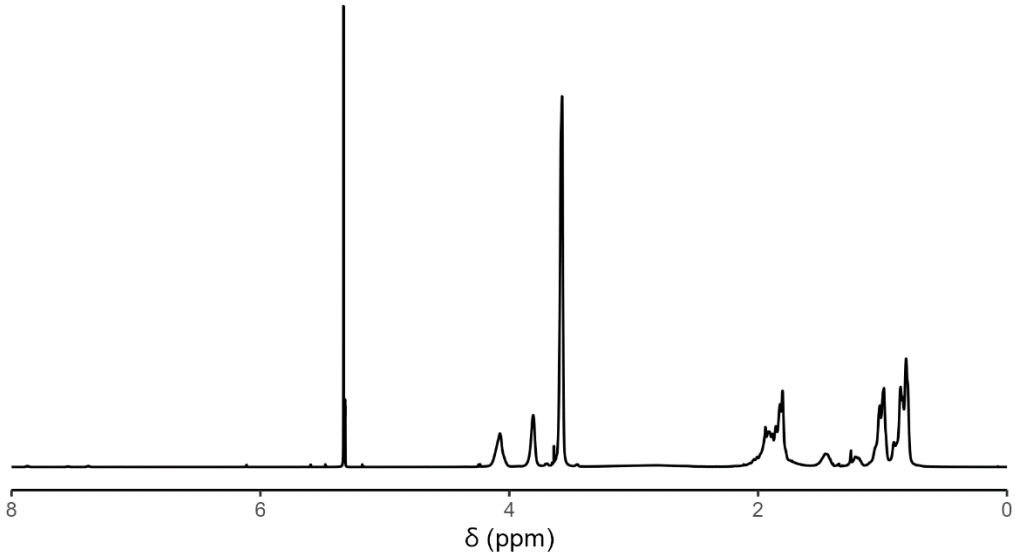

Figure 34: ^{1}H NMR spectrum of macroCTA-*38* in CD_2Cl_2.

Block copolymer synthesis

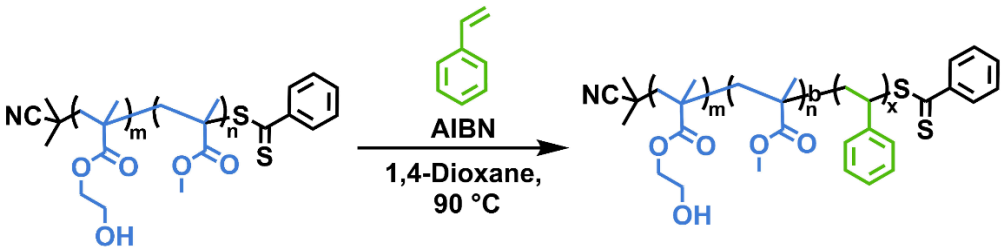

Figure 35: Scheme of the chain extension of the macroCTA using styrene.

The chain extension of the synthesized macroCTAs was performed using styrene, as shown in Figure 35, with monomer:macroCTA ratios between 13200:1 and 2000:1. Due to the high equivalents of styrene in respect to the macroCTA and thus small changes in the concentration during the polymerization it was not possible to follow the progress of the reaction *via* ^{1}H NMR. The GPC analysis showed a continuous increase in molecular weight until a timepoint where the reaction seemingly slows down and the dispersity increases, indicating loss of the controlled character, likely due to the increase in viscosity of the reaction mixture.

An exemplary GPC chromatogram as well as an NMR spectrum are shown in Figure 37 and Figure 36, while full analytical data of all synthesized BCPs are available in the appendix (Table A2, Figure A32 - Figure A 83).

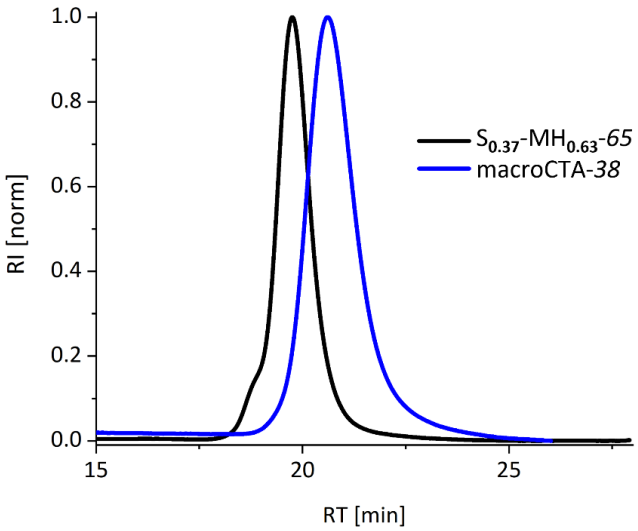

Figure 36: Exemplary GPC trace of $S_{0.37}$-$MH_{0.63}$-*65* together with the corresponding macroCTA-*38*.

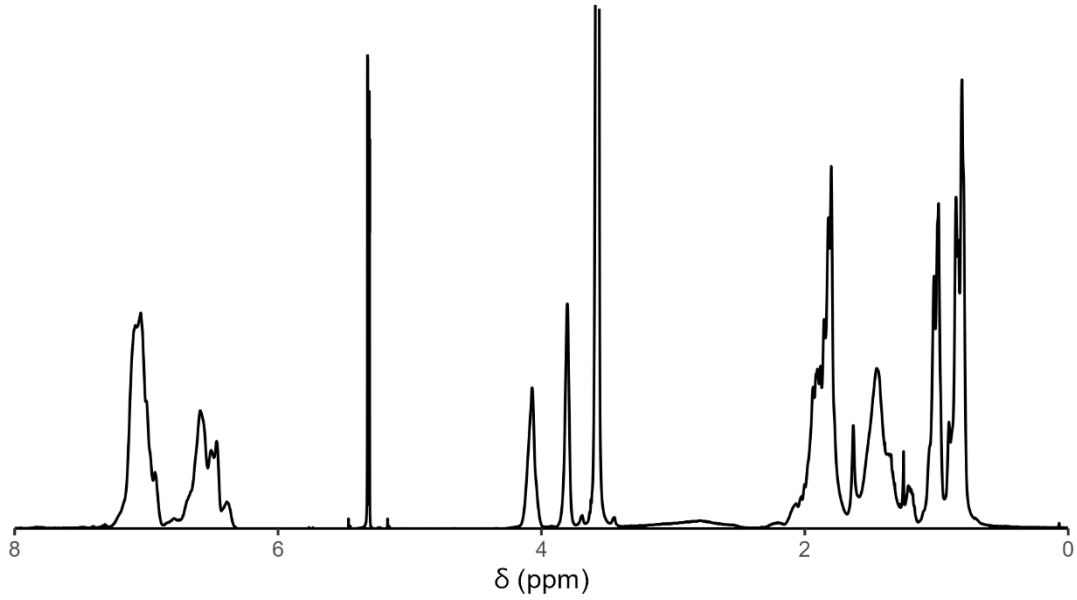

Figure 37: ^{1}H NMR spectrum of $S_{0.37}$-$MH_{0.63}$-*65* in CD_2Cl_2.

4.1.4 Post-Functionalization

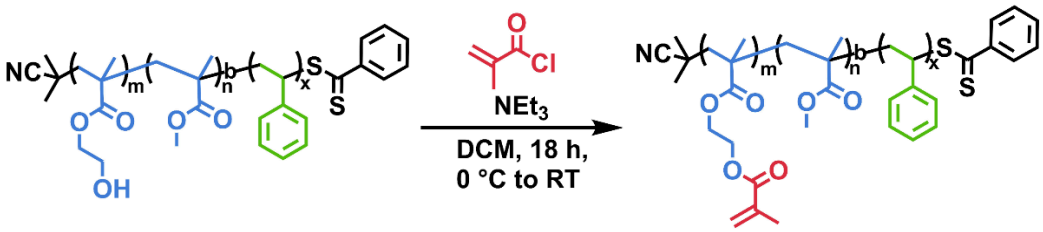

Figure 38: Scheme of the post-functionalization reaction using methacryloyl chloride.

Introducing the (meth)acrylate group was performed by esterification of the alcohol with (meth)acryloyl chloride. The optimization of the reaction contained several key challenges:

- Low conversion
- Loss of reaction control (dark orange, insoluble residue)
- Challenging purification, low yields
- Cross-linking of the final product even in the dark and cold

The first issue could be solved by increasing the equivalents of acid chloride and NEt_3 far above the amount usually applied (around 16 and 18, respectively, in respect to the OH groups on the polymer). Adding the acryloyl chloride, which was not dissolved in additional solvent, very slowly to a very dilute solution (approx 1 wt/vol% of polymer) resulted in control over the reaction with only slight discoloration of the reaction solution in the most cases. Removal of the unreacted acid chloride and

the NEt_3·HCl salt posed the next challenge. Alternative reaction conditions were therefore also explored.

Reactions using inorganic salts ($NaHCO_3$ and K_2CO_3) as the base in combination with or without DMAP in different solvents showed easy purification by filtrating off the salts but suffered from incomplete conversion even when increasing the reaction time up to 96 hours. When using pyridine as base, the removal during the workup was problematic. THF as an alternative solvent was also explored instead of DCM due to the precipitation of the NEt_3·HCl salt in THF, but as some of the salt remained in the polymer, purification was still an issue.

Dialysis worked for smaller amounts of polymer, but for bigger quantities the purification was not complete, and the salt remained. Furthermore, dialysis against acid presumably led to hydrolysis of the acrylic ester bonds as indicated by ^{1}H NMR.

The removal of the triethylamine hydrochloride salt was consistently successful by washing with 5% aq. $NaHCO_3$, but the yield was low, especially for upscaled reactions above 100 mg, where it was problematic to obtain more than about 20 mg of sample. The phase separation was incomplete even after long settling times and a third, emulsified phase formed. Different approaches were explored in order to improve the phase separation and yield.

When removing the reaction solvent DCM and adding PhMe, followed by washing with 5% aq. $NaHCO_3$, the phase separation was better, but there was product remaining in the aqueous phase which could be extracted containing impurities with DCM. Adding $CHCl_3$: iPrOH instead in a ratio of 3:1 after removal of DCM, and washing as described above, the phase separation was better than with pure DCM, but still not complete. The best results were obtained when using a procedure adapted from Wu et al.:[107]

The DCM was removed under reduced pressure and the crude product was dissolved in MeCN. The solution was poured into 5% $NaHCO_3$ aq. and shaken in a separating funnel. The product was then extracted three times with DCM. After drying and solvent removal, this procedure was repeated. This washing procedure showed complete, relatively fast phase separation and lead to full removal of the triethylamine hydrochloride salt.

After precipitation into diethyl ether to remove the residual, unreacted (meth)acryloyl chloride up to 70% yield of clean product were received. The full conversion of the reaction was ensured via ^{1}H NMR, as shown in Figure 39.

The original pathway of functionalizing with acryloyl chloride led to rapid cross-linking of the polymer when the concentration was high or in the solid, even under dark and cold conditions, after solvent removal while cooling and after adding copious amounts of BHT.

Instead, functionalization with methacryloyl chloride was chosen, which greatly improved this problem to give shelf stability on the month scale and was thus used for the formulations presented later in this work.

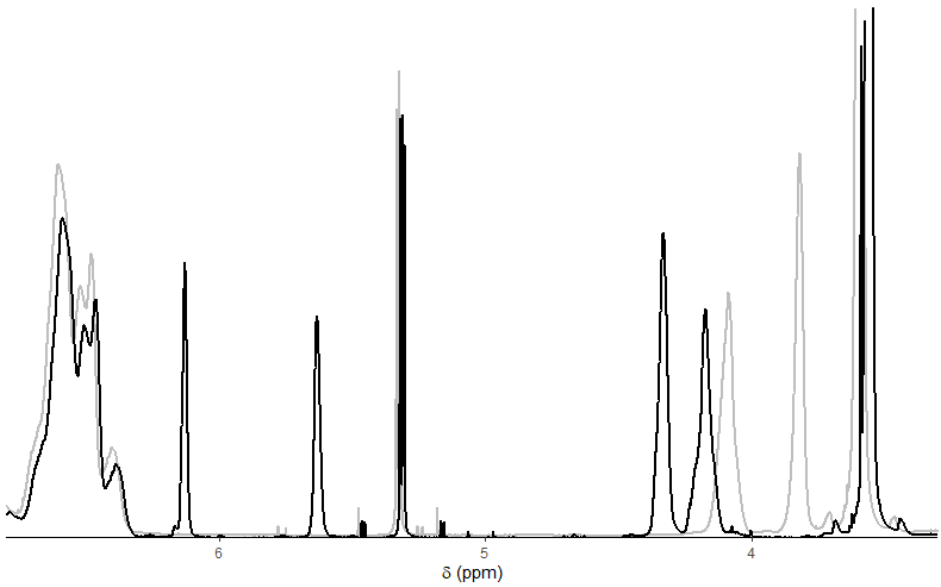

Figure 39: The ^{1}H NMR spectrum of a pure (grey) and a functionalized BCP (black) showing the signals of the two methacrylic protons and the shift of the CH_2 signals which belong to the aliphatic HEMA protons. The full spectra are shown in the appendix.

In summary, using a three-step synthesis approach consisting of a sequential RAFT polymerization for the block copolymer synthesis and an esterification between acid chloride and the free hydroxy groups, it was possible to synthesize a wide range of compositions and molecular weight of both functional and pristine block copolymers that could be investigated for their self-assembling behavior and printing properties.

4.2 Self-assembly characterization and evaluation

While a wide range of experimental phase diagrams and observations about the influence of introducing functionalization into block copolymer systems has been published, most of the investigated systems focus on AB polymers without a randomly dispersed co-monomer in one of the blocks. Additionally, the influence of the functionalization has not been investigated for photo-crosslinkable groups, as it has only been established that the morphology is retained upon crosslinking. For further applications of BCPs, the ability to crosslink could play an important role due to the improved thermal stability as well as resistance to solvents and changed material properties. Thus, our aim was, after the successful synthesis of a range of block copolymers with different compositions and molecular weights, to observe the morphologies of the self-assembled polymers using SEM imaging, SAXS and, as a supplement for some of the polymers, SNOM in addition. The collected data should then be used to plot the phase diagram for the investigated polymer systems.

4.2.1 Sample preparation

To investigate the bulk-self-assembly of the synthesized block copolymers, films were casted from solution by slow evaporation of the solvent over the course of days. After removal of the glass vial by immersing the film into liquid nitrogen and gently tapping with a hammer, the free-standing films were embedded in epoxy-resin, sectioned with the ultramicrotome and placed onto silicon wafers.

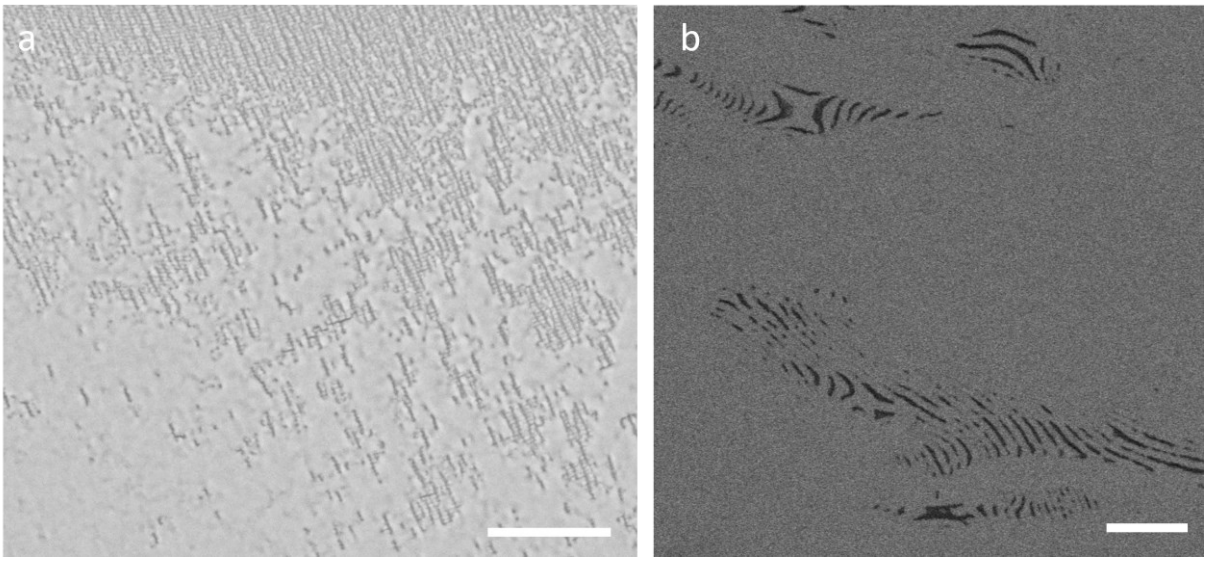

Figure 40: SEM images of a lamellar film ($S_{0.53}$-$MH_{0.47}$-*94*) that was overstained with RuO_4. The smooth layer is visible with both the SE2 detector (a) and the ESB detector (b). Scale bars = 200 nm.

Selective Staining Agents for a PS-*b*-PMMA system

Selective staining agents enhance the electron density contrast, as most organic polymers have similar compositions/densities. Ruthenium tetroxide stains both saturated and unsaturated moieties such as ether, alcohol, aromatic and amide moieties. Conversely, it does not stain for example PMMA, PVC or PAN. It has been found that it is a far more vigorous oxidant than OsO_4. Trent et al. tested the vapor staining properties of RuO_4 on 28 different polymers. For a PS-*b*-PMMA system they found that even for the unstained blend some contrast was visible in the electron micrographs, which may be the result of differences in thickness or density fluctuations, and enhanced contrast after staining, making RuO_4 vapor a suitable staining method for this polymer combination. Additionally, the RuO_4 diffusion rate could have an additional effect on the staining efficiency.[108] Chou et al. found that during the staining process RuO_2 nanocrystals with a diameter between 2 – 5 nm deposited. After exposure to the vapor for 3 days, a full layer formed on top of the polymer.[109]
Osmium tetroxide on the other hand is effective at reactions with the double or triple carbon-carbon bond, and also with hydroxyl groups attached to shorter carbon chains. Other functional groups such as -SH, -S- or amines are also oxidized, while esters are not showing reactivity.[110]

For SEM characterization the BCPs were thus stained with RuO_4 vapors. When performing the vapor staining in a closed glass jar instead of using an upside-down petri-dish as a cover, overstaining was observed in several cases. Hereby, a smooth layer deposited on the section, preventing the observation of the nanostructures, as shown here in Figure 40, which is in line with the findings of Chou et al.[109] The nanostructure was sometimes still visible as here for the lamellae, especially at the bigger nodes. It was also possible to stain the films using a solution of OsO_4 in H_2O, but the introduced contrast was lower than when using RuO_4 vapors, which could also be influenced by the permeability in water.

4.2.2 Phase diagram

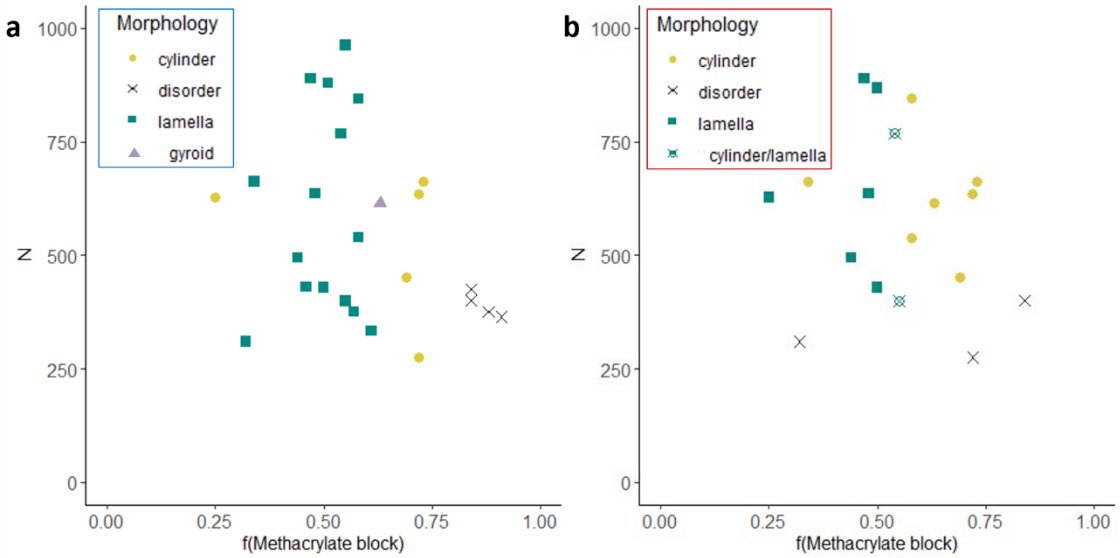

Figure 41: Phase diagrams of a) the unfunctionalized and b) the functionalized polymer systems.

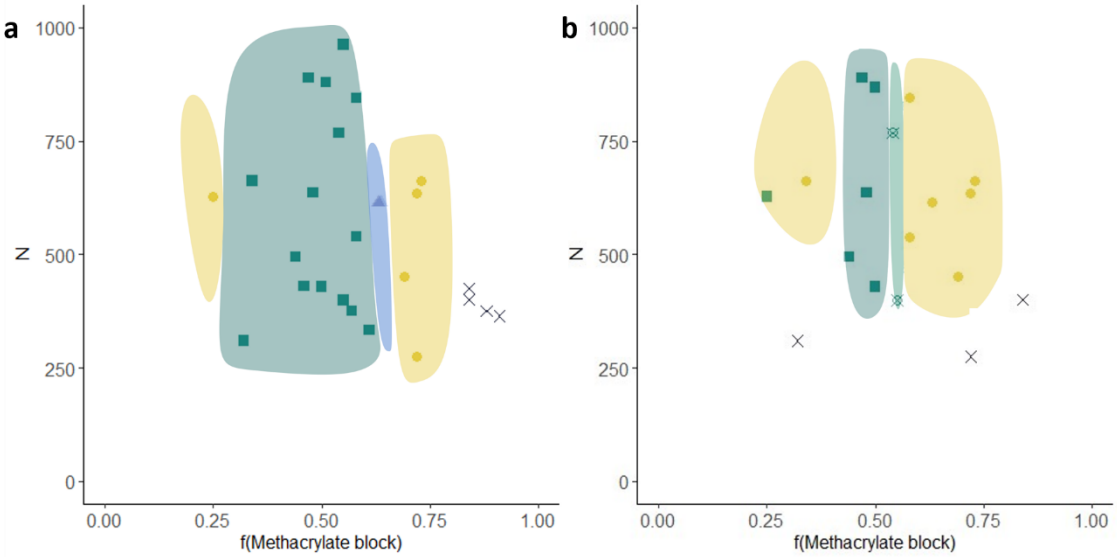

Figure 42: Phase diagrams of a) the unfunctionalized and b) the functionalized polymer systems with indicated phase boundaries. The shown boundaries are guides to the eye and there is the possibility of additional, non-imaged phases.

When summarizing the microscopical and scattering data of all the synthesized polymers and plotting the fraction of the methacrylate block (by molar ratio) against the degree of polymerization (for lack of a value of χ), as shown in Figure 41, several observations could be made. (A complete overview of the microscope images and SAXS scattering plots as well as bigger micrographs of those presented in the following chapter can be found in the appendix, chapter 7.3, while a summary of the assigned morphologies is presented in Table 2). Firstly, the measured data are in accordance with the expected morphologies and the transitions in-between. When visually underlying the experimental data along

the proposed phase boundaries as guides for the eye (as done in Figure 42), the change in the phase windows becomes quite apparent – the lamellar window becomes significantly smaller for the functionalized polymers, while the cylindrical window is bigger. This is the result of several BCP expressing a different morphology after their functionalization. Additionally, for several polymers with an ordered morphology in the original state, the morphology becomes disordered upon functionalization. These changes in morphology behavior are in accordance with literature and can be reasoned with a change in χ upon the functionalization of the hydroxyl group.

Table 2: Table detailing the assigned morphologies as well as the degree of polymerizations for the BCPs.

f	N	Polymer	Morphology pure	Functionalized polymer	Morphology functionalized
0.25	628	$S_{0.75}$-$MH_{0.25}$-*66*	cylinder	$S_{0.75}$-$MH^*_{0.25}$-*66*	lamella
0.32	310	$S_{0.68}$-$MH_{0.32}$-*33*	lamella	$S_{0.68}$-$MH^*_{0.32}$-*33*	disorder
0.34	662	$S_{0.66}$-$MH_{0.34}$-*70*	lamella	$S_{0.66}$-$MH^*_{0.34}$-*70*	cylinder
0.44	495	$S_{0.56}$-$MH_{0.44}$-*52*	lamella	$S_{0.56}$-$MH^*_{0.44}$-*52*	lamella
0.46	430	$S_{0.54}$-$MH_{0.46}$-*45*	lamella		
0.47	889	$S_{0.53}$-$MH_{0.47}$-*94*	lamella	$S_{0.53}$-$MH^*_{0.47}$-*94*	lamella
0.48	636	$S_{0.52}$-$MH_{0.48}$-*67*	lamella	$S_{0.52}$-$MH^*_{0.48}$-*67*	lamella
0.50	868			$S_{0.50}$-$MH^*_{0.50}$-*91*	lamella
0.50	429	$S_{0.50}$-$MH_{0.50}$-*45*	lamella	$S_{0.50}$-$MH^*_{0.50}$-*45*	lamella
0.51	879	$S_{0.49}$-$MH_{0.50}$-*92*	lamella		
0.54	768	$S_{0.46}$-$MH_{0.54}$-*81*	lamella	$S_{0.46}$-$MH^*_{0.54}$-*81*	cylinder/lamella
0.55	399	$S_{0.45}$-$MH_{0.55}$-*42*	lamella	$S_{0.45}$-$MH^*_{0.55}$-*42*	cylinder/lamella
0.55	963	$S_{0.45}$-$MH_{0.55}$-*102*	lamella		
0.57	376	$S_{0.43}$-$MH_{0.57}$-*40*	lamella		
0.58	845	$S_{0.42}$-$MH_{0.58}$-*89*	lamella	$S_{0.42}$-$MH^*_{0.58}$-*89*	cylinder
0.58	539	$S_{0.42}$-$MH_{0.58}$-*57*	lamella	$S_{0.42}$-$MH^*_{0.58}$-*57*	cylinder
0.61	333	$S_{0.39}$-$MH_{0.61}$-*35*	lamella		
0.63	615	$S_{0.37}$-$MH_{0.63}$-*65*	gyroid	$S_{0.37}$-$MH^*_{0.63}$-*65*	cylinder
0.69	451	$S_{0.31}$-$MH_{0.69}$-*48*	cylinder	$S_{0.31}$-$MH^*_{0.69}$-*48*	cylinder
0.72	634	$S_{0.28}$-$MH_{0.72}$-*67*	cylinder	$S_{0.28}$-$MH^*_{0.72}$-*67*	cylinder
0.72	275	$S_{0.28}$-$MH_{0.72}$-*29*	cylinder	$S_{0.28}$-$MH^*_{0.72}$-*29*	disorder
0.73	662	$S_{0.27}$-$MH_{0.73}$-*70*	cylinder	$S_{0.27}$-$MH^*_{0.73}$-*70*	cylinder
0.84	401	$S_{0.16}$-$MH_{0.84}$-*43*	disorder	$S_{0.16}$-$MH^*_{0.84}$-*43*	disorder
0.84	425	$S_{0.16}$-$MH_{0.84}$-*45*	disorder		
0.88	375	$S_{0.12}$-$MH_{0.88}$-*40*	disorder		
0.91	364	$S_{0.09}$-$MH_{0.91}$-*39*	disorder		

Taking a closer look at a few of the polymers changing morphology upon the functionalization, in the case of $S_{0.42}$-$MH_{0.58}$-*89* and $S_{0.42}$-$MH^*_{0.58}$-*89*, the pure polymer shows a lamellar morphology as visible in the SEM image (Figure 43). The lamellar structure was also confirmed by the SAXS measurement, where the pattern exhibited peaks with a ratio of their associated q-values of q*, 2q*, 3q*, up to 4q* and 5q*. Upon functionalization, the morphology changes to a cylindrical morphology, which is

indicated by both the visual change in the SEM image, as well as from the SAXS measurements with the reflections apparent at q, √4 q* and √7 q*.

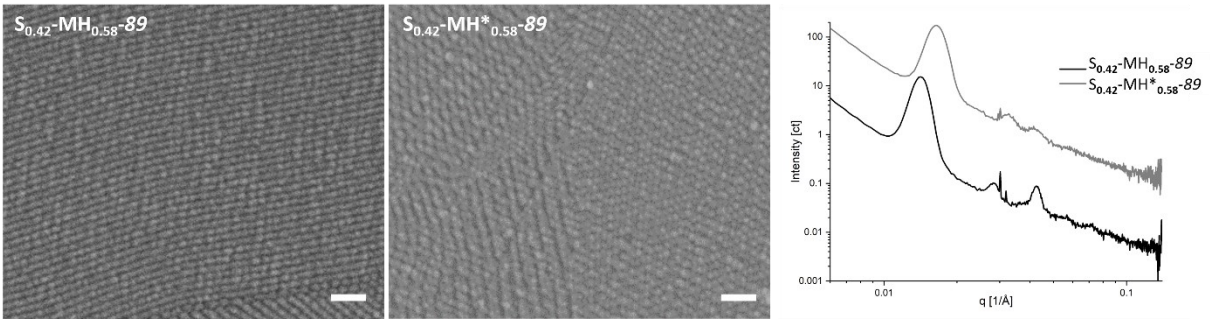

Figure 43: SEM images and SAXS spectra of $S_{0.42}$-$MH_{0.58}$-*89* and $S_{0.42}$-$MH^*_{0.58}$-*89*. Scale bars = 200 nm.

A similar effect could be observed for $S_{0.37}$-$MH_{0.63}$-*65* and $S_{0.37}$-$MH^*_{0.63}$-*65* with a higher MMA/HEMA:styrene ratio. A morphology that can be assigned to gyroid structures was observed, where the main indication is the characteristic shoulder at √(4/3) q* represented in the SAXS pattern (Figure 44).[111] When this BCP is functionalized, a cylindrical morphology is detected, confirmed by the SEM images in combination with the diffraction pattern.

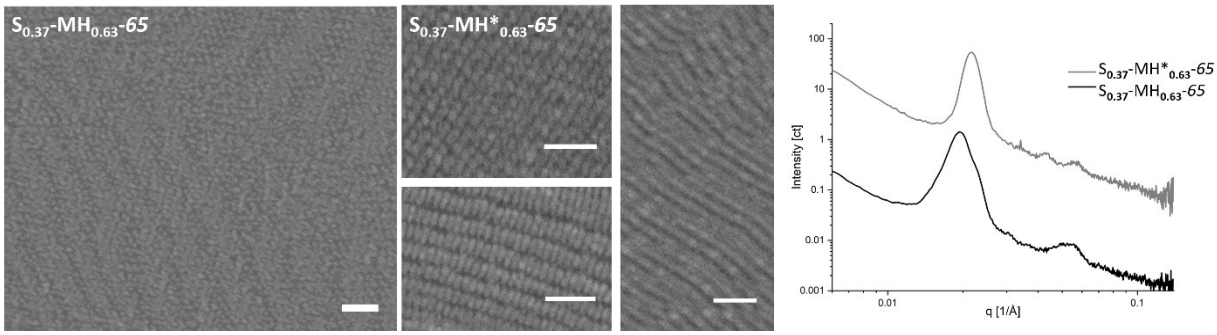

Figure 44: SEM images and SAXS spectra of $S_{0.37}$-$MH_{0.63}$-*65* and $S_{0.37}$-$MH^*_{0.63}$-*65*. Scale bars = 200 nm. $S_{0.37}$-$MH^*_{0.63}$-*65* is imaged along different planes of the ordered cylinders. 3D renderings of the sectioned planes can be found in Figure A1.

Due to the limited number of experimental sample points in this study, it is possible that other phases also exist, e.g. the other gyroid windows. It is also possible that the disordered morphologies also contain disordered spheres that are not imageable by the achievable SEM resolution and not easy to identify using the SAXS reflections due to the lack of higher order reflections. The single broad peak visible in the SAXS reflections, such as for $S_{0.68}$-$MH^*_{0.32}$-*33,* shown in Figure 45, could be an imaging of the correlation hole.[112,113]

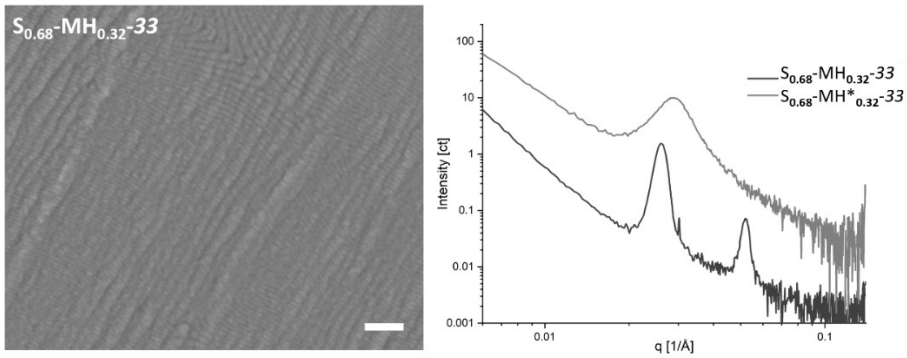

Figure 45: SEM image of $S_{0.68}$-$MH_{0.32}$-*33*, showing a lamellar morphology, and the SAXS spectra of $S_{0.68}$-$MH_{0.32}$-*33* and $S_{0.68}$-$MH^*_{0.32}$-*33*. Scale bars = 200 nm.

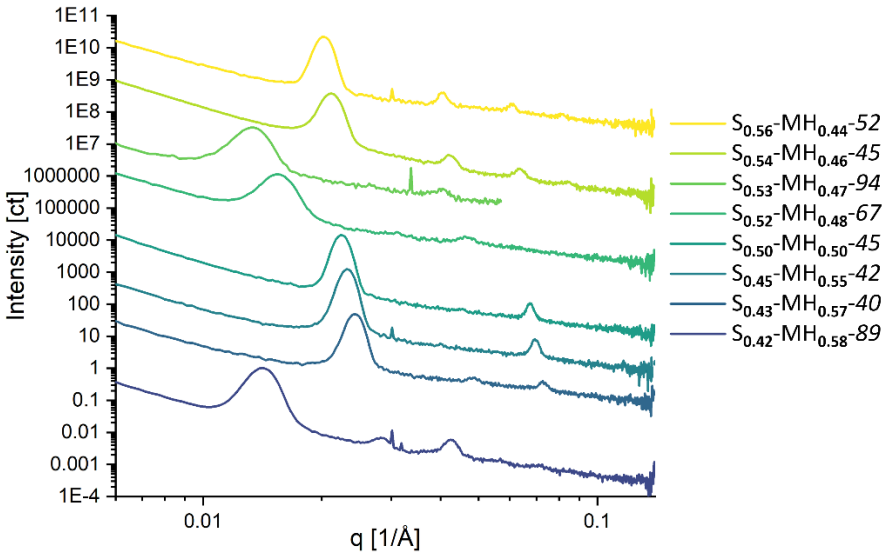

Figure 46: SAXS spectra of the lamellar forming pure BCPs, showing the development of the even reflections. Intensities are shifted for comparison.

When adjusting the fraction of the methacrylate block, it is natural that the volume fractions for the different blocks change. When both blocks have the same volume in a lamellar BCP, the even reflections (2q*, 4q*) are absent.[81,114] When plotting the SAXS diffractions of the lamellar, unfunctionalized polymer ordered by increasing methacrylate block fraction (Figure 46), it becomes apparent that for the highest as well as the lowest methacrylate fractions the even reflections, especially that at 2q*, are expressed at both lower as well as higher molecular weights. For those polymers in between, 2q* is either weakly expressed or not distinctly visible, which aligns with the expectation.

For further analysis, the domain spacings d were then determined from the scattering maxima of the SAXS spectra ($d= 2\pi/q$) for all polymer samples (d_{SAXS}) and for the lamella forming samples using the SEM images (d_{SEM}). Figure 47 shows plots of d_{SAXS} as well as d_{SEM} for the lamellar samples against the molecular weight $M_{n\ GPC}$. As discussed when investigating the phase diagrams, the morphological

behavior changes upon the functionalization, but it is also notable that upon functionalization the domain spacing becomes smaller.

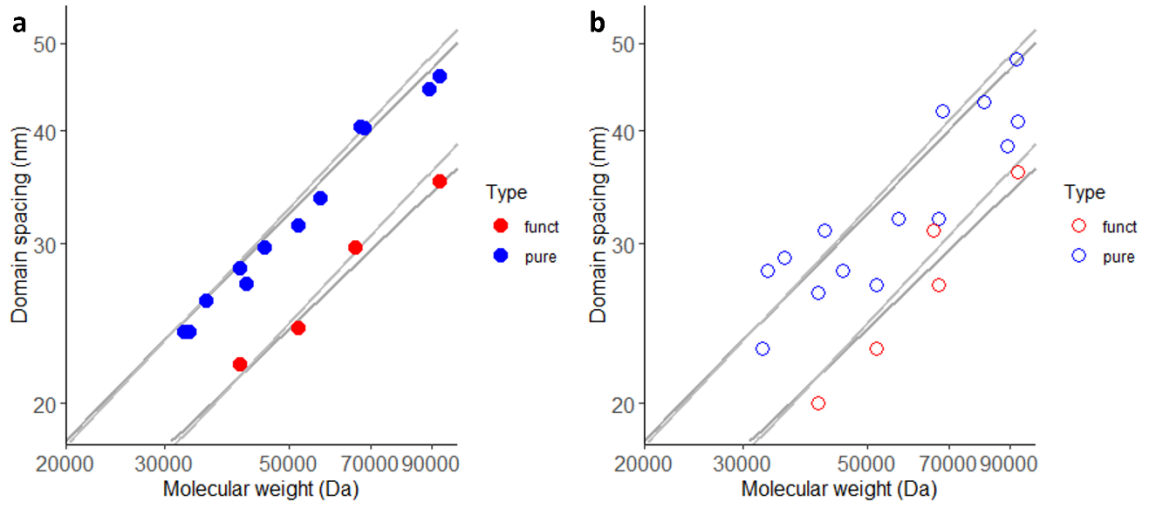

Figure 47: Double logarithmic plot of the domain spacing against the molecular weight for the lamellar morphology. a) d_{SAYS} and b) d_{SEM}. The dark grey lines are the power law fits with the parameters stated below, while the light grey lines are fits with a dependency of $d \sim M^{2/3}$. Blue = BCP and red = functionalized BCP.

Numerous experiments have confirmed that for a linear diblock copolymer the scaling behavior in the strong segregation limit is $D \sim N^{2/3}$ which is in alignment with the theoretical prediction.[115] The results found here when fitting the experimental values to a power law are in accordance with this behavior. It is notable that the proportion factor is smaller for the functionalized polymers, which could be an indicator of several things. Either, due to the change in χ the system is currently not in the strong segregation limit anymore or the fit is negatively influenced by the smaller number of samples. Additionally, the length of the functionalizing methacrylate moiety could have an influence, as it is introducing some architectural asymmetry. The effects of this asymmetry were found by Liberman et al.[38] when investigating the self-assembly of linear bottlebrush BCPs with varying degrees of architectural asymmetry by changing the side-chain length.

By fitting the data to the power law, it becomes apparent that when plotting the $d_{SAXS,}$ the deviation from the fit is far less, as determined both visibly and by the deviation from the fit (presented in Table 3). Similar effects were also observed by Richards and Thomason[115], where they found that the agreement of domain sizes measured from SAXS and SEM was best for spherical systems and worst for the lamellar systems. This was attributed to the high dependency of the SEM analysis on the orientation of the lamellae in the sections depending on the angle towards the microtome, while the thickness of the obtained section is also influential, which is most important for the lamellar domains. Thus, the imaged lamellae are more trapezoidal.

Table 3: Fit data for the power law for the different polymer types.

Morphology	Fit to power law	$D \sim N^x$	R^2
Lamella (d_{SAXS})	$0.03567^{+/-0.0115} * N^{0.62695 +/- 0.029}$	0.627	0.979
Lamella functionalized (d_{SAXS})	$0.0397^{+/- 0.035} * N^{0.5925 +/- 0.08}$	0.593	0.948
Lamella (d_{SEM})	$0.1411^{+/- 0.011} * N^{0.49873 +/- 0.07}$	0.499	0.795
Lamella funct (d_{SEM})	$0.00902^{+/-0.0116} * N^{0.72555 +/- 0.1159}$	0.725	0.931
Cylinder	$0.0432^{+/- 0.0} * N^{0.61811 +/- 0.2}$	0.618	0.853
Cylinder functionalized	$0.18727^{+/- 0.49} * N^{0.473+/- 0.32}$	0.473	0.4333

In Figure 48 lamellae with different thicknesses are shown in excerpts of one micrograph of $S_{0.45}$-$MH_{0.55}$-*102*, making this a likely possibility. While it was aimed at measuring the smallest visible domain spacing, the smaller imaged sample area in combination with nearing the maximum resolution achievable with the SEM made this more prone to error. Additionally, films can be stretched during processing, additionally influencing the measured domain spacing.

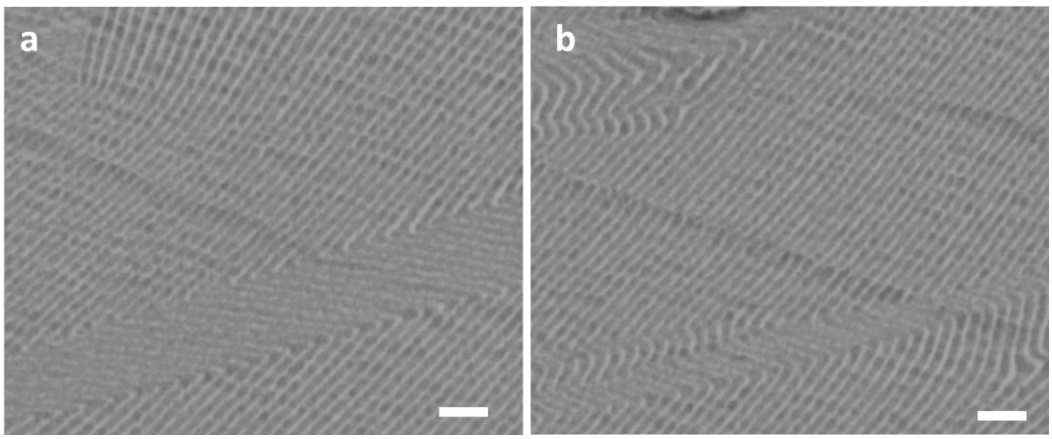

Figure 48: SEM micrographs showing the lamellar morphology of $S_{0.45}$-$MH_{0.55}$-*102* with different lamellar thickness within the same larger micrograph within one section. Scale bar = 200 nm.

It also becomes evident when plotting and fitting the data for the cylindrical morphology (Figure 49) that the deviation from the fit is far larger than for the lamellar samples. It is also noteworthy that while the exponent for the pure samples is relatively similar to those for the lamellar samples, (albeit the R^2 being much smaller), for the functionalized cylindrical sample both the exponent as well as the deviation are large. Grouping the sample points by methacrylate block fraction did not disclose any underlying dependency on this factor, which was also the case for the samples with lamellar morphology.

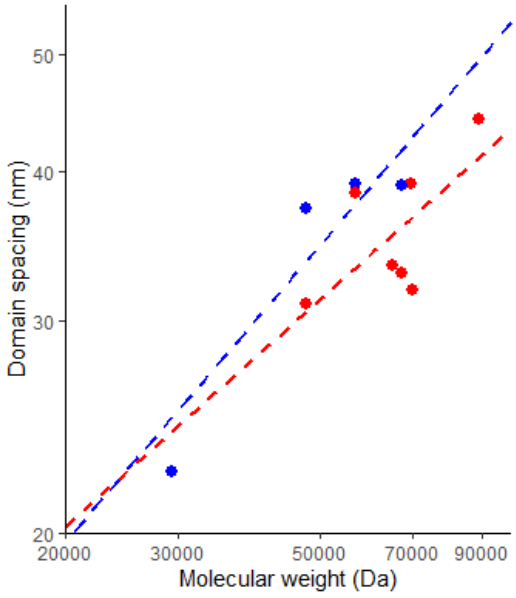

Figure 49: Double logarithmic plot of the domain spacing d_{SAXS} against the molecular weight for the cylindrical samples. The dotted lines are the power law fits with the parameters stated above. Blue = BCP and red = functionalized BCP.

The assembly approach chosen here is only a solvent evaporation approach, as thermal annealing was not accessible considering to the sensitivity of the free methacrylate moieties. Due to the slow evaporation of the solvent the reached state should not be differing strongly from the thermodynamic equilibrium, as χ is not very high, the total molecular weight is moderate and the chains are mostly linear, with short side chains, which are all factors that have been found to have a negative effect on chain reordering towards the thermodynamic equilibrium with order not only locally but over some μm^2.[81,116] This is supported by the good agreement with the theoretical dependency of d on the molecular weight for three of the four compound classes. The bigger deviation for the cylindrical functionalized polymers could stem from the property that the ordering into cylindrical as opposed to lamellar domains requires some transport between domains. This is not favorable from a kinetic or thermodynamic standpoint especially for solutions with higher viscosity as those present during the self-assembly procedure. The introduced asymmetry of the side chains here could thus hinder the reaching of the equilibrium. [115]

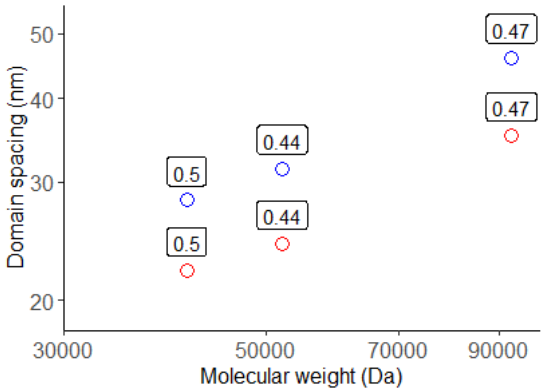

Figure 50: Change in domain spacings (as measured from SAXS) when introducing the methacrylate functionality for the polymers where both species show lamellar morphology.

In Figure 50, the change in the domain spacing is graphically represented for the three samples where the morphology was lamellar for both the original and the functionalized polymer. The trend of the decreasing d is clearly visible. As $d \sim N^{(2/3)}\chi^{(1/6)}$, the decrease confirms that χ becomes smaller upon introduction of the methacrylate group. The possible methacrylate block fraction where both polymer species show a lamellar morphology was between 0.44 and 0.5 for the measured samples, whereas samples with a methacrylate block fraction of 0.53 already showed a mix between lamellar and cylindrical morphology.

An additional interesting effect was observed when functionalizing a compound with an acrylate group instead of a methacrylate group. The peaks in the SAXS spectrum (Figure 51d) are at similar positions for both polymers, but the signals for the acrylated polymer are noticeably broader. This could either indicate a lower degree of organization, or a mixture of different morphologies, which aligns with the SEM excerpt shown in Figure 51 b) and c). Further investigation would be necessary, but it seems that the difference between acrylate and methacrylate group in the 20% HEMA content in one of the blocks is already enough to generate differences in the self-assembly, opening possibilities for further fine-tuning of the morphology by adding different or mixtures of functional groups.

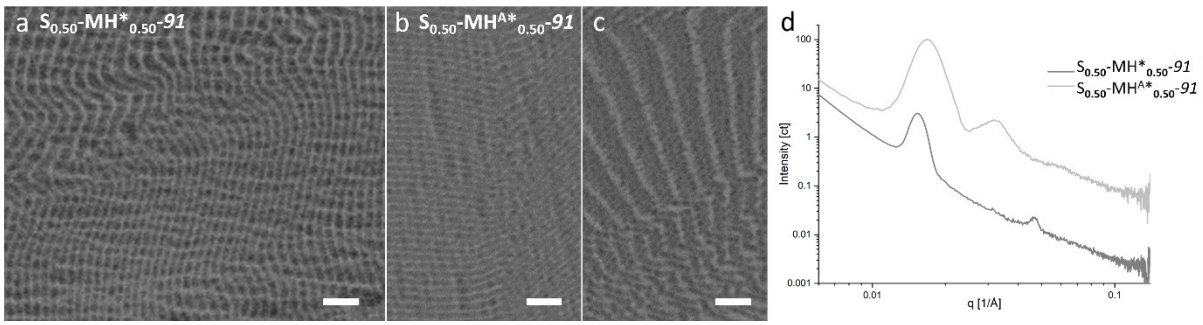

Figure 51: SEM images of a) $S_{0.50}$-MH*$_{0.50}$-*91*, b,c) $S_{0.50}$-MH$^{A}{}_{0.50}$-*91*, d) SAXS spectra of both compounds.

Additionally, partial functionalization of the HEMA with methacrylate groups in several BCPs was also investigated – for example for $S_{0.45}$-$MH^{50\%*}_{0.55}$-*42*, at only 50% functionalization the morphology already differs from the original polymer, switching from a lamellar to a cylindrical morphology as evidenced by both SEM and SAXS (Figure 52), so hereby a control of the morphology could also be possible. For the larger $S_{0.46}$-$MH_{0.54}$-*81* with a similar methacrylate block fraction, functionalizing lead to a shift in morphology from lamellae to a mixed morphology of cylinders and lamellae. When this polymer was only 50% functionalized, the morphology was purely lamellar (Figure A113Figure A114).

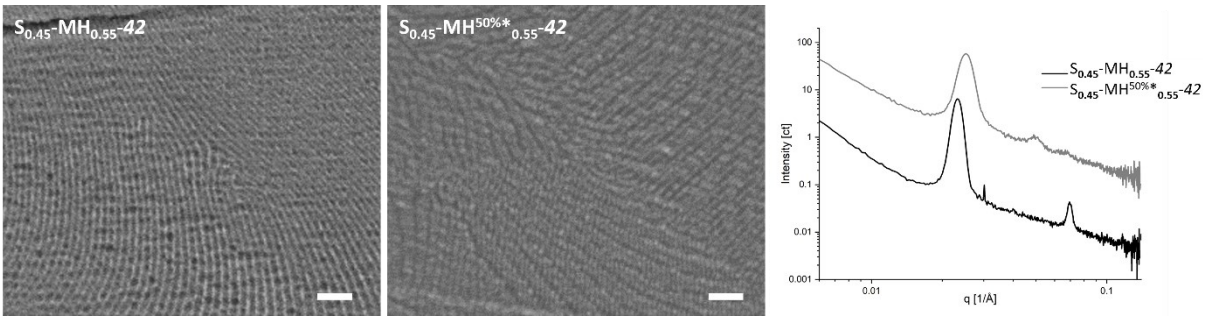

Figure 52: SEM images and SAXS spectra of $S_{0.45}$-$MH_{0.55}$-*42* and $S_{0.45}$-$MH^{50\%*}_{0.55}$-*42*.

To summarize, insights were gained into the complex phase behavior of the PS-*b*-P(MMA-*co*-HEMA) as well as the PS-*b*-P(MMA-*co*-MethacryEMA) block copolymer systems. The preliminary phase diagrams could be drawn, showing the different sizes of the phase windows in comparison, specifically a narrower lamellar window for the functionalized polymer species.

The domain spacing for the lamellar polymers could be fitted to a power law, and the fit was close to the predicted value by Helfand of $d \sim M^{2/3}$ especially for the unfunctionalized polymer. Additionally, the decrease of domain spacing/size upon functionalizing confirms the assumption that χ is decreasing when introducing the less polar methacrylate group in comparison to the more polar free hydroxy group.

The introduction of the acrylate group instead of methacrylate group led to broader peaks, while the change in morphology could in some cases be already observed when the polymer was only 50% functionalized.

4.3 3D printing hierarchically nano-ordered structures

After generating the library of functional BCPs and the detailed analysis of the self-assembly behavior, the key step, the generation of the hierarchically ordered microstructures using TPLP, was targeted. To this aim, BPCs exhibiting different nanostructures were used.

The key challenge was to ensure good printability of the self-assembled material while preserving the nano-order during the printing process and within the entire 3D structure.

First approaches were made printing directly in the self-assembled solid bulk film. While drop casting films on a glass slide followed by slow solvent evaporation did show self-assembly (shown in Figure A3), printing directly in the film led to melting/deforming, indicating that heat transfer in the solid resin is insufficient. Thus, using an ink formulation containing a solvent or additional monomer was essential.

4.3.1 Solvent selection and printing conditions

Based on the literature-known examples explored above, self-assembly of BCPs in highly concentrated solutions is possible[40–43] when using a suitable solvent and thus, the printability in concentrated solution was investigated for our printable BCPs.

It was possible to print in a wide variety of solvents, from toluene and chloroform to dioxane, THF and DMAc. In general, a higher boiling point of the solvent indicated a better printability and overall result. Using a low boiling point solvent resulted in solvent evaporation during sample transfer to the cover slides as well as a higher affinity for explosions due to overexposure or local heating. Using a fast-evaporating solvent for development also seems to influence the surface smoothness as seen in Figure 53, where a microstructure printed and developed in THF shows some bubble structures on the surface.

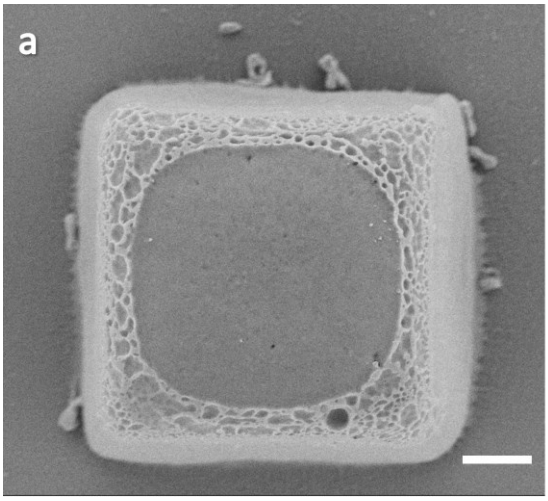

Figure 53: SEM image of a microstructure printed and developed using THF.

Interestingly, the structural integrity of the structures was also influenced by the solvent choice. Printing in DMAc, where it is later shown that highly ordered self-assembly was not possible, followed by development in isopropanol, it was possible to print and develop complex, overhanging structures such as the “benchy” boat and “buckyballs” (the Buckminster C_{60} fullerene), whereas with printing and development in dioxane or THF lead to collapse/deformation of these structures. One hypothetical explanation is that after development, the solvent evaporates gradually from the top, leading to solid polymer on top of still swollen polymer and hence, deformation. Development in a non-solvent for the BCP also lead to a rougher outer surface, perhaps because the swollen polymer network in the good solvent is “locally precipitated”. A comparison of these effects is shown in Figure 54 for structures printed in DMAc compared to 1,4-dioxane, otherwise printed under similar conditions.

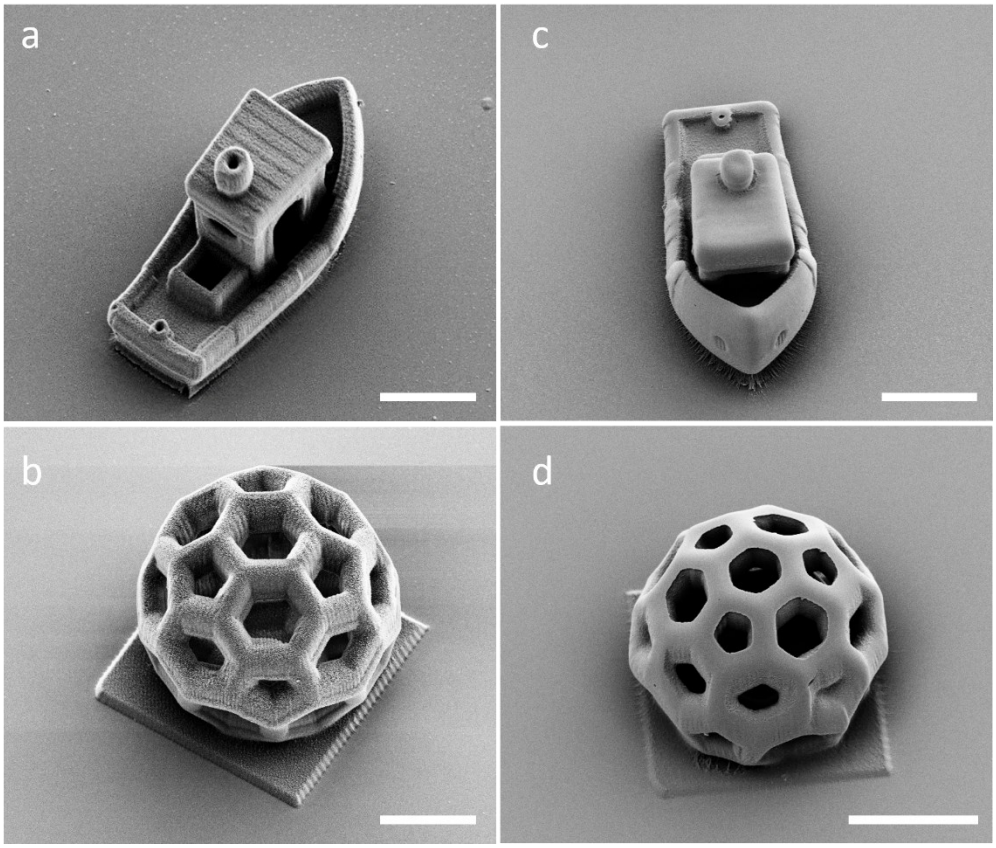

Figure 54: SEM images of printed benchys and C_{60} fullerenes, a,b) were printed in DMAc and developed in isopropanol, c,d) were printed and developed in 1,4-dioxane. Scale bars = 10 µm.

Performing SAXS measurements with the functionalized polymer in 50w% solutions in DMAc, THF and 1,4-dioxane showed the influence of the solvent on the self-assembly at identical concentrations, as shown in Figure 55. While the scattering signal is lower for DMAc, it is similar for THF and 1,4-dioxane, with the polymer in both solvents expressing lamellar structures similar to those found in the SAXS measurement of the functionalized block copolymer. Additionally, the domain spacings measured from the SAXS measurements in THF and 1,4-dioxane are in good agreement with those for the

functionalized BCP. The differences in the assembly behavior can be reasoned with the different Hansen solubility parameters for the solvents, as presented in Table 4. DMAc is a far better solvent for the PMMA block, which could result in the formation of tightly packed, poorly ordered micelles with the polystyrene block on the inside surrounded by the PMMA block. THF is a good solvent for both blocks, while 1,4-dioxane is a bit more selective towards PS, but not nearly as much as DMAc.

Table 4: R_a calculated from the Hansen solubility parameters for the respective polymer and solvent using $R_a^2 = 4(\delta D1-\delta D2)^2 + (\delta P1-\delta P2)^2 + (\delta H1-\delta H2)^2$

Solvent	R_a (PS)	R_a (PMMA)
DMAc	10.7	6.3
THF	6.2	6.7
1,4-dioxane	7.0	9.8

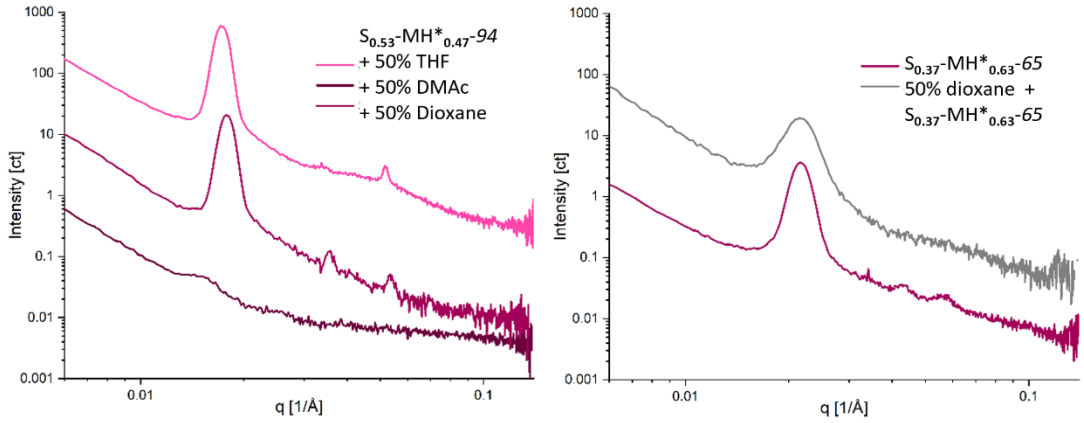

Figure 55: a) SAXS spectra of $S_{0.53}$-MH*$_{0.47}$-*94* in THF, 1,4-dioxane and DMAc in 50wt% solution, showing the good lamellar order for THF and 1,4-dioxane, and weak scattering for the mixture in DMAc. b) SAXS spectra of $S_{0.37}$-MH*$_{0.63}$-*65* in 1,4-dioxane in 50wt% solution and the bulk film for comparison of the signals.

When considering the self-assembly behavior of cylinder forming functionalized $S_{0.37}$-MH*$_{0.63}$-*65* in 1,4-dioxane, the scattering shows a broad peak, broader than for the bulk film, as shown in Figure 55. The higher order reflections are also weaker or not present, indicating that the ordering in solution is not as organized as for the bulk films.

In summary, the functionalized BCPs also showed the desired self-assembled morphology in solution of suitable solvents such as THF and dioxane. In careful consideration of the printability and processability described above, 1,4-dioxane proved to be a suitable candidate fulfilling all set criteria.

Another approach to generate a self-assembled resin in solution while retaining the best printability was done via a combined solvent-evaporation approach. A mixture of the polymer in combination with

DMAc and $CHCl_3$ or THF was added to a desiccator with an atmosphere of the respective solvent, followed by slow evaporation. The polymer/DMAc mixture was directly added to a cover slide or alternatively to a little "well" comprised of a polymer film with circular opening, attached to the cover slide e.g. with superglue. While it was possible to print with a resin prepared like this, the resin consistency was not ideal and inconsistent. Thus, the printing was performed directly in the gel-like polymer solution in the solvents determined suitable from the SAXS measurements.

Printing and development

It proved practical to transfer the viscous polymer mixture (gel-like) to the 22 x 22 mm coverslide using spatulas. After transferring, the ink was covered with a smaller circular coverslip to reduce solvent evaporation and to ensure surface contact between the ink and the glass.

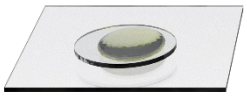

Figure 56: The printing ink on the 22x22 mm cover slide, covered with a smaller cover slide to avoid evaporation.

Depending on the solvent concentration of the ink as well as day by day variation, the interface could mostly be found automatically. Here it proved to be advantageous when the ink was spread regularly over a relatively large area.

Printing of the inks was possible in a range between 30 and 60wt% polymer content, but a polymer content of 50% was used for the printing tests and further investigation of the structures. As efficient multi-photon photoinitiator, DETC at a concentration of 0.25wt% was employed.
The printing parameters were optimized by printing arrays of the geometries of interest with systematically changing parameters. The suitable does for fully solid structures with a solid surface without print lines while avoiding microbubble formation and loss of details was structure dependent. The laser powers ranged from 17.5 to 22.5 mW with scanning speeds between 2000 and 2500 $\mu m\ s^{-1}$. To prove the versatility of the approach, shapes with different complexity, such as pillars, octopi, and a half cylinder as well as micrometric ducks with a size of 18 x 25 x 26 μm^3 were successfully 3D printed, as presented in Figure 57.

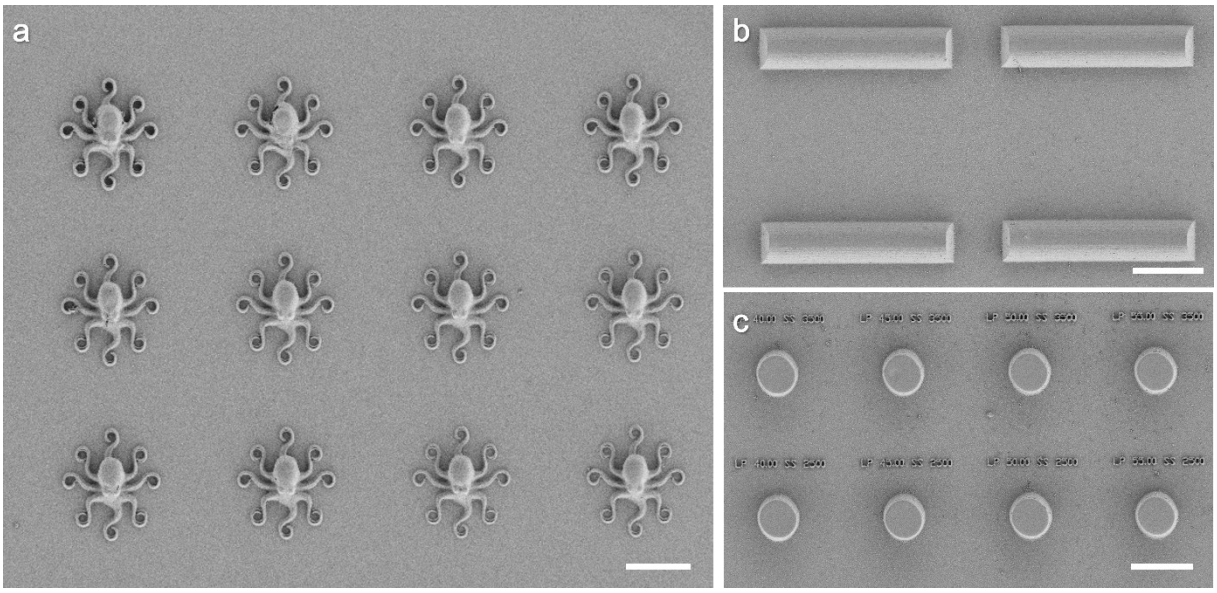

Figure 57: 3D-printed microstructures. Scale bars = 500 µm.

For the development by immersion of the slide in the development solvent taking off the circular coverslip sometimes removed the ink from the coverslide completetely, leading to the structures being removed as well. It proved most practical to add aluminum foil as a spacer between the two coverslips to ensure solvent diffusion, increasing the spacer thickness over time, until the circular slide detached.

4.3.2 Sample preparation for analysis

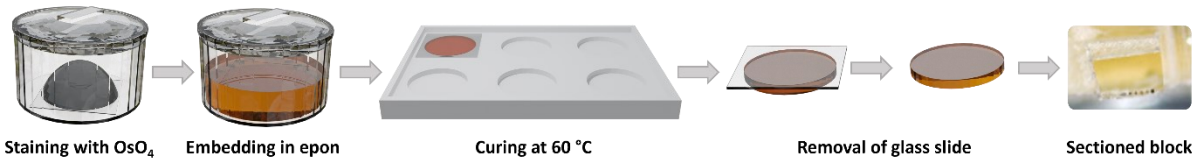

Figure 58: Workflow of the staining and embedding process.

To analyze the interior hierarchical nanostructure, the 3D printed microstructures were stained with OsO_4 in acetone (2%) or H_2O (0.5%) by adding the solution on top of the glass slide overnight in a weighing glass. After washing, they were embedded into epoxy resin by submersion and then upside-down placement in an embedding silicon mold. After curing, the samples were submerged in liquid nitrogen to remove the cover slide and obtain the microstructure encased in the resin. Interestingly, when the staining step was performed using the aqueous solution, removal of the cover slide proved problematic even when increasing the stress on the glass by heating on a hotplate before submersion in liquid nitrogen and shaking the sample in a box. Using the acetone solution, removal of the glass slide was not an issue in most of the cases. The free-standing epoxy resin containing the embedded, stained microstructures was then sectioned using the ultramicrotome to obtain cross-sectioned

microstructures. This process is visualized in Figure 58. The cross-sections could be imaged in the SEM directly or, for improved contrast, after post-staining with RuO_4 vapors.

4.3.3 Analysis of the printed, sectioned samples

The cross-sections were imaged using the SEM to analyze the morphology, to verify the retention of the pre-formed nanostructure after printing, and to our knowledge this was the first published example using this type of analysis for this kind of printable BCP materials The SEM images, as presented in Figure 59, confirmed the morphology already prominent in the bulk BCP and the SAXS measurements of the ink.

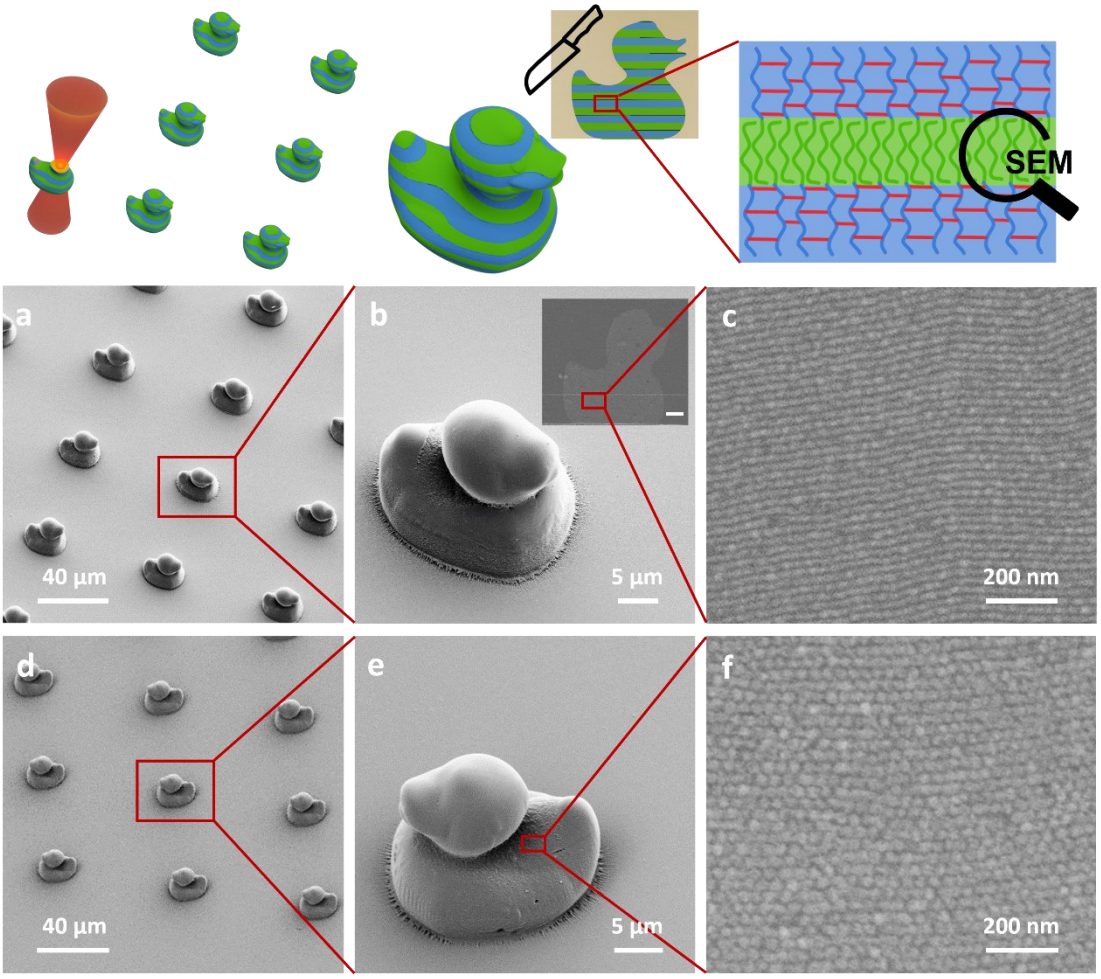

Figure 59: SEM characterization of 3D printed microstructures from a–c) $S_{0.53}$-MH*$_{0.47}$-*94* or d–f) $S_{0.37}$-MH*$_{0.63}$-*65*. Overall morphology (a,b and d,e) and cross sections prepared from resin-embedded microstructures (insets in b). High-resolution SEM images of cross sections (c,f) show lamella for $S_{0.53}$-MH*$_{0.47}$-*94* (c) and cylinders for $S_{0.37}$-MH*$_{0.63}$-*65* (f). Images of larger areas can be found in Figure A6and Figure A7. The microstructures were sectioned perpendicular to the substrate as illustrated by the inset in (b).

Highly ordered lamellae (for $S_{0.53}$-MH*$_{0.47}$-*94*) and cylinders (for $S_{0.37}$-MH*$_{0.63}$-*65*) are clearly visible in the cross-section of the 3D micrometric ducks (Figure 59 c,f). For the lamellae, the order is especially

remarkable. These lamellae are parallel without any junctions or other defects over areas of several μm^2. Importantly, the domain spacing measured from the images is 36 nm and thus in agreement with the distances calculated from the x-ray scattering pattern of the ink. This clearly indicates the retention of the morphology from the bulk polymer and the ink mixture during the 3D printing process and development, and more importantly, the nanostructures are also present in the inside (bulk) of the 3D structure.

To verify that the visible nanostructure is an inherent property of the self-assembly of the printable materials and not a printing artifact stemming from the printing of a higher molecular weight polymer in solution, we additionally prepared control samples in the solvents used for printing containing only the polymethacrylate-based block with photo-cross-linkable groups. The SEM images (Figure A4) of these cross-sectioned samples do not show any nanostructure, further proving that the hierarchical structures can only be achieved by BCP self-assembly.

5 Conclusions and Outlook

5.1 Conclusion

A novel ink suitable for high-resolution two-photon 3D printing based on self-assembled BCPs containing photo-cross-linkable groups has been presented. A library of BPCs having different compositions and degrees of functionalization has been synthesized using controlled radical polymerization and carefully characterized.

For the synthesis, a sequential RAFT polymerization approach at a relatively high temperature of 90 °C showed the best results, while for the functionalization careful optimization of the reaction and work-up conditions was necessary to reliably obtain the cross-linkable polymer in high yields.

After self-assembly from solution, the investigation of the employed PS-*b*-P(MMA-*co*-HEMA) revealed a phase behavior showing the classic morphologies presented by AB diblock copolymers, and the phase diagram could be drawn, showing the influence of the degree of polymerization and the polymer composition on the expressed morphology. Functionalization of the hydroxyl group with a cross linkable group was shown to have a strong influence on both the expressed phase behavior as well as reducing the domain spacings, indicating a decrease of χ as expected from the molecular design. For both polymer classes, the change in the domain spacing with varying degree of polymerization could be fitted to a power law in accordance with the literature.

The self-assembly could be retained during the 3D microprinting process as well as during the development by using a solution-based printing ink, which was shown by sectioning and imaging the printed microstructures.

It was demonstrated that the self-assembly and printability of the BCPs are strongly dependent on the solvent used. Highly concentrated solutions of $S_{0.53}$-MH*$_{0.47}$-*94* and $S_{0.37}$-MH*$_{0.63}$-*65* in 1,4 dioxane displayed good performance enabling the fabrication of complex 3D structures. Cross-sections of the 3D printed samples were imaged using SEM, showing highly ordered and defined nanostructures such as lamella and cylindric morphologies, depending on the BCP composition.

5.2 Outlook

Although this work has been focused on PS-*b*-PMMA-based polymers, the presented approach is very versatile and can be easily expanded to other functional BCPs. By modifying the macromolecular design, e.g., length of the blocks, sequence, and composition, further new nanostructures and functionalities can also potentially be obtained.

An initial investigation has been conducted towards the use of a PEO-based macroCTA which can be chain extended with e.g. styrene and 4-vinylbenzylchloride, as shown in Figure 60. The latter can then

be functionalized using (meth)acrylic acid. This BCP showed decent printability, but further investigation of the self-assembly needs to be performed.

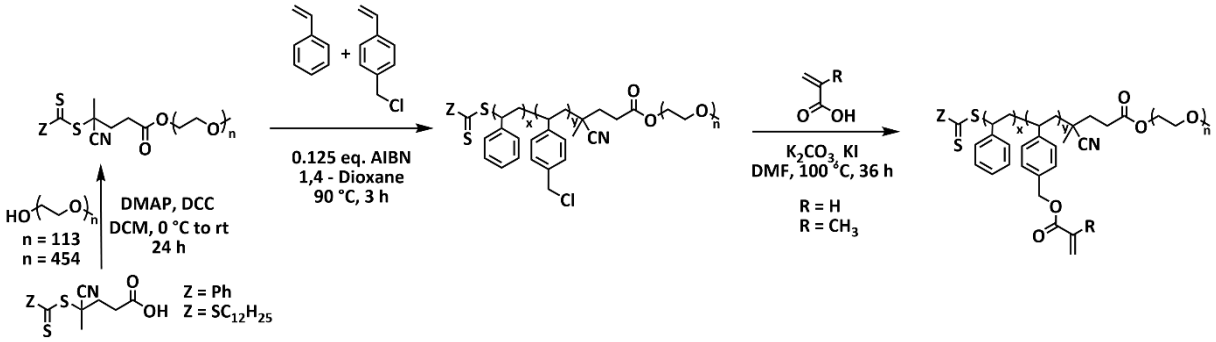

Figure 60: Proposed synthesis scheme for a PEO-*b*-P(Sty-4VBCl) BCP and its functionalization.

Additionally, incorporation of responsive monomers will enable the careful control of microactuation in the final 3D structure due to the hierarchical order. We also envision the use of 3D structures composed of lamellar structures alternating conductive and non-conductive domains with potential application in energy storage. Another possible application could be utilizing the unique property of the gyroid morphology – the formation of a bicontinuous network, which means that upon selective removal of one of the blocks (which has already been shown in the thin film) continuous pores are expressed, which is very interesting for applications such as filtering membranes, where the size of the pores can be finely tuned by both the molecular weight of the polymer as well the choice of polymer system.

Currently the self-assembly in the printing ink is reliant on the formed equilibrium, but it should also be possible to introduce some external control, e.g. by applying an electric or magnetic field. External fields not only facilitate the assembly but also provide the possibility to influence the directionality of the formed nanostructures. Meeting certain conditions, they can also be used to induce an order-to-order transition from the gyroid to the cylindrical phase. This means that depending on the BCP utilized, it could be possible not only to change the directionality of the order during printing, but even to print 3D structures containing several morphologies within.

Thus, I believe that the presented versatile approach enabling the manufacturing of precise functional materials with defined nanostructure will open new opportunities in a wide range of application fields, with the capability of finely tuning the properties on demand.

6 Experimental Section

Chemicals and Materials: chemicals and solvents were supplied from either Sigma–Aldrich or Fisher Scientific unless otherwise mentioned.

Synthesis and Structure Characterization: To synthesize the block copolymers, the sequential RAFT polymerization was performed following an approach modified from Varadhajaran and Delaittre.[36] The synthetic details are provided in the appendix.

All synthesized compounds were characterized with ^{1}H nuclear magnetic resonance (NMR) spectroscopy (Bruker Avance III 300, Bruker Avance III 600 or Bruker Avance Neo 700). Gel permeation chromatography (GPC) measurements were performed on a Shimadzu Nexera LC-40 system (with LC-40D pump, autosampler SIL-40C, DGU-403 (degasser), CBM-40 (controlling unit), column oven CTO-40C, UV-detector SPD40 and RI-detector RID-20A).
The system was equipped with 4 analytical GPC-columns (PSS): 1 x SDV precolumn 3 µm 8x50mm, 2 x SDV column 3µm 1000Å 8x300 mm, 1 x SDV column 3 µm 10e4Å 8x300 mm.
The measurements were performed in THF at a flow speed of 1 mL/min at a temperature of 40°C. Chromatograms were analysed using the LabSolutions (Shimadzu) software. Calibration was performed against different polymethylmethacrylate standards (800 - 2 200 000 Da, PSS) or polystyrene standards (370 - 2 520 000 Da, PSS).

BCP Ink preparation: Under yellow light conditions, to the respective block copolymer, a stock solution of DETC in 1,4-dioxane, DMAc, or THF was added to give a final concentration of 0.25 wt% photoinitiator and 30-60% block copolymer. The mixture was repeatedly mixed with a fine needle followed by centrifugation. Afterwards, the mixture was agitated on an orbital shaker for 5 hours followed by rest until the resin was used for printing.

Silanization Procedure: Glass coverslips (Marienfeld, 170 ± 5 µm) were washed with isopropanol and acetone and dried using pressurized N_2. Subsequently, the surface was activated for 5 min by plasma treatment. The coverslips were immersed in a 4×10^{-3} M solution of 3-(trimethoxysilyl)propyl methacrylate in toluene for 1.5 h. After washing twice in toluene and once in acetone, the methacrylate-functionalized glass slides were used for TPLP microfabrication.

Two-Photon Laser Printing of 3D Microstructures: 5-10 mg of the viscous ink were transferred to a silanised cover slide (22x22 mm, 170 µm thickness) with a spatula and covered with a smaller circular

slide, which was gently pressed on to ensure good contact between the ink and the glass slide and reduce solvent evaporation. Two-photon laser printing was performed within a commercially available setup (Photonic Professional GT2, Nanoscribe GmbH & Co. KG) in oil immersion configuration with a femtosecond laser (λ = 780 nm) focused by a 63x oil objective (NA = 1.4; WD = 190 µm; Zeiss). Employing Describe software (Nanoscribe), GWL files were generated from STL files of desired geometries and executed by the printer for 3D structure fabrication. Slicing was set to either 200 or 300 nm and hatching to 200 nm for all microgeometries. Printing was performed with a varied scan speed of from 2 to 2.5 mm s^{-1} and laser power in the range of 17.5 to 22.5 mW depending on the structure. For development, the cover slide was placed into the same solvent used for the ink preparation until all excess ink was dissolved.

Ultramicrotome: Self-assembled bulk films were cut into small pieces and embedded in Epon (prepared by mixing 26.2 g glycid ether 100, 14.8 g dodecenylsuccinic acid anhydride, 9.2 g methyl-5-norbornene-2,3-dicarboxylic anhydride and 1.2 g benzyldimethylamine; all chemicals purchased from SERVA) and polymerized for 2 days at 62 °C.

Printed samples were stained in OsO_4 (2% in Acetone) overnight, consecutively incubated in 50% and 70% solutions of Epon in acetone for 2-3 h and then embedded in 100% Epon following the same procedure as for the film samples. The cover slide was detached from the embedded sample by submerging in liquid nitrogen.
The resin blocks were trimmed to expose the structures. Ultrathin (100-120 nm) cross sections were cut using a PowerTome PC ultramicrotome (RMC Boeckeler) and placed on pieces of silicon wafer.

Scanning Electron Microscope: The sections were imaged in a field-emission scanning electron microscope (Ultra 55, Carl Zeiss Microscopy) at a primary electron energy of 1.5 keV, either with or without post-staining in RuO_4 vapour (0.5% in H_2O, Polysciences Inc) for 30 min.
Images of entire 3D-printed structures were obtained after sputter coating the sample with a 10-12 nm layer of Pt:Pd (80/20) using a field-emission scanning electron microscope (Ultra 55, Carl Zeiss Microscopy) at a primary electron energy of 3 keV.

SNOM: The sections were imaged in a commercial infrared scanning near-field optical microscope (neaSNOM, Neaspec GmbH). Near-field optical amplitude and phase images together with the topography of the sample (1 × 1 μm^2 or 2.5 × 2.5 μm^2, at least 200 × 200 pixels and 6.6 ms integration time) were acquired simultaneously by operating the system in tapping mode employing a pseudo-heterodyne detection scheme.[117] A platinum-iridium coated probe (Arrow-NCPt) with a resonance

frequency of about 280 kHz was used and illuminated with a mid-infrared quantum cascade laser (Daylight solutions). The laser was optimized using a power setting of 1.5 mW. The signal, which was detected with a mercury cadmium telluride detector, was demodulated at the third harmonic of the tapping frequency to suppress the background signal. By illuminating the sample at an independent absorption band of the methacrylate-functionalized P(MMA-*co*-HEMA) at 1152 cm^{-1},[86] it is possible to distinguish between the different block copolymer units and to image phase segregation via spectroscopic contrast. Regions with a high optical phase value can be assigned to P(MMA-*co*-HEMA)-rich areas and those with low optical phase value to polystyrene-rich areas.

Small angle X-ray scattering: SAXS experiments were performed using a Xeuss 2.0 Q-Xoom (Xenocs SA, Grenoble, France) instrument, equipped with a Genix3D Cu ULC (ultra-low divergence) micro focus source of Cu Kα with an energy of 8.04 keV, a wavelength of 1.5406 Å, and a Pilatus3 R 300K detector (Dectris Ltd., Baden, Switzerland). The 3D printing ink was placed in a gel holder, packed between two polyimide foils with a sample thickness of 0.5 mm. Solid films were measured without substrate. The 2D scattering patterns were obtained using a sample-to-detector distance of 2500 mm, resulting in the range of accessible scattering vector (q) from 0.003 to 0.14 $Å^{-1}$. We used an azimuthal integration of the scattering patterns to obtain 1D plots of the intensity I(q) versus q with $q = 4\pi\sin(2\theta/2)/\lambda$, where 2θ is the scattering angle and λ is the wavelength of the Cu Kα source. The measurement time was set to 600s for both the film samples and the 3D printing inks.

7 Appendix

7.1 Supplementary Figures

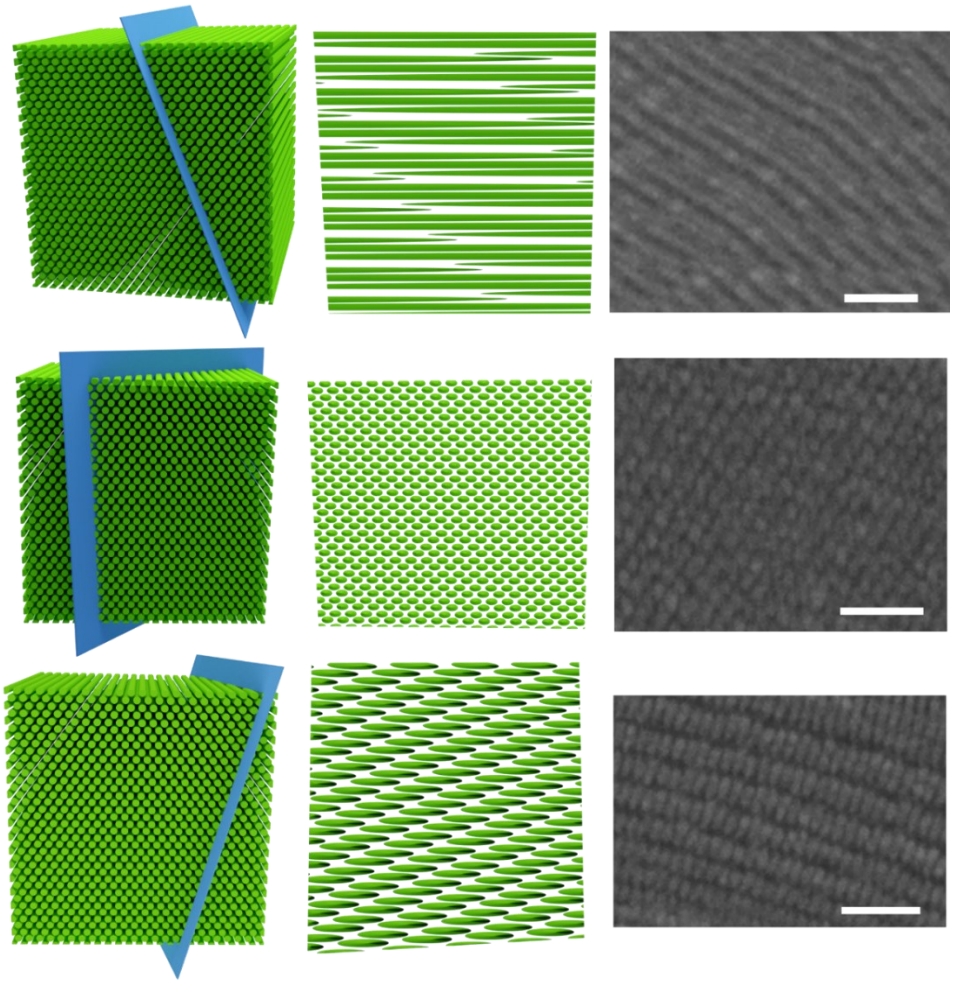

Figure A1: SEM images of cylindrical block copolymer $S_{0.37}$-MH*$_{0.63}$-*65*, in comparison with 3D modeled, rendered images cut along different planes of the ordered cylinders. Scale bar = 200 nm.

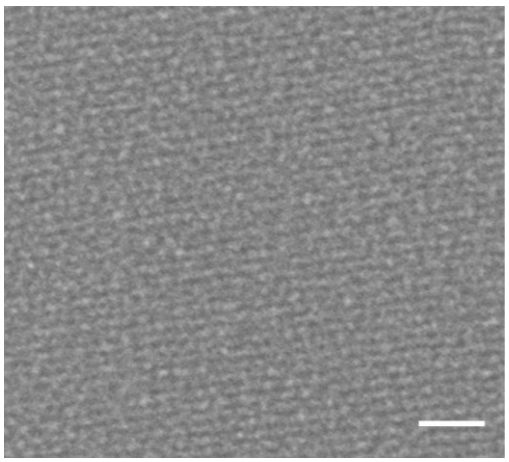

Figure A2: Zoomed in area in the cross-section of a microstructure printed with $S_{0.53}$-MH*$_{0.47}$-*94* in 50% THF. Scale bar = 200 nm.

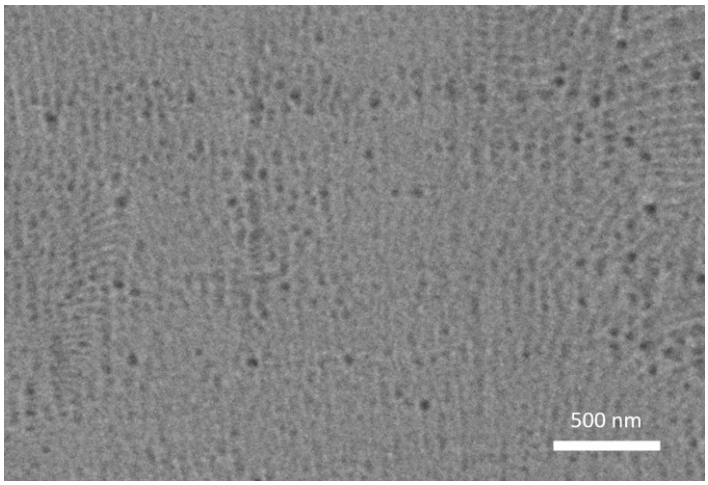

Figure A3: SEM image of dropcasted polymer $S_{0.49}$-$MH_{0.50}$-*92* showing a lamellar morphology.

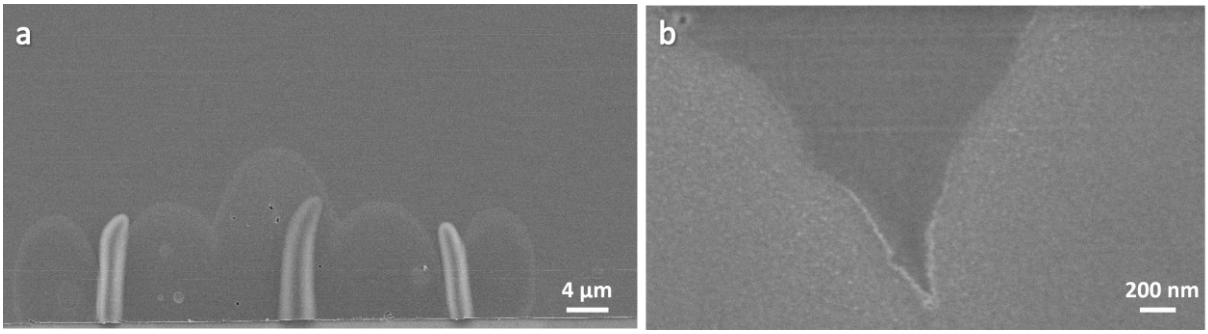

Figure A4: Cross-section (a) and zoomed in area (b) of a microstructure printed with functionalized P(MMA-co-MethacryEMA) polymer in 1,4-dioxane as control sample.

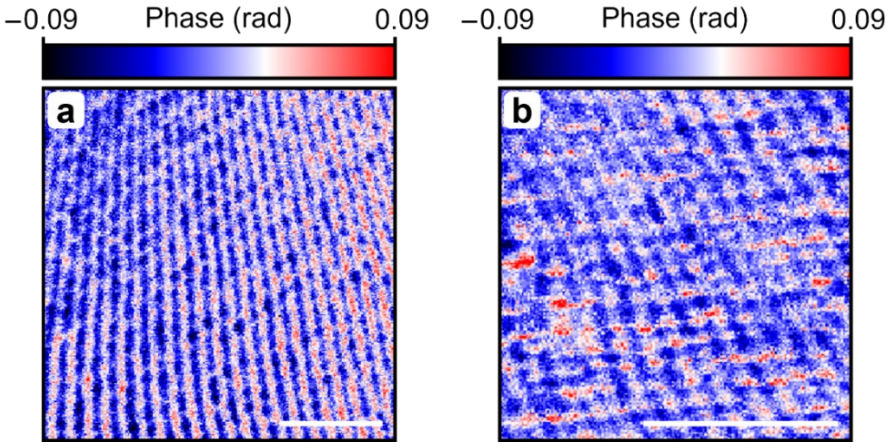

Figure A5: IR-SNOM analysis of cross-sectioned self-assembled films: a) near-field optical phase image mapped at 1152 cm^{-1} of $S_{0.53}$-MH*$_{0.47}$-*94*, b) near-field optical phase image mapped at 1152 cm^{-1} of $S_{0.37}$-MH*$_{0.63}$-*65*. Scale bars = 500 nm.

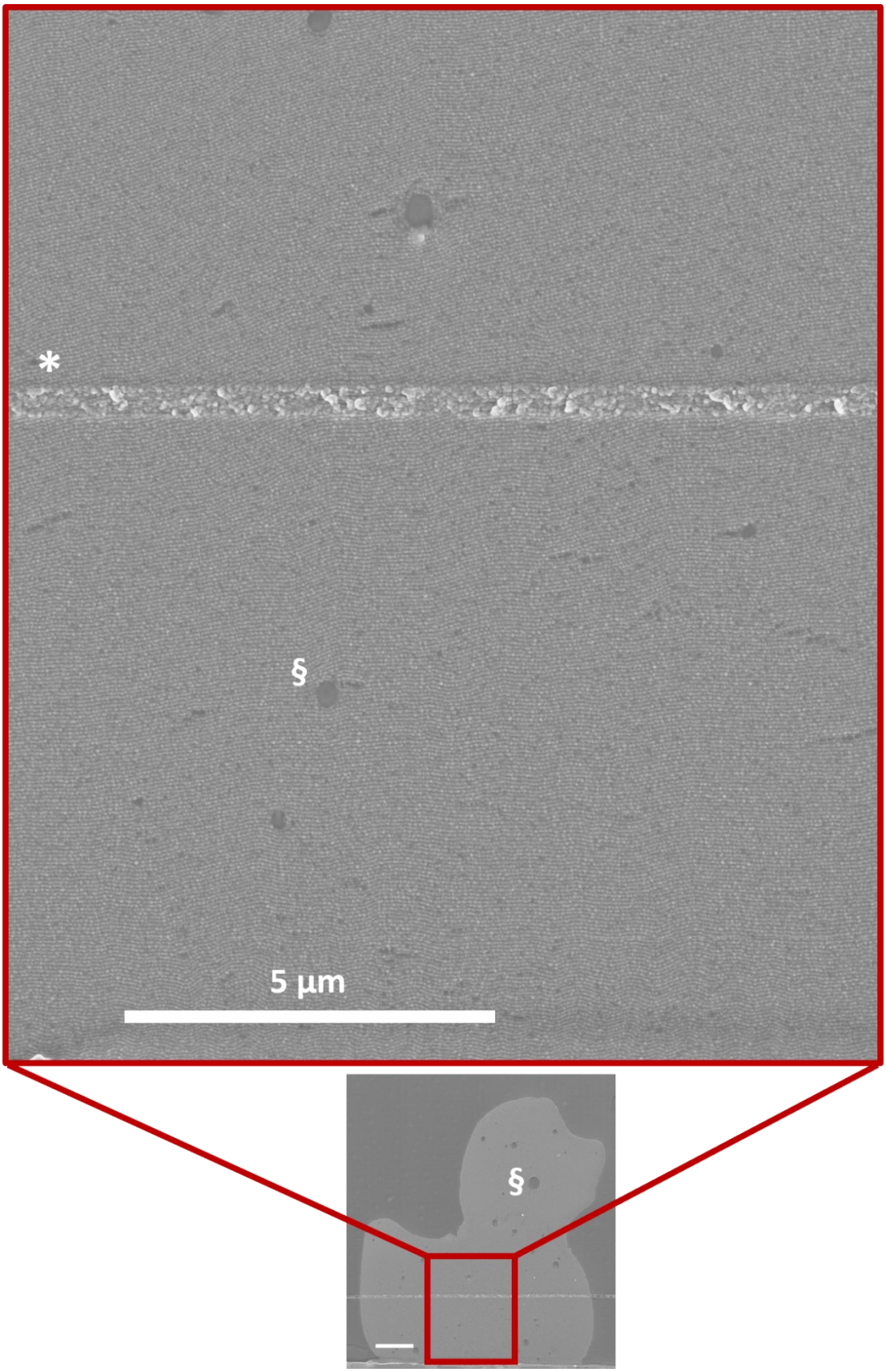

Figure A6: Zoom-in on the cross-section of a 3D microprinted duck using $S_{0.53}$-$MH_{0.47}$-*94*. * indicates a knife mark from processing with the ultramicrotome whereas § indicates a small defect introduced by handling of the printing ink.

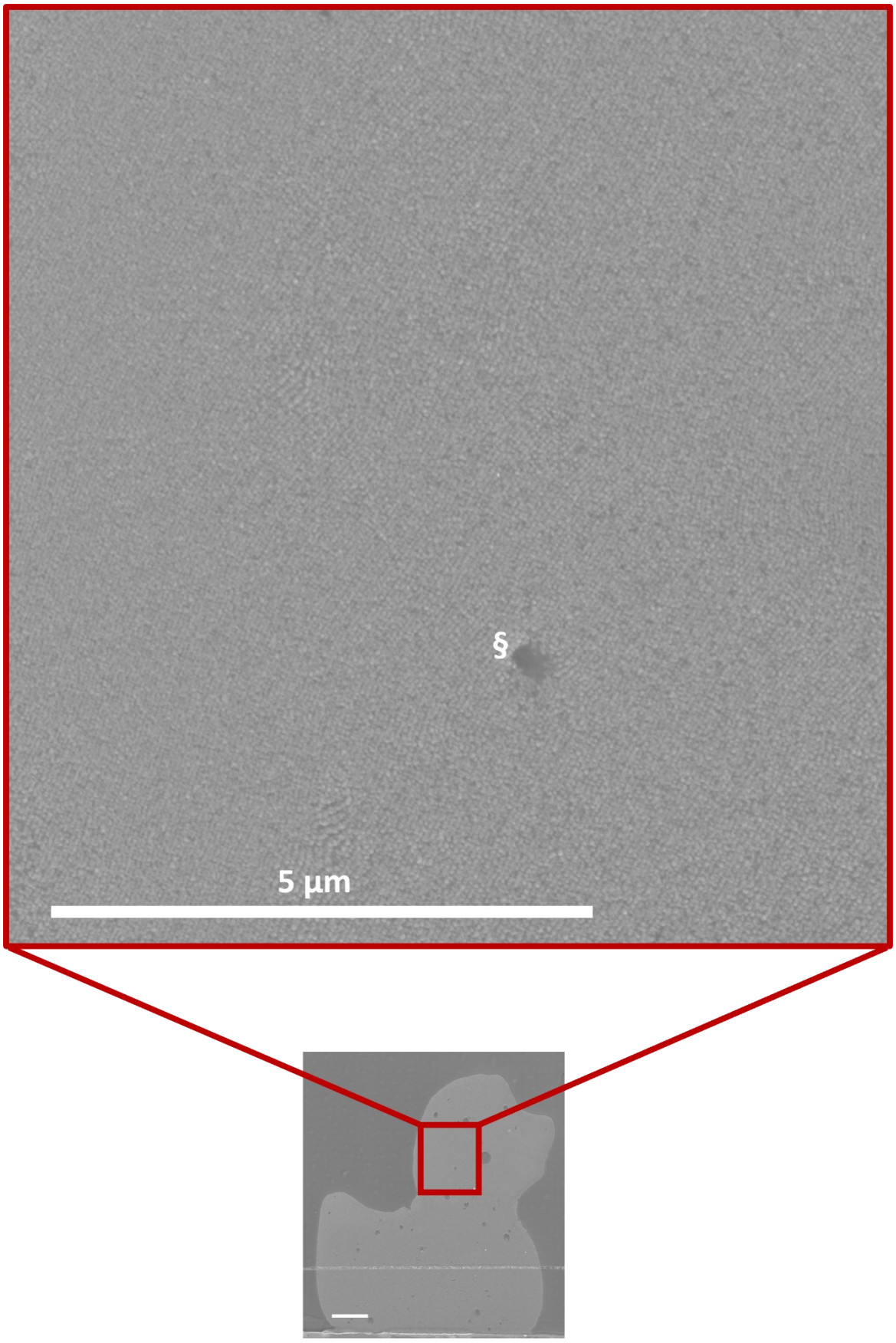

Figure A7: Zoom-in on the cross-section of a 3D microprinted duck using $S_{0.53}$-$MH_{0.47}$-*94*. § indicates a small defect introduced by handling of the printing ink.

7.2 Synthesis and Characterization of BCPs

7.2.1 Exemplary Synthesis of P(MMA-*co*-HEMA) MacroCTAs:

In a Schlenk tube, MMA (6.40 g, 64.0 mmol, 819 eq.), HEMA (2.08 g, 16.0 mmol, 204 eq.) and CPDB (17.3 mg, 78.1 µmol, 1.0 eq.) were dissolved in 1,4-dioxane (8 mL). AIBN solution (323 mg, 9.78 µmol, 0.125 eq., 10 mg in 2.010 mg 1,4-dioxane) was added. The solution was degassed via freeze-pump-thaw (3 x 8 min), followed by backfilling with nitrogen. The reaction mixture was stirred at 90°C for 2.5 h, cooled in liquid nitrogen and opened to the atmosphere. After dilution with DCM, the solution was precipitated into diethyl ether twice. After centrifugation and decanting of the supernatant, copolymer macroCTA1 was received as a light pink solid.

^{1}H NMR 600 MHz (CD_2Cl_2): δ [ppm] = 7.80 (m), 7.47 (m), 7.31 (m), 4.0 (bs), 3.74 (bs), 3.50 (s), 2.00 - 0.61 (m).

Table A1: Monomer ratio, reaction time, molecular weight, and dispersity of the synthesized MacroCTAs.

Polymer	MMA:HEMA:CPDB:AIBN	T [h]	M_n(GPC)	Đ	Precursor for
macroCTA-*22*	304:76:1:0.125	4	22454	1.11	$S_{0.54}$-$MH_{0.46}$-*45*
macroCTA-*29*	441:110:1:0.125	4	28749	1.12	$S_{0.52}$-$MH_{0.48}$-*67*
macroCTA-*21*	304:76:1:0.125	2	20667	1.13	$S_{0.75}$-$MH_{0.25}$-*66*
macroCTA-*54*	819:204:1:0.125	5	53925	1.05	$S_{0.49}$-$MH_{0.51}$-*92*
macroCTA-*23*	304:76:1:0.125	2.5	23083	1.08	$S_{0.45}$-$MH_{0.55}$-*42*, $S_{0.66}$-$MH_{0.34}$-*70*
macroCTA-*48*	819:204:1:0.125	2.5	48065	1.12	$S_{0.45}$-$MH_{0.55}$-*102*, $S_{0.50}$-$MH_{0.50}$-*91*
macroCTA-*39*	819:204:1:0.125	2.5	38850	1.17	$S_{0.46}$-$MH_{0.54}$-*81*, $S_{0.42}$-$MH_{0.58}$-*89*
macroCTA-*43*	819:204:1:0.125	3.2	43205	1.15	$S_{0.28}$-$MH_{0.72}$-*67,* $S_{0.27}$-$MH_{0.73}$-*70*
macroCTA-*38*	819:204:1:0.125	2.5	37641	1.10	$S_{0.37}$-$MH_{0.63}$-*65*, $S_{0.53}$-$MH_{0.47}$-*94*
macroCTA-*34*	819:204:1:0.125	2.6	33587	1.13	$S_{0.42}$-$MH_{0.58}$-*57*, $S_{0.09}$-$MH_{0.91}$-*39*, $S_{0.31}$-$MH_{0.69}$-*48*, $S_{0.16}$-$MH_{0.84}$-*45*, $S_{0.12}$-$MH_{0.88}$-*40*, $S_{0.16}$-$MH_{0.84}$-*43*
macroCTA-*19*	304:76:1:0.125	2	18985	1.10	$S_{0.39}$-$MH_{0.61}$-*35*, $S_{0.43}$-$MH_{0.57}$-*40*, $S_{0.28}$-$MH_{0.72}$-*29*, $S_{0.50}$-$MH_{0.50}$-*45*, $S_{0.56}$-$MH_{0.44}$-*52*
macroCTA-*9*	224:56:1:0.125	1	9303	1.12	$S_{0.68}$-$MH_{0.32}$-*33*

NMR spectra of P(MMA-*co*-HEMA) MacroCTAs

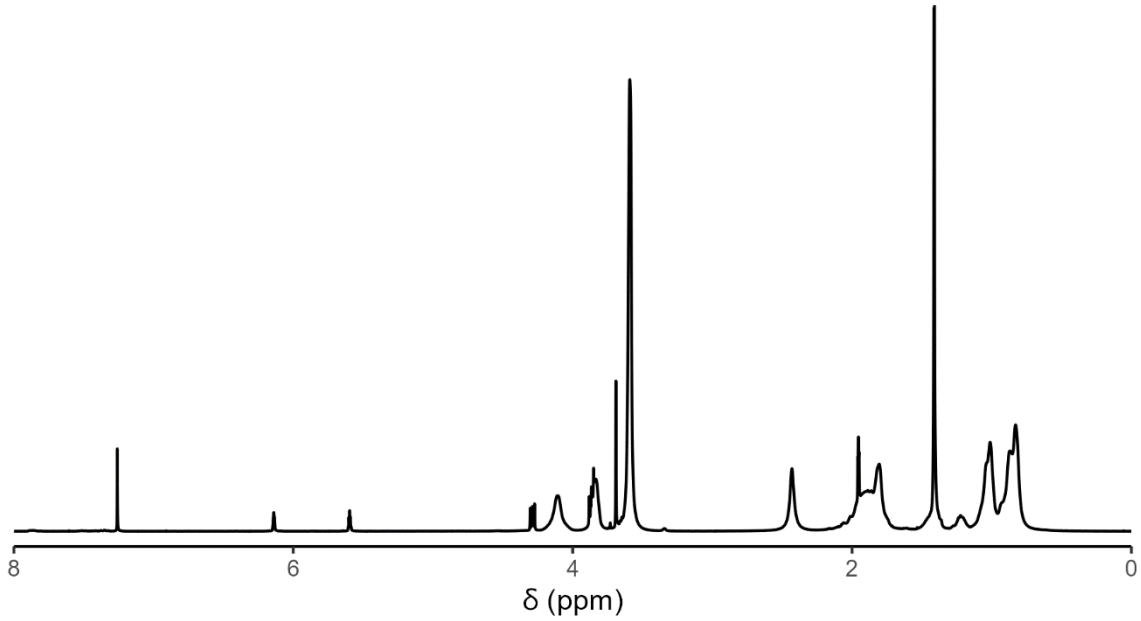

Figure A8: ^{1}H NMR spectrum of macroCTA-*22* in $CDCl_3$.

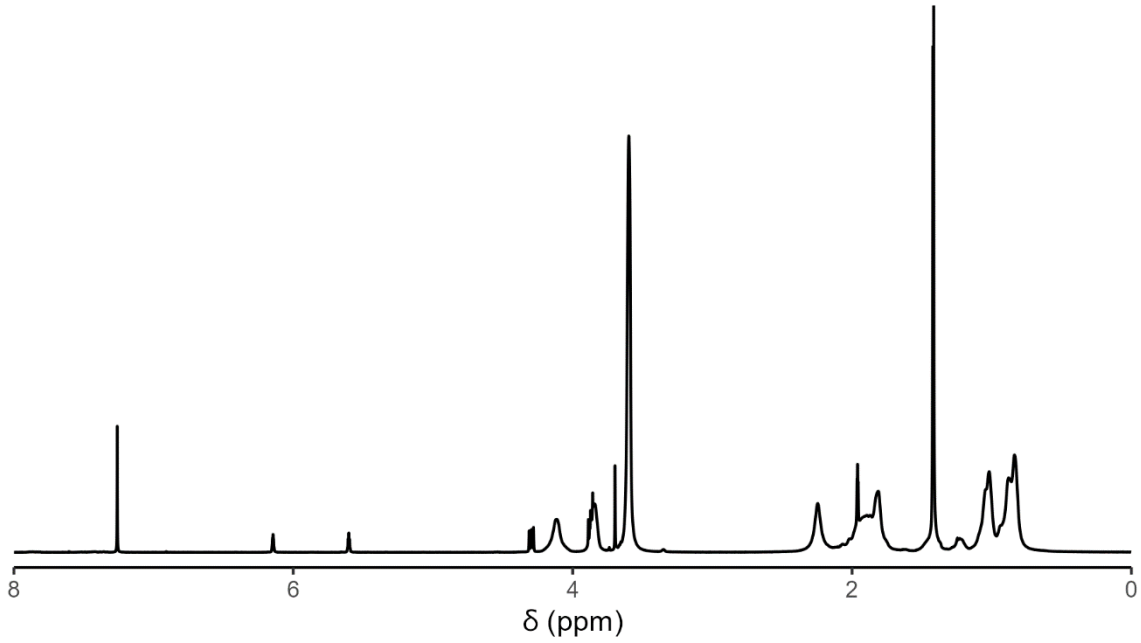

Figure A9: ^{1}H NMR spectrum of macroCTA-*29* in $CDCl_3$.

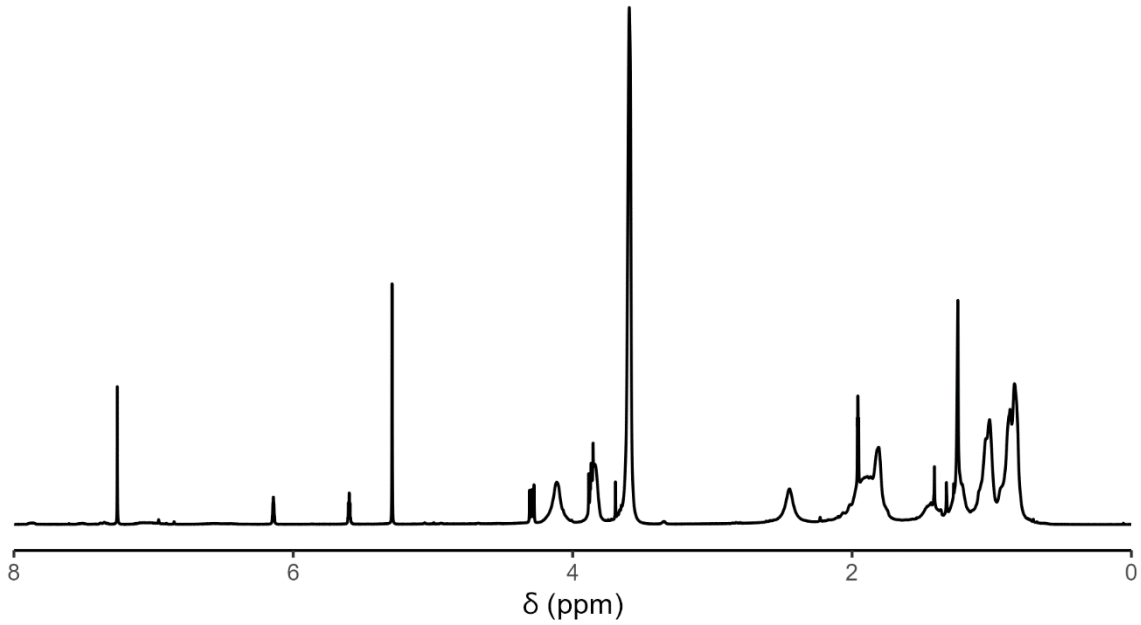

Figure A10: ^{1}H NMR spectrum of macroCTA-*21* in $CDCl_3$.

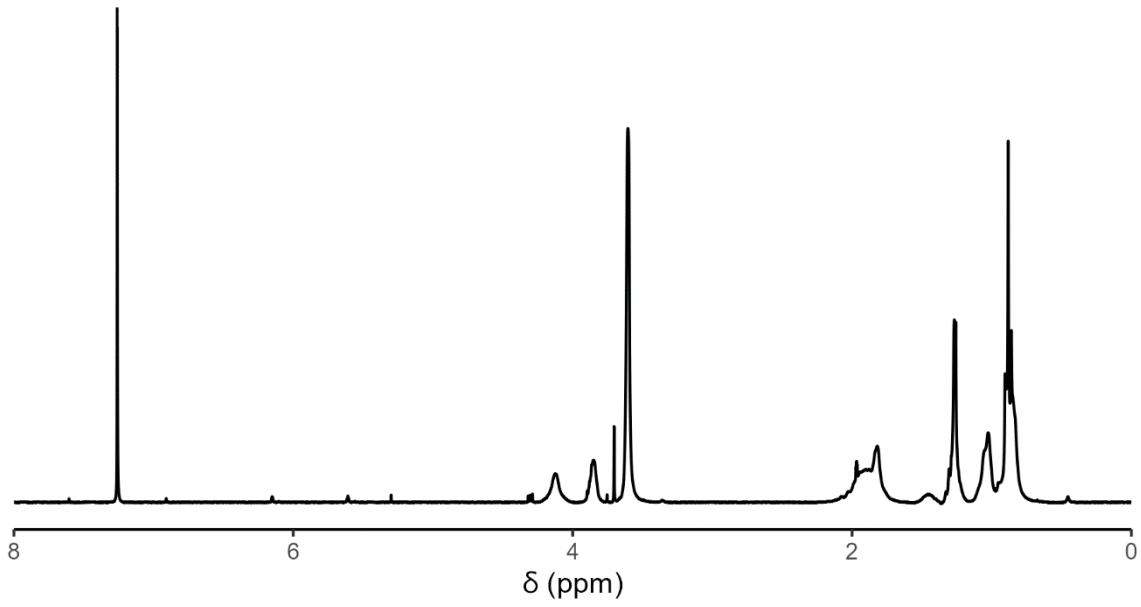

Figure A11: ^{1}H NMR spectrum of macroCTA-*54* in $CDCl_3$.

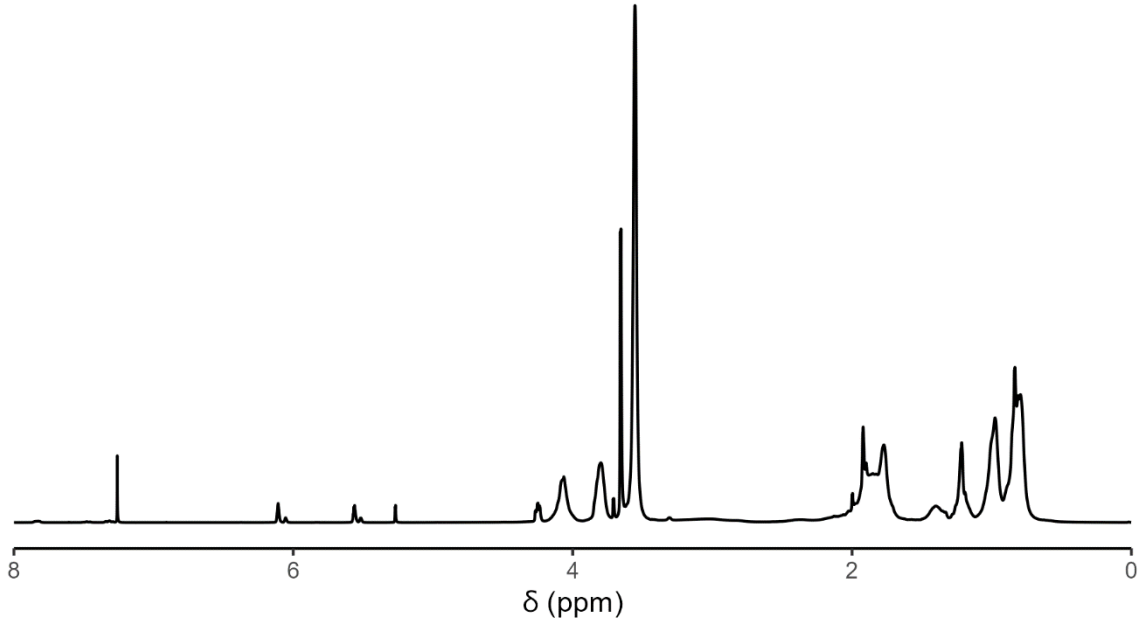

Figure A12: ^{1}H NMR spectrum of macroCTA-*23* in $CDCl_3$.

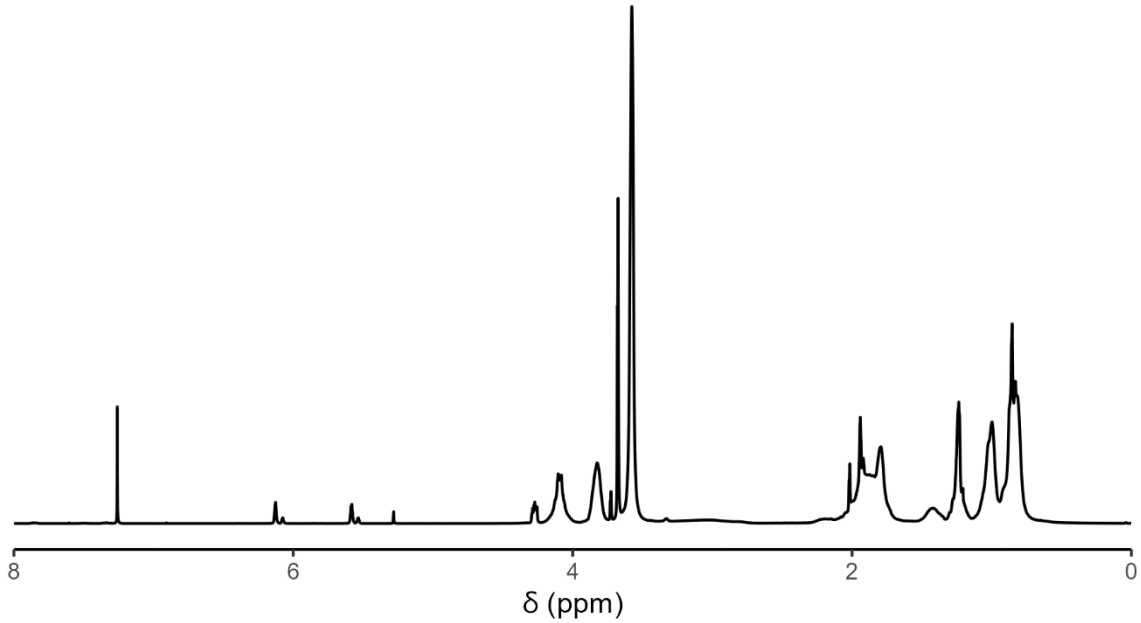

Figure A13: ^{1}H NMR spectrum of macroCTA-*48* in $CDCl_3$.

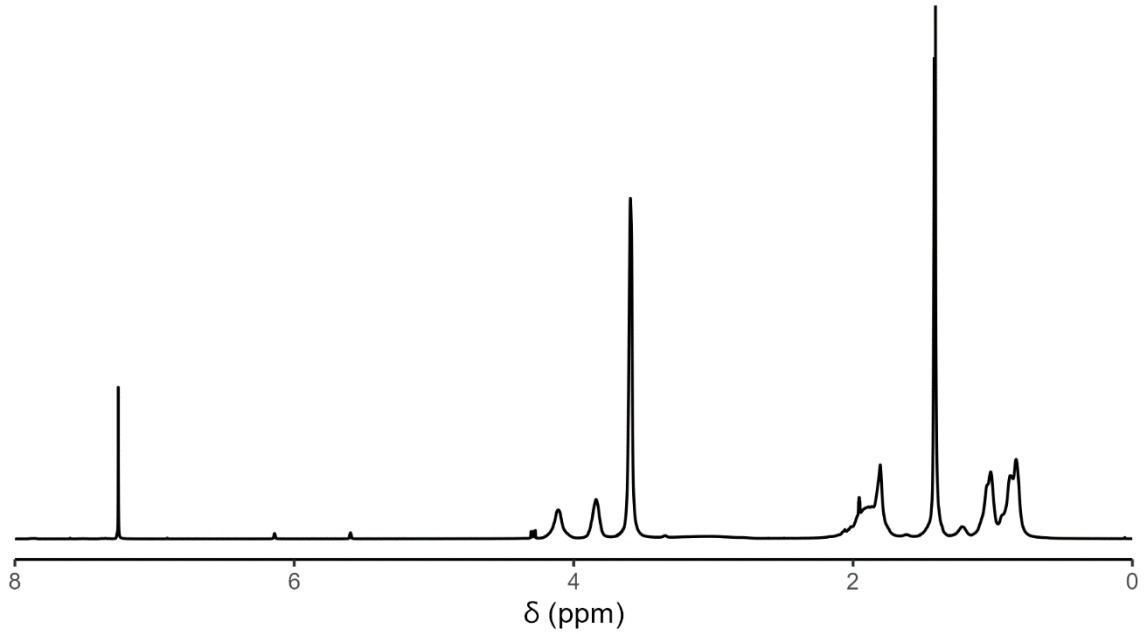

Figure A14: ^{1}H NMR spectrum of macroCTA-*39* in $CDCl_3$.

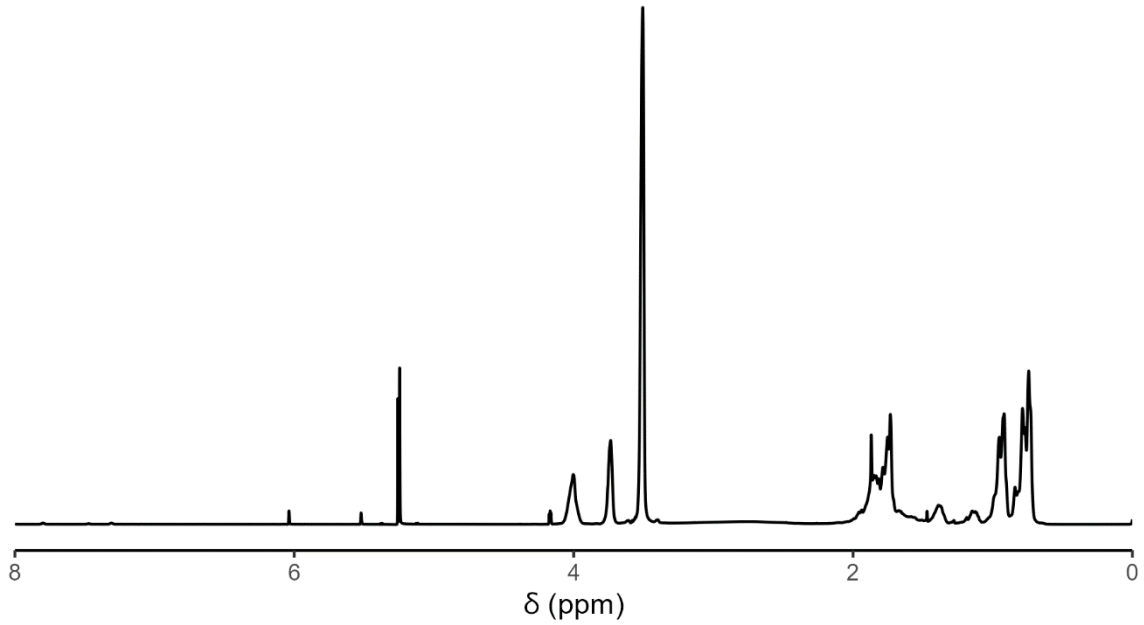

Figure A15: ^{1}H NMR spectrum of macroCTA-*43* in CD_2Cl_2.

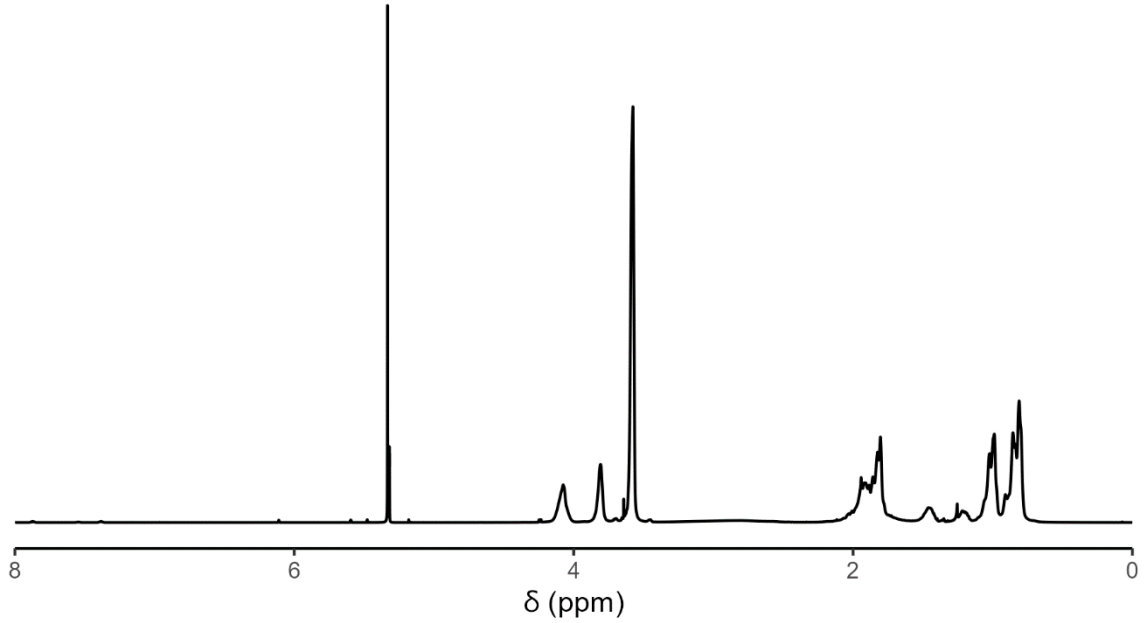

Figure A16: ^{1}H NMR spectrum of macroCTA-*38* in CD_2Cl_2.

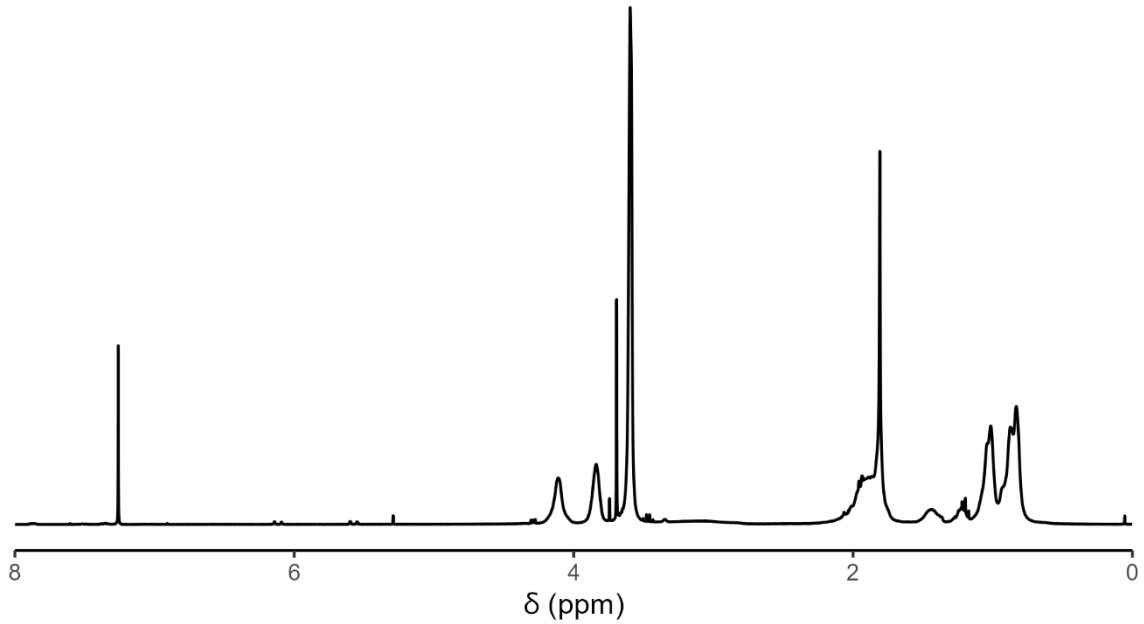

Figure A17: ^{1}H NMR spectrum of macroCTA-*34* in $CDCl_3$.

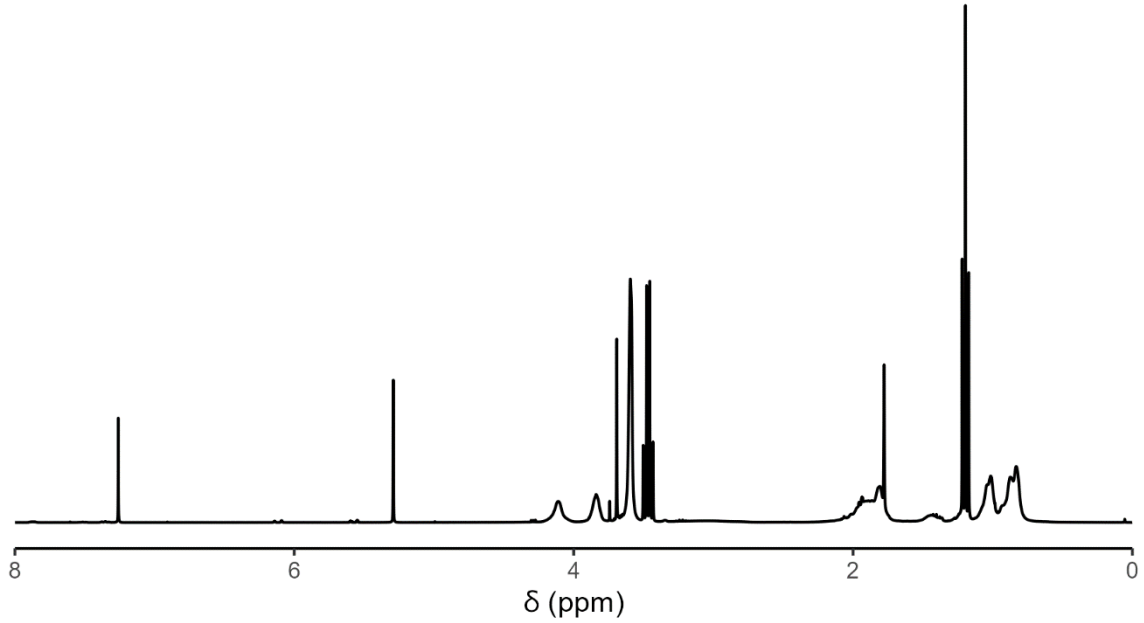

Figure A18: ^{1}H NMR spectrum of macroCTA-*19* in $CDCl_3$.

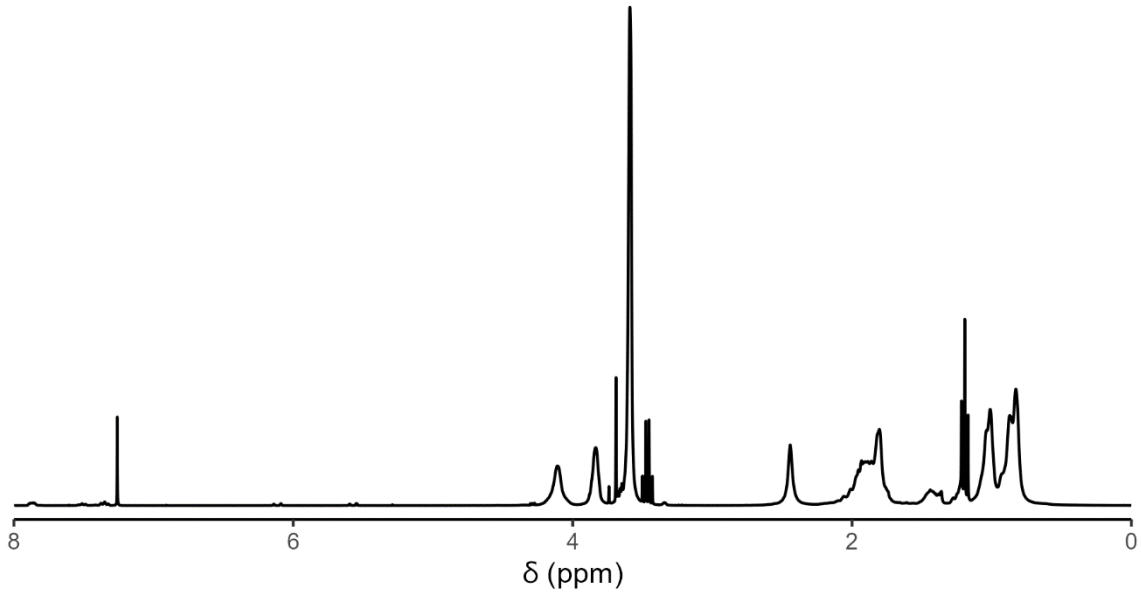

Figure A19: ^{1}H NMR spectrum of macroCTA-*9* in $CDCl_3$.

GPC traces of P(MMA-*co*-HEMA) MacroCTAs

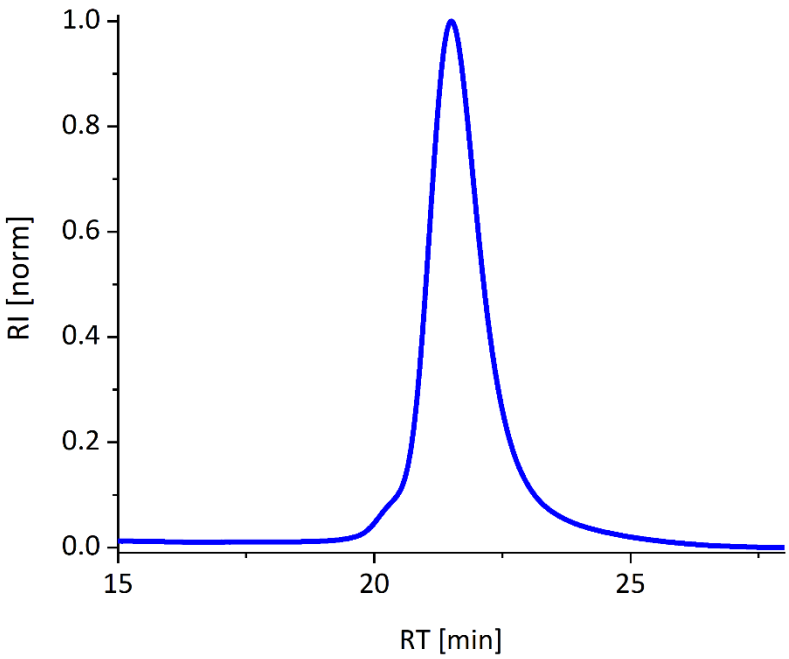

Figure A 20: GPC chromatogram (RI detector) of macroCTA-*22*.

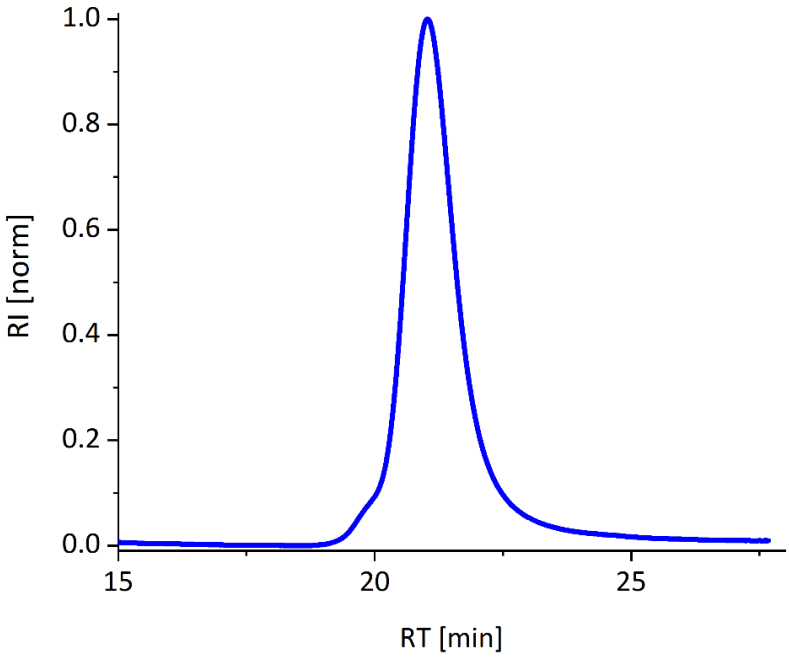

Figure A 21: GPC chromatogram (RI detector) of macroCTA-*29*.

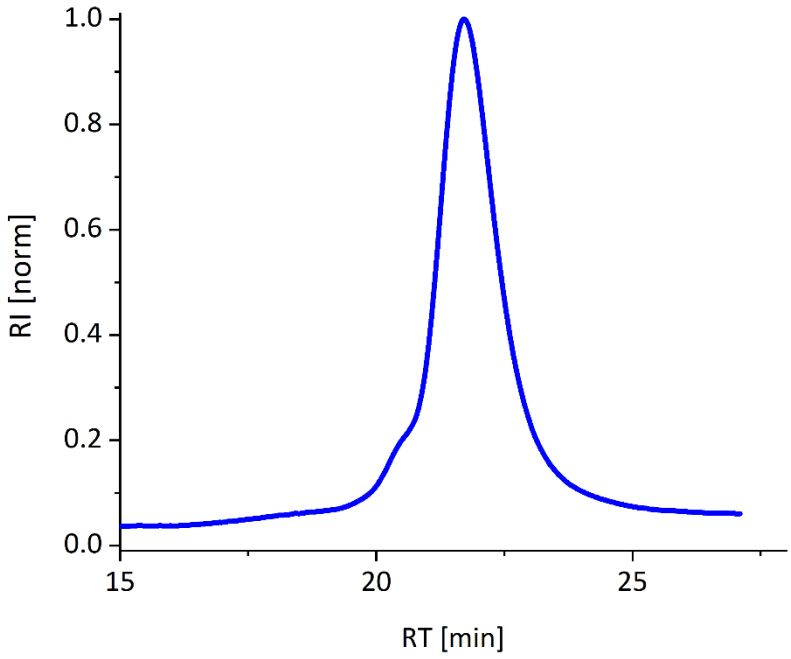

Figure A 22: GPC chromatogram (RI detector) of macroCTA-*21*.

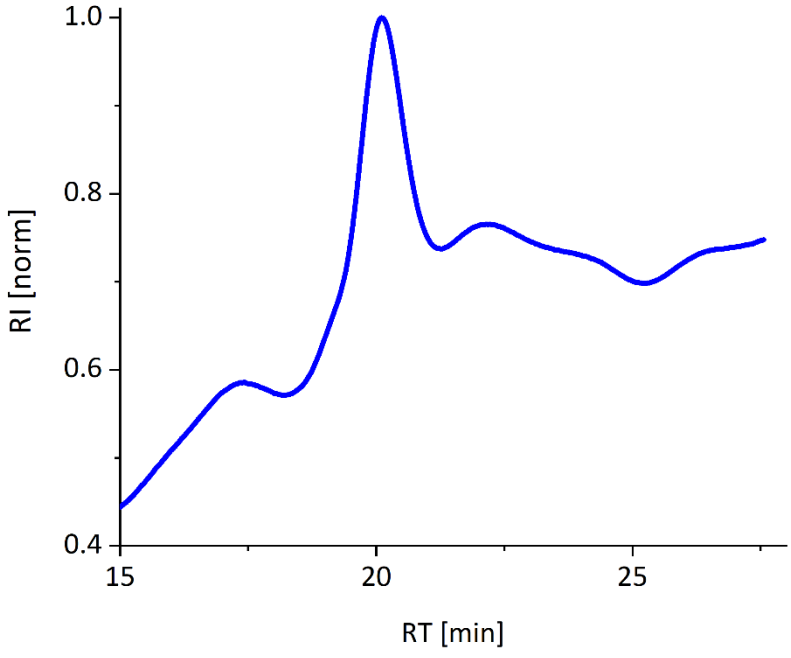

Figure A 23: GPC chromatogram (RI detector) of macroCTA-*54*.

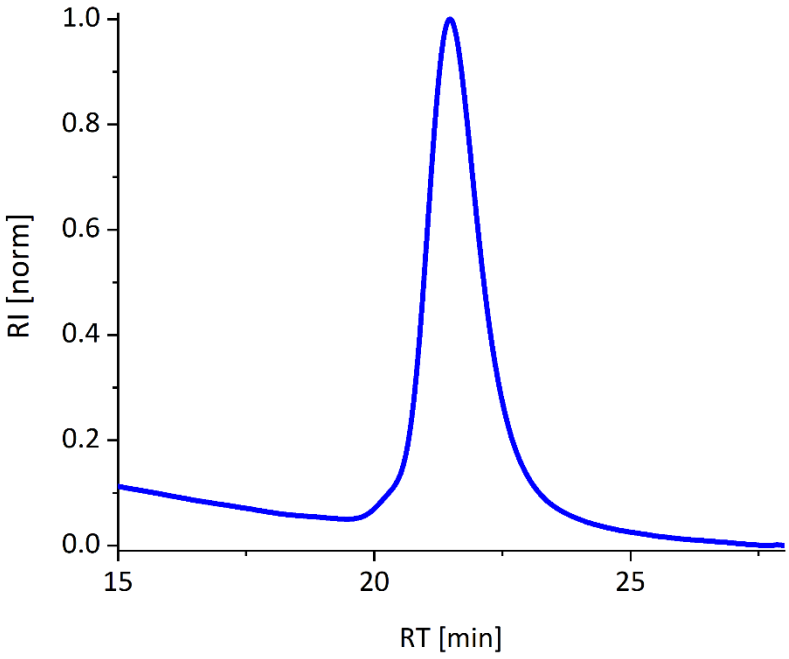

Figure A 24: GPC chromatogram (RI detector) of macroCTA-*23*.

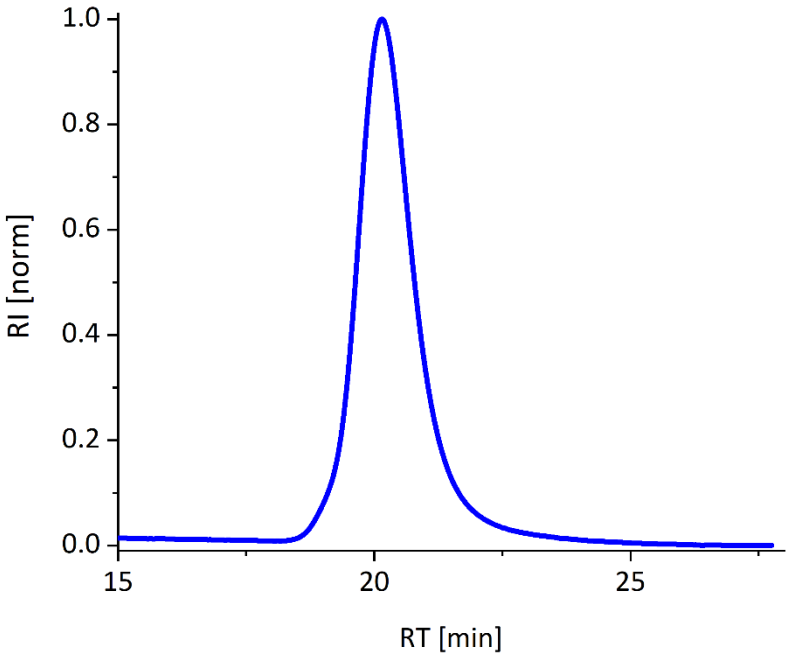

Figure A 25: GPC chromatogram (RI detector) of macroCTA-*48*.

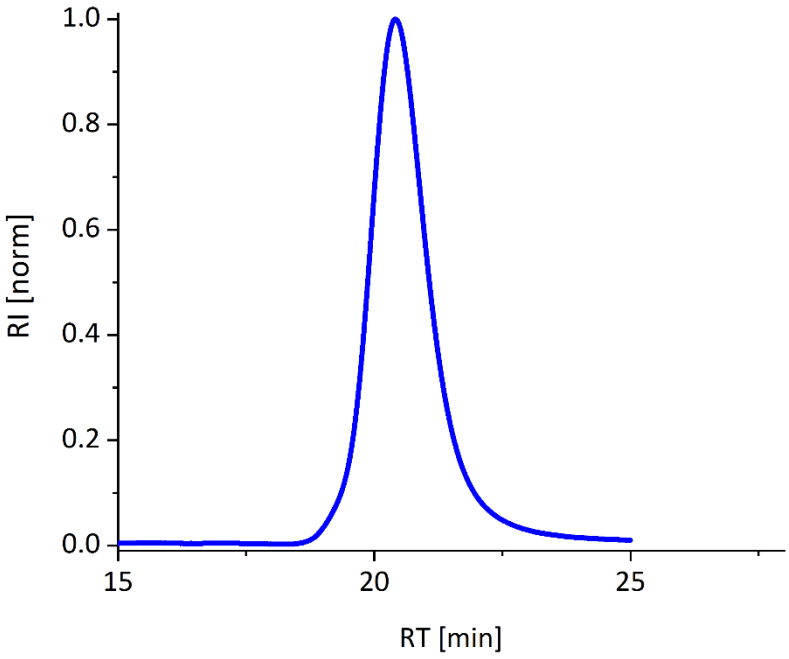

Figure A 26: GPC chromatogram (RI detector) of macroCTA-*39*.

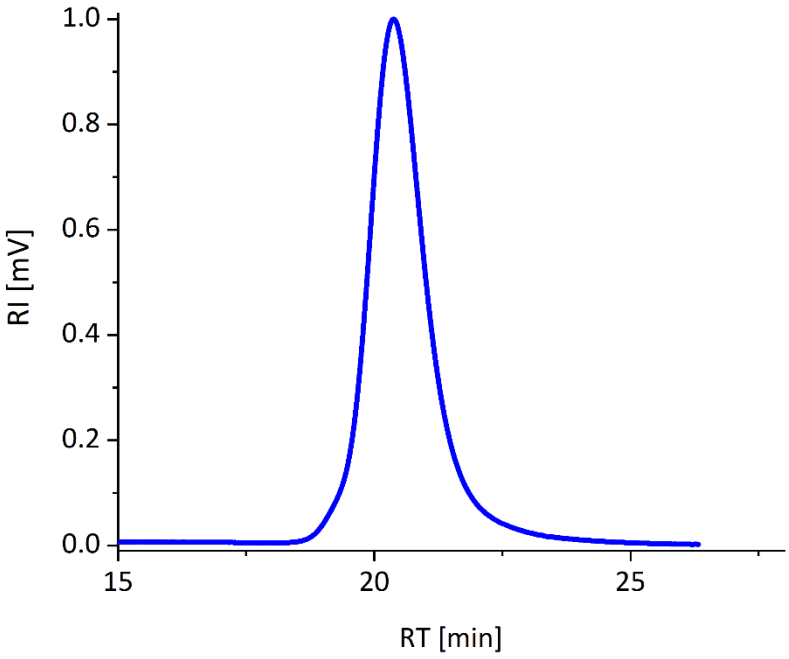

Figure A 27: GPC chromatogram (RI detector) of macroCTA-*43*.

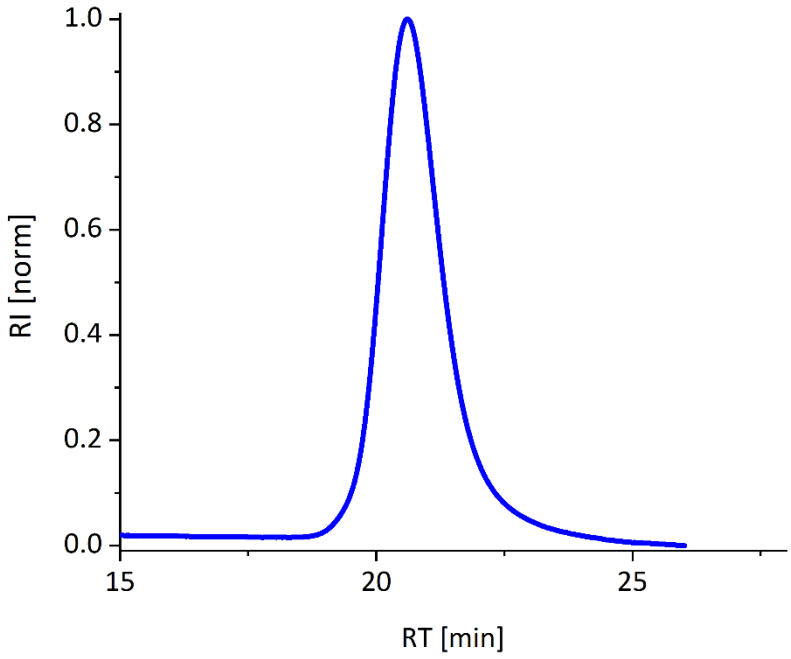

Figure A 28: GPC chromatogram (RI detector) of macroCTA-*38*.

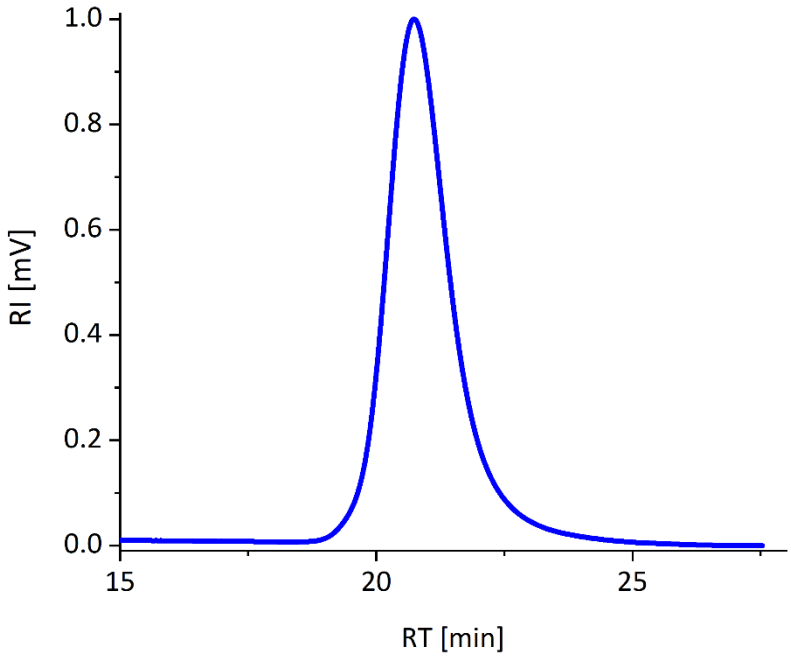

Figure A 29: GPC chromatogram (RI detector) of macroCTA-*34*.

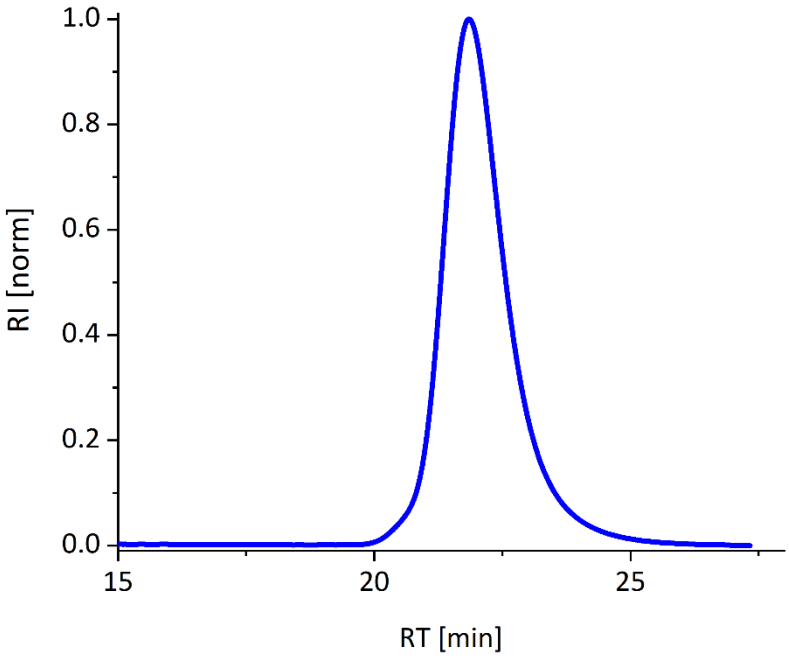

Figure A 30: GPC chromatogram (RI detector) of macroCTA-*19*.

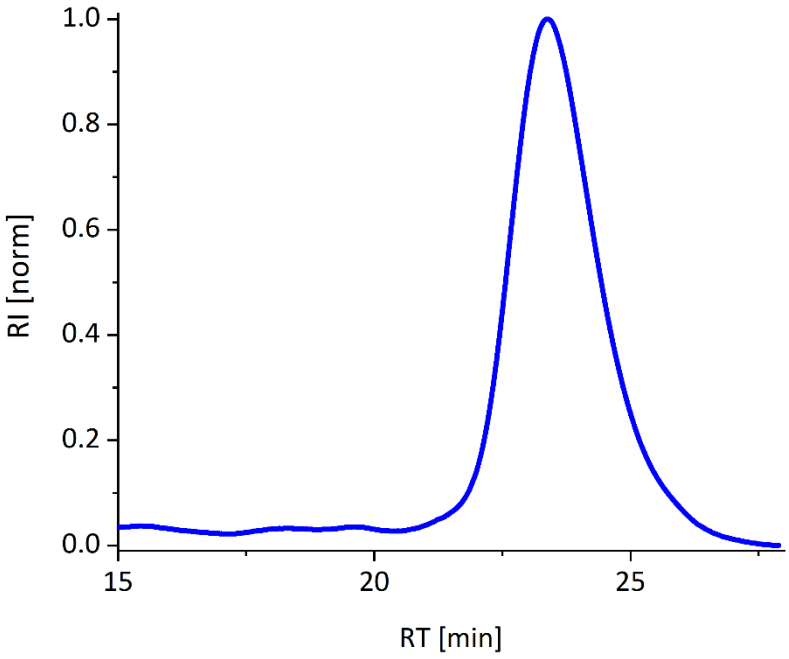

Figure A 31: GPC chromatogram (RI detector) of macroCTA-*9*.

7.2.2 Exemplary Synthesis of PS-*b*-P(MMA-*co*-HEMA) BCPs:

In a Schlenk tube, 560 mg (MW = 37641, 0.0149 mmol, 1 eq.) of macroCTA-*38* were dissolved in 18 mL 1,4-dioxane. Styrene (18.3 g, 176 mmol, 11800 eq.) and AIBN stock solution (79 mg, 0.0032 mmol, 7.5 mg in 1.125 g 1,4-dioxane, 0.2 eq.) were added. The solution was degassed via freeze-pump-thaw (3 x 8 min), followed by backfilling with nitrogen. The reaction mixture was stirred at 90 C for 2 h, cooled in liquid nitrogen and opened to the atmosphere. The solvent and most of the remaining styrene were removed in vacuo, the viscous mixture was dissolved in small amounts of DCM and precipitated into diethyl ether twice. After centrifugation and decanting of the supernatant, BCP1 was received as a light pink solid.

^{1}H NMR 600 MHz (CD_2Cl_2): δ [ppm] = 7.80 (m), 7.47 (m), 7.31 (m), 7.28 - 6.31 (m), 4.07 (bs), 3.80 (bs), 3.56 (s), 2.14 - 0.63 (m).

NMR spectra of PS-*b*-P(MMA-*co*-HEMA) BCPs

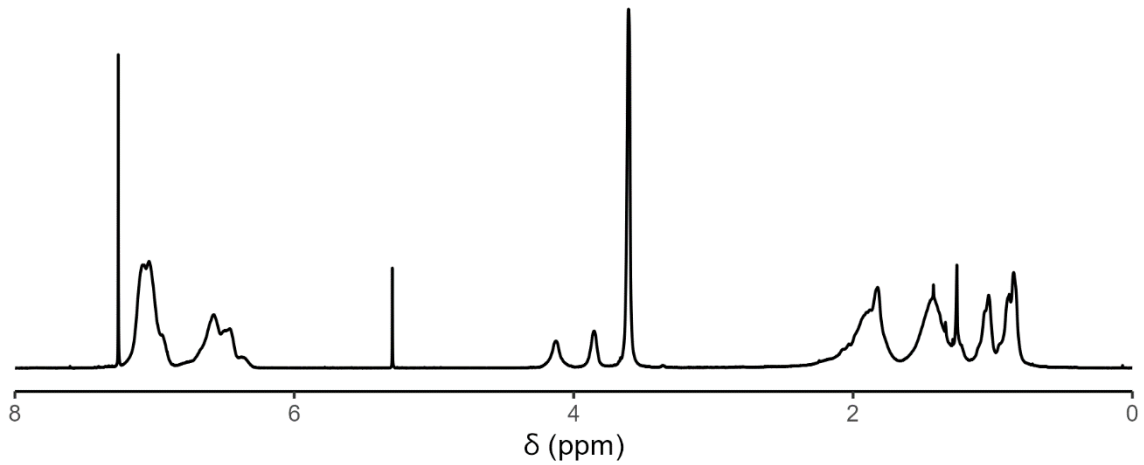

Figure A32: ^{1}H NMR spectrum of $S_{0.54}$-$MH_{0.46}$-*45* in $CDCl_3$.

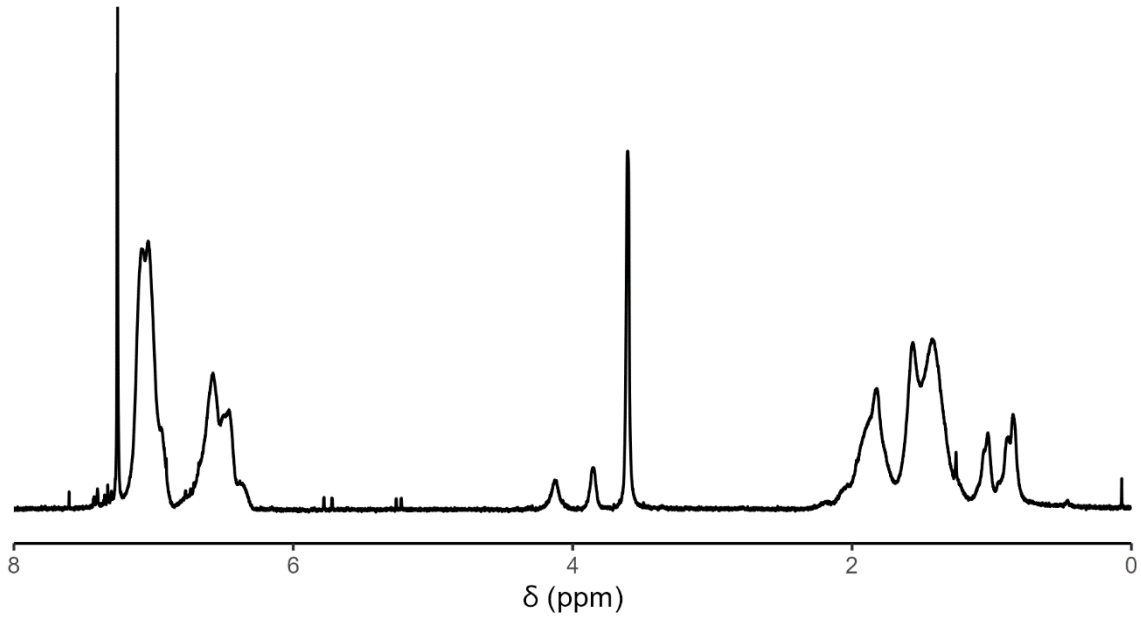

Figure A33: ^{1}H NMR spectrum of $S_{0.75}$-$MH_{0.25}$-*66* in $CDCl_3$.

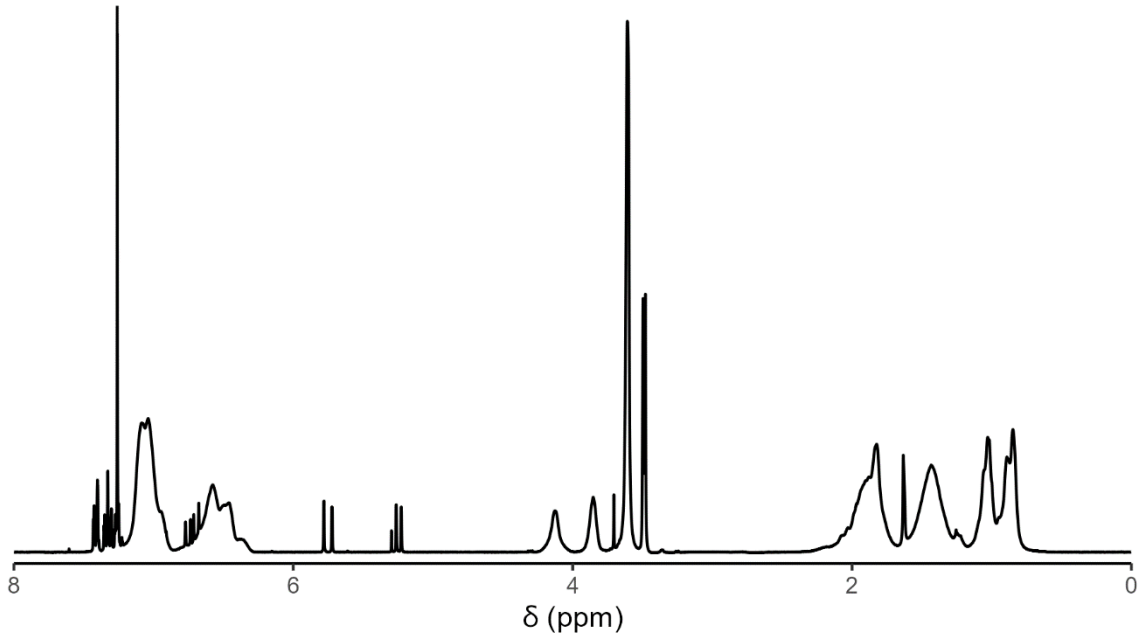

Figure A34: ^{1}H NMR spectrum of $S_{0.49}$-$MH_{0.51}$-*92* in $CDCl_3$.

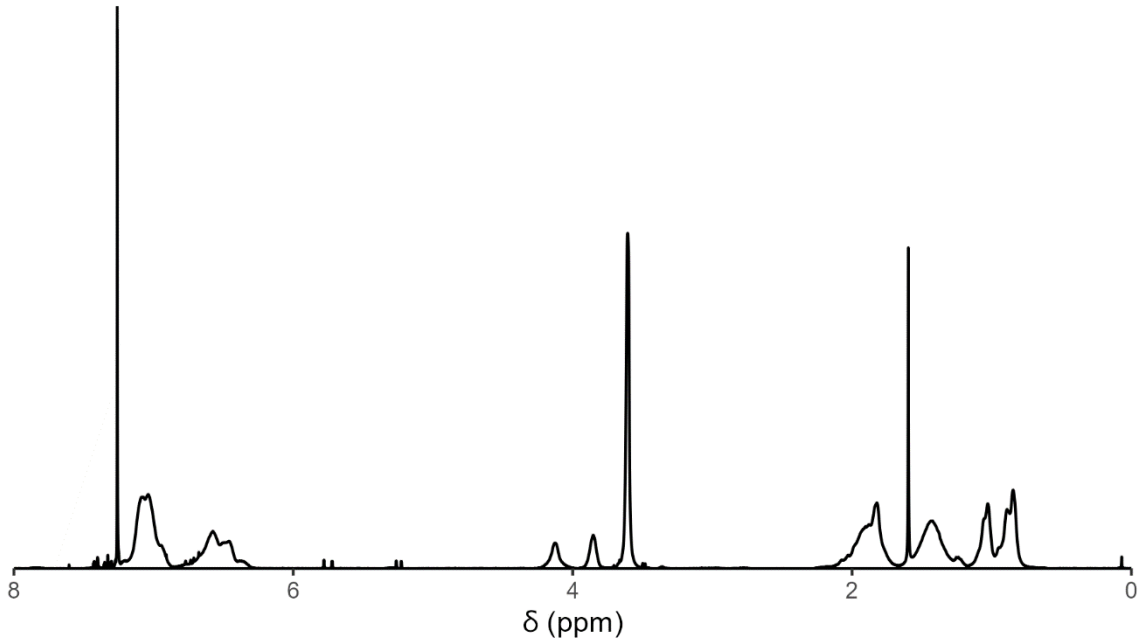

Figure A35: ^{1}H NMR spectrum of $S_{0.45}$-$MH_{0.55}$-*42* in $CDCl_3$.

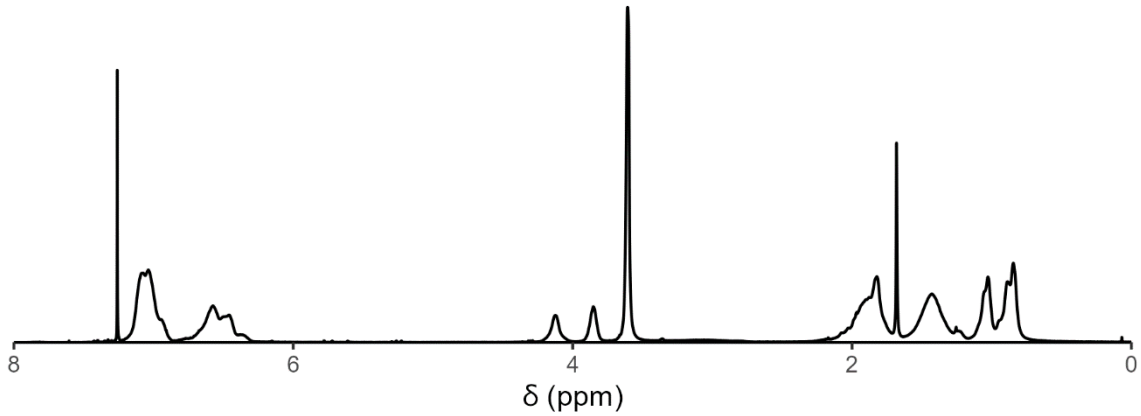

Figure A36: ^{1}H NMR spectrum of $S_{0.45}$-$MH_{0.55}$-*102* in $CDCl_3$.

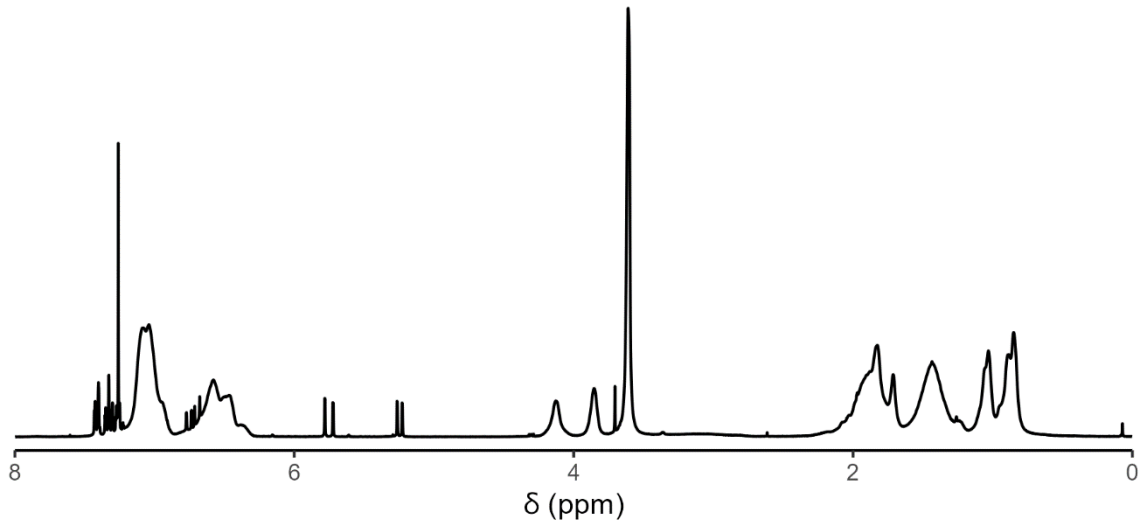

Figure A37: ^{1}H NMR spectrum of $S_{0.50}$-$MH_{0.50}$-*91* in $CDCl_3$.

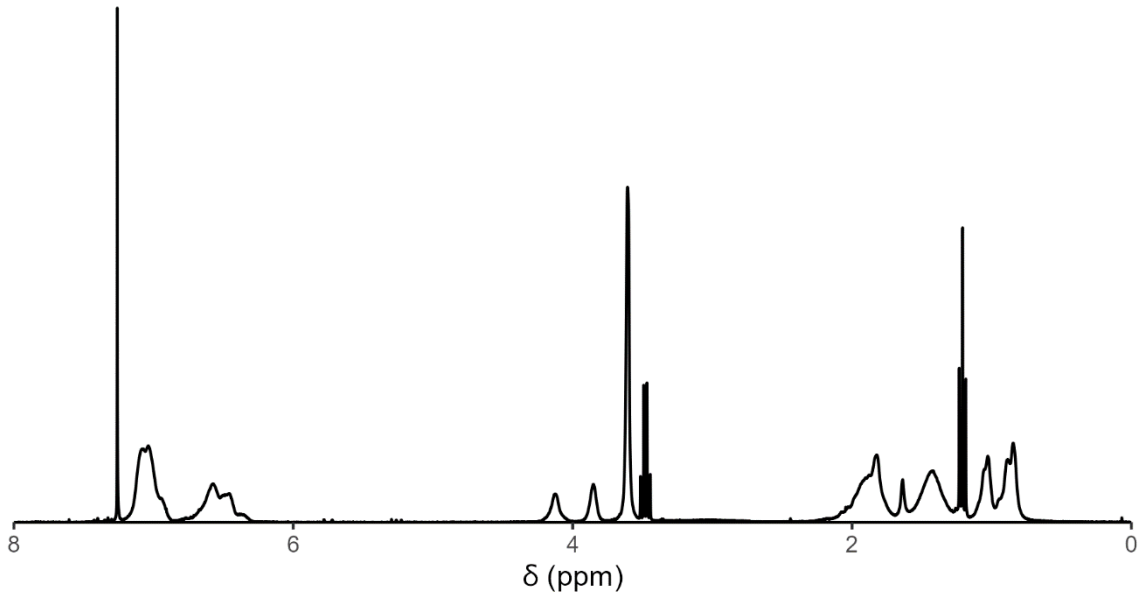

Figure A38: ^{1}H NMR spectrum of $S_{0.46}$-$MH_{0.54}$-*81* in $CDCl_3$.

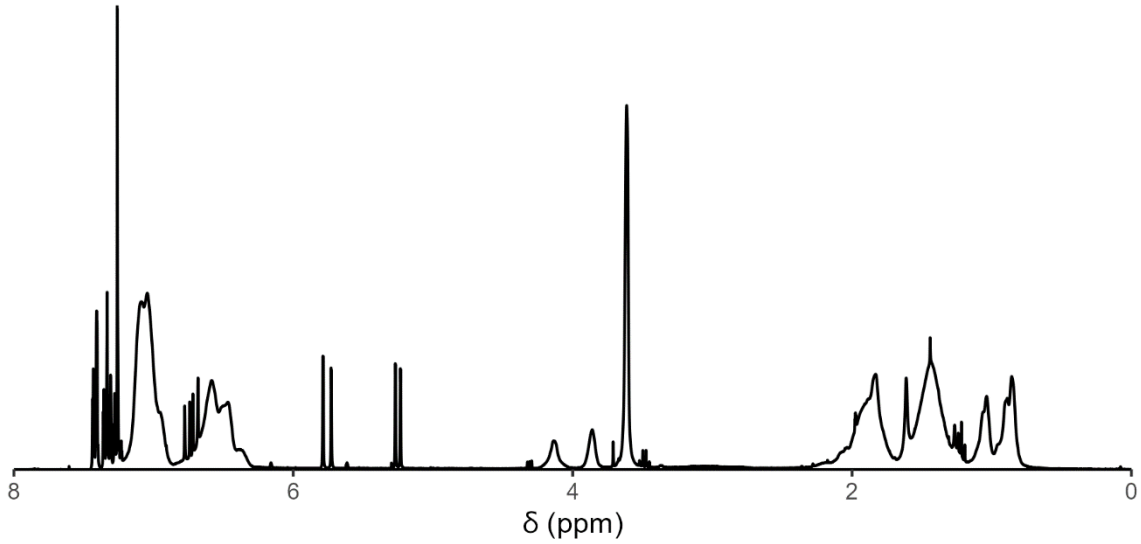

Figure A39: ^{1}H NMR spectrum of $S_{0.66}$-$MH_{0.34}$-*70* in $CDCl_3$.

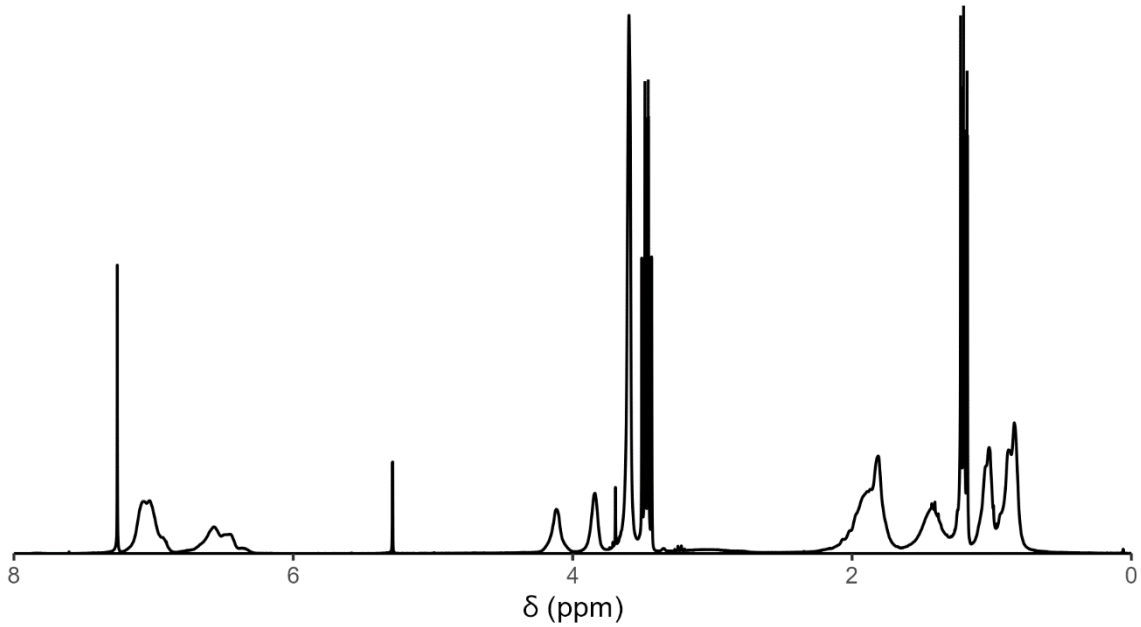

Figure A40: ^{1}H NMR spectrum of $S_{0.27}$-$MH_{0.73}$-*70* in $CDCl_3$.

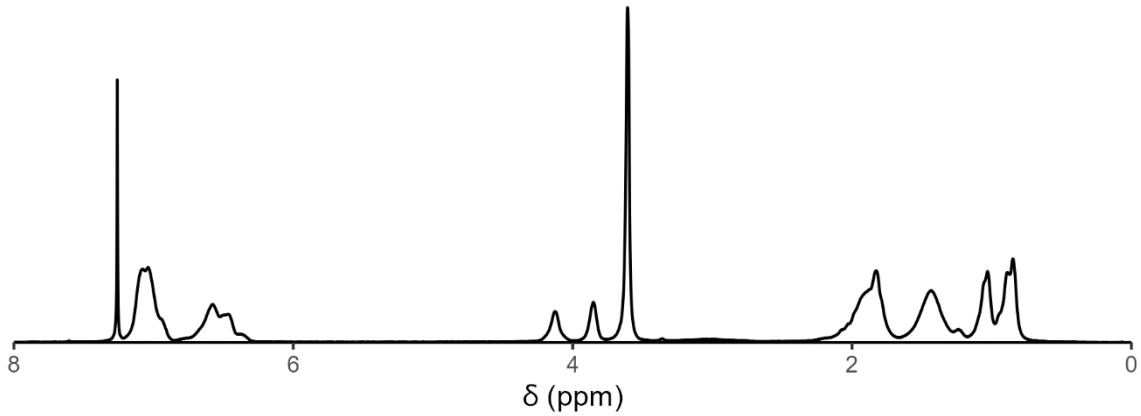

Figure A41: ^{1}H NMR spectrum of $S_{0.42}$-$MH_{0.58}$-*89* in $CDCl_3$.

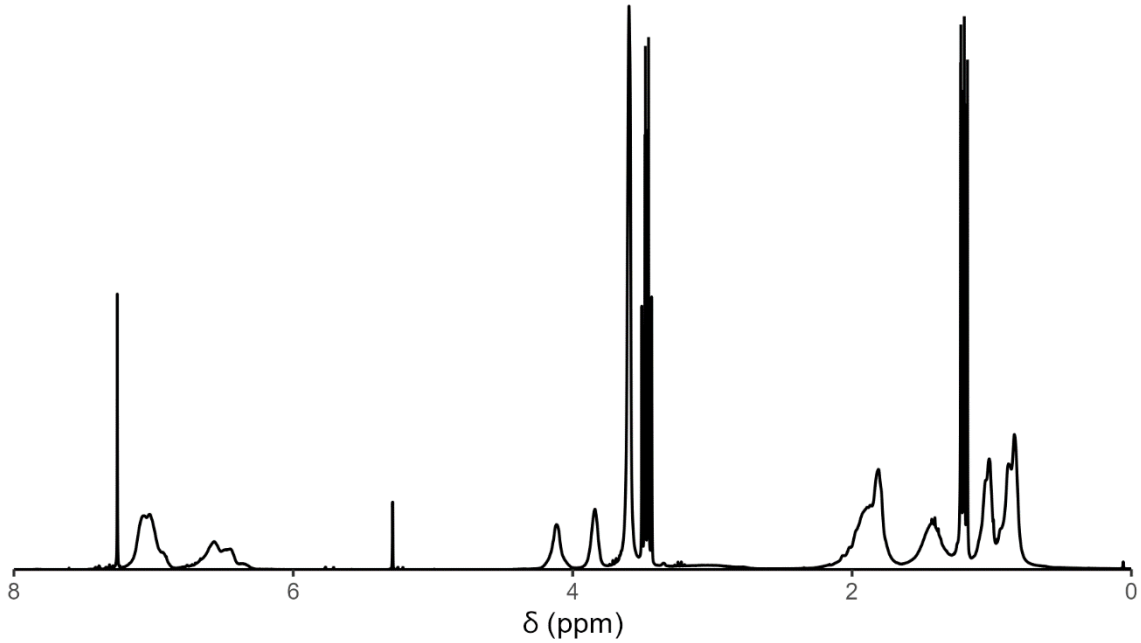

Figure A42: ^{1}H NMR spectrum of $S_{0.28}$-$MH_{0.72}$-*67* in $CDCl_3$.

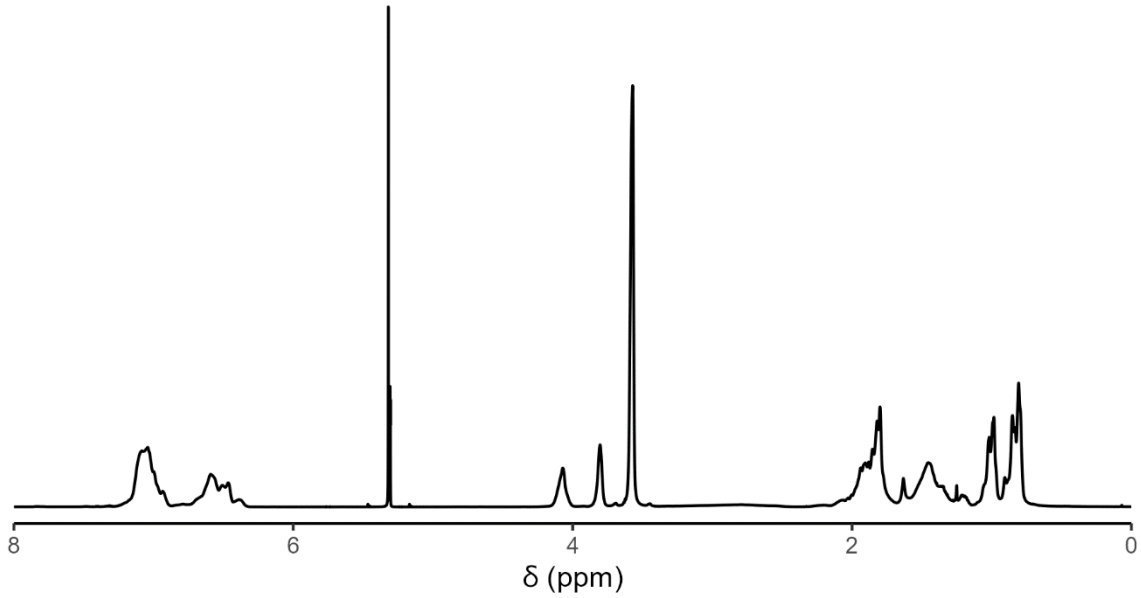

Figure A43: ^{1}H NMR spectrum of $S_{0.37}$-$MH_{0.63}$-*65* in $CDCl_3$.

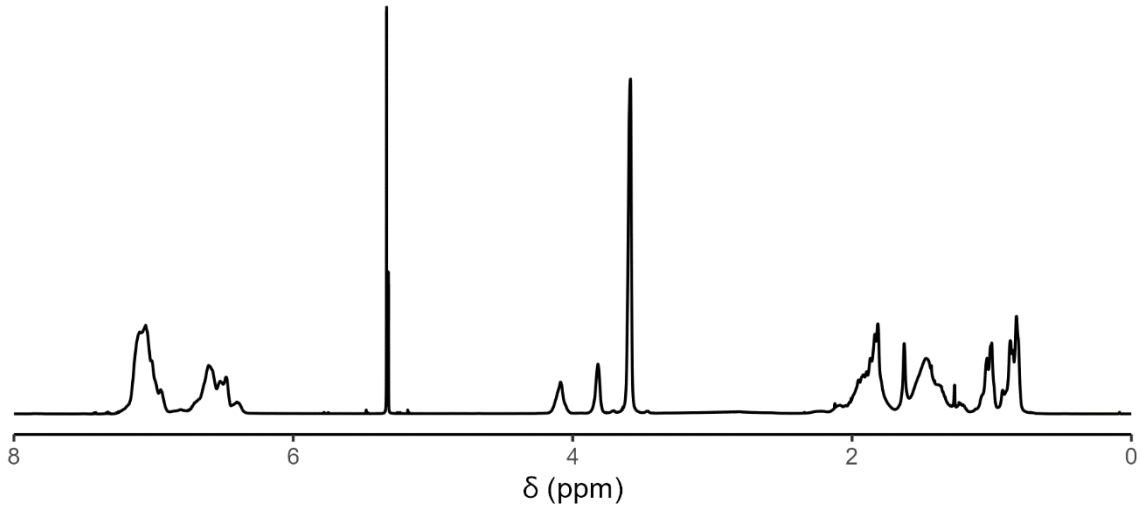

Figure A44: ^{1}H NMR spectrum of $S_{0.54}$-$MH_{0.46}$-*45* in $CDCl_3$.

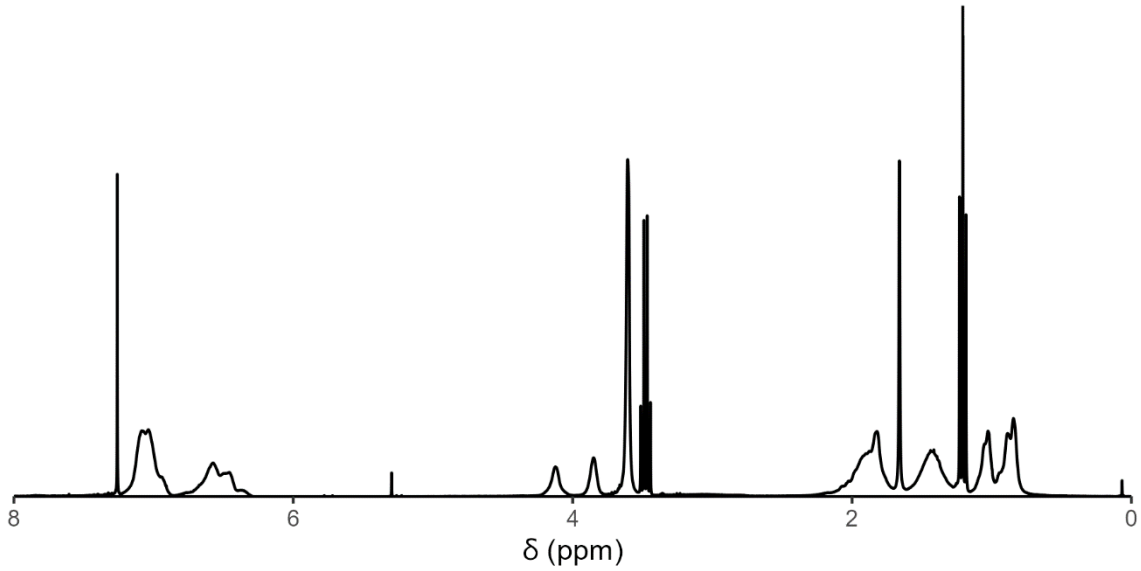

Figure A45: ^{1}H NMR spectrum of $S_{0.39}$-$MH_{0.61}$-*35* in $CDCl_3$.

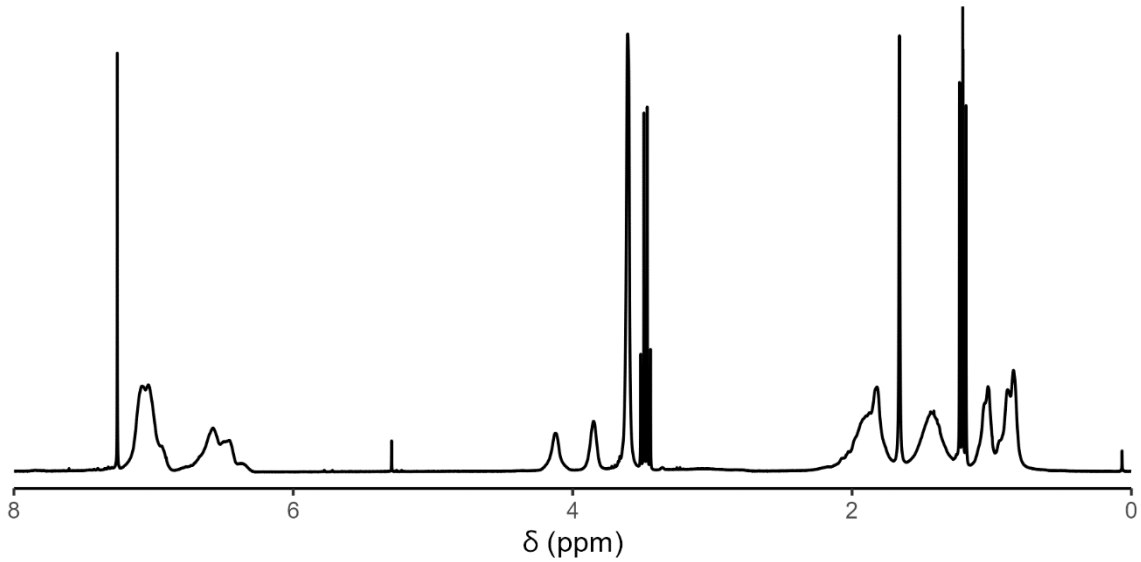

Figure A46: ^{1}H NMR spectrum of $S_{0.43}$-$MH_{0.57}$-*40* in $CDCl_3$.

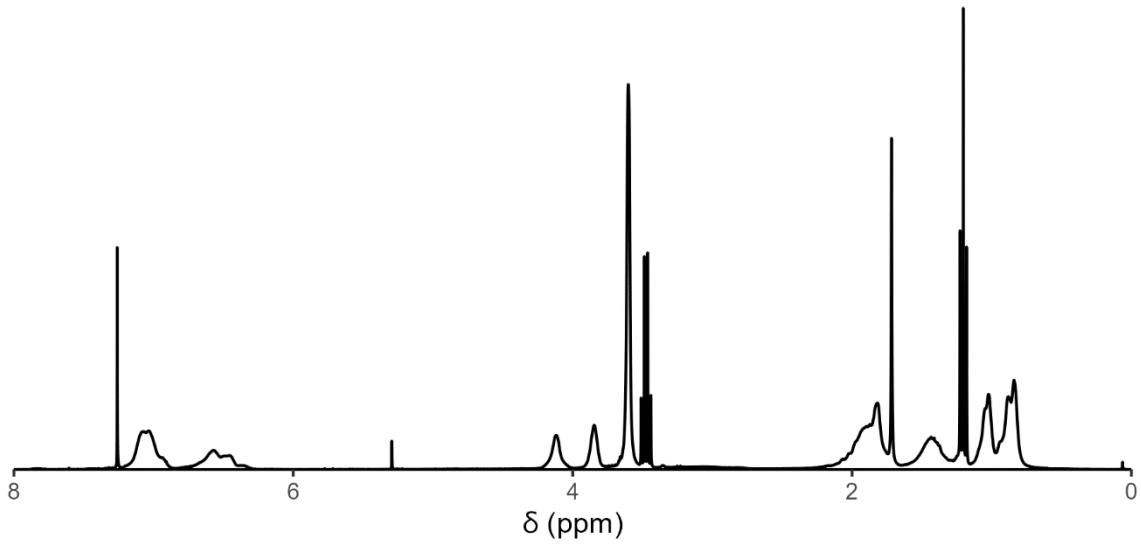

Figure A47: ^{1}H NMR spectrum of $S_{0.28}$-$MH_{0.72}$-*29* in $CDCl_3$.

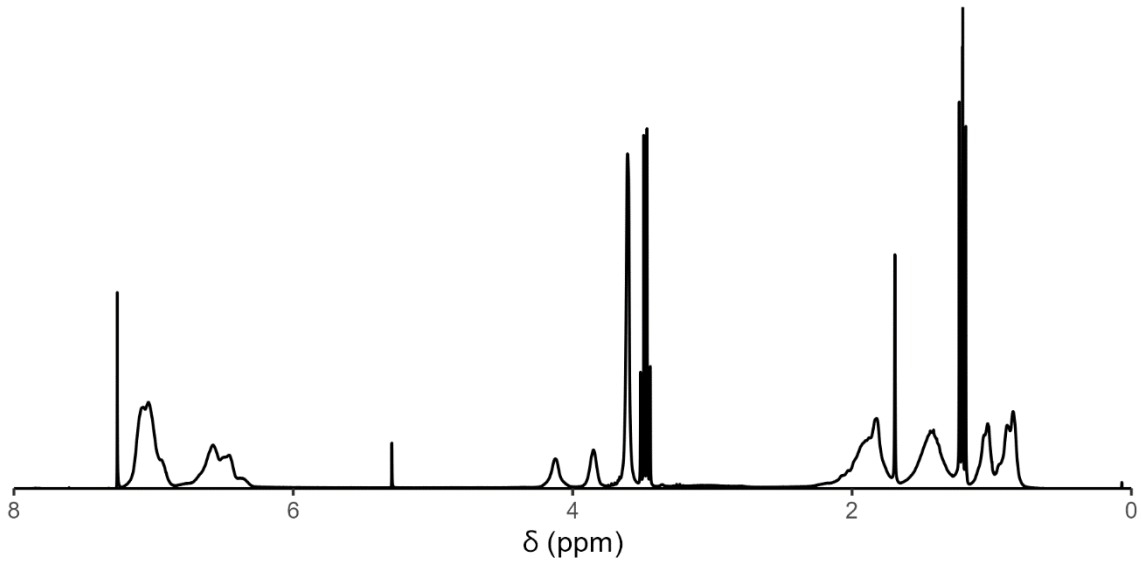

Figure A48: ^{1}H NMR spectrum of $S_{0.50}$-$MH_{0.50}$-*45* in $CDCl_3$.

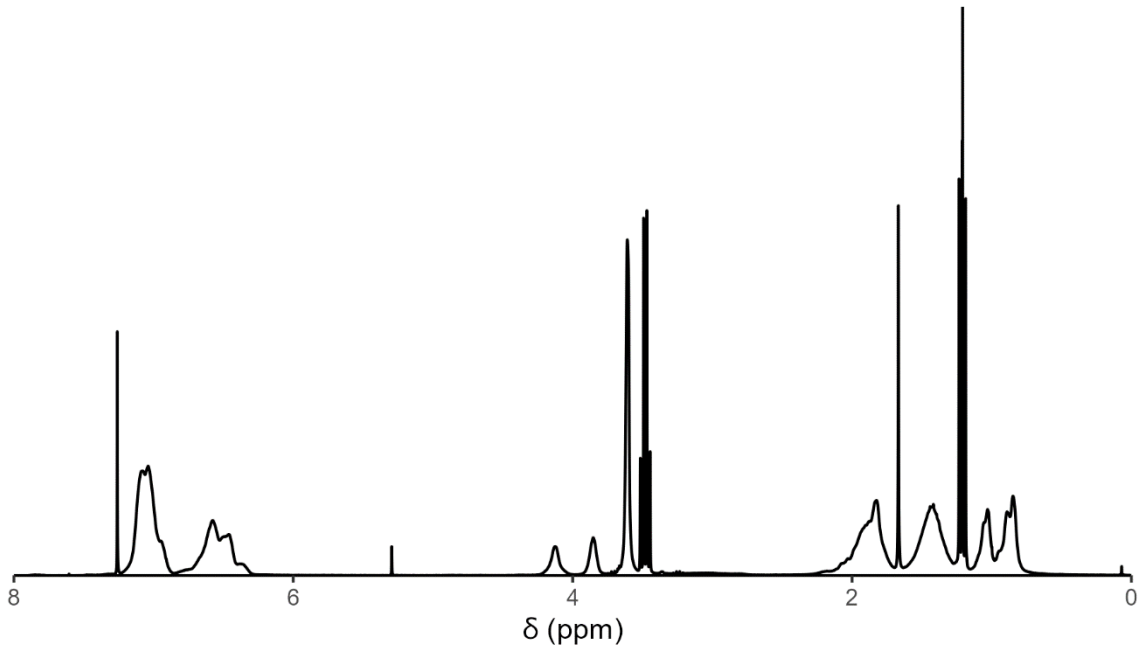

Figure A49: ^{1}H NMR spectrum of $S_{0.56}$-$MH_{0.44}$-*52* in $CDCl_3$.

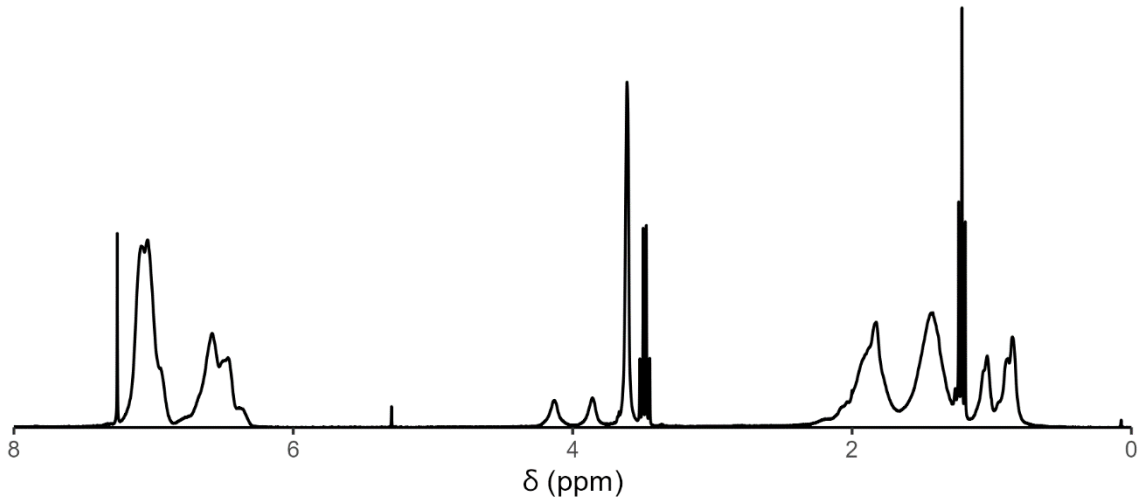

Figure A50: ^{1}H NMR spectrum of $S_{0.68}$-$MH_{0.32}$-*33* in $CDCl_3$.

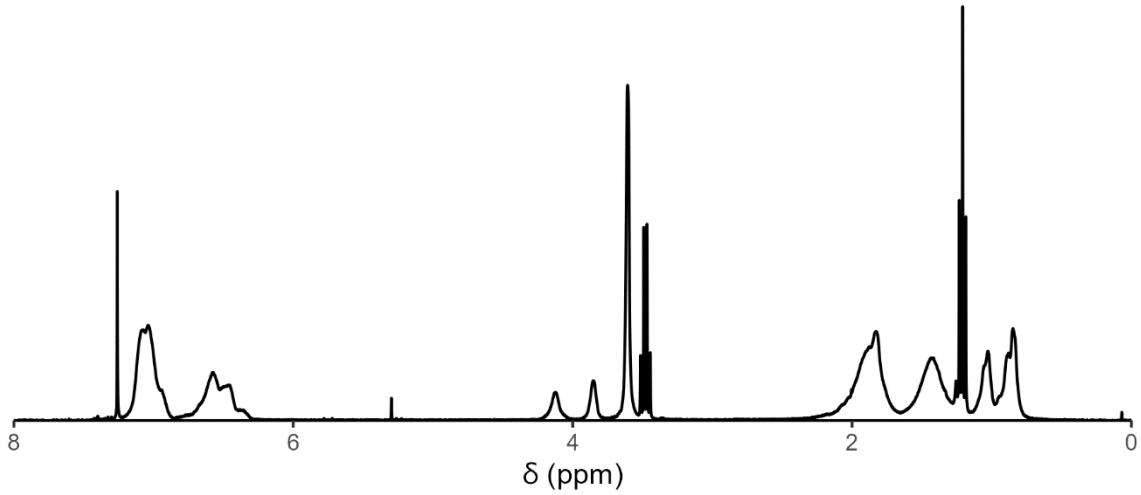

Figure A51: ^{1}H NMR spectrum of $S_{0.52}$-$MH_{0.48}$-*67* in $CDCl_3$.

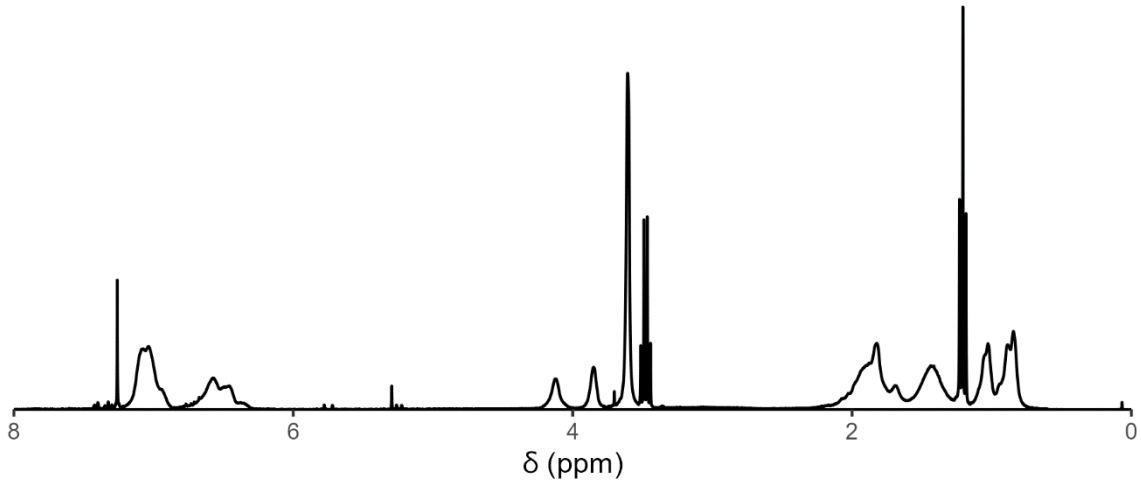

Figure A52: ^{1}H NMR spectrum of $S_{0.42}$-$MH_{0.58}$-*57* in $CDCl_3$.

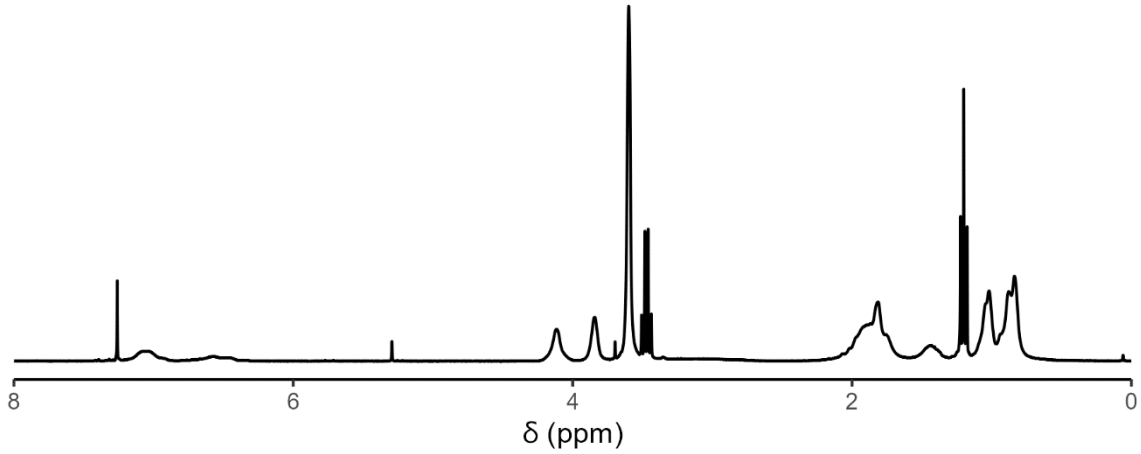

Figure A53: ^{1}H NMR spectrum of $S_{0.09}$-$MH_{0.91}$-*39* in $CDCl_3$.

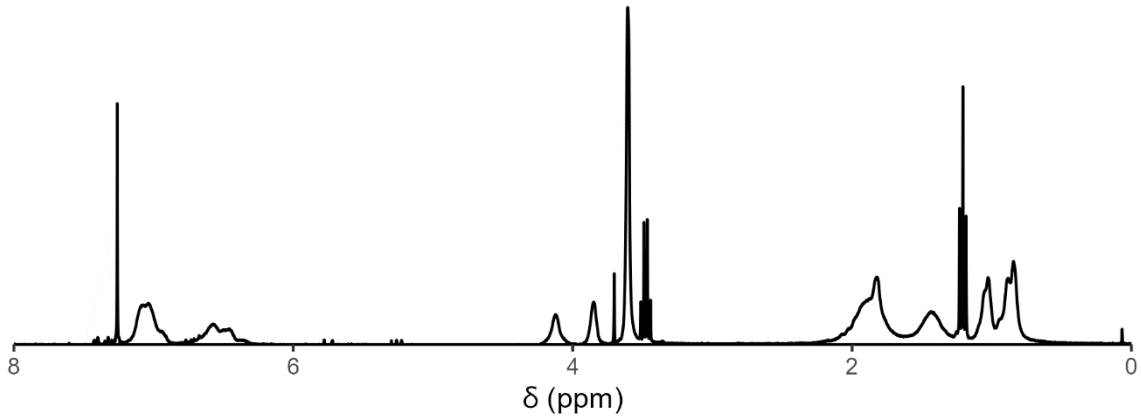

Figure A54: ^{1}H NMR spectrum of $S_{0.31}$-$MH_{0.69}$-*48* in $CDCl_3$.

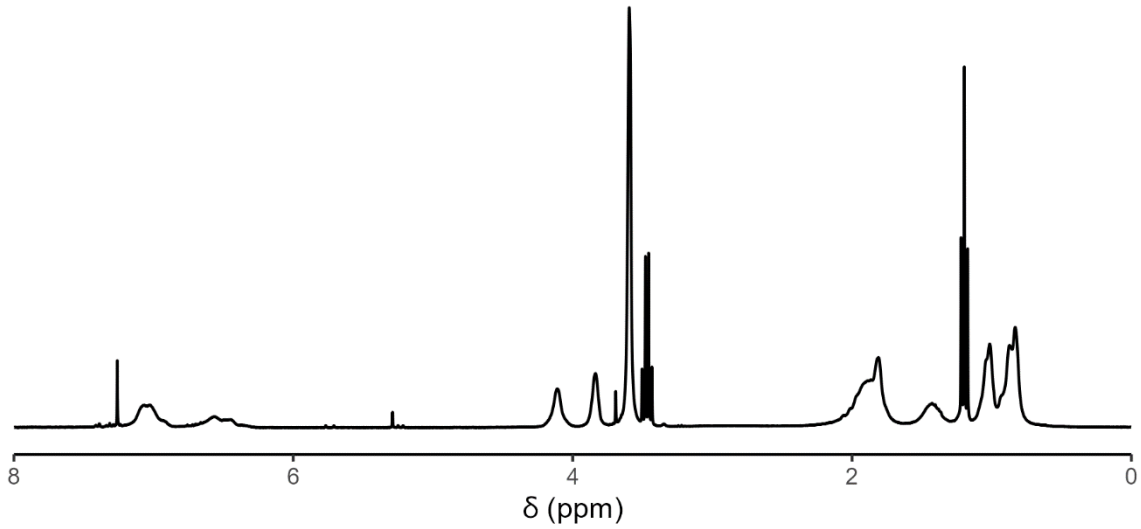

Figure A55: ^{1}H NMR spectrum of $S_{0.16}$-$MH_{0.84}$-*45* in CDCl3.

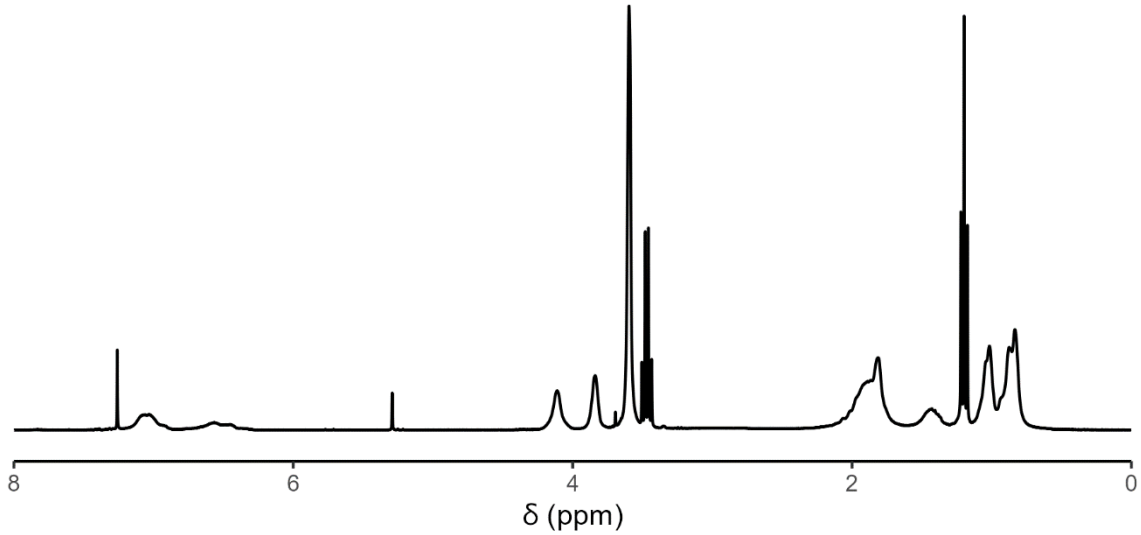

Figure A56: 1H NMR spectrum of $S_{0.12}$-$MH_{0.88}$-*40* in CDCl3.

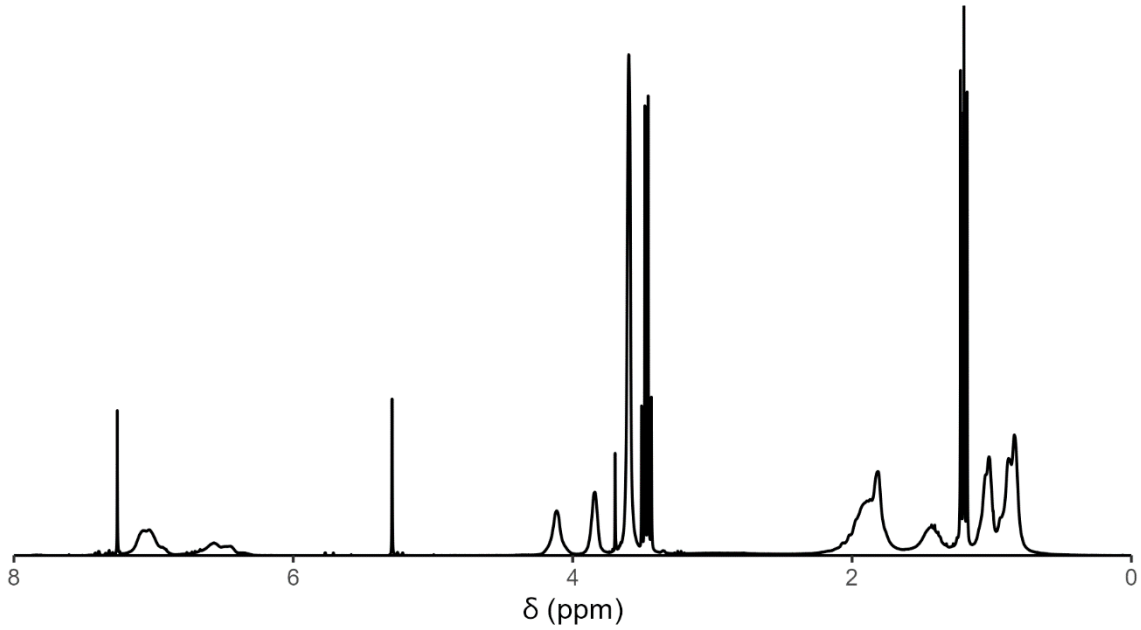

Figure A57: ^{1}H NMR spectrum of $S_{0.16}$-$MH_{0.84}$-*43* in $CDCl_3$.

GPC chromatograms of PS-*b*-P(MMA-*co*-HEMA) BCPs

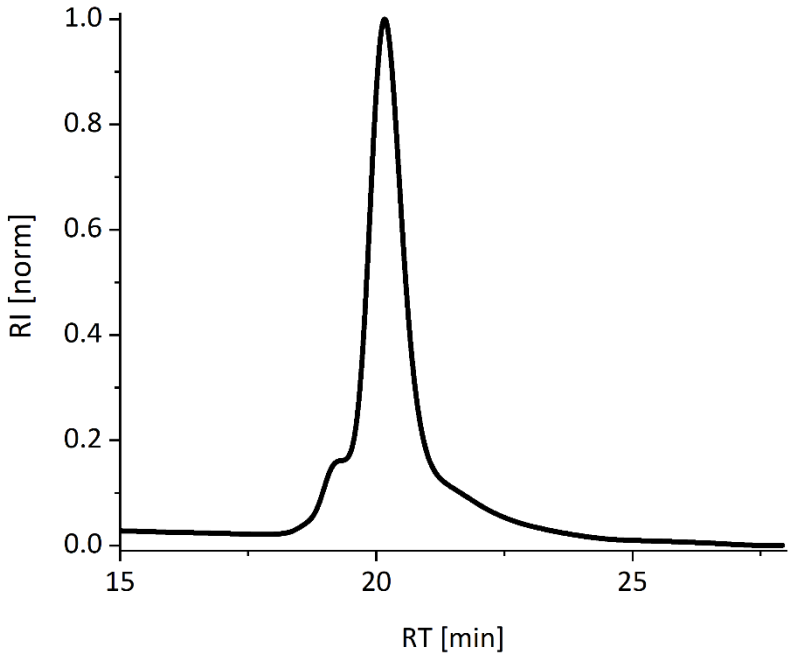

Figure A 58: GPC chromatogram (RI detector) of $S_{0.54}$-$MH_{0.46}$-*45*.

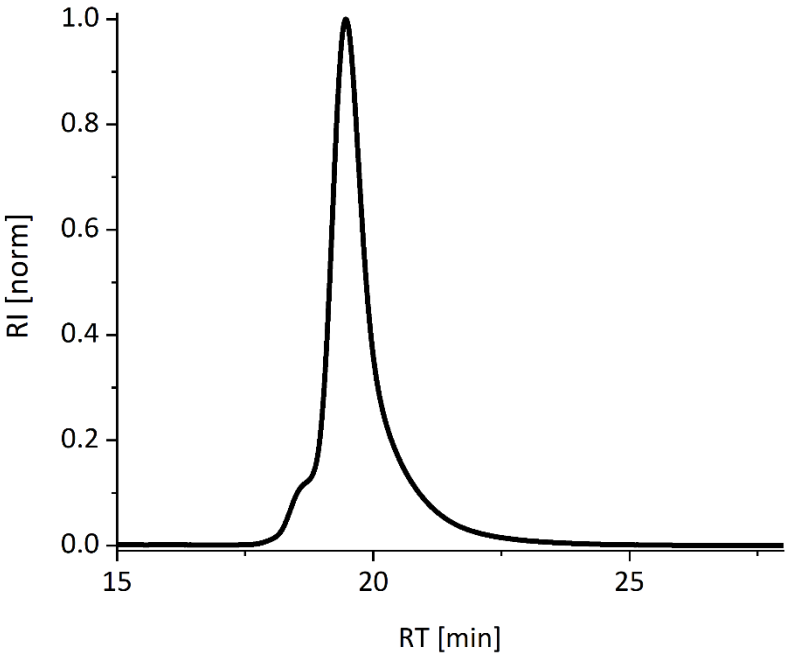

Figure A 59: GPC chromatogram (RI detector) of $S_{0.75}$-$MH_{0.25}$-*66*.

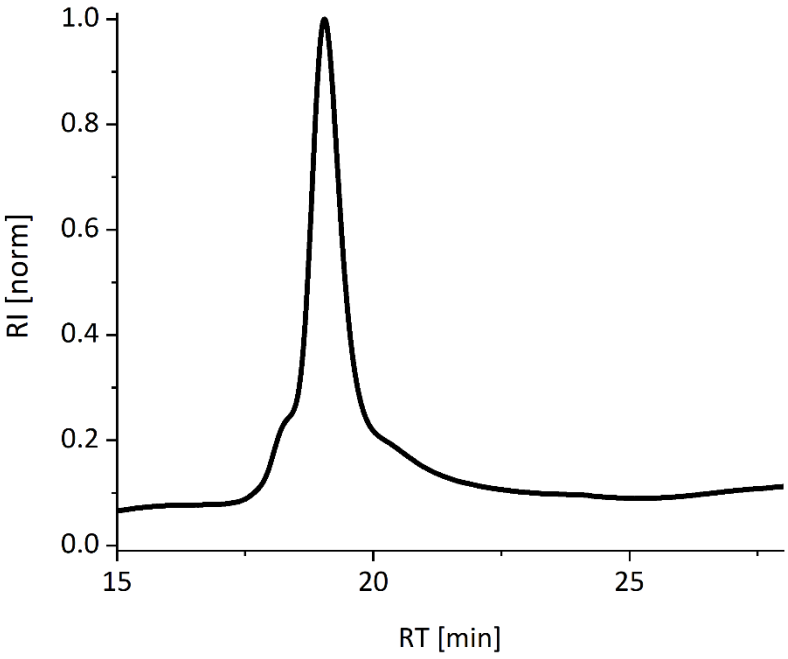

Figure A 60: GPC chromatogram (RI detector) of $S_{0.49}$-$MH_{0.51}$-*92*.

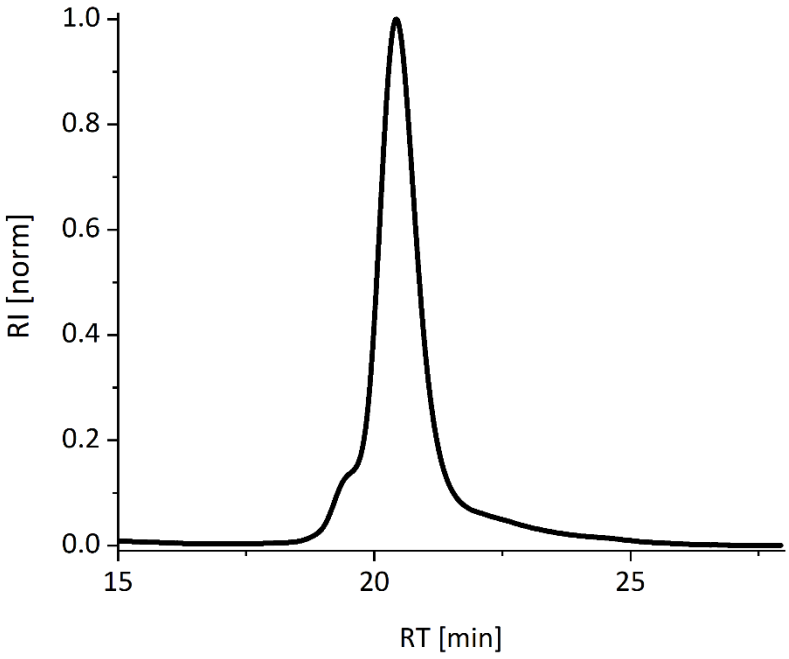

Figure A 61: GPC chromatogram (RI detector) of $S_{0.45}$-$MH_{0.55}$-*42*.

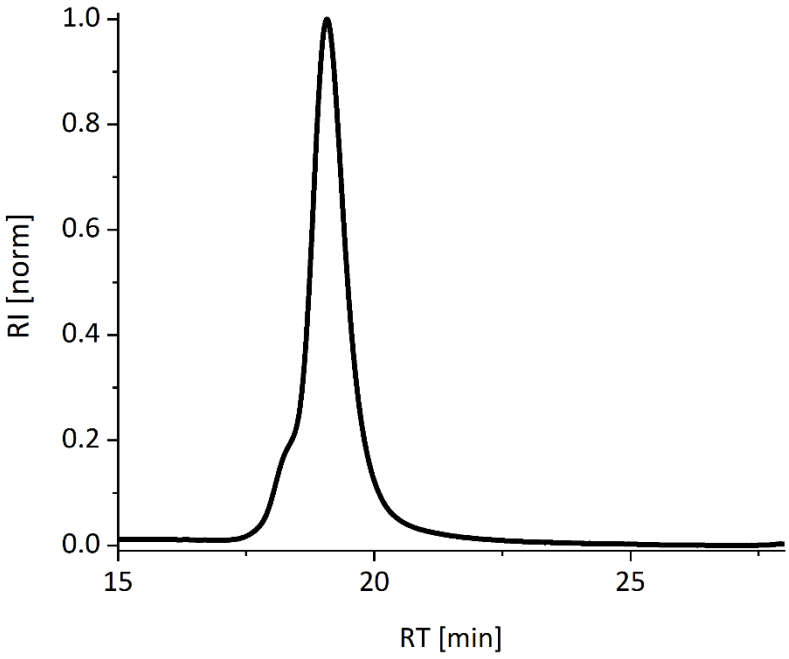

Figure A 62: GPC chromatogram (RI detector) of $S_{0.45}$-$MH_{0.55}$-*102*.

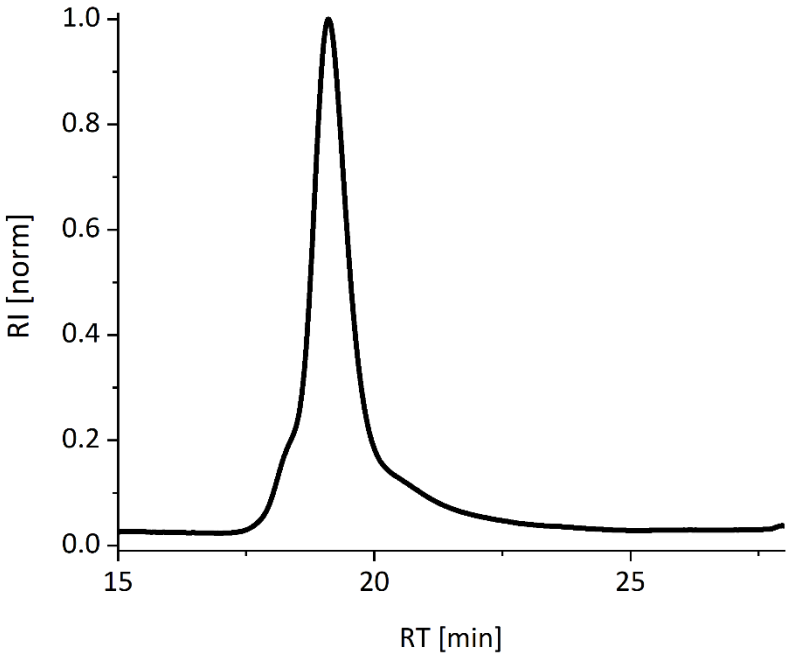

Figure A 63: GPC chromatogram (RI detector) of $S_{0.50}$-$MH_{0.50}$-*91*.

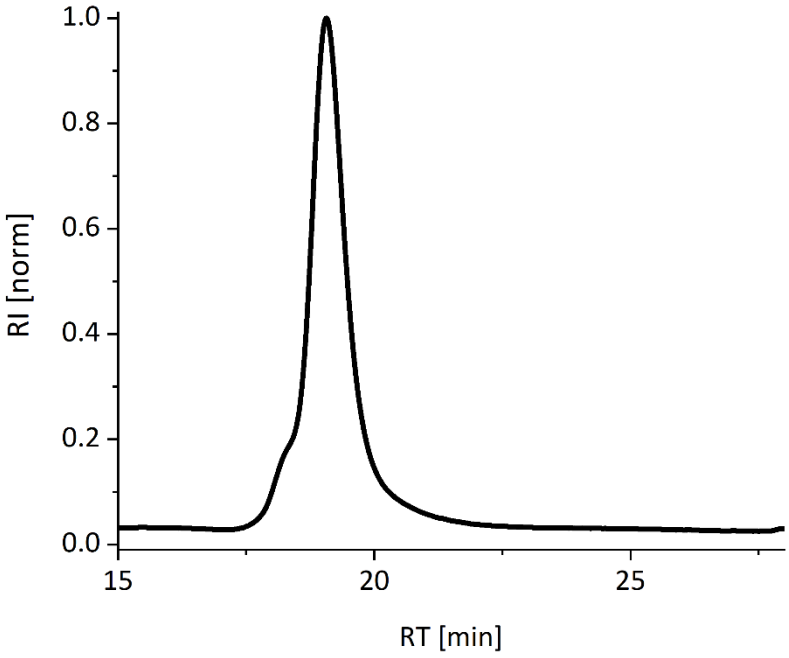

Figure A 64: GPC chromatogram (RI detector) of $S_{0.46}$-$MH_{0.54}$-*81*.

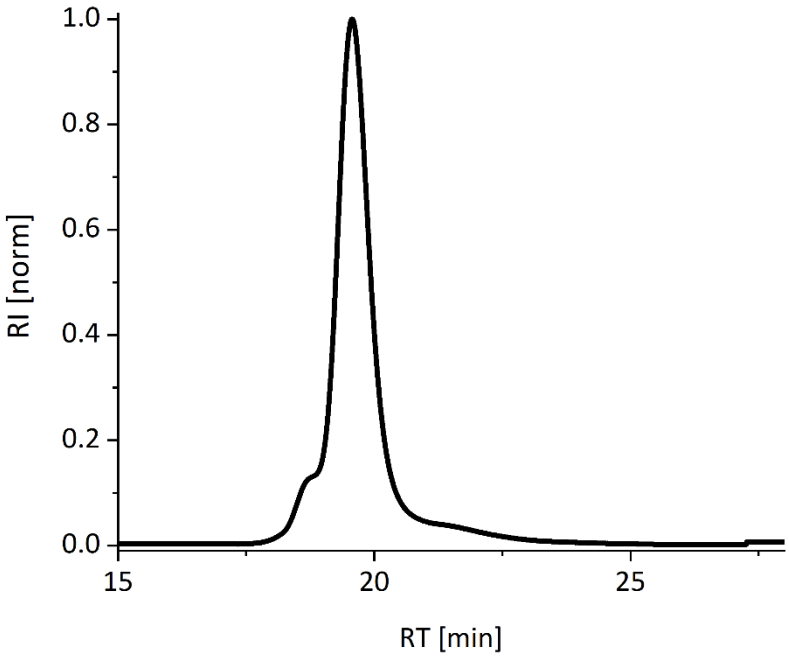

Figure A 65: GPC chromatogram (RI detector) of $S_{0.66}$-$MH_{0.34}$-*70*.

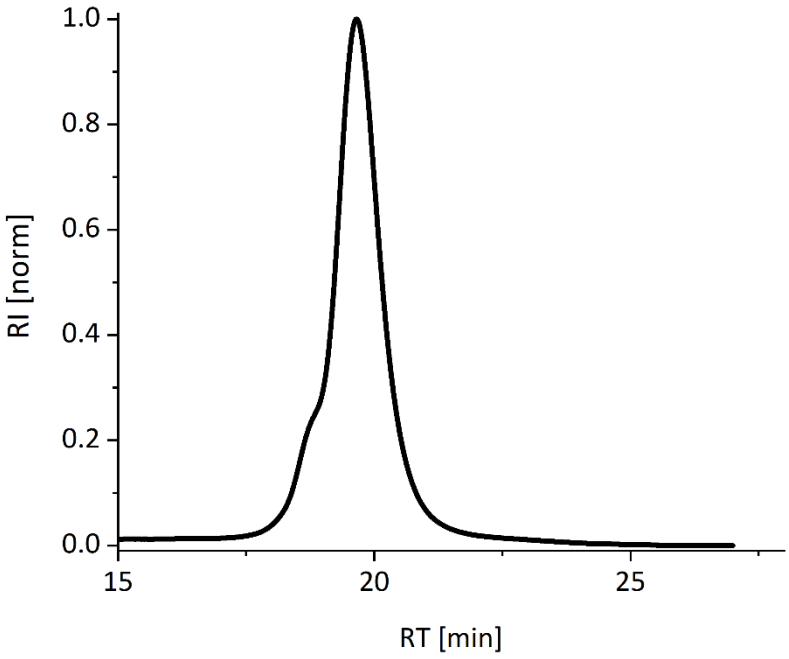

Figure A 66: GPC chromatogram (RI detector) of $S_{0.27}$-$MH_{0.73}$-*70*.

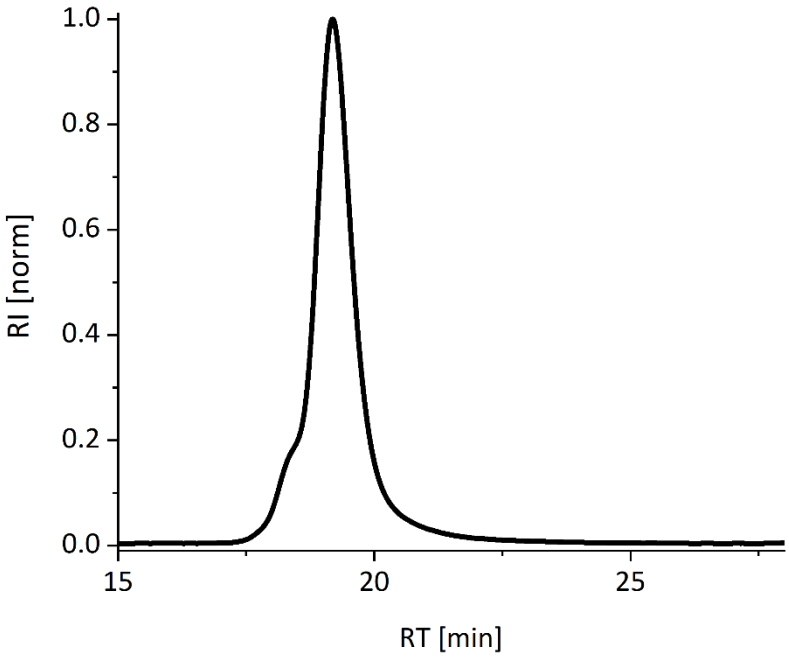

Figure A 67: GPC chromatogram (RI detector) of $S_{0.42}$-$MH_{0.58}$-*89*.

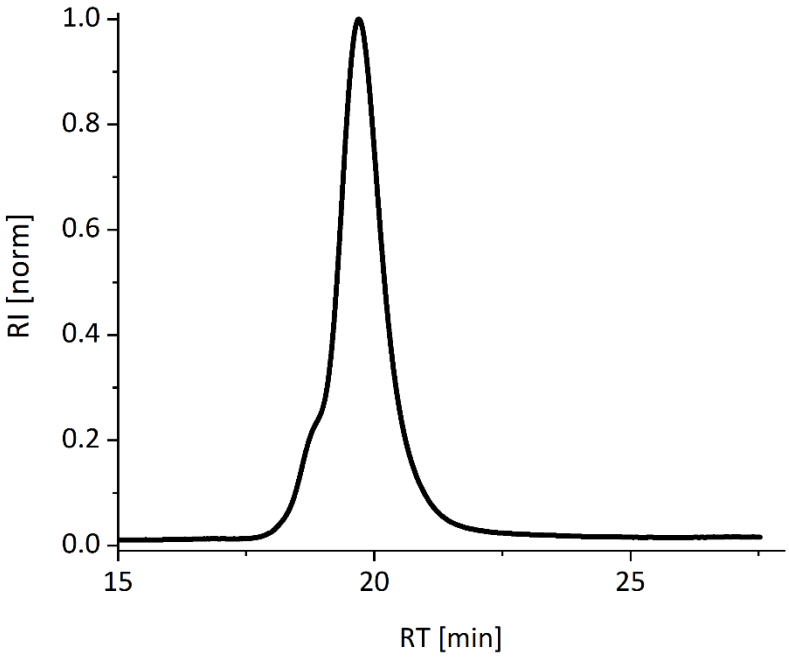

Figure A 68: GPC chromatogram (RI detector) of $S_{0.28}$-$MH_{0.72}$-*67*.

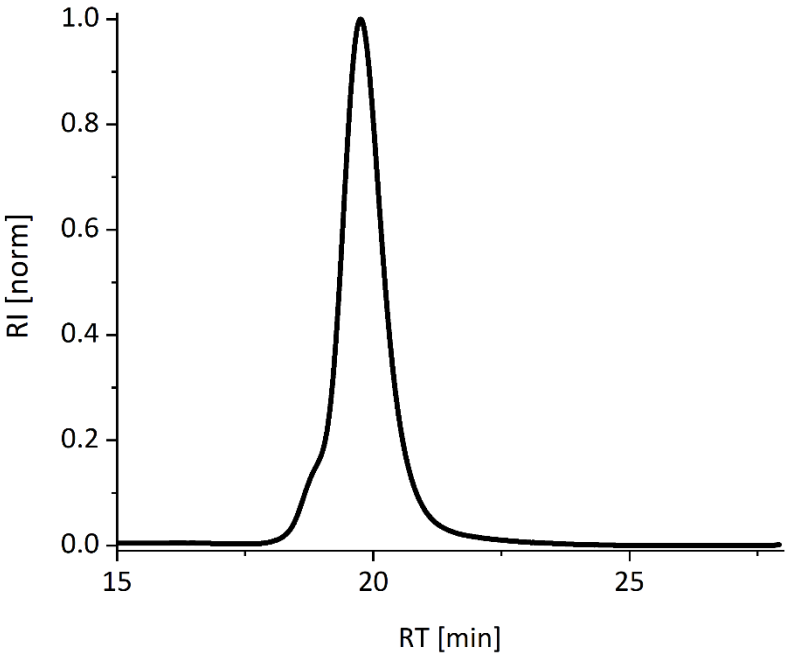

Figure A 69: GPC chromatogram (RI detector) of $S_{0.37}$-$MH_{0.63}$-*65*.

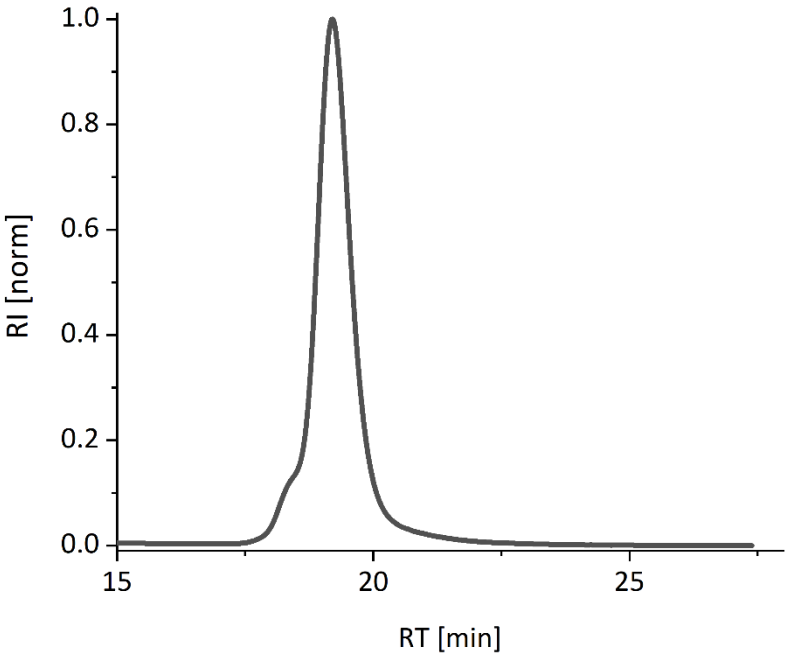

Figure A 70: GPC chromatogram (RI detector) of $S_{0.54}$-$MH_{0.46}$-*45*.

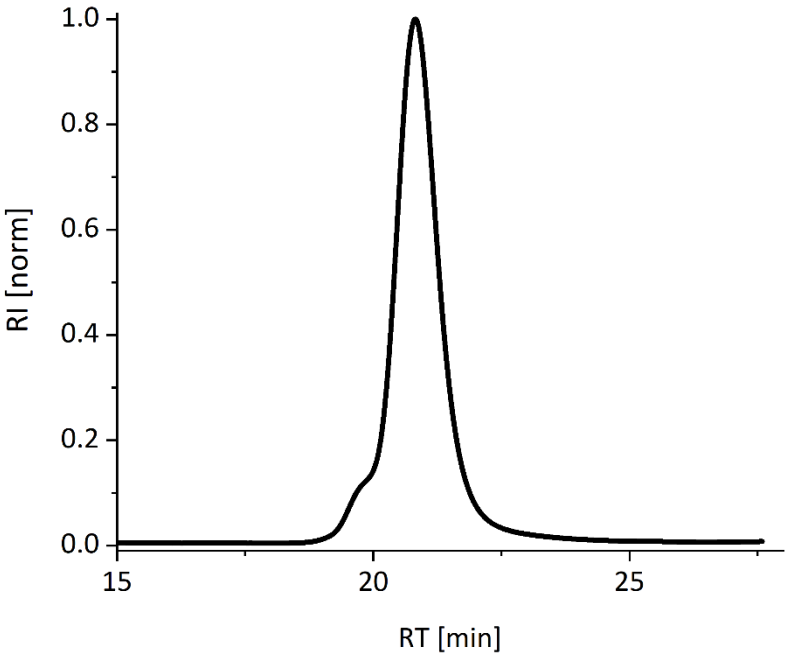

Figure A 71: GPC chromatogram (RI detector) of $S_{0.39}$-$MH_{0.61}$-*35*.

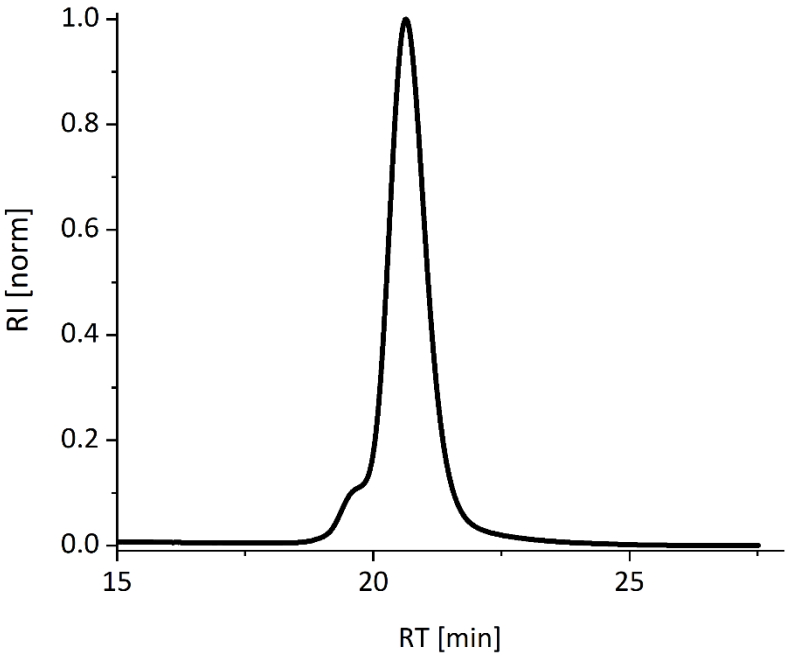

Figure A 72: GPC chromatogram (RI detector) of $S_{0.43}$-$MH_{0.57}$-*40*.

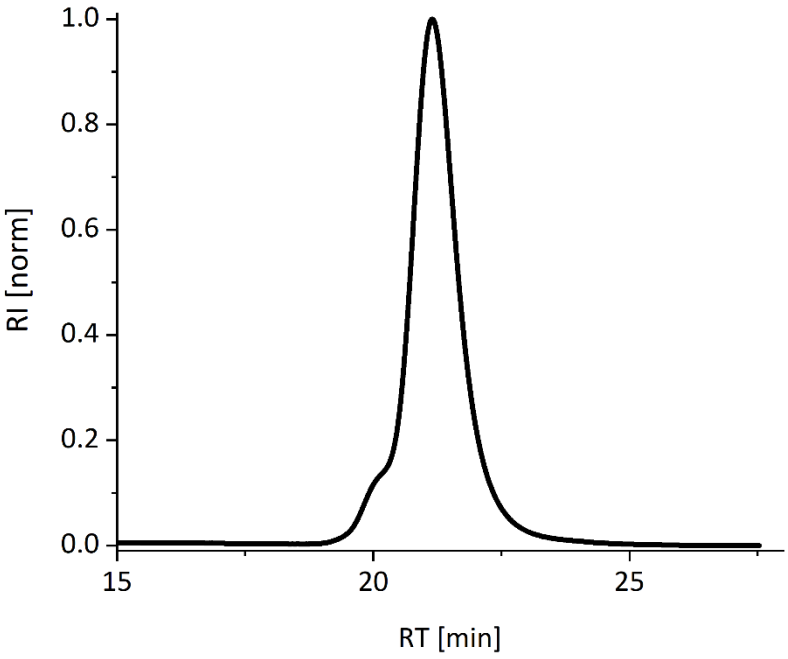

Figure A 73: GPC chromatogram (RI detector) of $S_{0.28}$-$MH_{0.72}$-*29*.

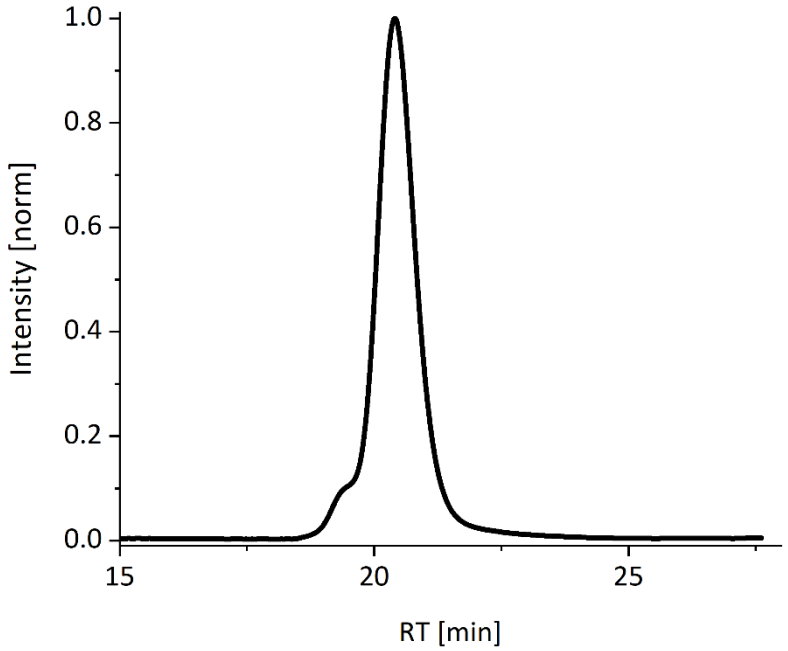

Figure A 74: GPC chromatogram (RI detector) of $S_{0.50}$-$MH_{0.50}$-*45*.

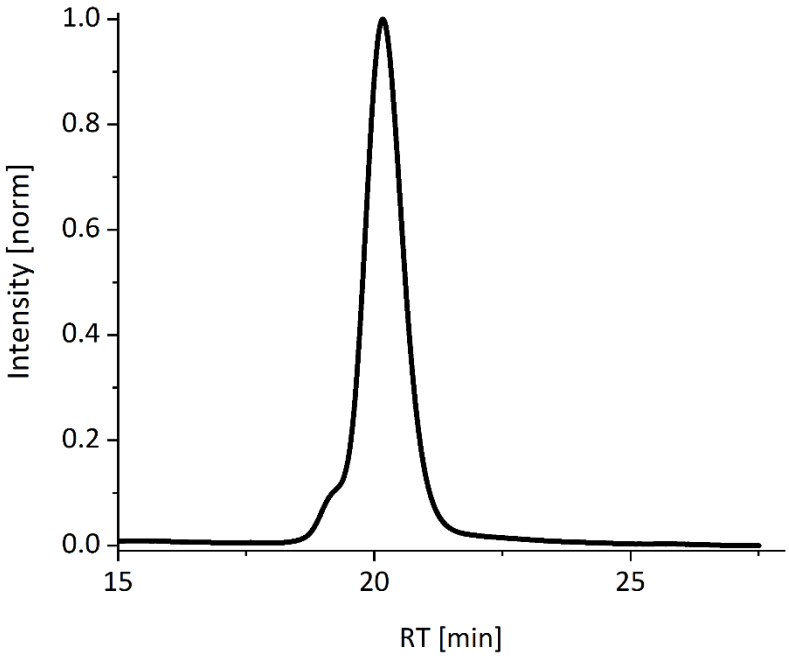

Figure A 75: GPC chromatogram (RI detector) of $S_{0.56}$-$MH_{0.44}$-*52*.

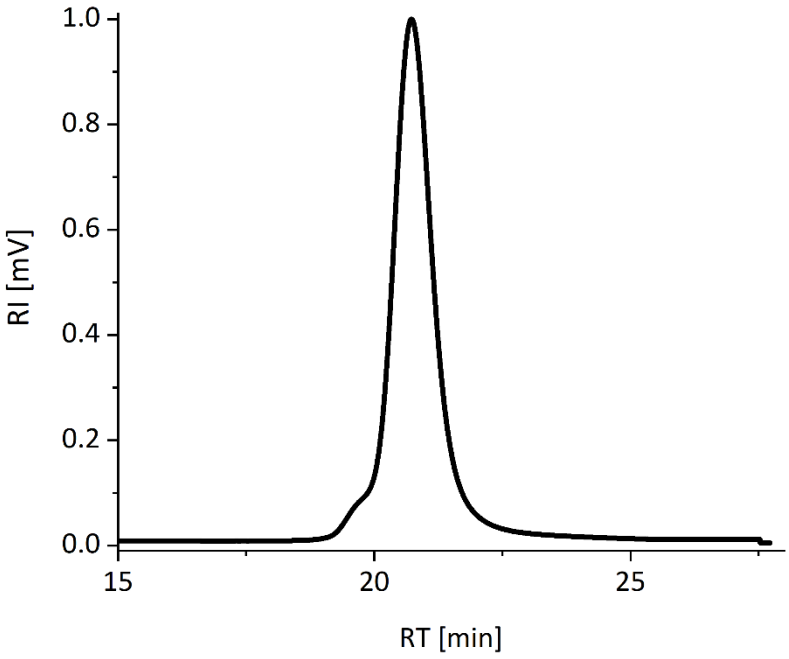

Figure A 76: GPC chromatogram (RI detector) of $S_{0.68}$-$MH_{0.32}$-*33*.

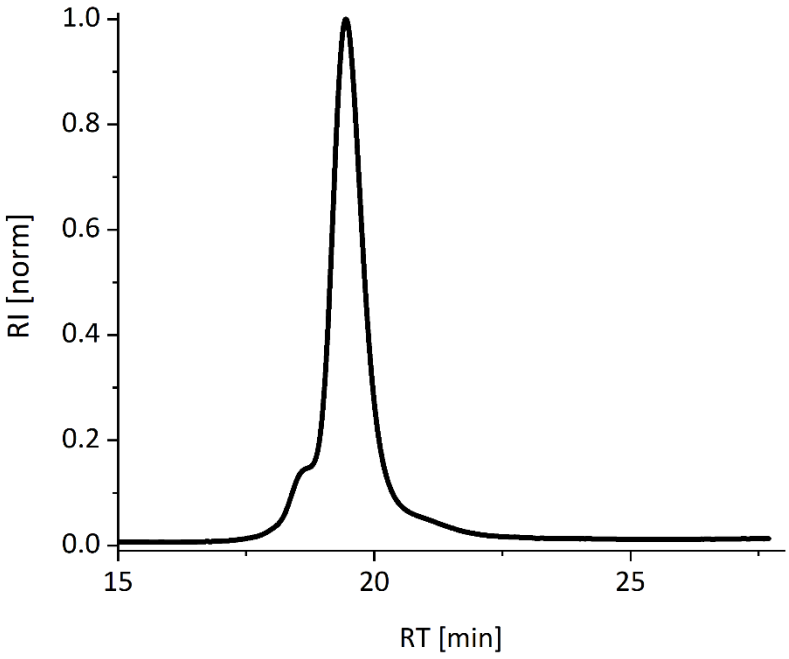

Figure A 77: GPC chromatogram (RI detector) of $S_{0.52}$-$MH_{0.48}$-*67*.

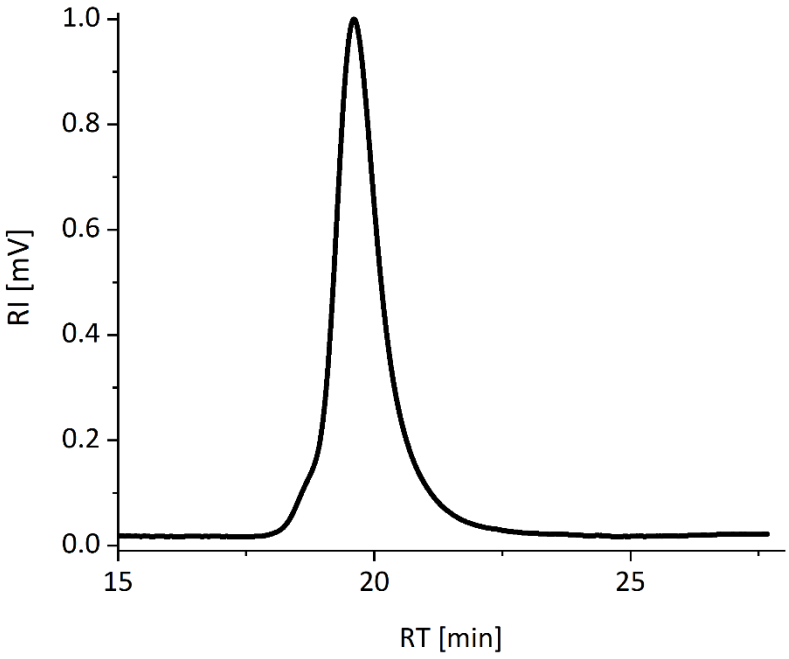

Figure A 78: GPC chromatogram (RI detector) of $S_{0.42}$-$MH_{0.58}$-*57*.

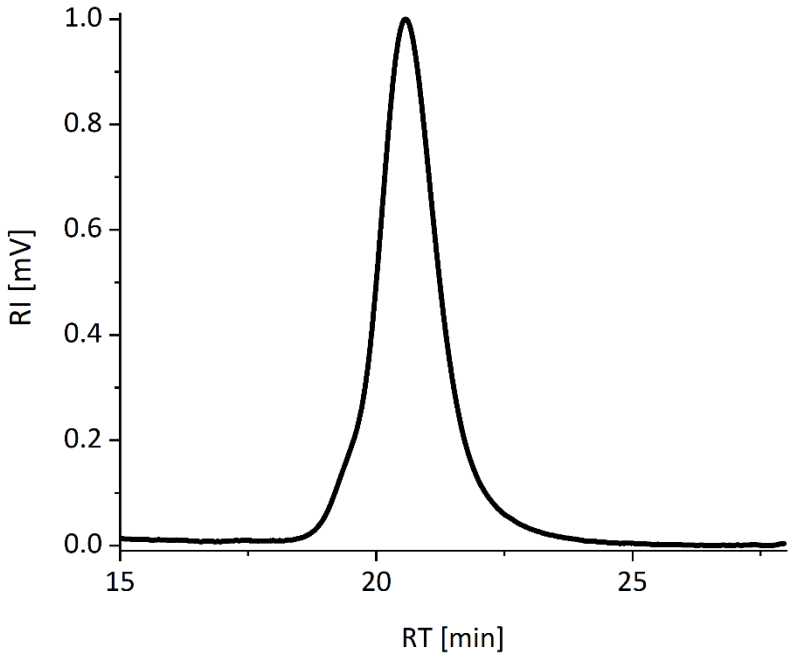

Figure A 79: GPC chromatogram (RI detector) of $S_{0.09}$-$MH_{0.91}$-*39*.

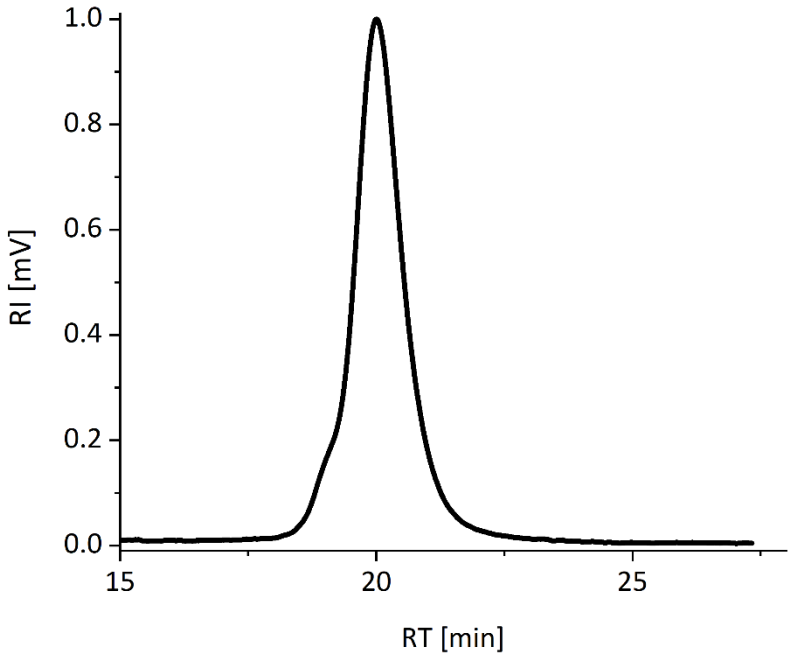

Figure A 80: GPC chromatogram (RI detector) of $S_{0.31}$-$MH_{0.69}$-*48*.

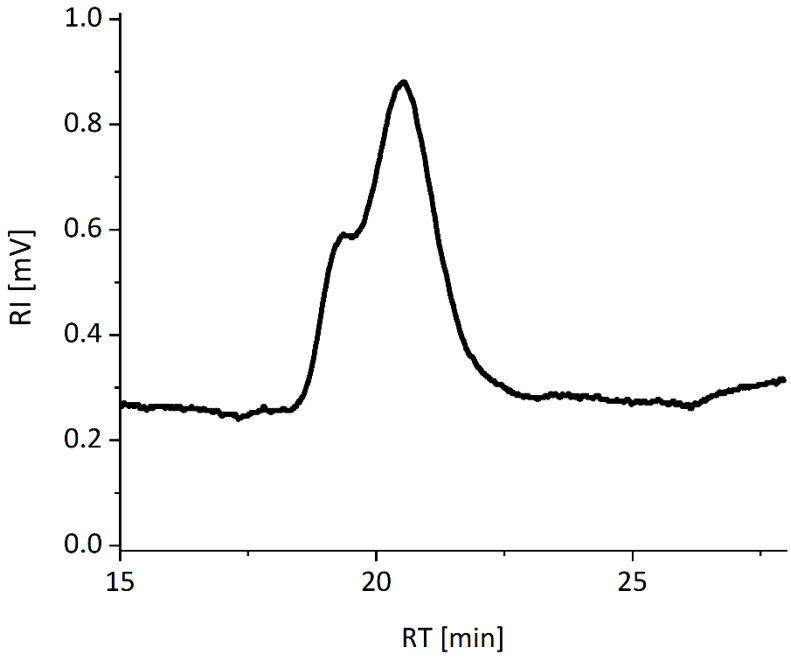

Figure A 81: GPC chromatogram (RI detector) of $S_{0.16}$-$MH_{0.84}$-*45*.

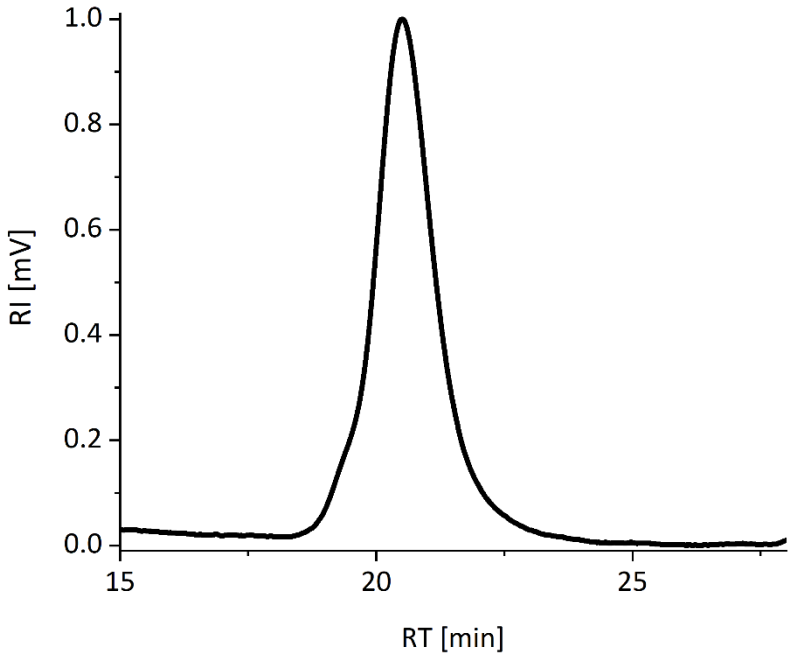

Figure A 82: GPC chromatogram (RI detector) of $S_{0.12}$-$MH_{0.88}$-*40*.

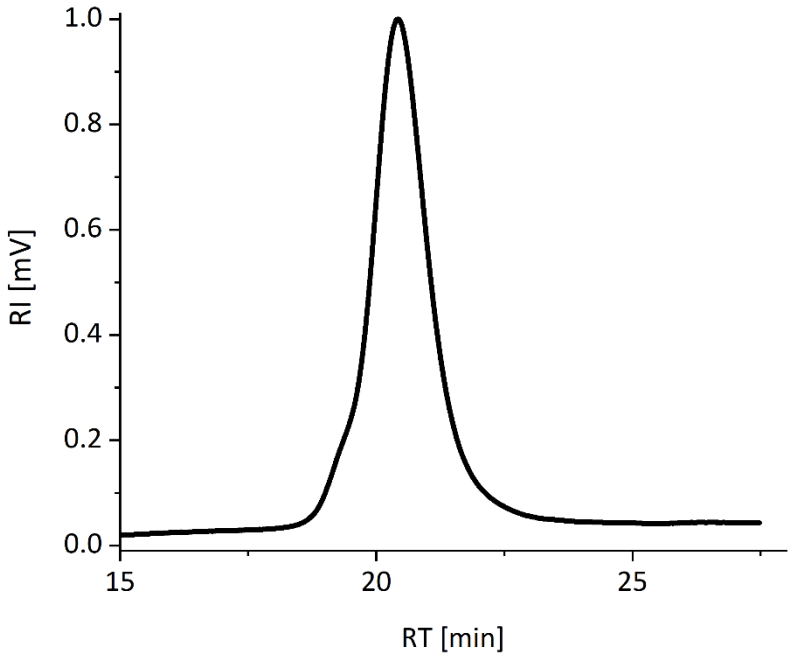

Figure A 83: GPC chromatogram (RI detector) of $S_{0.16}$-$MH_{0.84}$-*43*.

7.2.3 Exemplary Synthesis of functionalized BCPs:

$S_{0.53}$-$MH_{0.47}$-*94* (250 mg, MW = 93566, 2.67 µmol, 207 µmol OH-groups) was added to a Schlenk flask. After flushing with nitrogen, dry DCM (19 mL) was added. After dissolving, NEt_3 (592 µL, 430 mg, 4.24 mmol, 20 eq.) was added, the solution was cooled to 0 °C and methacryloyl chloride (348 µL, 389 mg, 3.74 mmol, 18 eq.) was added slowly under stirring. After stirring at 0°C to RT for 16-72 h, most of the DCM was removed in vacuo. MeCN (65 mL) was added and the mixture was poured into $NaHCO_{3\,aq.}$(5%, 130 mL). After extracting with DCM (3 x 65 mL) the united organic fractions were dried over Na_2SO_4, the solvent was removed in vacuo and the washing step was repeated if NEt_3HCl was still present. After precipitation in Et_2O, $S_{0.53}$-$MH^*_{0.47}$-*94* was obtained as a solid.

^{1}H NMR 600 MHz (CD_2Cl_2): δ [ppm] = 7.80 (m), 7.47 (m), 7.31 (m), 7.28 - 6.31 (m), 6.12 (bs), 5.63 (bs), 4.32 (bs), 4.17 (bs), 3.56 (s), 2.14 - 0.63 (m).

Table A2: Table detailing the reaction conditions and analytical data of the BCPs.

Polymer	MacroCTA	Styrene:MacroCTA:AIBN	T [min]	M_n(GPC)	Đ	Funct. polymer
$S_{0.68}$-$MH_{0.32}$-*33*	macroCTA-*9*	5000:1:0.2	80	32524	1.06	$S_{0.68}$-$MH^*_{0.32}$-*33*
$S_{0.39}$-$MH_{0.61}$-*35*	macroCTA-*19*	3720:1:0.2	40	35156	1.09	-
$S_{0.43}$-$MH_{0.57}$-*40*	macroCTA-*19*	3720:1:0.2	40	39637	1.08	-
$S_{0.28}$-$MH_{0.72}$-*29*	macroCTA-*19*	2000:1:0.2	40	29291	1.09	$S_{0.28}$-$MH^*_{0.72}$-*29*
$S_{0.50}$-$MH_{0.50}$-*45*	macroCTA-*19*	6150:1:0.2	60	45136		$S_{0.50}$-$MH^*_{0.50}$-*45*
$S_{0.56}$-$MH_{0.44}$-*52*	macroCTA-*19*	10000:1:0.2	60	52082	1.07	$S_{0.56}$-$MH^*_{0.44}$-*52*
$S_{0.75}$-$MH_{0.25}$-*66*	macroCTA-*21*	5000:1:0.2	120	65769	1.20	$S_{0.75}$-$MH^*_{0.25}$-*66*
$S_{0.45}$-$MH_{0.55}$-*42*	macroCTA-*23*	3720:1:0.2	40	42064	1.11	$S_{0.45}$-$MH^{50\%*}_{0.55}$-*42*
$S_{0.66}$-$MH_{0.34}$-*70*	macroCTA-*23*	8000:1:0.2	120	69535	1.10	$S_{0.66}$-$MH^*_{0.34}$-*70*
$S_{0.54}$-$MH_{0.46}$-*45*	macroCTA-*22*	3720:1:0.2	60	45272	1.18	-
$S_{0.52}$-$MH_{0.48}$-*67*	macroCTA-*22*	7000:1:0.2	120	66991	1.10	$S_{0.52}$-$MH^*_{0.48}$-*67*
$S_{0.45}$-$MH_{0.55}$-*102*	macroCTA-*48*	6150:1:0.2	90	101536	1.13	-
$S_{0.50}$-$MH^*_{0.50}$-*91*	macroCTA-*48*	6150:1:0.2	90	91421	1.14	$S_{0.50}$-$MH^*_{0.50}$-*91*
$S_{0.46}$-$MH_{0.54}$-*81*	macroCTA-*39*	6150:1:0.2	90	81005	1.14	$S_{0.46}$-$MH^*_{0.54}$-*81*, $S_{0.46}$-$MH^{50\%*}_{0.54}$-*81*
$S_{0.42}$-$MH_{0.58}$-*89*	macroCTA-*39*	6150:1:0.2	90	89172	1.16	$S_{0.42}$-$MH^*_{0.58}$-*89*
$S_{0.37}$-$MH_{0.63}$-*65*	macroCTA-*38*	6150:1:0.2	90	65036	1.09	$S_{0.37}$-$MH^*_{0.63}$-*65*
$S_{0.54}$-$MH_{0.46}$-*45*	macroCTA-*38*	11000:1:0.2	120	93566	1.10	$S_{0.53}$-$MH^*_{0.47}$-*94*

$S_{0.42}$-$MH_{0.58}$-*57*	macroCTA-*34*	10000:1:0.2	120	56861	1.11	$S_{0.42}$-$MH^*_{0.58}$-*57*
$S_{0.09}$-$MH_{0.91}$-*39*	macroCTA-*34*	2500:1:0.2	23	38743	1.13	
$S_{0.31}$-$MH_{0.69}$-*48*	macroCTA-*34*	5000:1:0.2	90	47659	1.09	$S_{0.31}$-$MH^*_{0.69}$-*48*
$S_{0.12}$-$MH_{0.88}$-*40*	macroCTA-*34*	2400:1:0.2	28	39858	1.13	
$S_{0.16}$-$MH_{0.84}$-*45*	macroCTA-*34*	13200:1:0.2	120	45079	1.23	
$S_{0.16}$-$MH_{0.84}$-*43*	macroCTA-*34*	3500:1:0.2	30	42621	1.13	$S_{0.16}$-$MH^*_{0.84}$-*43*
$S_{0.27}$-$MH_{0.73}$-*70*	macroCTA-*43*	3720:1:0.2	60	70191	1.13	$S_{0.27}$-$MH^*_{0.73}$-*70*
$S_{0.28}$-$MH_{0.72}$-*67*	macroCTA-*43*	3720:1:0.2	90	67188	1.13	$S_{0.28}$-$MH^*_{0.72}$-*67*

NMR spectra of functionalized BCPs

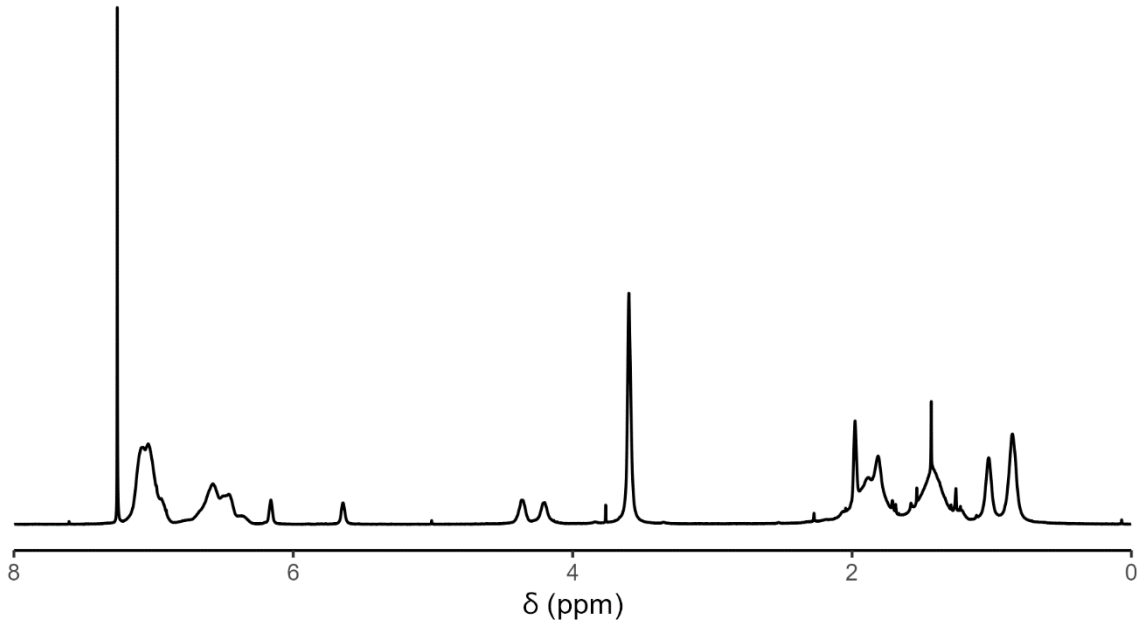

Figure A84: ^{1}H NMR spectrum of $S_{0.50}$-MH*$_{0.50}$-*91* in $CDCl_3$.

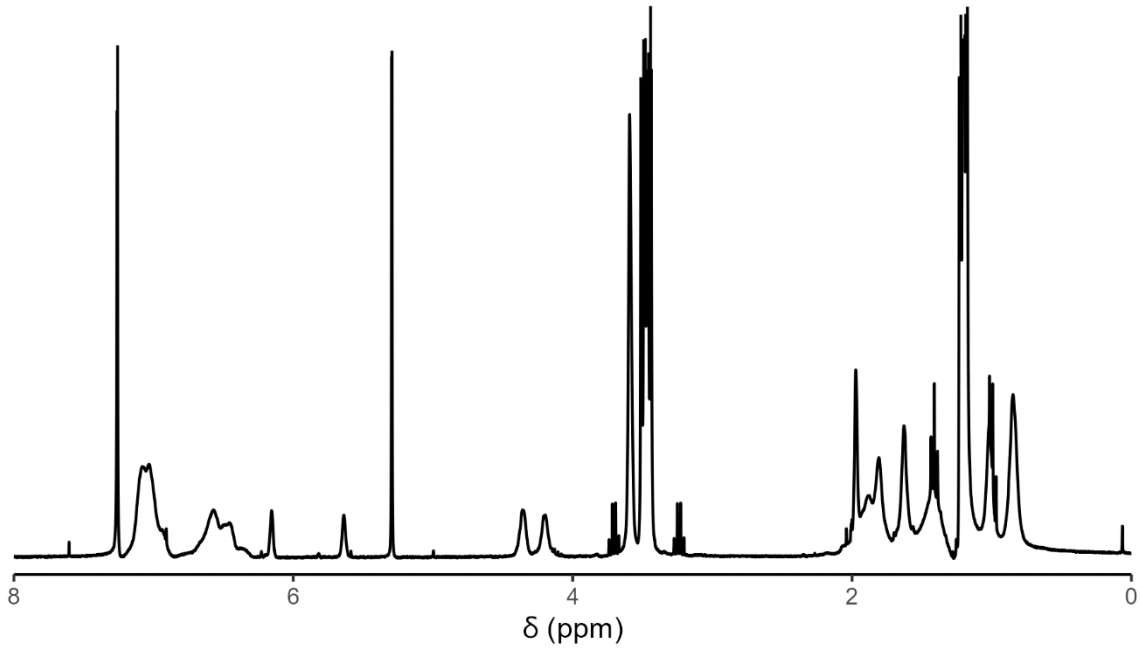

Figure A85: ^{1}H NMR spectrum of $S_{0.46}$-MH*$_{0.54}$-*81* in $CDCl_3$.

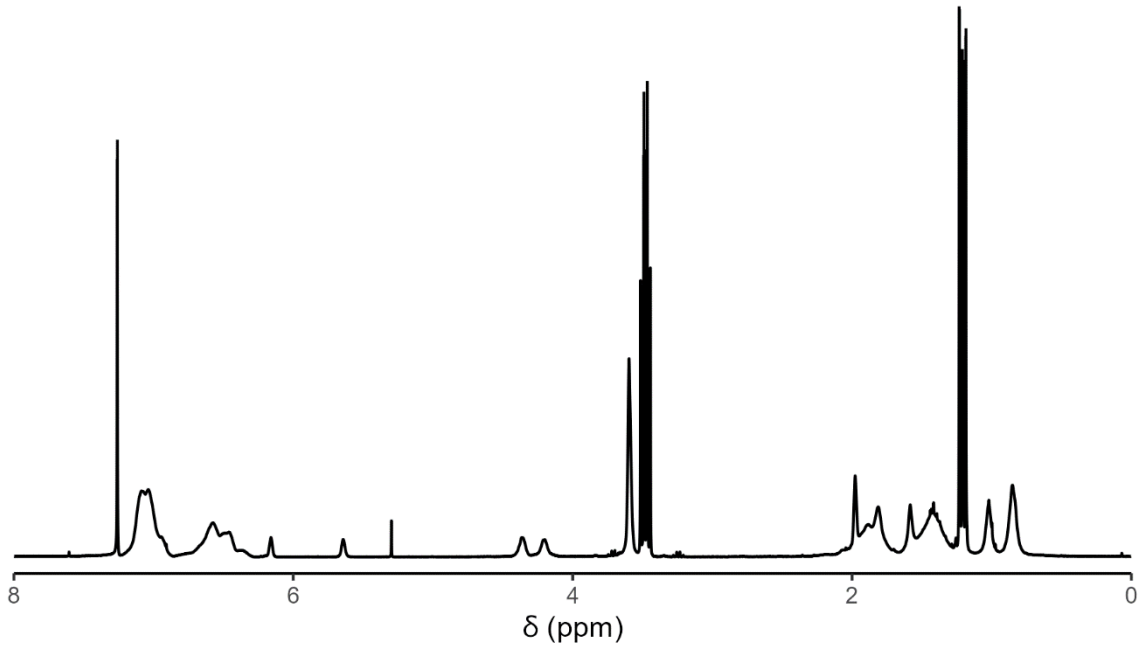

Figure A86: ^{1}H NMR spectrum of $S_{0.66}$-MH*$_{0.34}$-*70* in $CDCl_3$.

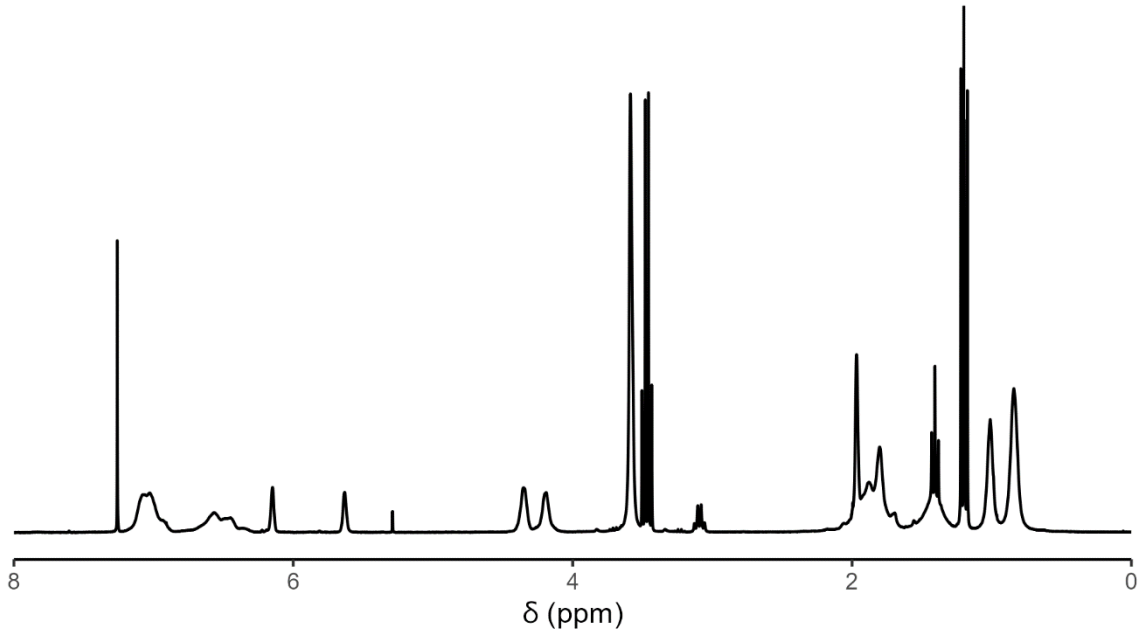

Figure A87: ^{1}H NMR spectrum of $S_{0.27}$-MH*$_{0.73}$-*70* in $CDCl_3$.

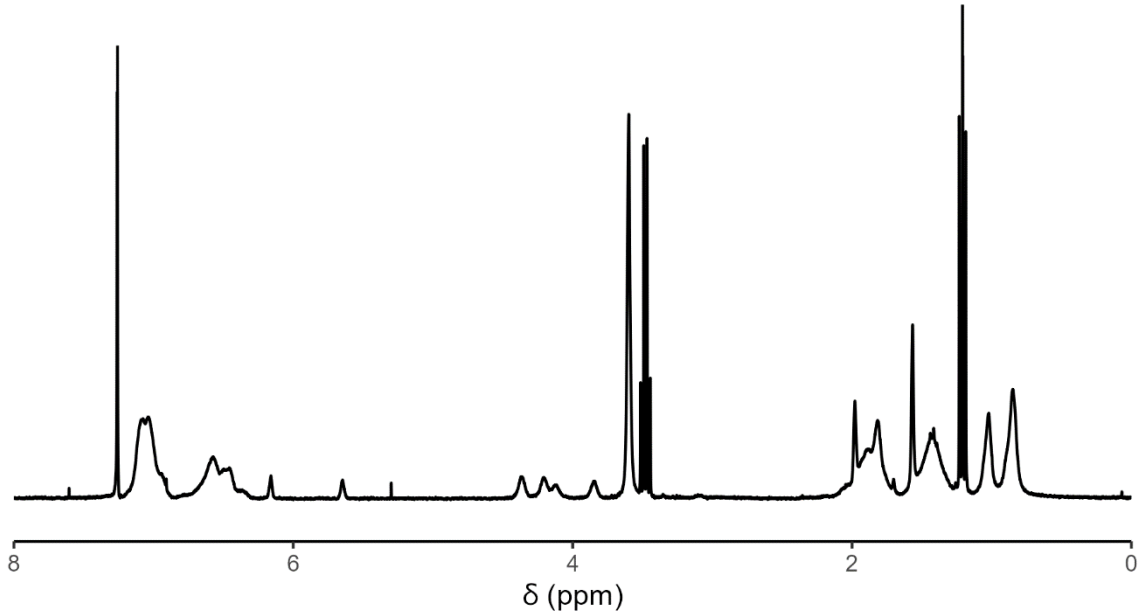

Figure A88: ^{1}H NMR spectrum of $S_{0.46}$-MH$^{50\%}$*$_{0.54}$-*81* in $CDCl_3$.

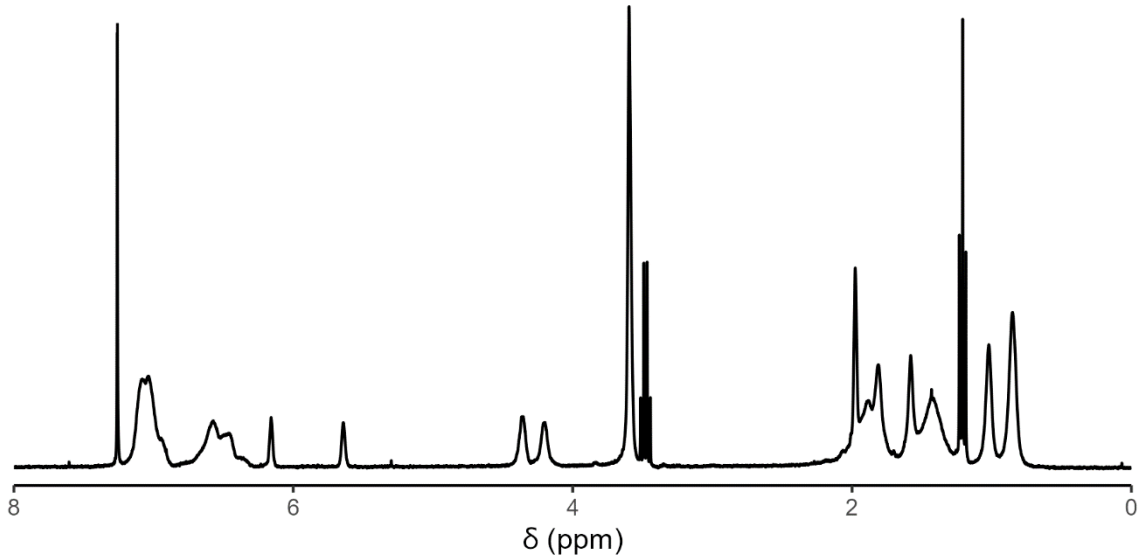

Figure A89: ^{1}H NMR spectrum of $S_{0.42}$-MH*$_{0.58}$-*89* in $CDCl_3$.

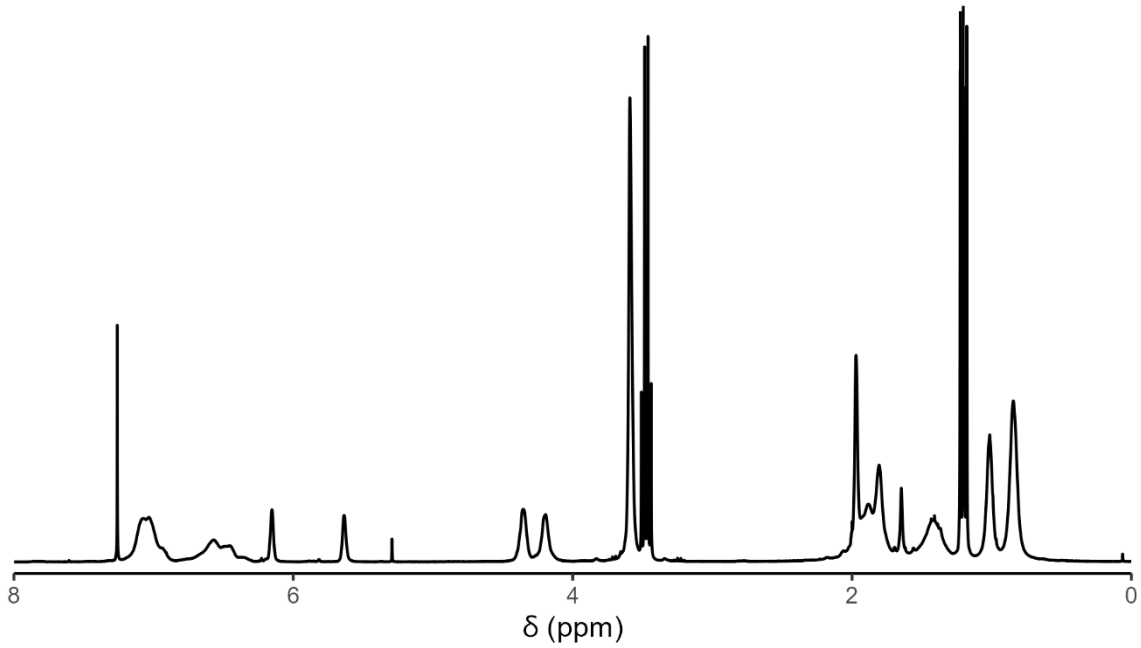

Figure A90: ^{1}H NMR spectrum of $S_{0.28}$-MH*$_{0.72}$-*29* in $CDCl_3$.

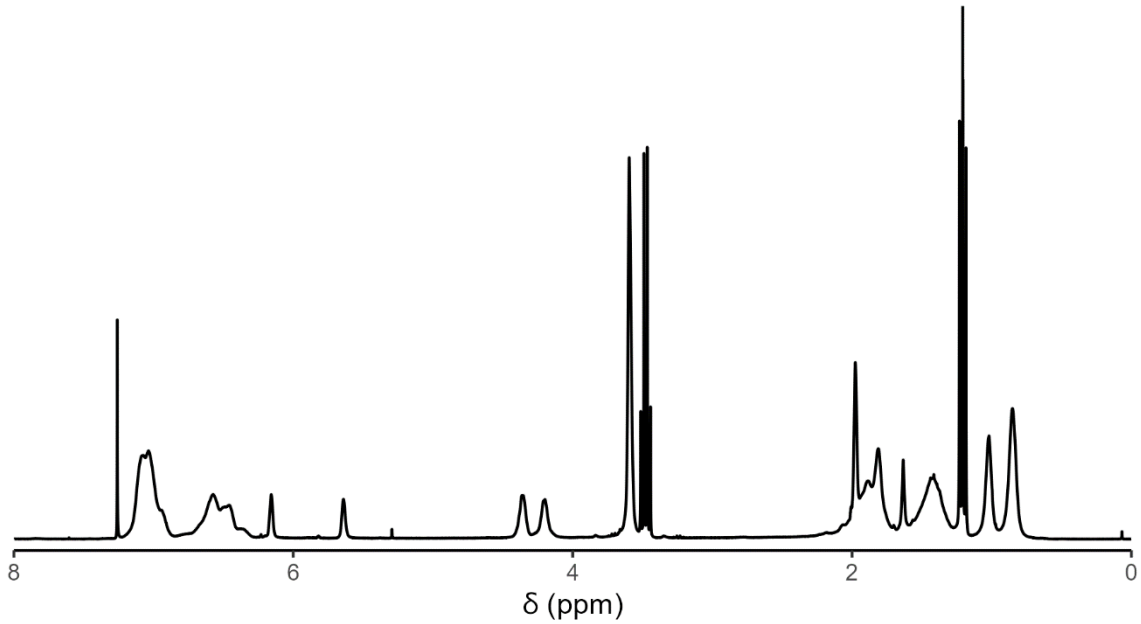

Figure A91: ^{1}H NMR spectrum of $S_{0.50}$-MH*$_{0.50}$-*45* in $CDCl_3$.

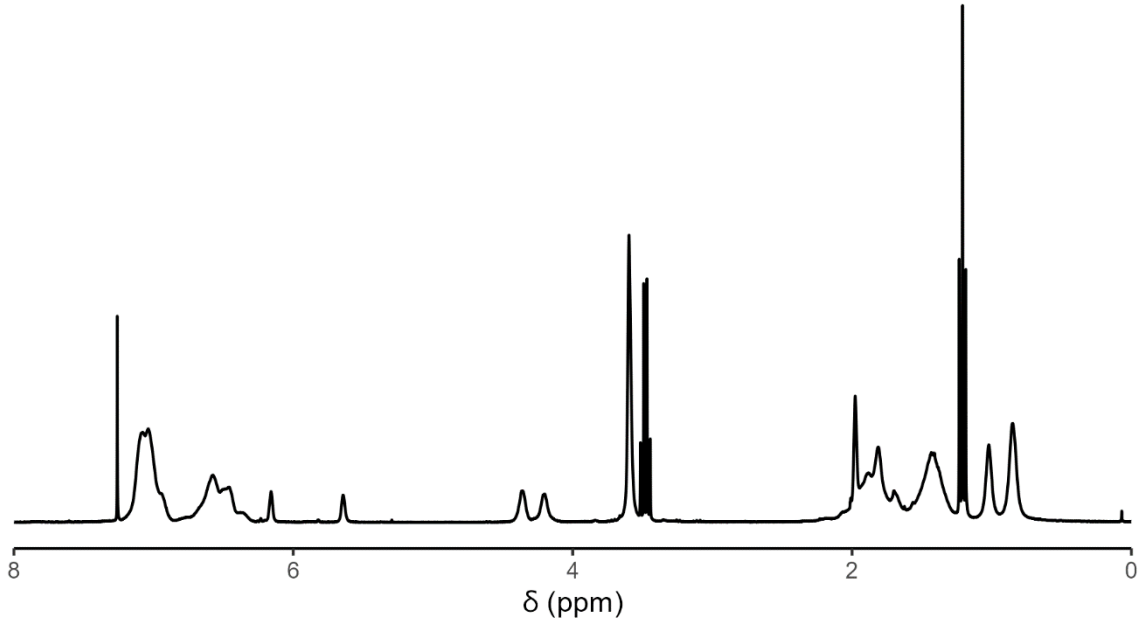

Figure A92: ^{1}H NMR spectrum of $S_{0.56}$-MH*$_{0.44}$-*52* in $CDCl_3$.

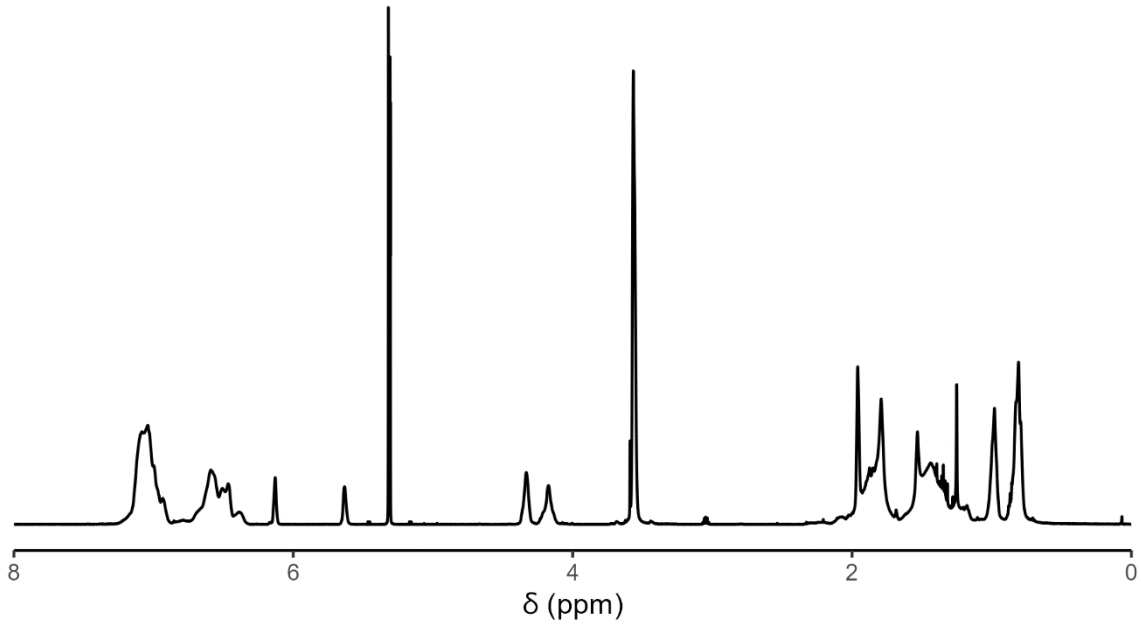

Figure A93: ^{1}H NMR spectrum of $S_{0.53}$-MH*$_{0.47}$-*94* in CD_2Cl_2.

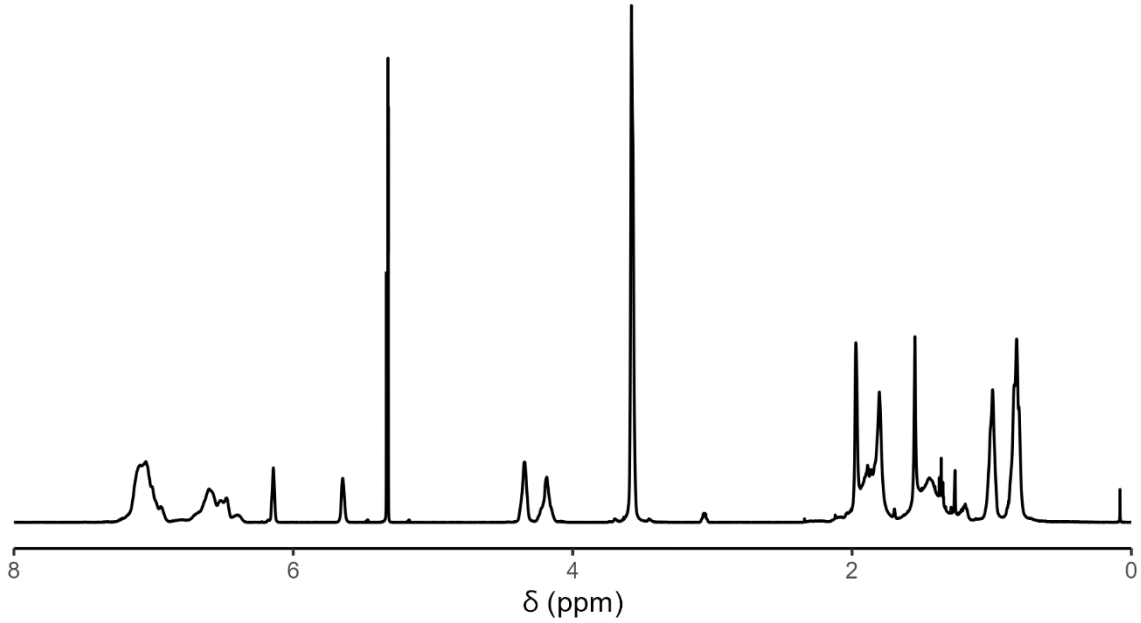

Figure A94: ^{1}H NMR spectrum of $S_{\mathbf{0.37}}$-MH*$_{\mathbf{0.63}}$-*65* in CD_2Cl_2.

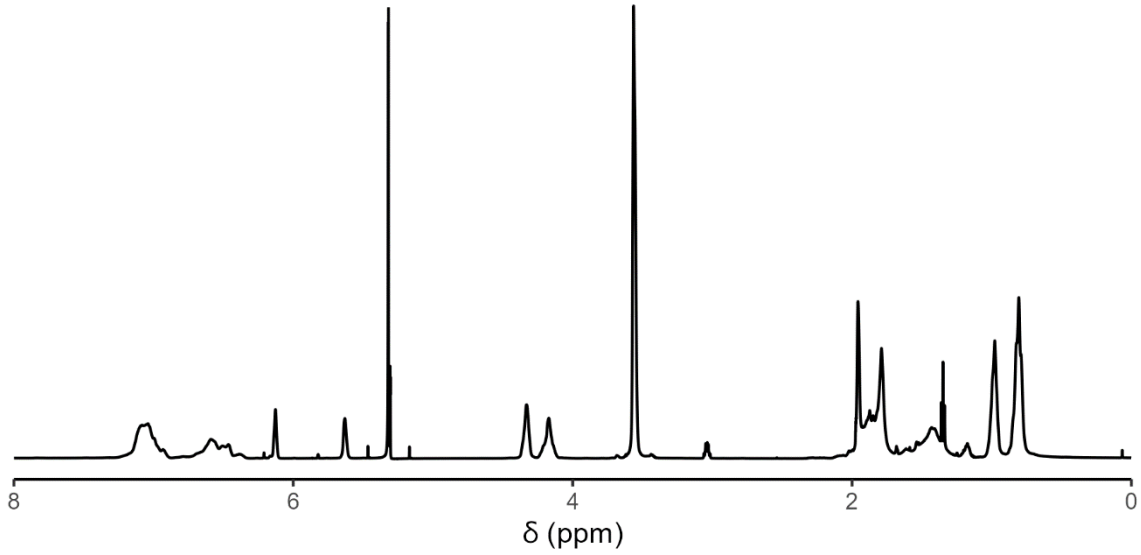

Figure A95: ^{1}H NMR spectrum of $S_{\mathbf{0.28}}$-MH*$_{\mathbf{0.72}}$-*67* in CD_2Cl_2.

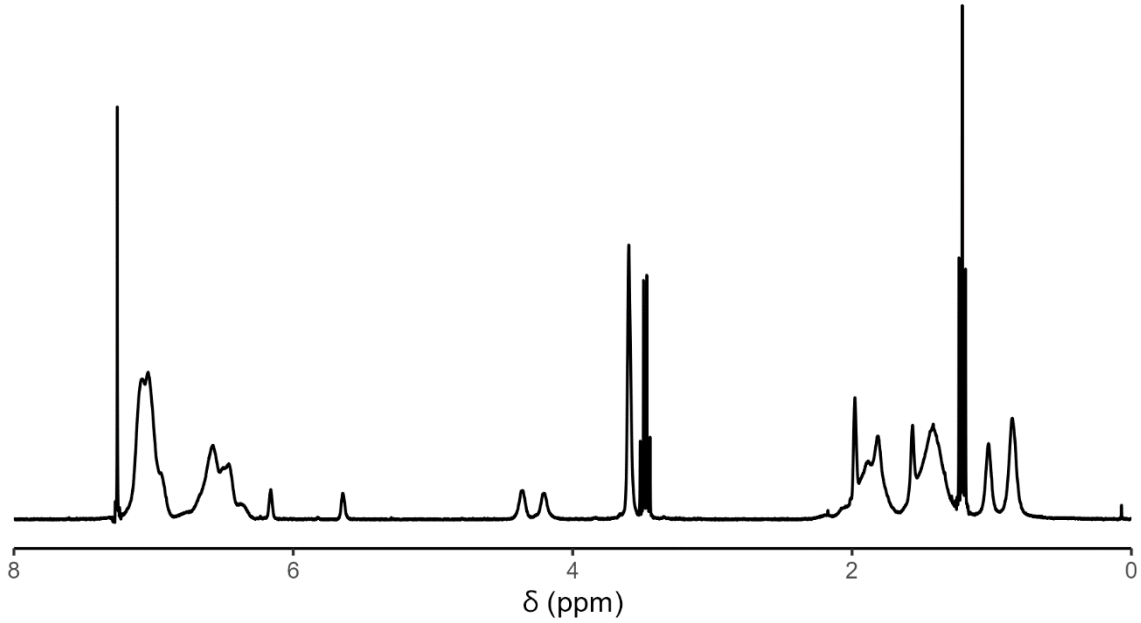

Figure A96: ^{1}H NMR spectrum of $S_{0.75}$-MH*$_{0.25}$-*66* in $CDCl_3$.

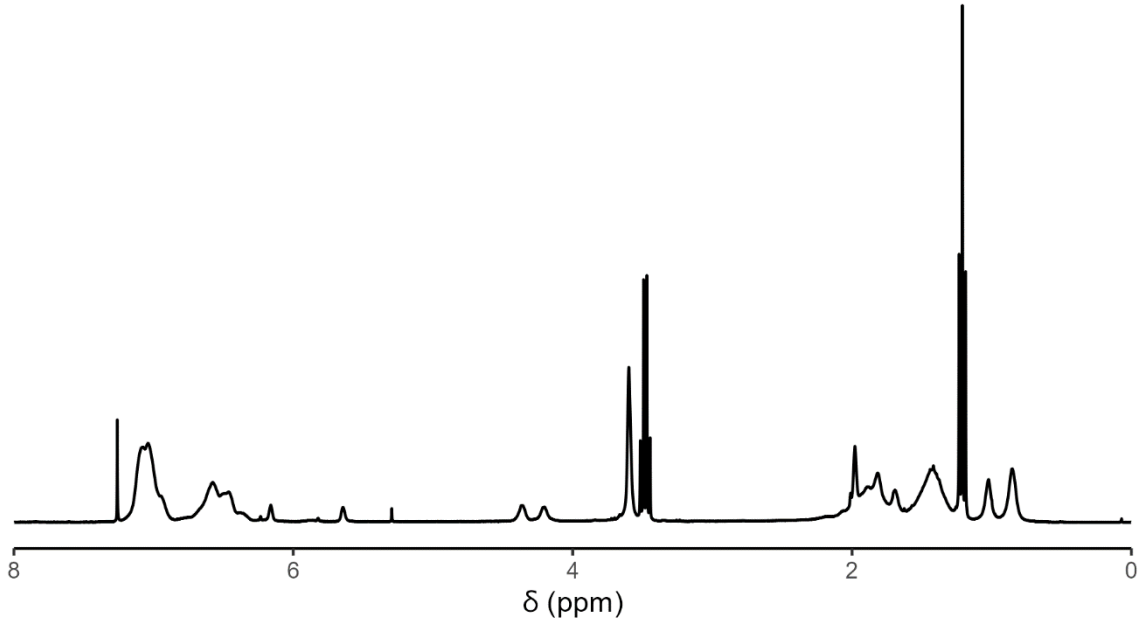

Figure A97: ^{1}H NMR spectrum of $S_{0.68}$-MH*$_{0.32}$-*33* in $CDCl_3$.

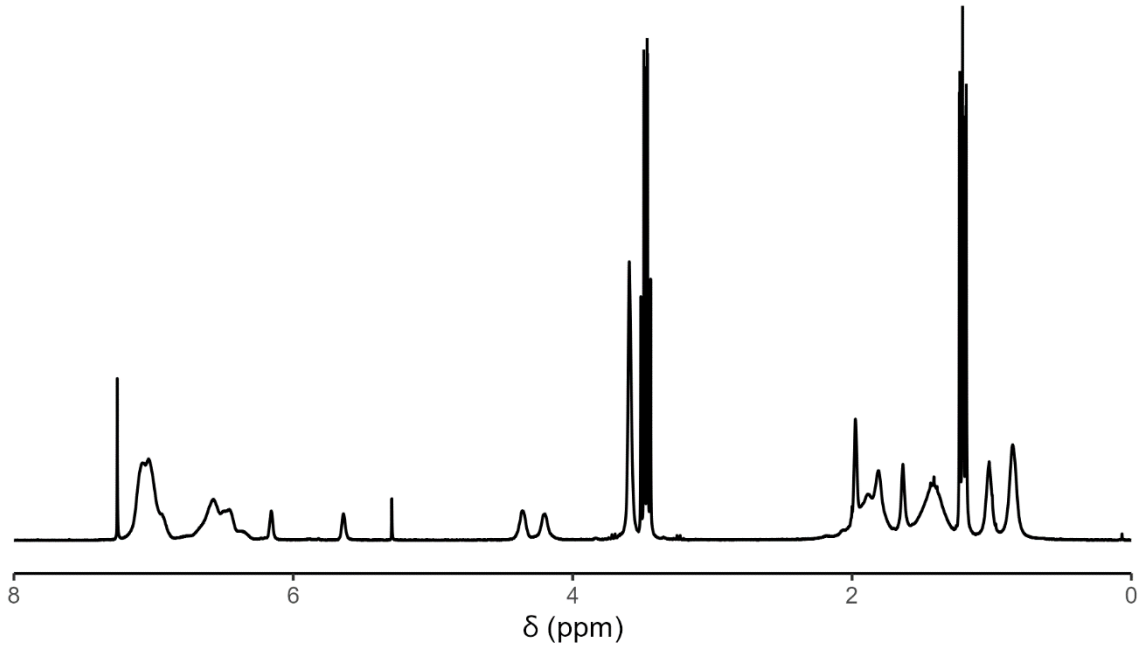

Figure A98: ^{1}H NMR spectrum of $S_{0.52}$-MH*$_{0.48}$-*67* in $CDCl_3$.

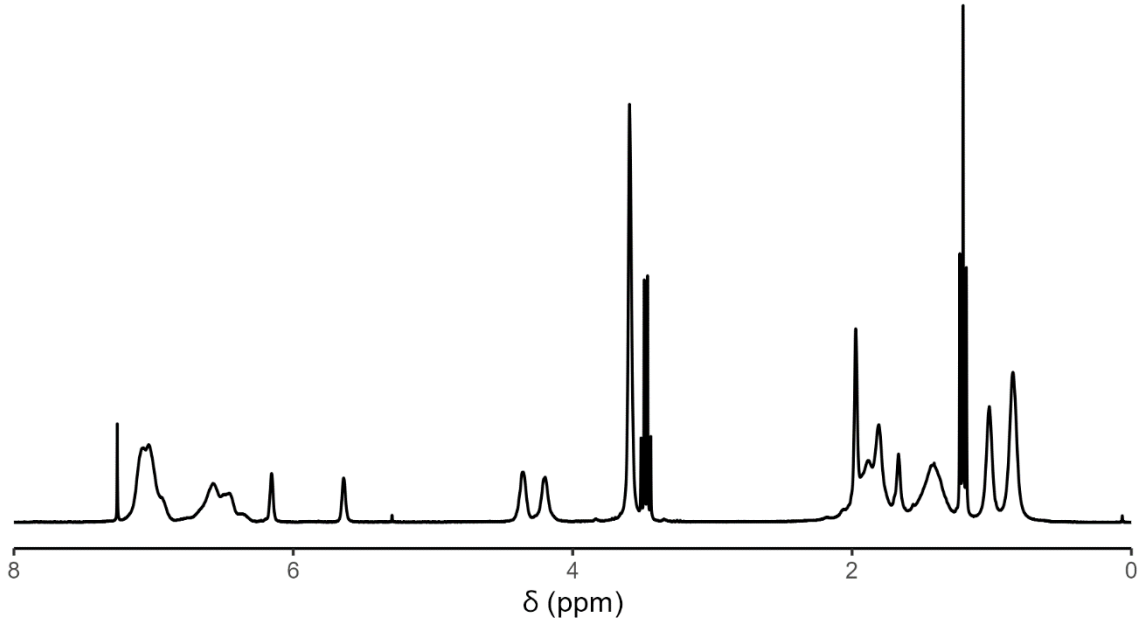

Figure A99: ^{1}H NMR spectrum of $S_{0.42}$-MH*$_{0.58}$-*57* in $CDCl_3$.

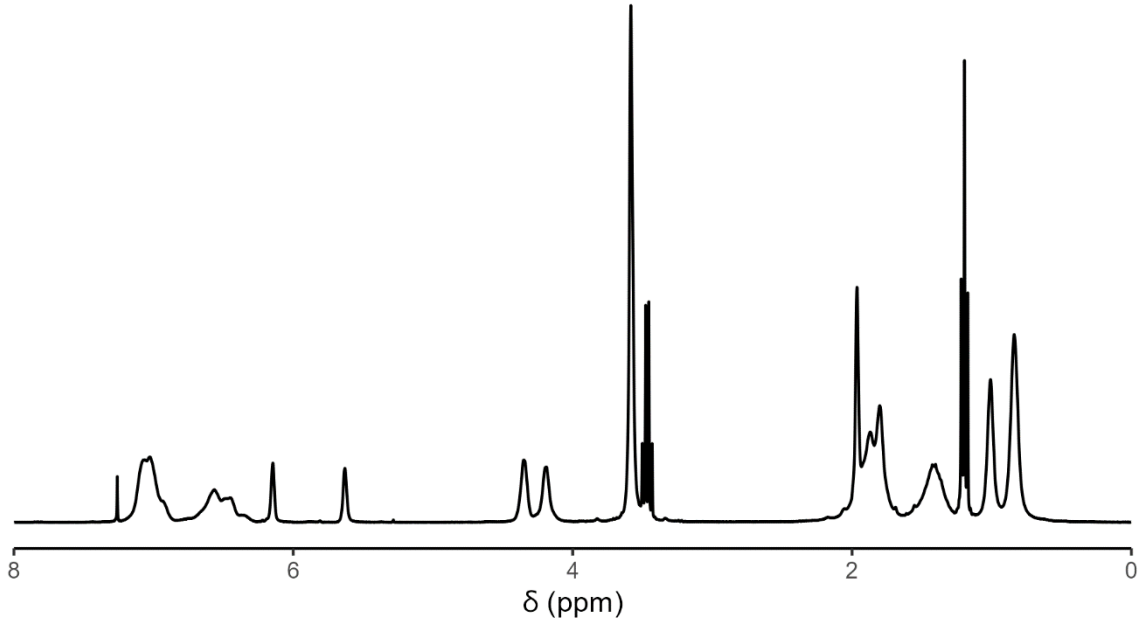

Figure A100: ^{1}H NMR spectrum of $S_{0.31}$-MH*$_{0.69}$-*48* in $CDCl_3$.

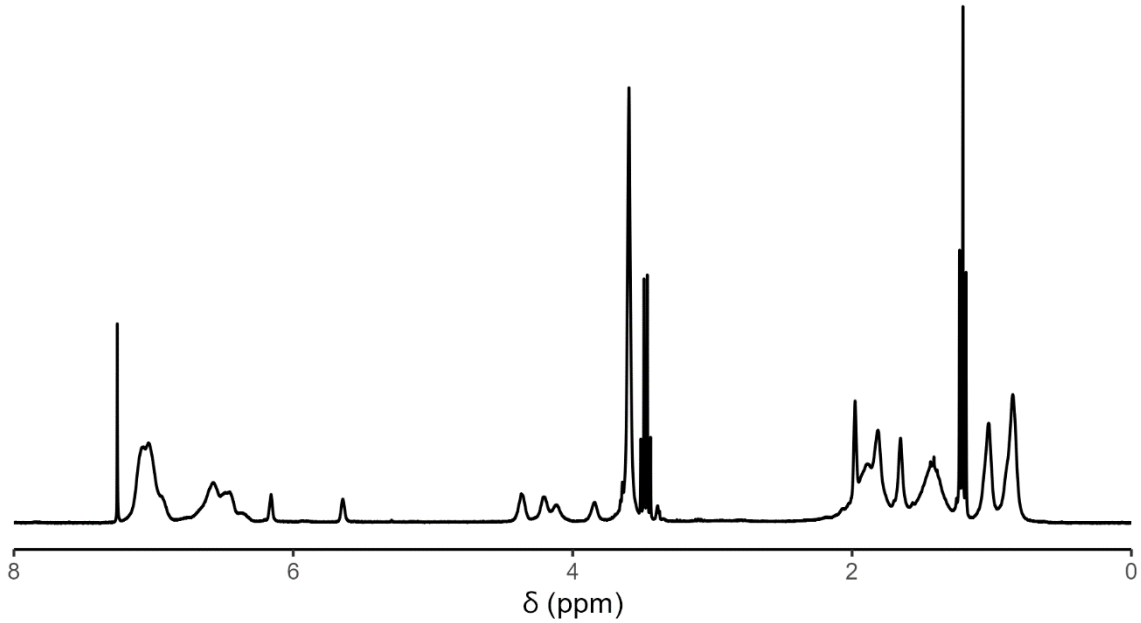

Figure A101: ^{1}H NMR spectrum of $S_{0.45}$-MH*$_{0.55}$-*42* in $CDCl_3$.

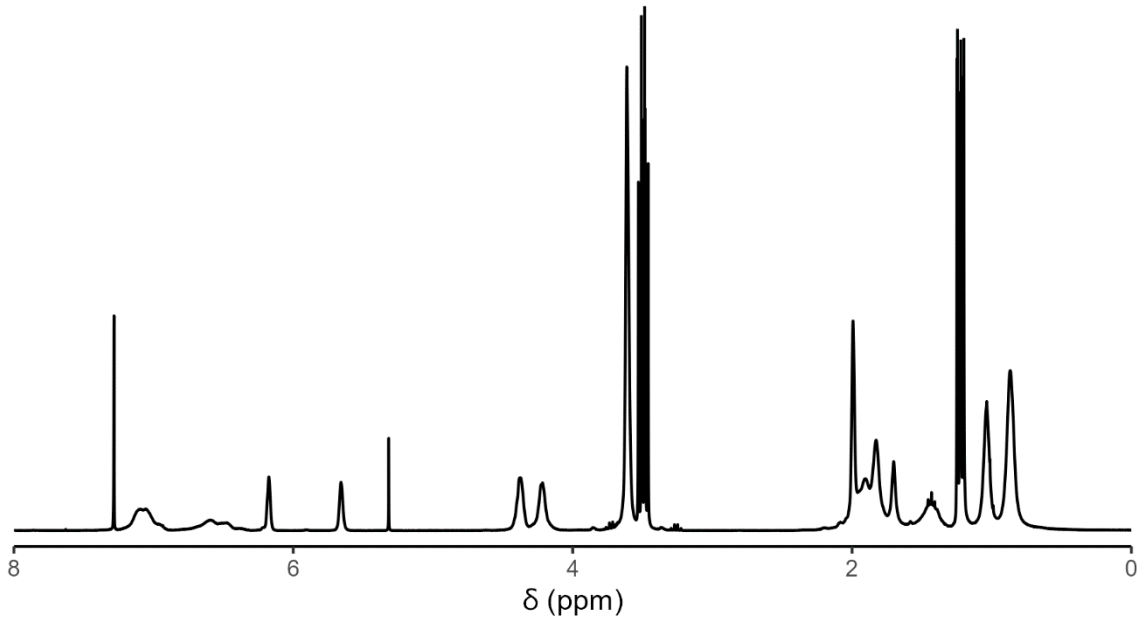

Figure A102: ^{1}H NMR spectrum of $S_{0.16}$-$MH_{0.84}$-*43* in $CDCl_3$.

7.3 Characterization of the self-assembled polymers

Calculation of d_{SAXS} for cylindrical samples:

$d = 2/\mathrm{sqrt}(3) * d_{\text{calculated from q}}$

SEM images and SAXS spectra

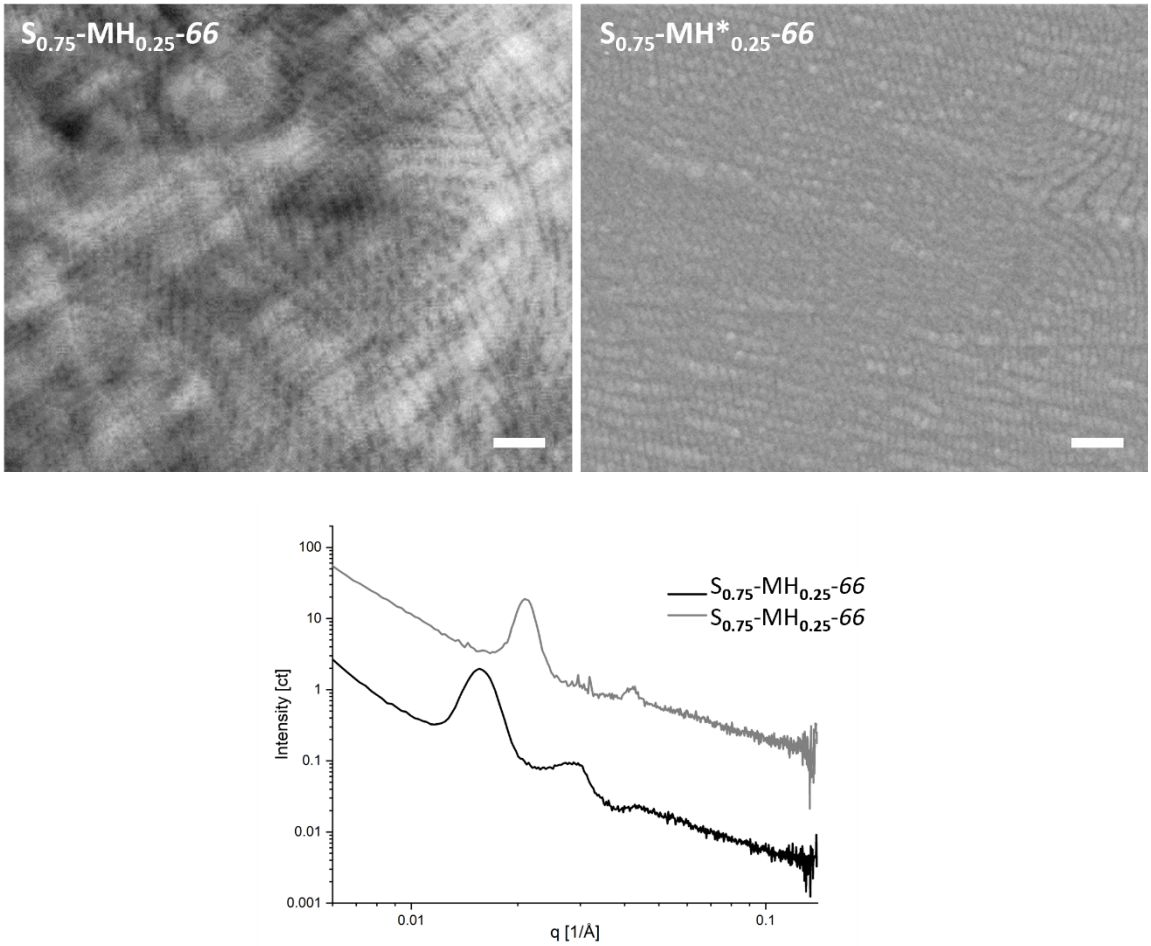

Figure A103: SEM images and SAXS spectra for $S_{0.75}$-$MH_{0.25}$-*66* and $S_{0.75}$-$MH_{0.25}$-*66*. Scale bars = 200 nm.

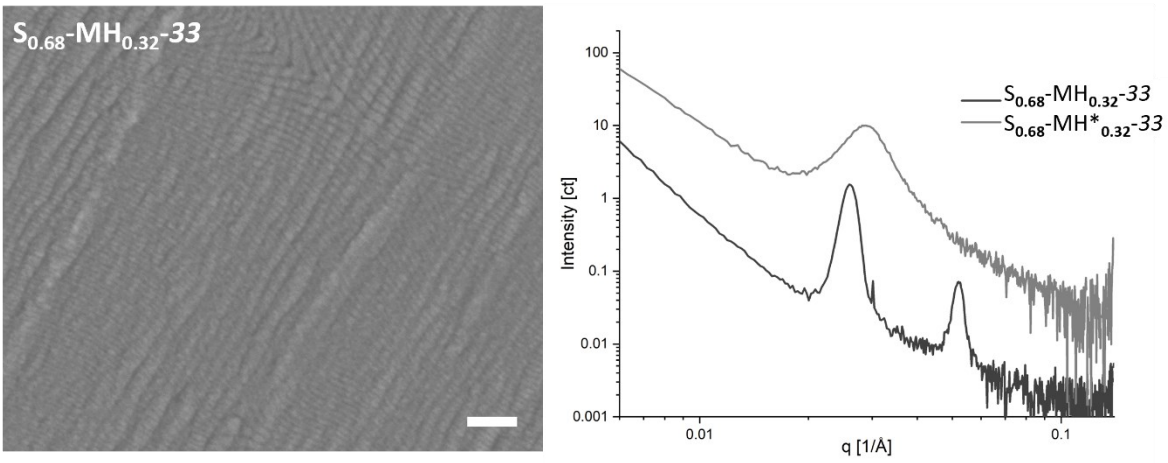

Figure A104: SEM images and SAXS spectra for $S_{0.68}$-$MH_{0.32}$-*33* and $S_{0.68}$-$MH^*_{0.32}$-*33*. Scale bar = 200 nm.

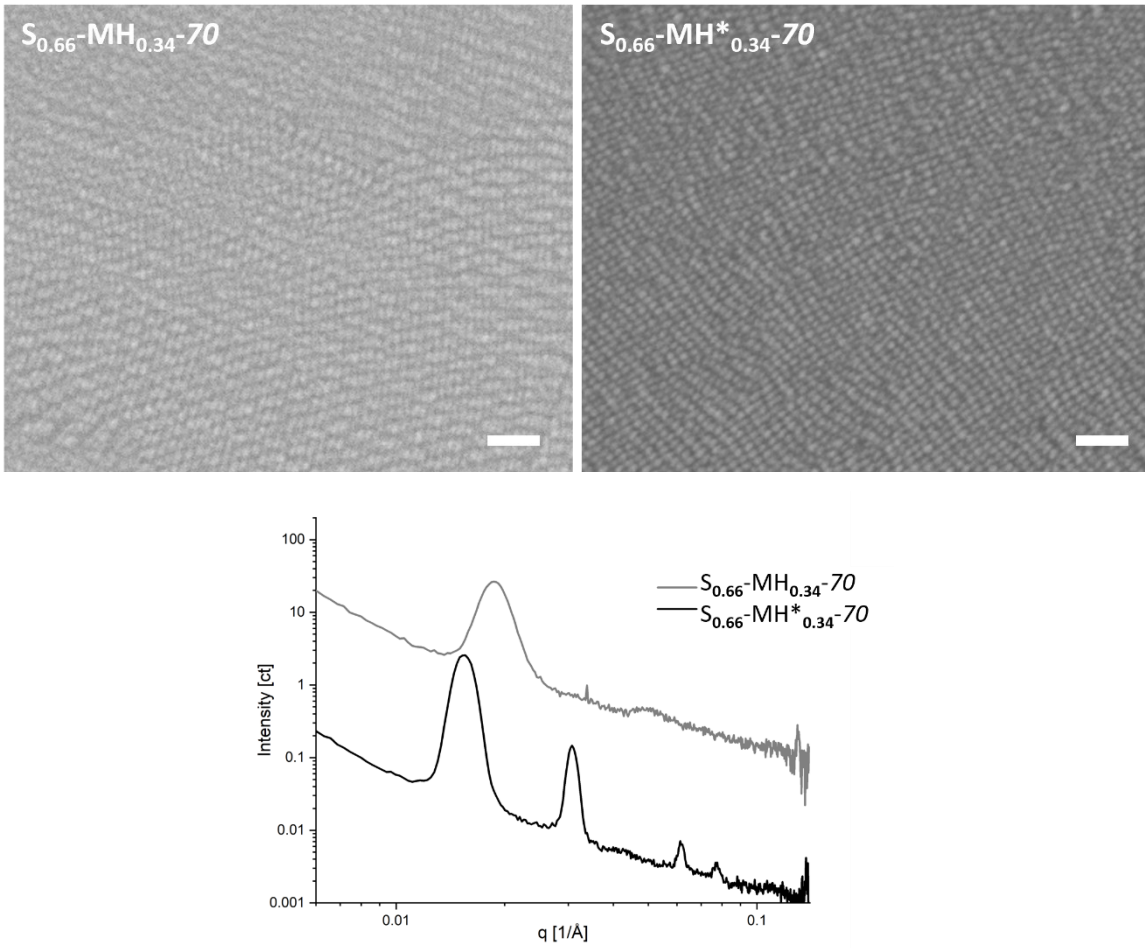

Figure A105: SEM images and SAXS spectra for $S_{0.66}$-$MH_{0.34}$-*70* and $S_{0.66}$-$MH^*_{0.34}$-*70*. Scale bars = 200 nm.

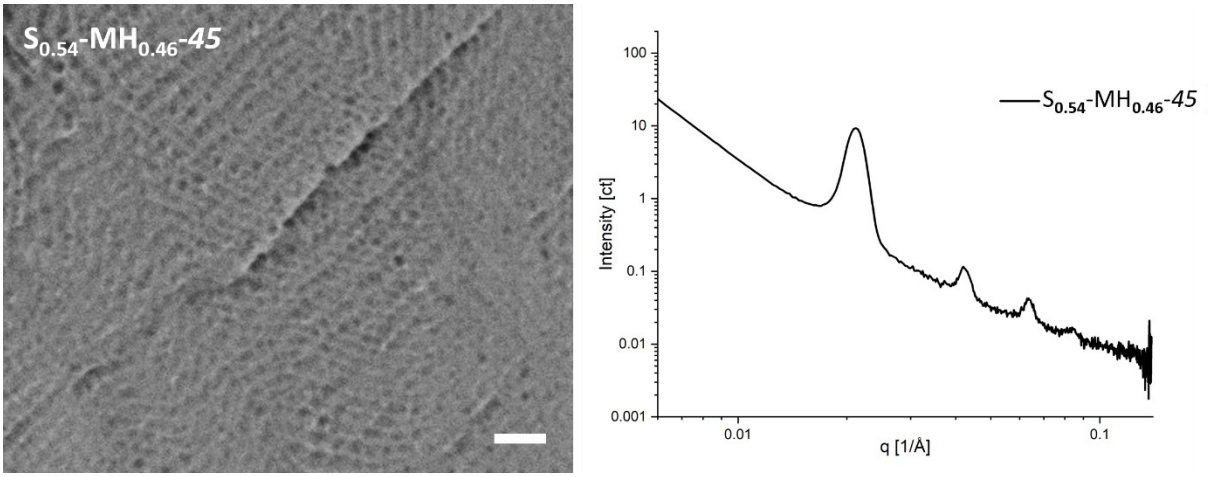

Figure A106: SEM images and SAXS spectra for $S_{0.54}$-$MH_{0.46}$-*45*. Scale bars = 200 nm.

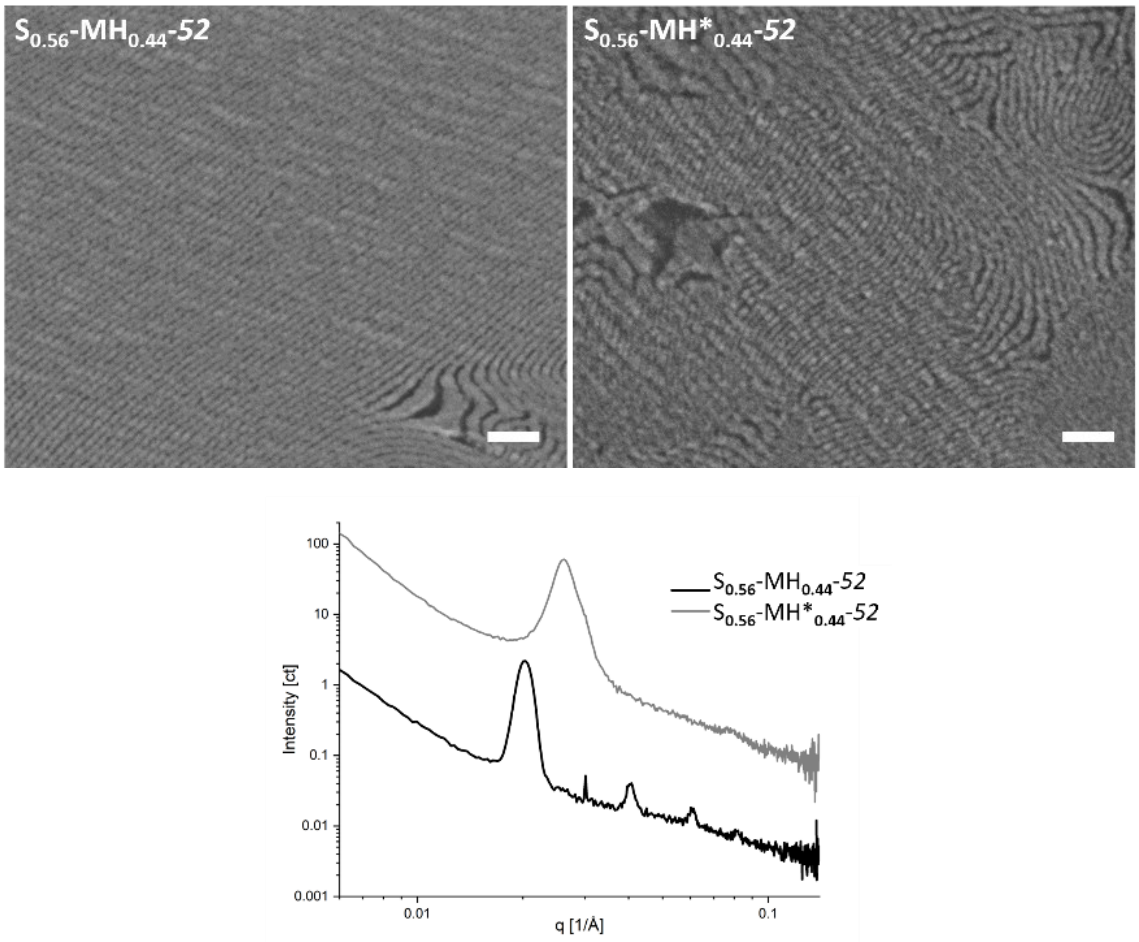

Figure A107: SEM images and SAXS spectra for $S_{0.56}$-$MH_{0.44}$-*52* and $S_{0.56}$-$MH^*_{0.44}$-*52*. Scale bars = 200 nm.

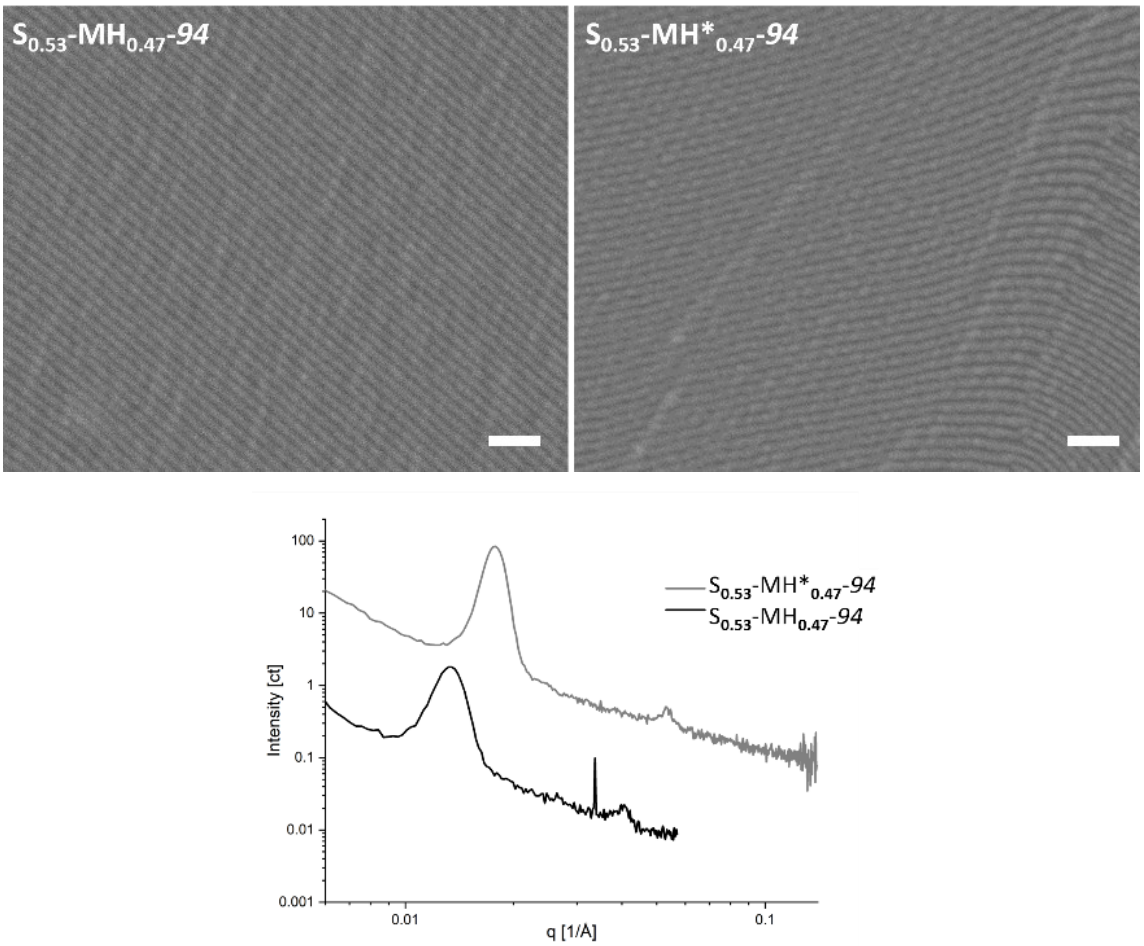

Figure A108: SEM images and SAXS spectra for $S_{0.53}$-$MH_{0.47}$-*94* and $S_{0.53}$-$MH^*_{0.47}$-*94*. Scale bars = 200 nm.

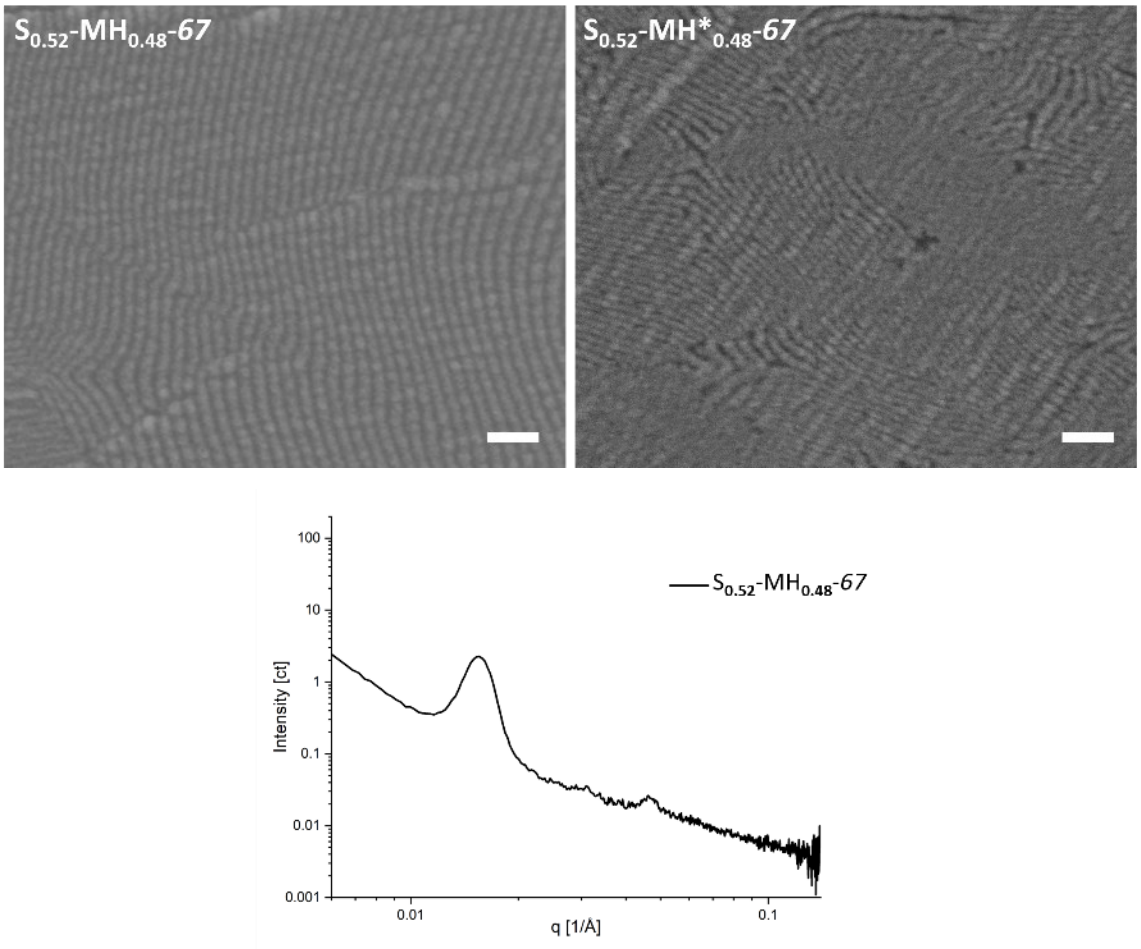

Figure A109: SEM images and SAXS spectra for $S_{0.52}$-$MH_{0.48}$-*67* and $S_{0.52}$-$MH^*_{0.48}$-*67*. Scale bars = 200 nm.

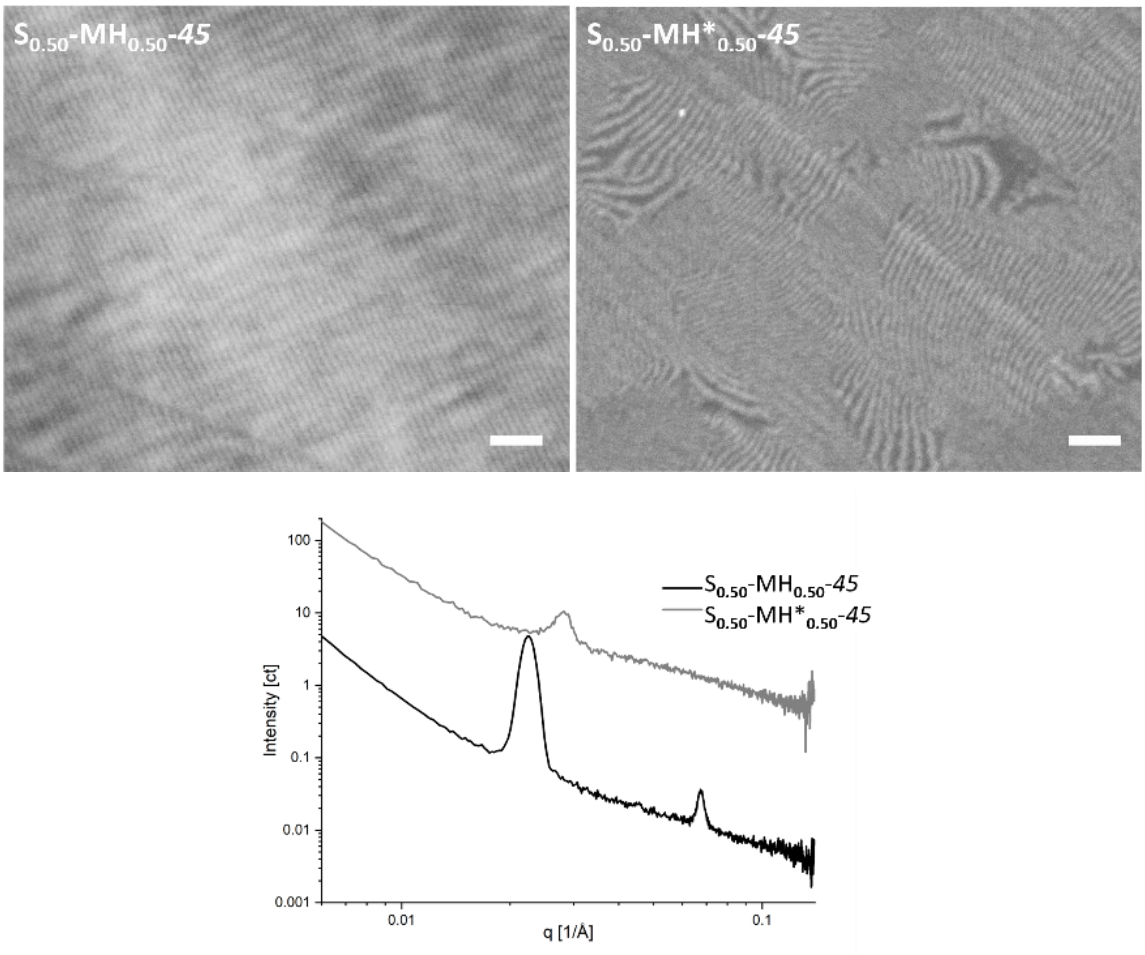

Figure A110: SEM images and SAXS spectra for $S_{0.50}$-$MH_{0.50}$-*45*and $S_{0.50}$-$MH^*_{0.50}$-*45*. Scale bars = 200 nm.

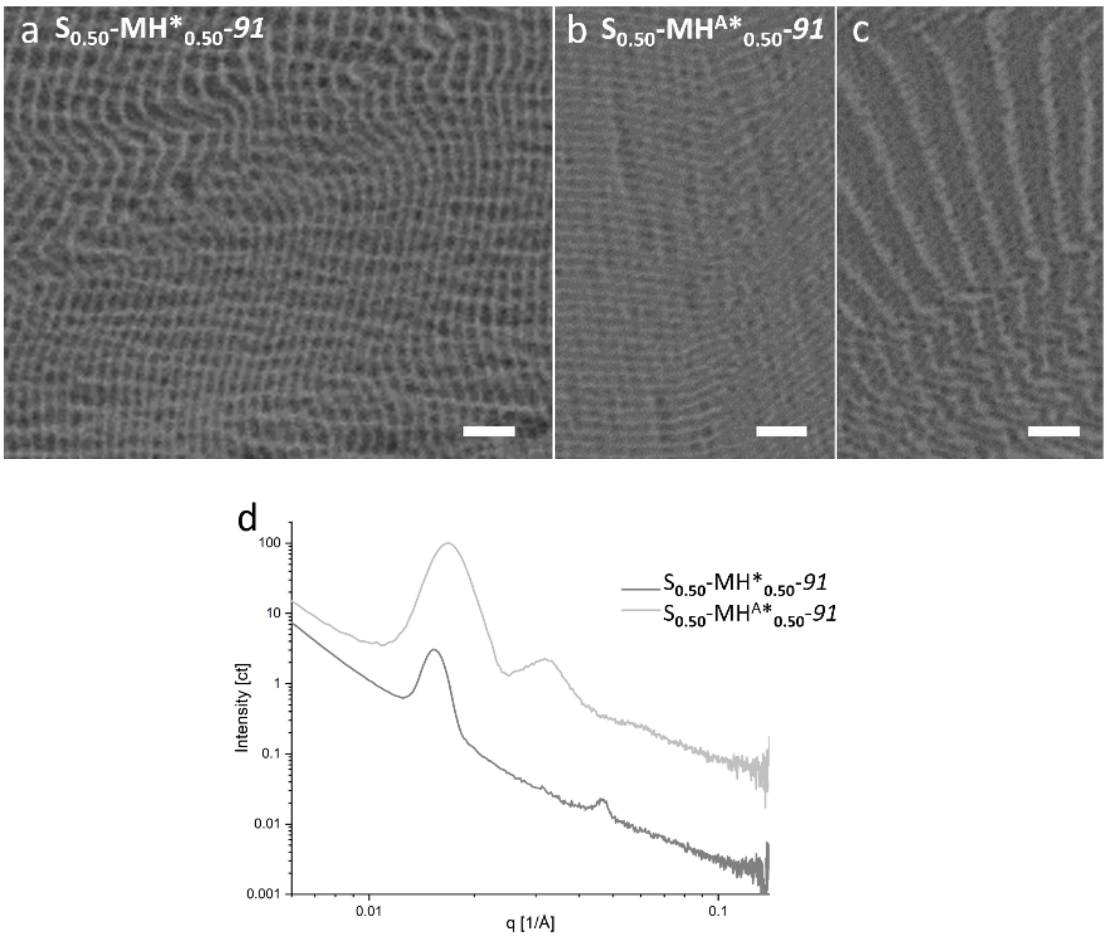

Figure A111: SEM images and SAXS spectra for $S_{0.50}$-$MH^*_{0.50}$-*91* and $S_{0.50}$-$MH^{A*}_{0.50}$-*91*. Scale bars = 200 nm.

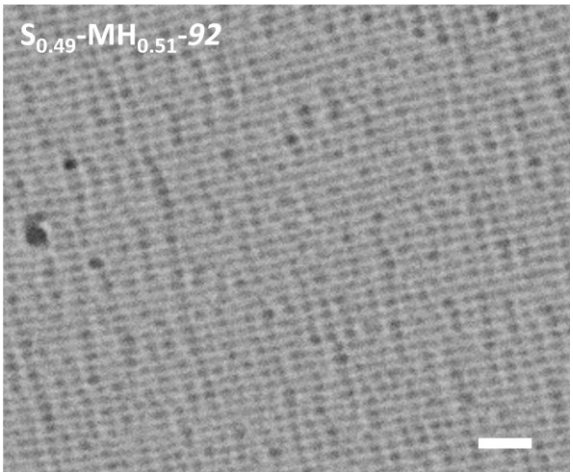

Figure A112: SEM images and SAXS spectra for $S_{0.49}$-$MH_{0.51}$-*92*. Scale bar = 200 nm.

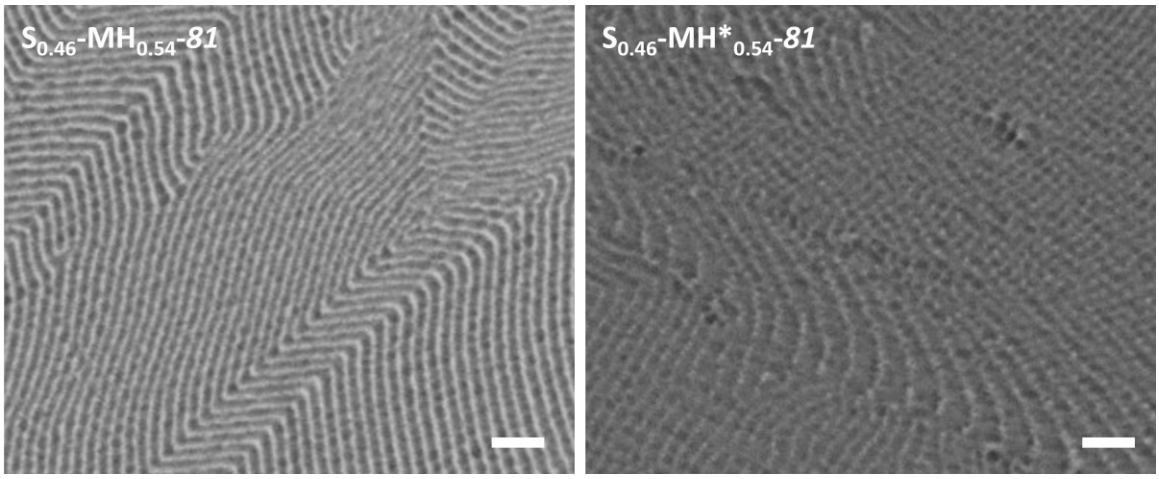

Figure A113: SEM images and SAXS spectra for $S_{0.46}$-$MH_{0.54}$-*81* and $S_{0.46}$-$MH^*_{0.54}$-*81*. Scale bars = 200 nm.

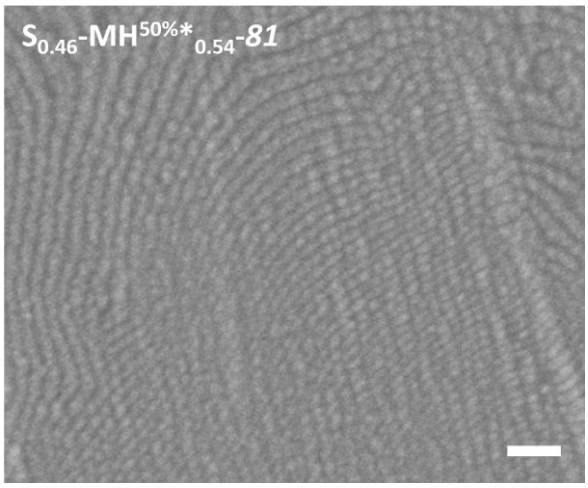

Figure A114: SEM image for $S_{0.46}$-$MH^{50\%*}_{0.54}$-*81*. Scale bars = 200 nm.

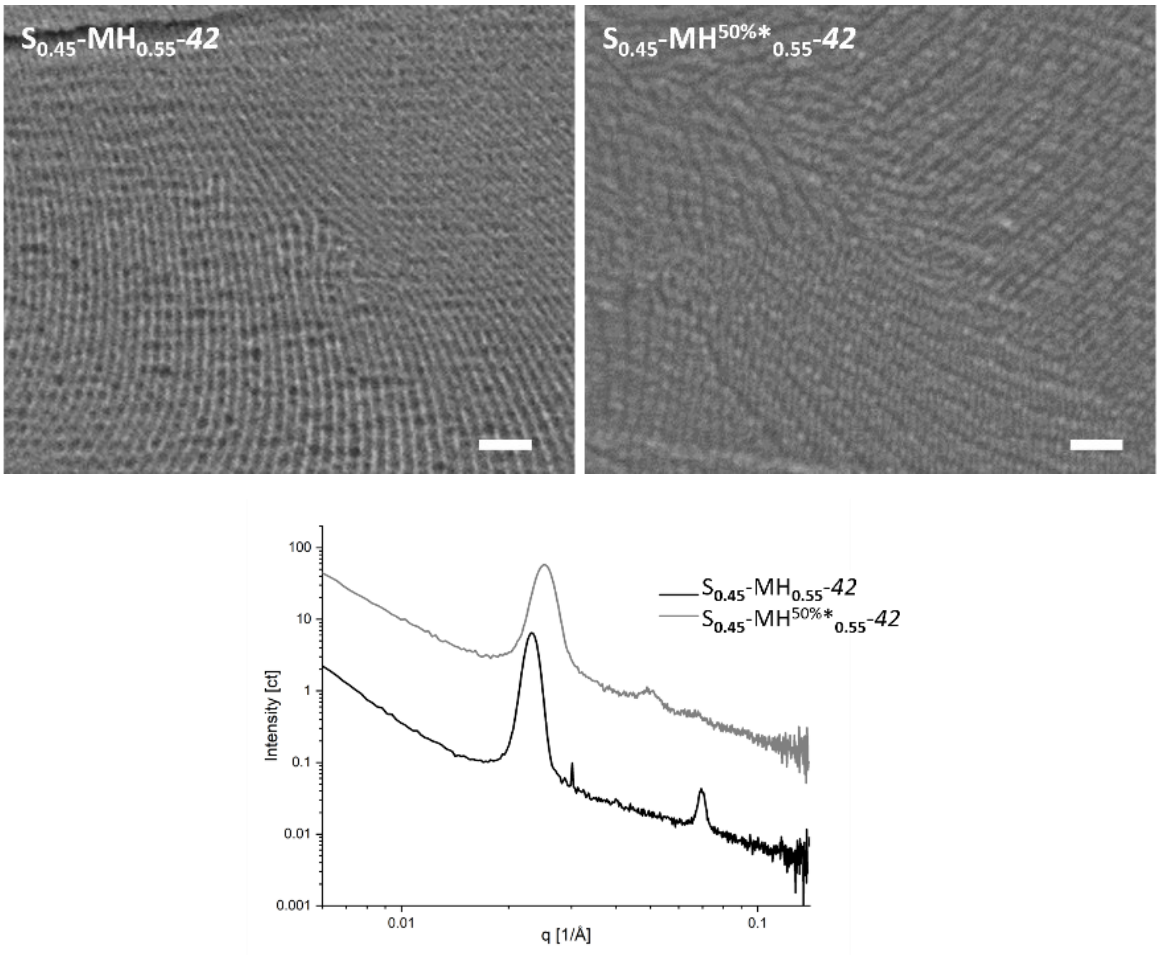

Figure A115: SEM images and SAXS spectra for $S_{0.45}$-$MH_{0.55}$-*42* and $S_{0.45}$-$MH^{50\%*}_{0.55}$-*42*. Scale bars = 200 nm.

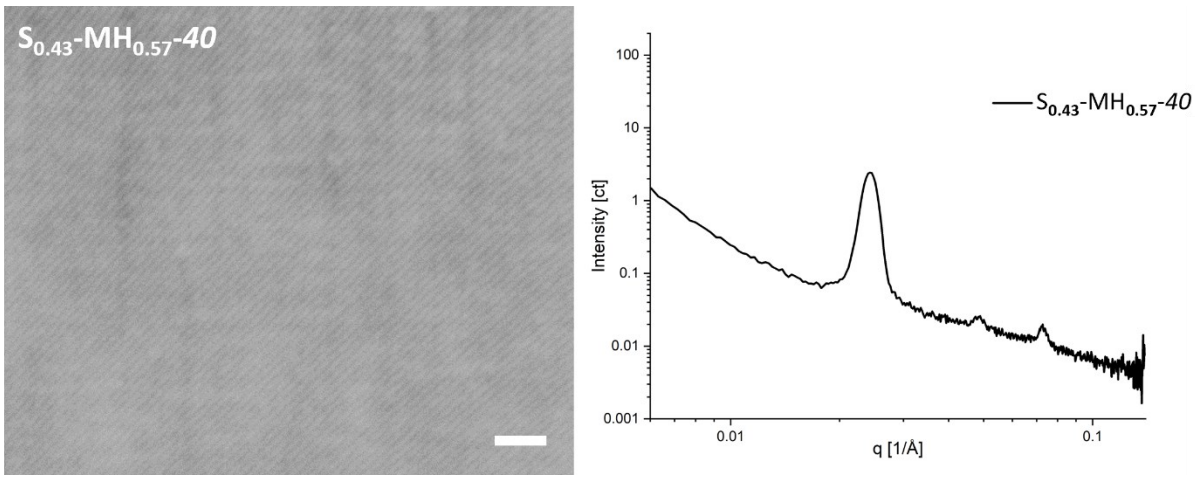

Figure A116: SEM images and SAXS spectra for $S_{0.43}$-$MH_{0.57}$-*40*. Scale bars = 200 nm.

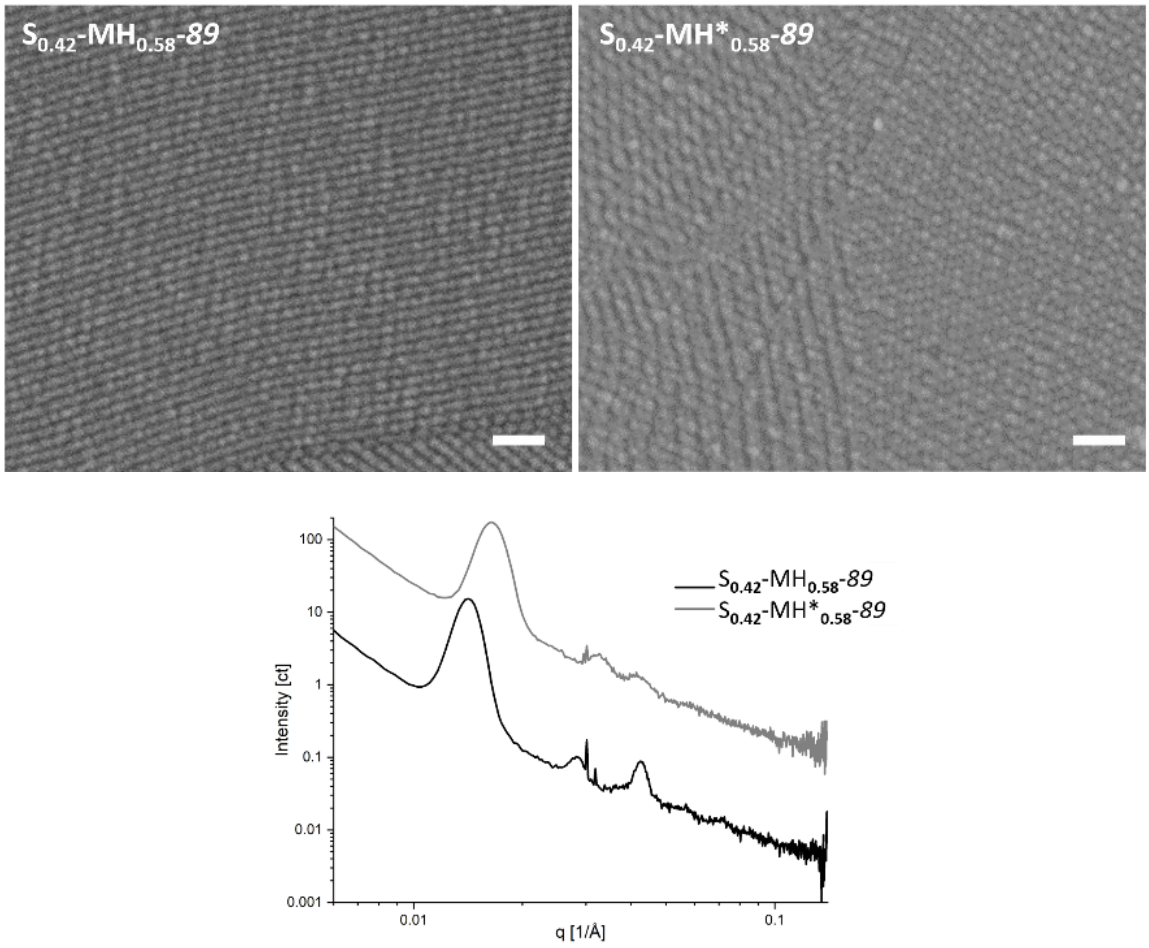

Figure A117: SEM images and SAXS spectra for $S_{0.42}$-$MH_{0.58}$-*89* and $S_{0.42}$-$MH^*_{0.58}$-*89*. Scale bars = 200 nm.

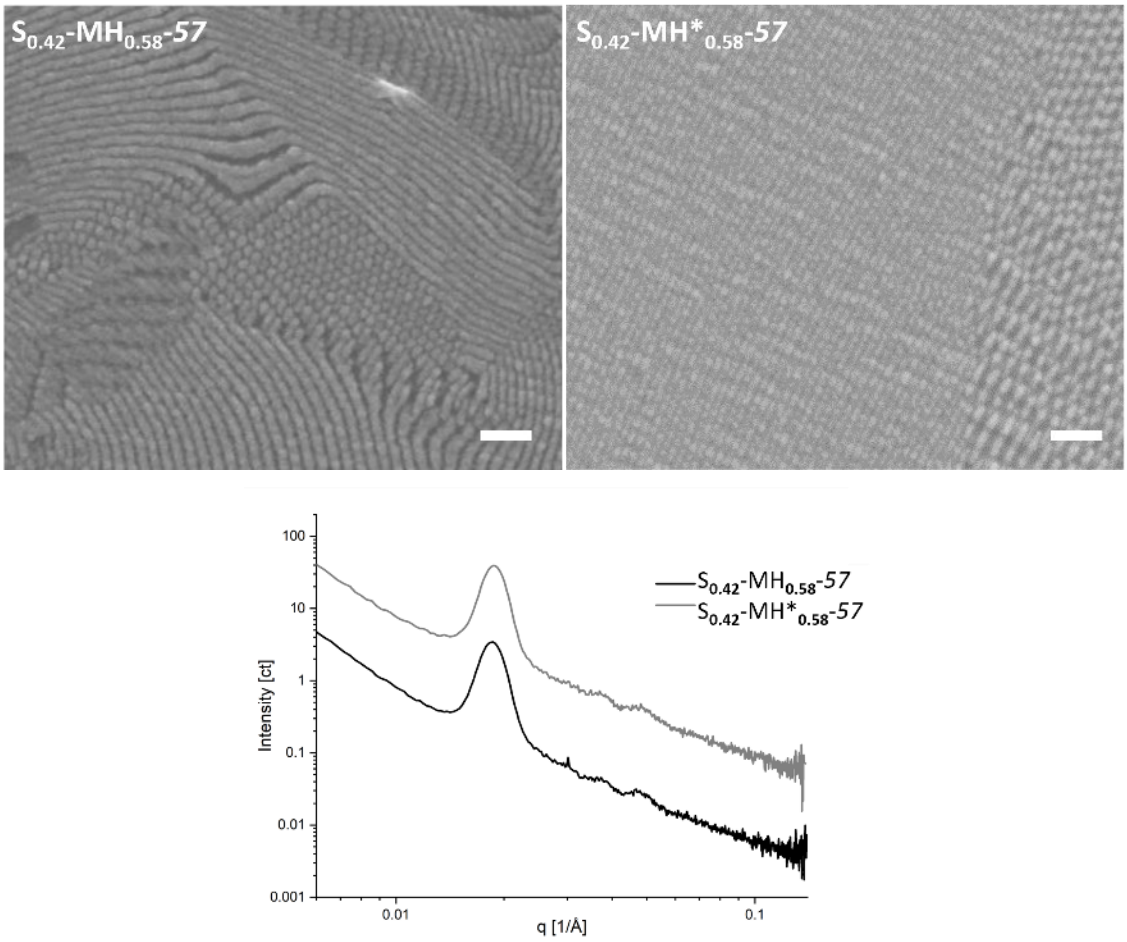

Figure A118: SEM images and SAXS spectra for $S_{0.42}$-$MH_{0.58}$-*57* and $S_{0.42}$-$MH^*_{0.58}$-*57*. Scale bars = 200 nm.

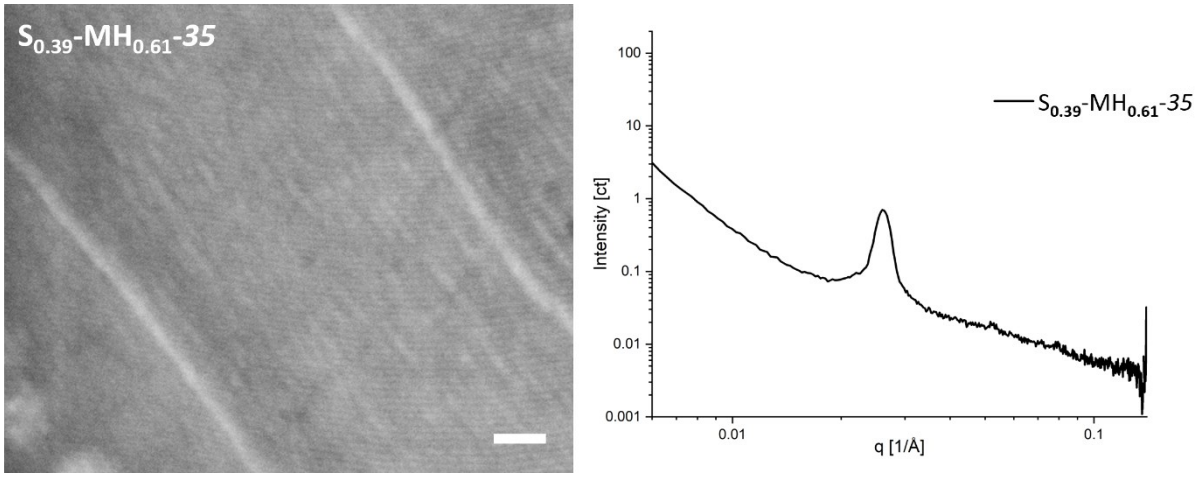

Figure A119: SEM images and SAXS spectra for $S_{0.39}$-$MH_{0.61}$-*35*. Scale bar = 200 nm.

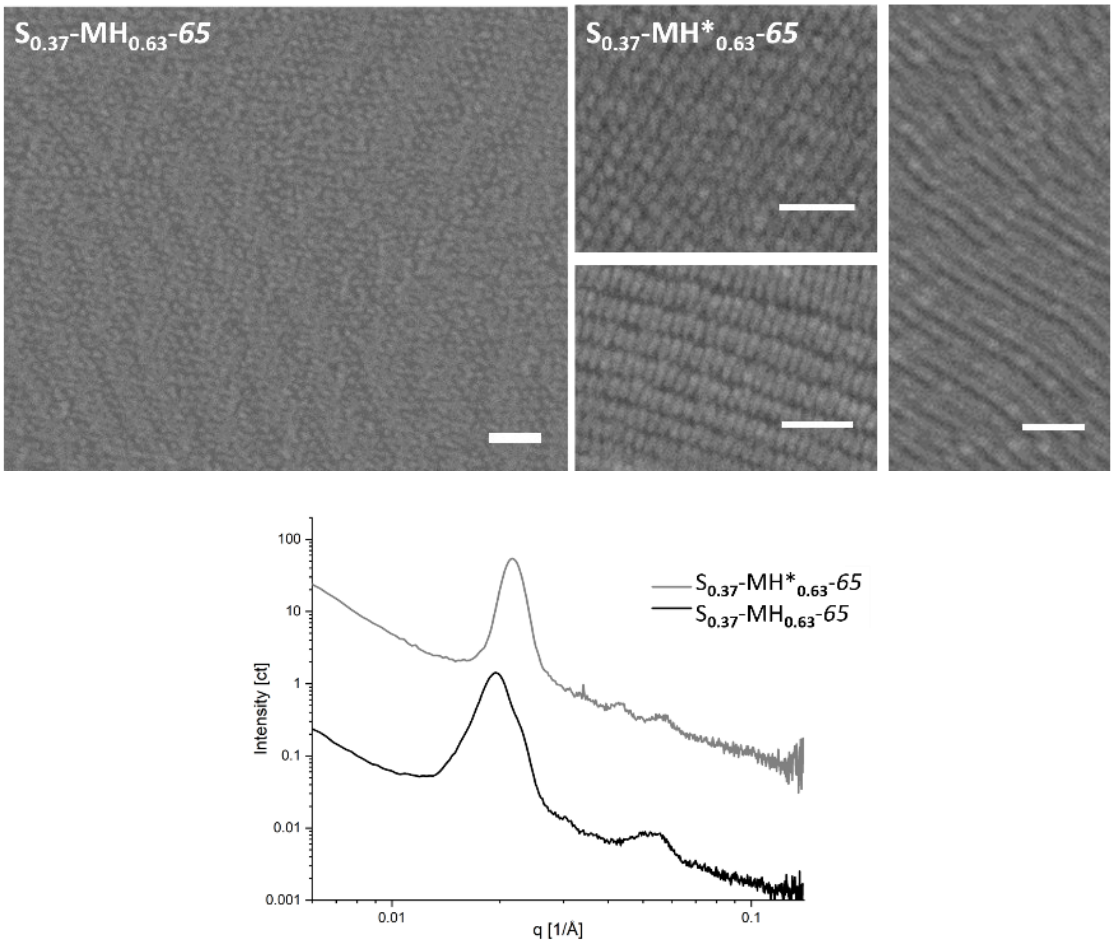

Figure A120: SEM images and SAXS spectra for $S_{0.37}$-$MH_{0.63}$-*65* and $S_{0.37}$-$MH^*_{0.63}$-*65*. Scale bars = 200 nm.

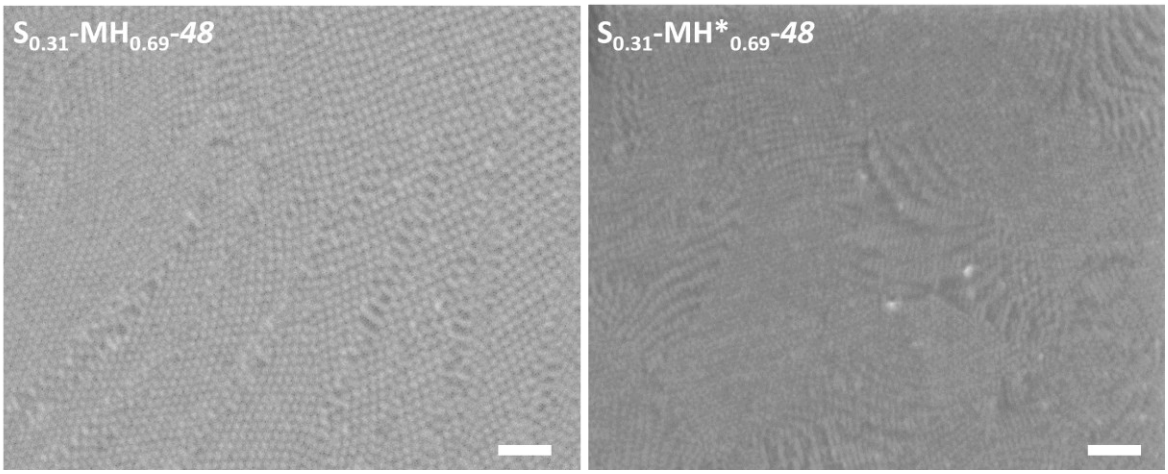

Figure A121: SEM images for $S_{0.31}$-$MH_{0.69}$-*48* and $S_{0.31}$-$MH^*_{0.69}$-*48*. Scale bars = 200 nm.

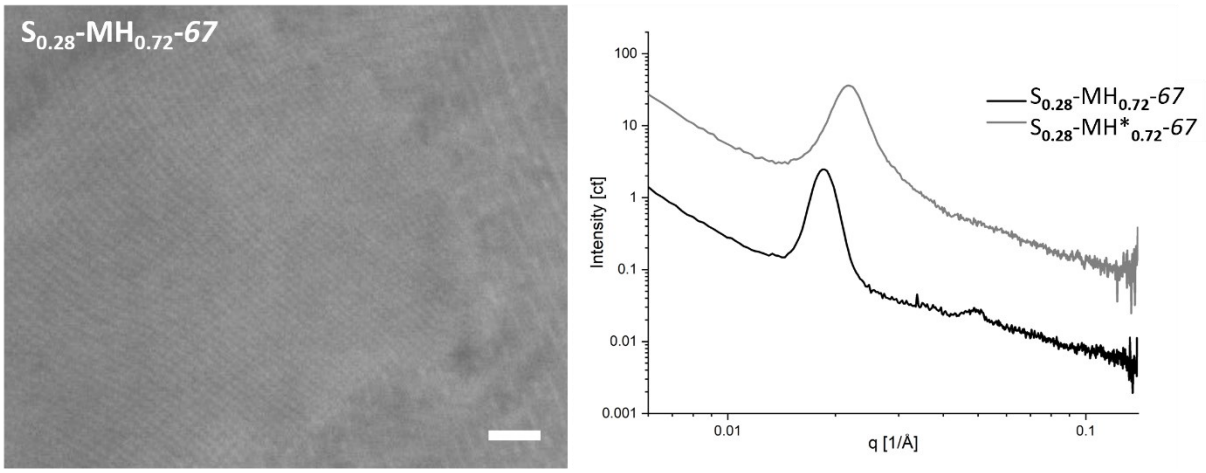

Figure A122: SEM images and SAXS spectra for $S_{0.28}$-$MH_{0.72}$-*67* and $S_{0.28}$-$MH^*_{0.72}$-*67*. Scale bar = 200 nm.

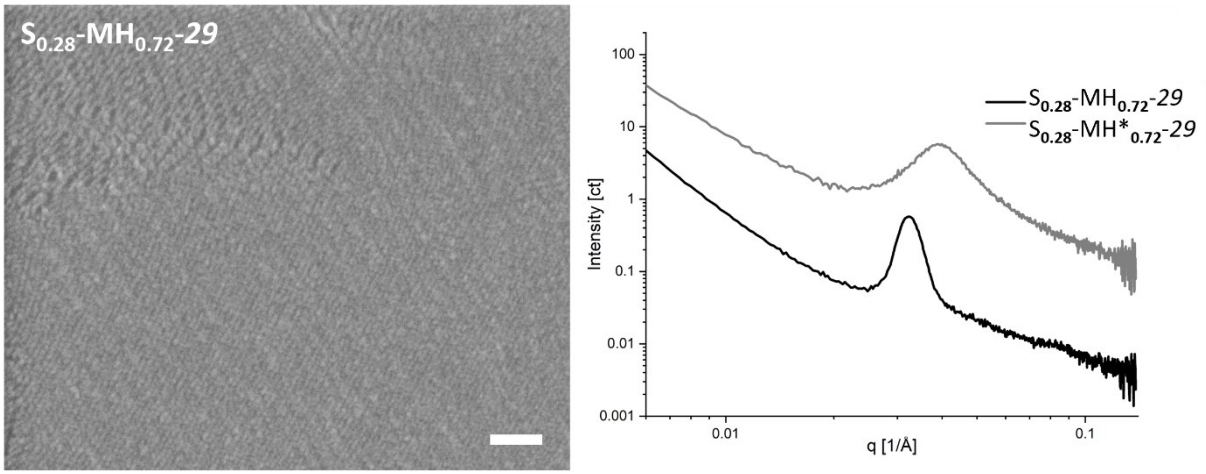

Figure A123: SEM images and SAXS spectra for $S_{0.28}$-$MH_{0.72}$-*29* and $S_{0.28}$-$MH^*_{0.72}$-*29*. Scale bar = 200 nm.

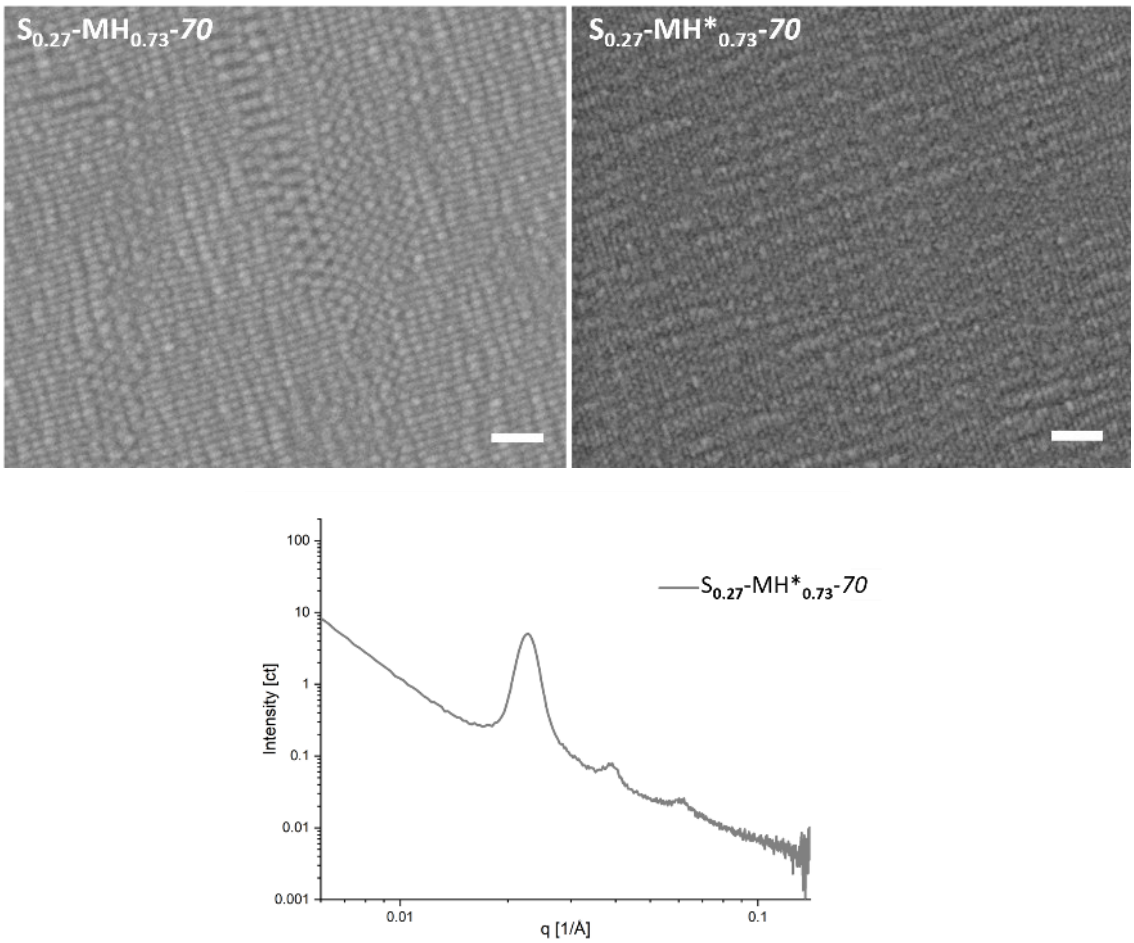

Figure A124: SEM images and SAXS spectra for $S_{0.27}$-$MH_{0.73}$-*70* and $S_{0.27}$-$MH^*_{0.73}$-*70*. Scale bars = 200 nm.

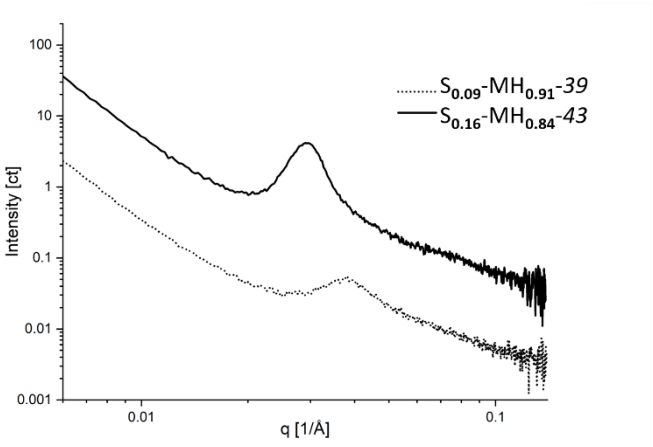

Figure A125: SEM images and SAXS spectra for $S_{0.16}$-$MH_{0.84}$-*43* and $S_{0.09}$-$MH_{0.91}$-*39*.

7.4 Procedures for the ATRP and click-chemistry approaches

3-(1,1,1-trimethylsilyl)-2-propynyl 2-bromo-2-methylpropanoate

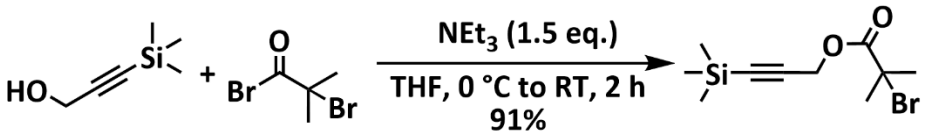

To a solution of 3-trimethylsilyl-2-propyn-1-ol (777 mg, 6.06 mmol, 1.0 eq.) and triethyl amine (905 mg, 8.93 mmol, 1.5 eq.) in THF (40 mL) in a 250 mL roundbottom flask, 2-bromoisobutyryl bromide (2.05 g, 8.93 mmol, 1.5 eq.) in THF (20 mL) was added dropwise at 0 °C. After complete addition, the white mixture was stirred for an additional hour at room temperature. Methanol (5 mL) was added to quench excess 2-bromoisobutyryl bromide. The triethyl amine salt was removed by filtering and the solvents were evaporated. The yellow oil was diluted with DCM, washed with sat. aq. NH_4Cl (2 x 75 mL) and H_2O (2 x 75 mL) and filtered over $MgSO_4$. The solvent was removed and the obtained yellow oil was purified via column chromatography (silica, EtOAc/c-hexan = 1/19). 3-(1,1,1-trimethylsilyl)-2-propynyl 2-bromo-2-methylpropanoate (1.53 g, 5.52 mmol, 91%) was yielded as a colourless oil.

^{1}H NMR 400 MHz ($CDCl_3$): δ [ppm] = 4.77 (s, 2H), 1.96 (s, 6H), 0.19 (s, 9H).

Deprotection of TMS - protected polymer endgroup

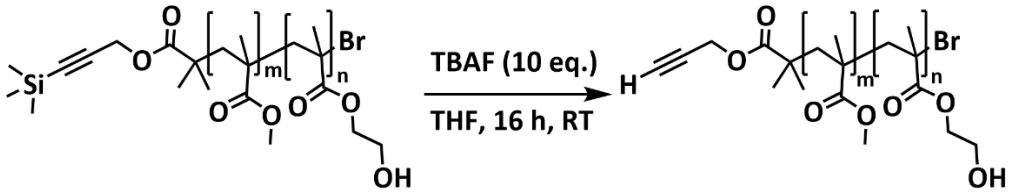

The polymer was diluted in THF to a 0.01 M solution. TBAF in THF (1 M, 10 eq.) was added dropwise and the solution was stirred for 16 h. The THF was removed in vacuo and the crude was dissolved in DCM and washed with a mixture of water/brine. The solvent was reduced in vacuo and the polymer mixture was purified via dialysis.

^{1}H NMR 400 MHz ($CDCl_3$): δ [ppm] = 4.12 (s, 0.5H), 3.85 (s, 0.5H), 3.60 (s, 2.3H), 2.15 - 0.77 (m, 9.4H).

Transformation of the bromine-endgroup into an azide

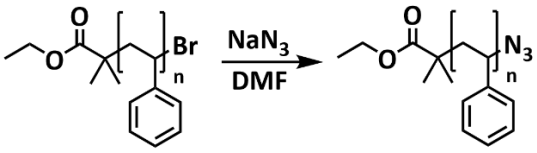

Bromine-terminated polymer (0.048 mmol) was dissolved in DMF (10 mL). NaN_3 (0.048 mmol, 10 eq., 31 mg) was added and the mixture was stirred at RT for 24 h. The reaction mix was diluted with DCM (15 mL) washed with H_2O (4 x 25 mL). After reducing the solvent, the polymer was precipitated in MeOH and yielded as a colorless solid.

Copper mediated coupling

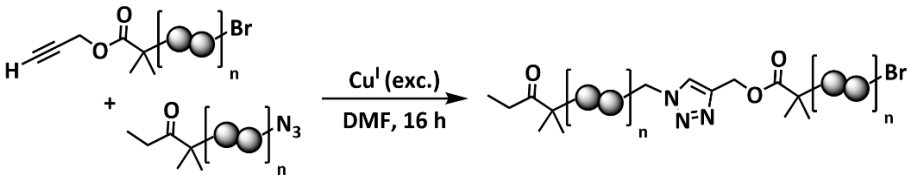

N_3-terminated polymer (0.006 mmol, 1.0 eq.), alkyne-terminated polymer (0.006 mmol, 1.0 eq.), $CuSO_4$*5 H_2O (7.5 mg, 0.03 mmol, 5.0 eq.) and Na-L-ascorbate (6 mg, 0.03 mmol, 5.0 eq.) were placed in a round bottom flask. The air was removed by purging the flask with argon and dry DMF (1 mL per 100 mg polymer) was added. The mixture was stirred at RT for 24 h to 4 d and the reaction mixture was precipitated into MeOH. The block copolymer was dried under vacuum and yielded as a light green solid.

One-pot ATRP synthesis of P(MMA-*b*-S)

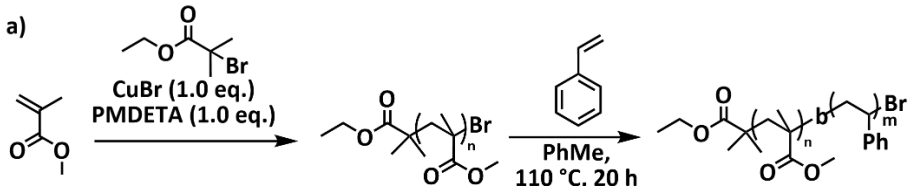

CuBr (35.9 mg, 0.25 mmol, 1.0 eq.) was added to a Schlenk flask and evacuated. MMA (2.00 g, 20 mmol, 80 eq.), PMDETA (43.3 mg, 0.25 mmol, 1.0 eq.) and EaBriB (48.8 mg, 0.25 mol, 1.0 eq.) were added together with PhMe (4 mL). The solution was degassed with freeze-pump-thaw three times and backfilled with N_2. The mixture was stirred at 90 °C for 19 h, and a mixture of styrene (2.6 g, 25 mmol, 100 eq.) in PhMe (2.5 mL) was added after degassing via freeze-pump-thaw. The mixture was stirred at 90 °C for 4 h and 110 °C for 16 h.

M_n = 20758, PD = 1.51, $M_{n\,PMMA}$ = 10065, PD = 1.15.

^{1}H NMR 400 MHz ($CDCl_3$): δ [ppm] = 7.22 - 6-68 (m, 3H), 6.82 - 6.25 (m, 2H), 4.12 (s, 0.5H), 3.85 (s, 0.5H), 3.60 (s, 2.3H), 2.15 - 0.77 (m, 9.4H).

One-pot ATRP synthesis of P(S-*b*-MMA)

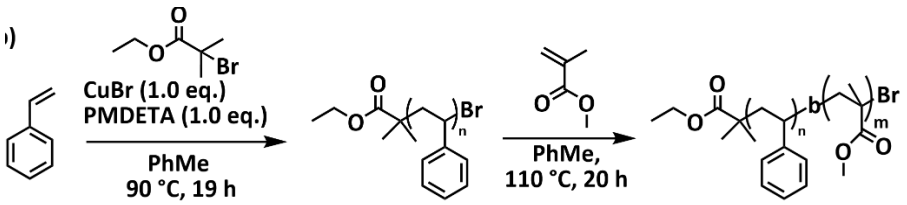

CuBr (41.6 mg, 0.29 mmol, 1.0 eq.) was added to a Schlenk flask and evacuated. Styrene (3.00 g, 28.8 mmol, 99 eq.), PMDETA (50.2 mg, 0.29 mmol, 1.0 eq.) and EaBriB (56.5 mg, 0.29 mol, 1.0 eq.) were added together with PhMe (3 mL). The solution was degassed with freeze-pump-thaw three times and backfilled with N_2. The mixture was stirred at 110 °C for 19 h, and a mixture of MMA (2.3 g, 23 mmol, 100 eq.) in PhMe (3 mL) was added after degassing via freeze-pump-thaw. The mixture was stirred at 110 °C for 20 h.

M_n = 22833, PD = 1.58, $M_{n\ PMMA}$ = 10848, PD = 1.12.

^{1}H NMR 400 MHz ($CDCl_3$): δ [ppm] = 7.22 - 6-68 (m, 3H), 6.82 - 6.25 (m, 2H), 4.12 (s, 0.5H), 3.85 (s, 0.5H), 3.60 (s, 2.3H), 2.15 - 0.77 (m, 9.4H).

Synthesis of Polystyrene via ATRP

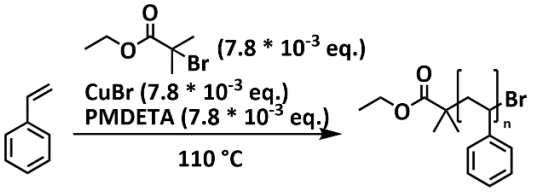

CuBr (7.3 mg, 0.051 mmol, 1.0 eq.), styrene (6.6 g, 63.4 mmol, 1235 eq.), PMDETA (8.9 mg, 0.051 mmol, 1.0 eq.) and EaBriB (10 mg, 0.051 mol, 1.0 eq.) were added to a Schlenk flask. The solution was degassed with freeze-pump-thaw three times and backfilled with N_2. The mixture was stirred at 110 °C for 2 h, quenched in $N_{2\ liq.}$ and opened to the atmosphere. The mixture was diluted in DCM, filtered over $Al_2O_{3\ neutral}$ and precipitated in MeOH after removal of the solvent. Polystyrene was obtained as a colorless solid.

M_n = 11073, PD = 1.15

^{1}H NMR 400 MHz ($CDCl_3$): δ [ppm] = 7.19 - 6.85 (m, 3H), 6.84 - 6.30 (m, 2H), 2.29 - 1.66 (m, 2H), 1.64 - 1.19 (m, 2H).

Chain extension of Polystyrene with MMA via ATRP

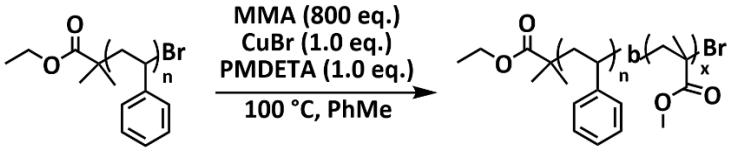

CuBr (1.4 mg, 0.01 mmol, 1.0 eq.) and polystyrene (11073 g/mol, 110 mg, 0.01 mmol, 1.0 eq.) were added to a Schlenk tube.PhMe (1.5 mL), MMA (0.795 g, 7.95 mmol, 800 eq.), and PMDETA (1.7 mg, 0.01 mmol, 1.0 eq.) were added. The solution was degassed with freeze-pump-thaw three times and backfilled with N_2. The mixture was stirred at 100 °C for 1 h, quenched in $N_{2\ liq.}$ and opened to the atmosphere. The mixture was diluted in DCM, filtered over $Al_2O_{3\ neutral}$ and precipitated in MeOH after removal of the solvent. P(S-*b*-MMA) was obtained as a colorless solid.

^{1}H NMR 400 MHz ($CDCl_3$): δ [ppm] = 7.22 - 6-68 (m, 3H), 6.82 - 6.25 (m, 2H), 4.12 (s, 0.5H), 3.85 (s, 0.5H), 3.60 (s, 2.3H), 2.15 - 0.77 (m, 9.4H).

Synthesis of poly(methylmethacrylate) via ATRP

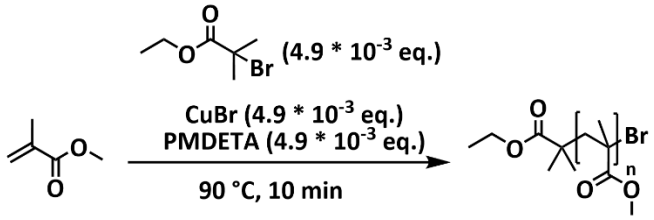

CuBr (28.4 mg, 0.198 mmol, 4.9 * 10^{-3} eq.) was added to a dry schlenk vial. A solution of MMA (4.00 g, 40.0 mmol, 1.0 eq.), PMDETA (34.4 mg, 0.198 mmol, 4.9 * 10^{-3} eq.) and EαB*i*B (38.6 mg, 0.198 mmol, 4.9 * 10^{-3} eq.) was added. The mixture was degassed with four freeze-pump-thaw cycles, refilled with argon and stirred at 90 °C for 10 min. The reaction was quenched in $N_{2\ fl.}$, warmed to room temperature and the vial was opened to atmosphere. The solution was diluted with DCM, filtered over neutral Al_2O_3 and most of the solvent was removed in vacuo. The polymer solution was added dropwise to an excess of *c*-hexan and the supernatant was removed from the precipitated polymer by decantation or filtration. The polymer was dried under vacuum and PMMA was yielded as a white solid.

^{1}H NMR 400 MHz ($CDCl_3$): δ [ppm] = 3.59 (s, 3H), 2.09 - 1.75 (b, 2H), 1.09- 1.76 (b, 2H).

Bibliography

[1] H. Staudinger, *Berichte der deutschen chemischen Gesellschaft (A and B Series)* **1926**, *59*, 3019–3043.

[2] Eds.: M. Ni£, J. Jirát, B. Ko²ata, A. Jenkins, A. McNaught, IUPAC, *IUPAC Compendium of Chemical Terminology*, Research Triagle Park, NC, **2009**.

[3] H. Ritter, *Makromoleküle I*, Springer, Berlin, Heidelberg, **2018**.

[4] M. Shen, M. B. Bever, *J Mater Sci* **1972**, *7*, 741–746.

[5] D. Braun, H. Cherdron, M. Rehahn, H. Ritter, B. Voit, *Polymer Synthesis: Theory and Practice: Fundamentals, Methods, Experiments*, Springer, Berlin, Heidelberg, **2013**.

[6] M. Szwarc, *Nature* **1956**, *178*, 1168–1169.

[7] N. Corrigan, K. Jung, G. Moad, C. J. Hawker, K. Matyjaszewski, C. Boyer, *Progress in Polymer Science* **2020**, *111*, 101311.

[8] J. Qiu, B. Charleux, K. Matyjaszewski, *Polimery* **2001**, *46*, 453–460.

[9] H. Fischer, *Macromolecules* **1997**, *30*, 5666–5672.

[10] J. Nicolas, Y. Guillaneuf, C. Lefay, D. Bertin, D. Gigmes, B. Charleux, *Progress in Polymer Science* **2013**, *38*, 63–235.

[11] K. Matyjaszewski, *Macromolecules* **2012**, *45*, 4015–4039.

[12] G. Moad, E. Rizzardo, S. H. Thang, G. Moad, E. Rizzardo, S. H. Thang, *Aust. J. Chem.* **2012**, *65*, 985–1076.

[13] D. J. Keddie, *Chem. Soc. Rev.* **2013**, *43*, 496–505.

[14] S. Z. Zard, *Aust. J. Chem.* **2006**, *59*, 663–668.

[15] S. Perrier, *Macromolecules* **2017**, *50*, 7433–7447.

[16] J.-S. Wang, K. Matyjaszewski, *J. Am. Chem. Soc.* **1995**, *117*, 5614–5615.

[17] M. Kato, M. Kamigaito, M. Sawamoto, T. Higashimura, *Macromolecules* **1995**, *28*, 1721–1723.

[18] Xiaoyun He, Min Zeng, D. Brabazon, in *Reference Module in Materials Science and Materials Engineering*, Elsevier, **2016**.

[19] H. Gleiter, *Acta Materialia* **2000**, *48*, 1–29.

[20] I. W. Hamley, *Nanotechnology* **2003**, *14*, R39.

[21] J.-S. Wang, R. Jerome, Ph. Bayard, Ph. Teyssie, *Macromolecules* **1994**, *27*, 4908–4913.

[22] G. Hild, J.-P. Lamps, *Polymer* **1998**, *39*, 2637–2649.

[23] J. Bolton, J. Rzayev, *ACS Macro Lett.* **2012**, *1*, 15–18.

[24] S. Eggers, F. Lauterbach, V. Abetz, *Polymer* **2016**, *107*, 357–367.

[25] H. C. Kolb, M. G. Finn, K. B. Sharpless, *Angewandte Chemie International Edition* **2001**, *40*, 2004–2021.

[26] J. A. Opsteen, J. C. M. van Hest, *Chem. Commun.* **2005**, 57–59.

[27] M. W. Matsen, *Macromolecules* **2012**, *45*, 2161–2165.

[28] N. A. Lynd, M. A. Hillmyer, **2005**, *38*, 8.

[29] N. A. Lynd, M. A. Hillmyer, *Macromolecules* **2007**, *40*, 8050–8055.

[30] D. T. Gentekos, J. Jia, E. S. Tirado, K. P. Barteau, D.-M. Smilgies, R. A. DiStasio, B. P. Fors, *J. Am. Chem. Soc.* **2018**, *140*, 4639–4648.

[31] D. Bendejacq, V. Ponsinet, M. Joanicot, Y.-L. Loo, R. A. Register, *Macromolecules* **2002**, *35*, 6645–6649.

[32] S. Li, R. A. Register, B. G. Landes, P. D. Hustad, J. D. Weinhold, *Macromolecules* **2010**, *43*, 4761–4770.

[33] A.-V. Ruzette, S. Tencé-Girault, L. Leibler, F. Chauvin, D. Bertin, O. Guerret, P. Gérard, *Macromolecules* **2006**, *39*, 5804–5814.

[34] J. M. Widin, A. K. Schmitt, A. L. Schmitt, K. Im, M. K. Mahanthappa, *J. Am. Chem. Soc.* **2012**, *134*, 3834–3844.

[35] M. F. Schulz, A. K. Khandpur, F. S. Bates, K. Almdal, K. Mortensen, D. A. Hajduk, S. M. Gruner, *Macromolecules* **1996**, *29*, 2857–2867.

[36] D. A. Hajduk, M. B. Kossuth, M. A. Hillmyer, F. S. Bates, *J. Phys. Chem. B* **1998**, *102*, 4269–4276.
[37] L. Liberman, M. L. Coughlin, S. Weigand, J. Edmund, F. S. Bates, T. P. Lodge, *Macromolecules* **2022**, *55*, 4947–4955.
[38] L. Liberman, M. L. Coughlin, S. Weigand, F. S. Bates, T. P. Lodge, *Macromolecules* **2022**, *55*, 2821.
[39] T. Smart, H. Lomas, M. Massignani, M. V. Flores-Merino, L. R. Perez, G. Battaglia, *Nano Today* **2008**, *3*, 38–46.
[40] C. C. Kathrein, Phase Transitions and Ordering of Microphase Separated Block Copolymer Nanostructures in Electric, RWTH Aachen, **2016**.
[41] D. Salomon Marques, U. Vainio, N. Moreno Chaparro, V. Manuel Calo, A. Reza Bezahd, J. W. Pitera, K.-V. Peinemann, S. P. Nunes, *Soft Matter* **2013**, *9*, 5557.
[42] M. Radjabian, C. Abetz, B. Fischer, A. Meyer, V. Abetz, *ACS Appl. Mater. Interfaces* **2017**, *9*, 31224.
[43] B. B. Patel, T. Pan, Y. Chang, D. J. Walsh, J. J. Kwok, K. S. Park, K. Patel, D. Guironnet, C. E. Sing, Y. Diao, *ACS Polym. Au* **2022**, *2*, 232.
[44] E. Han, K. O. Stuen, Y.-H. La, P. F. Nealey, P. Gopalan, *Macromolecules* **2008**, *41*, 9090–9097.
[45] K. Brassat, J. K. N. Lindner, *Advanced Materials Interfaces* **2020**, *7*, 1901565.
[46] J. Hahm, S. J. Sibener, *Journal of Chemical Physics* **2001**, *114*, 4730–4740.
[47] C.-J. Hung, A. S. Panda, Y.-C. Lee, S.-Y. Liu, J.-W. Lin, H.-F. Wang, A. Avgeropoulos, F.-G. Tseng, F.-R. Chen, R.-M. Ho, *ACS Macro Lett.* **2023**, 570–576.
[48] C. Sinturel, M. Vayer, M. Morris, M. A. Hillmyer, *Macromolecules* **2013**, *46*, 5399–5415.
[49] M. A. Chavis, D.-M. Smilgies, U. B. Wiesner, C. K. Ober, *Advanced Functional Materials* **2015**, *25*, 3057–3065.
[50] J. Y. Cheng, C. A. Ross, E. L. Thomas, H. I. Smith, G. J. Vancso, *Applied Physics Letters* **2002**, *81*, 3657–3659.
[51] P. W. Majewski, M. Gopinadhan, W.-S. Jang, J. L. Lutkenhaus, C. O. Osuji, *J. Am. Chem. Soc.* **2010**, *132*, 17516–17522.
[52] V. Olszowka, M. Hund, V. Kuntermann, S. Scherdel, L. Tsarkova, A. Böker, *ACS Nano* **2009**, *3*, 1091–1096.
[53] J. Oh, M. Shin, I. S. Kim, H. S. Suh, Y. Kim, J. K. Kim, J. Bang, B. Yeom, J. G. Son, *ACS Nano* **2021**, *15*, 8549.
[54] L. Dong, A. Chandra, K. Wylie, Y. Nabae, T. Hayakawa, *International Journal of Polymer Science* **2022**, *2022*, e8286518.
[55] H. Feng, M. Dolejsi, N. Zhu, P. J. Griffin, G. S. W. Craig, W. Chen, S. J. Rowan, P. F. Nealey, *Advanced Functional Materials* **2022**, *32*, 2206836.
[56] F. McCallum, J. Zhao, Md. D. Hossain, J. A. Kaitz, J. F. Cameron, P. III. Trefonas, I. Blakey, H. Peng, A. K. Whittaker, *Macromolecules* **2023**, *56*, 2651–2662.
[57] K. Bosson, P. Marcasuzaa, A. Bousquet, G. E. M. Tovar, V. Atanasov, L. Billon, *European Polymer Journal* **2022**, *179*, 111560.
[58] S. C. Ligon, R. Liska, J. Stampfl, M. Gurr, R. Mülhaupt, *Chem. Rev.* **2017**, *117*, 10212.
[59] B. Sun, Q. Ma, X. Wang, J. Liu, M. R. M. Rejab, *IOP Conf. Ser.: Mater. Sci. Eng.* **2021**, *1078*, 012007.
[60] F. H. Froes, R. Boyer, *Additive Manufacturing for the Aerospace Industry*, Elsevier, **2019**.
[61] ASTM Committee F42 on Additive Manufacturing Technologies, & ASTM Committee F42 on Additive Manufacturing Technologies. Subcommittee F42. 91 on Terminology., **2021**.
[62] C. Barner-Kowollik, M. Bastmeyer, E. Blasco, G. Delaittre, P. Müller, B. Richter, M. Wegener, *Angewandte Chemie International Edition* **2017**, *56*, 15828–15845.
[63] H. Kodama, *Review of Scientific Instruments* **1981**, *52*, 1770–1773.
[64] Herbert, Alan J., *Jour Appl Photo Eng* **1982**, 185.
[65] C. W. Hull, *Apparatus for Production of Three-Dimensional Objects by Stereolithography United States Patent, Appl., No. 638905*, **1984.**
[66] André, J. C., Alain Le Méhauté, and Olivier De Witte., *Dispositif Pour Réaliser Un Modèle de Pièce Industrielle. French Patent 8411241*, **1984.**
[67] M. Göppert-Mayer, *Annalen der Physik* **2009**, *521*, 466–479.
[68] W. Kaiser, C. G. B. Garrett, *Phys. Rev. Lett.* **1961**, *7*, 229–231.

[69] "Rapid sub-diffraction-limit laser micro/nanoprocessing in a threshold material system | Applied Physics Letters | AIP Publishing," can be found under https://pubs.aip.org/aip/apl/article/80/2/312/514879/Rapid-sub-diffraction-limit-laser-micro.
[70] T. Gissibl, S. Thiele, A. Herkommer, H. Giessen, *Nature Photon* **2016**, *10*, 554–560.
[71] S. Maruo, O. Nakamura, S. Kawata, *Opt. Lett., OL* **1997**, *22*, 132–134.
[72] M. Carlotti, V. Mattoli, *Small* **2019**, *15*, 1902687.
[73] F. Jin, J. Liu, Y.-Y. Zhao, X.-Z. Dong, M.-L. Zheng, X.-M. Duan, *Nat Commun* **2022**, *13*, 1357.
[74] O. Tricinci, F. Pignatelli, V. Mattoli, *Advanced Functional Materials* **2023**, *33*, 2206946.
[75] L. Yang, H. Hu, A. Scholz, F. Feist, G. Cadilha Marques, S. Kraus, N. M. Bojanowski, E. Blasco, C. Barner-Kowollik, J. Aghassi-Hagmann, M. Wegener, *Nat Commun* **2023**, *14*, 1103.
[76] W. Gao, H. Chao, Y.-C. Zheng, W.-C. Zhang, J. Liu, F. Jin, X.-Z. Dong, Y.-H. Liu, S.-J. Li, M.-L. Zheng, *ACS Appl. Mater. Interfaces* **2021**, *13*, 27796–27805.
[77] Y. Jia, C. A. Spiegel, A. Welle, S. Heißler, E. Sedghamiz, M. Liu, W. Wenzel, M. Hackner, J. P. Spatz, M. Tsotsalas, E. Blasco, *Advanced Functional Materials* **2022**, 2207826.
[78] J. Fischer, M. Wegener, *Laser & Photonics Reviews* **2013**, *7*, 22–44.
[79] W. H. Bragg, W. L. Bragg, *Proc. R. Soc. Lond. A* **1913**, *88*, 428–438.
[80] C. M. Jeffries, J. Ilavsky, A. Martel, S. Hinrichs, A. Meyer, J. S. Pedersen, A. V. Sokolova, D. I. Svergun, *Nat Rev Methods Primers* **2021**, *1*, 1–39.
[81] H. Hasegawa, T. Hashimoto, H. Kawai, T. P. Lodge, E. J. Amis, C. J. Glinka, C. C. Han, *Macromolecules* **1985**, *18*, 67.
[82] M. Knoll, E. Ruska, *Z. Physik* **1932**, *78*, 318–339.
[83] G. H. Michler, Ed. , in *Electron Microscopy of Polymers*, Springer, Berlin, Heidelberg, **2008**, pp. 87–120.
[84] M. Dendisová, A. Jeništová, A. Parchaňská-Kokaislová, P. Matějka, V. Prokopec, M. Švecová, *Analytica Chimica Acta* **2018**, *1031*, 1–14.
[85] C. Szymanski, C. Wu, J. Hooper, M. A. Salazar, A. Perdomo, A. Dukes, J. McNeill, *J. Phys. Chem. B* **2005**, *109*, 8543–8546.
[86] J. Kim, W. Lee, H. Kim, D. Y. Ryu, H. Ahn, B. Chae, *Spectrochimica Acta Part A: Molecular and Biomolecular Spectroscopy* **2022**, *274*, 121095.
[87] P. Fratzl, R. Weinkamer, *Progress in Materials Science* **2007**, *52*, 1263–1334.
[88] N. K. Katiyar, G. Goel, S. Hawi, S. Goel, *NPG Asia Mater* **2021**, *13*, 1–16.
[89] F. Versluis, J. H. van Esch, R. Eelkema, *Advanced Materials* **2016**, *28*, 4576–4592.
[90] J. F. Galisteo-López, M. Ibisate, R. Sapienza, L. S. Froufe-Pérez, Á. Blanco, C. López, *Advanced Materials* **2011**, *23*, 30–69.
[91] S. Ganda, M. H. Stenzel, *Progress in Polymer Science* **2020**, *101*, 101195.
[92] J. Monti, E. Blasco, *Polymer Chemistry* **2020**, *11*, 7316–7329.
[93] Z. Dong, H. Cui, H. Zhang, F. Wang, X. Zhan, F. Mayer, B. Nestler, M. Wegener, P. A. Levkin, *Nat Commun* **2021**, *12*, 247.
[94] Z. Dong, M. Vuckovac, W. Cui, Q. Zhou, R. H. A. Ras, P. A. Levkin, *Advanced Materials* **2021**, *33*, 2106068.
[95] V. A. Bobrin, K. Lee, J. Zhang, N. Corrigan, C. Boyer, *Advanced Materials* **2022**, *34*, 2107643.
[96] X. Shi, V. A. Bobrin, Y. Yao, J. Zhang, N. Corrigan, C. Boyer, *Angewandte Chemie International Edition* **2022**, *61*, e202206272.
[97] B. B. Patel, D. J. Walsh, D. H. Kim, J. Kwok, B. Lee, D. Guironnet, Y. Diao, *Sci. Adv.* **2020**, *6*, eaaz7202.
[98] H. K. Raut, H. Wang, Q. Ruan, H. Wang, J. G. Fernandez, J. K. W. Yang, *Nano Lett.* **2021**, *21*, 8602.
[99] I. Kawarazaki, M. Hayashi, K. Yamamoto, A. Takasu, *ChemistrySelect* **2020**, *5*, 2842–2847.
[100] M. B. Sims, B. Zhang, Z. M. Gdowski, T. P. Lodge, F. S. Bates, *Macromolecules* **2022**, *55*, 3317.
[101] C. J. Hawker, T. P. Russell, *MRS Bulletin* **2005**, *30*, 952.
[102] C. R. Kagan, T. Hyeon, D.-H. Kim, R. Ruiz, M. C. Tung, H.-S. P. Wong, *MRS Bulletin* **2020**, *45*, 807.
[103] J. N. L. Albert, T. H. Epps, *Materials Today* **2010**, *13*, 24.
[104] L. Wan, R. Ruiz, H. Gao, K. C. Patel, T. R. Albrecht, J. Yin, J. Kim, Y. Cao, G. Lin, *ACS Nano* **2015**, *9*, 7506.

[105] H. Tsai, J. W. Pitera, H. Miyazoe, S. Bangsaruntip, S. U. Engelmann, C.-C. Liu, J. Y. Cheng, J. J. Bucchignano, D. P. Klaus, E. A. Joseph, D. P. Sanders, M. E. Colburn, M. A. Guillorn, *ACS Nano* **2014**, *8*, 5227.
[106] D. Varadharajan, G. Delaittre, *Polym. Chem.* **2016**, *7*, 7488.
[107] H. Wu, F. Xu, G. Gao, X. Feng, *Macromolecules* **2021**, *54*, 5856.
[108] J. S. Trent, J. I. Scheinbeim, P. R. Couchman, *Macromolecules* **1983**, *16*, 589–598.
[109] T. M. Chou, P. Prayoonthong, A. Aitouchen, M. Libera, *Polymer* **2002**, *43*, 2085–2088.
[110] G. F. Bahr, *Experimental Cell Research* **1954**, *7*, 457–479.
[111] D. A. Hajduk, P. E. Harper, S. M. Gruner, C. C. Honeker, G. Kim, E. L. Thomas, L. J. Fetters, *Macromolecules* **1994**, *27*, 4063–4075.
[112] F. S. Bates, *Macromolecules* **1987**, *20*, 2221–2225.
[113] F. S. Bates, *Macromolecules* **1985**, *18*, 525–528.
[114] I. W. Hamley, V. Castelletto, *Progress in Polymer Science* **2004**, *29*, 909–948.
[115] R. W. Richards, J. L. Thomason, *Macromolecules* **1983**, *16*, 982–992.
[116] C. M. Papadakis, K. Almdal, K. Mortensen, D. Posselt, *J. Phys. II France* **1997**, *7*, 1829–1854.
[117] N. Ocelic, A. Huber, R. Hillenbrand, *Applied Physics Letters* **2006**, *89*, 101124.

Eidestattliche Versicherung